

# FINAL REPORT

A Complex Approach to UXO Discrimination: Combining  
Advanced EMI Forward Models and Statistical Signal Processing

SERDP Project MR-1572

JANUARY 2012

Fridon Shubitidze  
**Sky Research, Inc.**

**Partner:** *Thayer School of Engineering, Dartmouth  
College*

*This document has been cleared for public release*



<b>Report Documentation Page</b>		<i>Form Approved OMB No. 0704-0188</i>
<p>Public reporting burden for the collection of information is estimated to average 1 hour per response, including the time for reviewing instructions, searching existing data sources, gathering and maintaining the data needed, and completing and reviewing the collection of information. Send comments regarding this burden estimate or any other aspect of this collection of information, including suggestions for reducing this burden, to Washington Headquarters Services, Directorate for Information Operations and Reports, 1215 Jefferson Davis Highway, Suite 1204, Arlington VA 22202-4302. Respondents should be aware that notwithstanding any other provision of law, no person shall be subject to a penalty for failing to comply with a collection of information if it does not display a currently valid OMB control number.</p>		
1. REPORT DATE <b>JAN 2012</b>	2. REPORT TYPE	3. DATES COVERED <b>00-00-2012 to 00-00-2012</b>
4. TITLE AND SUBTITLE <b>A Complex Approach to UXO Discrimination: Combining Advanced EMI Forward Models and Statistical Signal Processing</b>		
5a. CONTRACT NUMBER 5b. GRANT NUMBER 5c. PROGRAM ELEMENT NUMBER		
6. AUTHOR(S) 		
5d. PROJECT NUMBER 5e. TASK NUMBER 5f. WORK UNIT NUMBER		
7. PERFORMING ORGANIZATION NAME(S) AND ADDRESS(ES) <b>Sky Research, Inc,445 Dead Indian Memorial Road,Ashland,OR,97520</b>		
8. PERFORMING ORGANIZATION REPORT NUMBER		
9. SPONSORING/MONITORING AGENCY NAME(S) AND ADDRESS(ES)		
10. SPONSOR/MONITOR'S ACRONYM(S)		
11. SPONSOR/MONITOR'S REPORT NUMBER(S)		
12. DISTRIBUTION/AVAILABILITY STATEMENT <b>Approved for public release; distribution unlimited</b>		
13. SUPPLEMENTARY NOTES		

## 14. ABSTRACT

**The research described in this report was conducted in fulfillment of Project MM-1572, ?A Complex Approach to UXO Discrimination: Combining Advanced EMI Forward and Statistical Signal Processing,? submitted to the Strategic Environmental Research and Development Program (SERDP) in response to the Munitions Management Statement of Need MMSON-07-04 ?Advanced Technologies for Detection, Discrimination, and Remediation of Munitions and Explosives of Concern (MEC): UXO Technology?. The primary objective of the project MM-1572 was to develop and validate innovative, robust and practical approaches for UXO localization and classification under realistic (noisy, cluttered background) field conditions by combining advanced electromagnetic induction (EMI) forward and statistical signal processing methodologies. In a real field the electromagnetic signals become convoluted with noise due to the instrument, magnetic soil and widespread background clutter. Therefore, the rationale for a statistical approach is to use an advanced statistical approach to reduce the impact of these noises to minimum. This project provides mathematical fundamentals, physical meanings and practical realizations of forward, inverse and statistical signal processing approaches for unexploded ordnance (UXO) detection and discrimination at live-UXO sites. Namely, under this project first we developed and implemented advanced, physically complete forward EMI models such as, the normalized surface magnetic source (charge/dipole) model (NSMS), and ortho-normalized volume magnetic source (ONVMS) technique for accurately representing the EMI responses of subsurface metallic targets, then we combined these advanced models with EMI data inversion approaches, such as the gradient search direct search-differential evolution and etc, for advanced EMI sensor data inversion; third we extended the advanced statistical signal processing approaches, i.e. support vector machines, Gaussian mixture models, for discriminating UXO targets from non-hazardous anomalies. Finally, the combined advanced EMI forward and statistical models were applied to ESTCP live site UXO data sets. Live site discrimination studies showed the excellent discrimination performance of the advanced models when applied to next-generation-sensor data collected at various live sites, such as Camp Sibert, AL, San Luis Obispo (SLO), CA, and Camp Butner, NC as well as APG test sites. The technology was able to single out UXO ranging in caliber from 25 mm up to 155 mm. In addition, the ONVMS technique was seen to provide excellent classification in both single- and multiple-target scenarios when combined with advanced multi-axis/transmitter/receiver sensors data.**

## 15. SUBJECT TERMS

16. SECURITY CLASSIFICATION OF:			17. LIMITATION OF ABSTRACT	18. NUMBER OF PAGES	19a. NAME OF RESPONSIBLE PERSON
a. REPORT <b>unclassified</b>	b. ABSTRACT <b>unclassified</b>	c. THIS PAGE <b>unclassified</b>	<b>Same as Report (SAR)</b>	<b>147</b>	

This report was prepared under contract to the Department of Defense Strategic Environmental Research and Development Program (SERDP). The publication of this report does not indicate endorsement by the Department of Defense, nor should the contents be construed as reflecting the official policy or position of the Department of Defense. Reference herein to any specific commercial product, process, or service by trade name, trademark, manufacturer, or otherwise, does not necessarily constitute or imply its endorsement, recommendation, or favoring by the Department of Defense.

## Table of Contents

Table of Contents .....	ii
List of Figures .....	v
List of Tables .....	xi
List of Acronyms .....	xii
Abstract .....	1
Acknowledgements .....	2
1      Introduction .....	3
1.1    Background and objectives .....	3
1.2    Report structure .....	4
2      Forward models .....	5
2.1    Introduction .....	5
2.2    The single-dipole approximation .....	7
2.3    Normalized surface magnetic source model .....	9
2.3.1    Governing equations .....	9
2.3.2    Theoretical basis of NSMS .....	11
2.3.3    Formulation for bodies of revolution; determining NSMS amplitudes from data .....	13
2.3.4    The dipole model as a limiting case of NSMS .....	16
2.3.5    Invariance properties of the total NSMS .....	18
2.3.6    Interpretation of the total NSMS .....	19
2.3.7    The parameterized NSMS .....	19
2.4    The orthonormalized volume magnetic source model .....	20
2.4.1    Orthonormal Green functions .....	22
2.4.2    ONVMS procedure .....	24
2.5    Joint diagonalization for multi-target data pre-processing .....	25
2.5.1    The multi-static response matrix .....	25
2.5.2    Interpretation and diagonalization of the MSR matrix .....	26
2.5.3    Algorithm for joint diagonalization .....	29

3	Inverse Models.....	31
3.1	Introduction .....	31
3.2	Gradient-based methods of optimization.....	32
3.2.1	Stepwise optimization.....	34
3.2.2	Simultaneous optimization .....	34
3.2.3	Condensed algorithm.....	34
3.3	Differential evolution .....	35
3.4	The HAP method.....	37
3.4.1	Estimating the location and orientation of buried objects .....	37
3.4.2	A simplified HAP method .....	39
3.4.3	Determining the HAP amplitudes.....	39
3.4.4	The HAP method with gradient information .....	41
4	Statistical approaches.....	42
4.1	Introduction .....	42
4.2	Mixed modeling applied to advanced EMI features.....	43
4.3	Gaussian mixture models.....	48
4.3.1	Model-based supervised clustering .....	48
4.3.2	Unsupervised classification using the multivariate normal mixture approach .....	49
4.4	Support vector machines for subsurface object classification .....	51
5	Advanced models applied to next-generation sensors: Modeling and validation.....	54
5.1	Introduction .....	54
5.2	MetalMapper .....	54
5.3	TEMTADS .....	59
5.3.1	TEMTADS modeling .....	59
5.3.2	APG test-site classification.....	61
5.4	BUD.....	67
5.5	MPV .....	71
6	ESTCP live-site classification studies using advanced models .....	74
6.1	Introduction .....	74
6.2	Camp Sibert.....	74
6.2.1	Target location and characterization; preliminary pattern-matching classification .....	75

6.2.2	SVM classification .....	79
6.2.3	SVM analysis of Camp Sibert data: summary.....	84
6.2.4	Mixed model approach applied to Camp Sibert data.....	85
6.3	Camp San Luis Obispo (TEMTADS, MM, BUD) .....	87
6.3.1	The total NSMS for discrimination .....	89
6.3.2	SLO discrimination results .....	89
6.3.3	Comparisons between NSMS and Dipole models.....	94
6.3.4	SLO BUD data inversion and classification studies.....	97
6.3.5	SLO retrospective analysis .....	98
6.4	Camp Butner.....	101
6.4.1	TEMTADS data discrimination strategy and classification results using supervised clustering.....	102
6.4.2	MetalMapper data discrimination strategy and classification results using supervised clustering.....	106
6.4.3	A Comparison between ONVMS and Dipole model .....	109
6.4.4	Camp Butner retrospective study using semi-supervised clustering .....	110
7	Conclusions.....	119
8	Publications.....	122
8.1	Journal Articles.....	122
8.2	Ph.D Thesis.....	122
8.3	Conference Papers .....	122
8.4	Presentations and posters.....	124
9	References.....	125

## List of Figures

Figure 1: A dipole's location in a global coordinate system.....	8
Figure 2: The NSMC that are distributed on a prolate spheroidal surface is implemented for a body of revolution. The prolate spheroidal coordinate system is specified by $(\xi, \eta, \phi)$ .....	14
Figure 3: A schematic diagram for a dipole model.....	17
Figure 4: A metallic object under the transmitter. The target's EMI response at the receiver coil can be calculated from the equivalent surface or volume magnetic dipole moment $d\mathbf{m}$ .....	21
Figure 5: The HAP approach for a dipole.....	37
Figure 6: Determining the location and orientation of a buried target. The method assumes the object is a point dipole and exploits an analytic relation between the field measured at $\mathbf{r}_i$ and the scalar potential at the same point to find the location $\mathbf{r}_d$ . The potential is constructed using a layer of equivalent magnetic sources placed between the sensor and the object; $\mathbf{r}_{s'}$ is a typical location on the layer. ....	40
Figure 7: The MetalMapper during SLO site deployment (left) and its schematic diagram (right). ....	55
Figure 8. The MetalMapper geometry. The observation point $\mathbf{r}$ is defined with respect to the global Cartesian coordinate system XYZO; $\mathbf{r}'_{3,i}$ is the location of the $i$ -th current element on (in this case) the $T = 3$ transmitter, which carries a current $I_3$ in the direction $\ell_{3,i}$ .....	56
Figure 9. Response of an 81-mm mortar illuminated by the MM Z-transmitter: measured (left), ONVMS prediction (center), and mismatch between modeled and actual data (right). The mortar is placed 35 cm below the sensor center and oriented 45 degrees nose down. The data are plotted in $\log_{10}$ scale. ....	57
Figure 10. Response of an 81-mm mortar illuminated by the MM Y-transmitter: measured (left), ONVMS prediction (center), and mismatch between modeled and actual data (right). The mortar is placed 35 cm below the sensor center and oriented 45 degrees nose down. The data are plotted in $\log_{10}$ scale. ....	58
Figure 11. Response of an 81-mm mortar illuminated by the MM X-transmitter: measured (left), ONVMS prediction (center), and mismatch between modeled and actual data (right). The mortar is placed 35 cm below the sensor center and oriented 45 degrees nose down. The data are plotted in $\log_{10}$ scale. ....	58
Figure 12: Photo of the TEMTADS in deployment at Blossom Point Test Site (left) and a schematic diagram of its Tx/Rx sensors (right).....	59
Figure 13. Measured (top five rows) and ONVMS-modeled (bottom five) TEMTADS data for a 105-mm projectile at the 25th time channel. The target is buried at a depth of 30 cm and oriented horizontally relative to the TEMTADS system.....	60
Figure 14: The APG TOI.....	61
Figure 15: Comparison between the inverted and actual depth for all 65 APG calibration targets.....	62
Figure 16: Inverted total NSMS for APG test-stand 105 mm projectile and 81 mm mortar.....	63
Figure 17: Scatter plot of inverted $\beta$ vs. $\ln k$ classification features for APG test-stand TOI .....	64

Figure 18: Scatter plot of inverted $\gamma$ vs $\ln k$ (left) and $\beta$ (right) parameters for APG test-stand TOI .....	64
Figure 19: Scatter plot of inverted $\beta$ vs. $\ln k$ classification features for all 214 APG blind-test anomalies.....	65
Figure 20: Comparison between library (green lines) and inverted (red and blue lines) blind-test total NSMS for 105-mm projectiles, 81-mm munitions, and 60-mm mortars. ....	66
Figure 21: Comparisons between library (green lines) and inverted (red and blue lines) blind-test total NSMS for 37-mm and 25-mm mortars. ....	66
Figure 22: Schematic diagram of the BUD system.....	67
Figure 23: The BUD system in operation .....	68
Figure 24: Comparisons between actual and predicted data for an M75 UXO illuminated by the BUD Z transmitter. Solid lines are actual data, circles stand for NSMS predictions. ....	69
Figure 25: Comparisons between actual and predicted data for an M75 UXO illuminated by the BUD X transmitter. Solid lines are actual data, circles stand for NSMS predictions.....	69
Figure 26: Comparisons between actual and predicted data for an M75 UXO illuminated by the BUD Y transmitter. Solid lines are actual data, circles stand for NSMS predictions. ....	70
Figure 27: Recovered total NSMS from calibration BUD measurements for M-75 (blue), 37-mm (green), and M-60 (red) UXO. ....	70
Figure 28. Photo and schematic diagram of the MPV sensor.....	71
Figure 29: Multi-object MPV data collection setup (right). The red circle corresponds to the MPV head, which was placed stationary; the targets were moved along the blue line. The center of the first target (the 81-mm) was placed at the blue points, and the distance between the first and second targets was kept fixed. ....	72
Figure 30: Inverted polarizability principal elements for two targets in three different setups; results for the 81-mm projectile at left and for the 40-mm munition at right. In all three cases the targets were horizontal, and the vertical distance between the MPV center and the 81-mm was 40 cm. The center to the center coordinate differences between the 81-mm and 40-mm projectiles are $(-25, 0, 0)$ cm, $(-40, 0, 0)$ cm, and $(-25, 0, 25)$ cm. ....	73
Figure 31: Inverted total ONMS for 81 mm (left) and 40 mm (right) projectiles for three different cases.....	73
Figure 32: Camp Sibert anomalies: 4.2 inch, base plates and partial mortars. ....	75
Figure 33: Camp Sibert EM-63 near field distributions: Left and middle columns: actual and modeled data respectively. Right column: misfits.....	77
Figure 34: Inverted total NSMS for all anomalies: 4.2" mortars, base plates, and partial mortars. ....	78
Figure 35: <i>Left</i> : Classification features. <i>Right</i> : ROC curve of NSMS performance.....	78
Figure 36: a) Unexploded shell from Cell No. 7 and (b,c) the two false alarms obtained by the SVM classifier using $k$ and $Q(t_{15})/Q(t_1)$ as discriminators.....	79
Figure 37: Result of the SVM classification for the Camp Sibert anomalies using the logarithms of $k$ and $R = Q(t_{15})/Q(t_1)$ . The SVM has been trained with capacity $C = 10$ and kernel width $\sigma = 1/200$ . The small markers denote the ground truth for both training (hollow) and testing	

(solid) cells. The larger markers highlight the cases where there is disagreement between the ground truth and the SVM prediction.....	80
Figure 38: Result of the SVM classification for the Camp Sibert anomalies using the logarithms of the Pasion-Oldenburg parameters $k$ and $\gamma$ . The SVM here has a capacity $C = 9$ . The small markers denote the ground truth for both training (hollow) and testing (solid) cells. The larger markers show the wrong SVM predictions. ....	82
Figure 39: Result of the SVM classification for the Camp Sibert Anomalies using the logarithms of the Pasion- Oldenburg parameters $\beta$ and $\gamma$ . The SVM capacity $C = 10^5$ . The small markers denote the ground truth for both training (hollow) and testing (solid) cells. The larger markers highlight the wrong predictions made by the SVM.....	82
Figure 40: SVM classification of the Camp Sibert Anomalies using the logarithms of $k$ , $b$ , and $g$ . The SVM has $C = 9$ . The small markers denote the ground truth for both training and testing cells. The larger markers highlight the cases where there is disagreement between the ground truth and the SVM prediction. ....	83
Figure 41: Log-scale plot of $Q(t_{15}) / Q(t_1)$ vs. $k$ for Camp Sibert data classification. <i>Left:</i> Ground truth. <i>Right:</i> $K$ -means clustering result.....	86
Figure 42: Classification of 216 targets into five classes using a bivariate normal mixture. Also shown are the 95% confidence ellipses. ....	86
Figure 43: Five ROC curves that indicate the performance of the mixed model approach to Camp Sibert data.....	87
Figure 44: Found Clutter Items on SLO UXO live sites.....	88
Figure 45: Inverted total NSMS time decay profiles for the 2.36" partial rocket. The green lines depict calibration data and the red lines correspond to blind SLO TEMTADS data sets. ....	90
Figure 46: Inverted total NSMS time decay profiles for 4.2" mortars (top left), 81-mm projectiles (top right), 2.36" rockets (bottom left), and 60-mm mortars (bottom right) in the SLO TEMTADS test. The green lines depict calibration data and the red lines correspond to blind data sets. ....	90
Figure 47: Result of the supervised clustering classification for the SLO-TEMTADS anomalies using the logarithms of $M_{\alpha\alpha}(t_1)$ and $M_{\alpha\alpha}(t_1) / M_{\alpha\alpha}(t_{80})$ . The supervised clustering has been trained with calibration data. The red markers correspond to clutters and the white ones to TOI. ....	91
Figure 48: ROC curve for SLO TEMTADS test data.....	92
Figure 49: ROC curve for SLO MetalMapper test data. ....	93
Figure 50: ROC for SLO TEMTADS data for individual TOI. ....	93
Figure 51: ROC for SLO MetalMapper data sets: individual TOI. ....	94
Figure 52: 60-mm mortars actually found in calibration cells #410 and #489. ....	95
Figure 53: <i>Left:</i> Principal elements of the polarizability tensor versus time for a 60mm mortar in the SLO study. <i>Right:</i> Total NSMS time-decay curves for the same cases. The red curve corresponds to calibration Cell #489 and the blue curve to calibration Cell #410.....	95
Figure 54: Comparison between library and inverted blind tests for the dipole model (left) and NSMS model (right). ....	96

Figure 55: ROC curves for SLO TEMTADS and SLO MetalMapper discrimination studies. Green and red curves: Sky/UBC dipole results; blue curve: NSMS results obtained by our Dartmouth/Sky group.....	96
Figure 56: ROC curves for SLO BUD discrimination studies.....	97
Figure 57: SLO TEMTADS test Cell #16. <i>Left</i> : All 25 eigenvalues vs. time. <i>Right</i> : Four highest eigenvalues vs. time. The target response is weak and mixed with the sensor's electronic and background noise.....	98
Figure 58: SLO TEMTADS test Cell #103. <i>Left</i> : All 25 eigenvalues vs. time. <i>Right</i> : Above-threshold eigenvalues vs. time. Only two eigenvalues are above the threshold, indicating a low signal-to-noise ratio.....	98
Figure 59: SLO TEMTADS test Cell #241. <i>Left</i> : All 25 eigenvalues vs. time. <i>Right</i> : Above-threshold eigenvalues vs. time. There more than three eigenvalues above the threshold, which indicates that the cell contains more than one target. The curves decay fast, illustrating that the targets are small.....	99
Figure 60: SLO TEMTADS test Cell #441. <i>Left</i> : All 25 eigenvalues vs. time. <i>Right</i> : Above-threshold eigenvalues vs. time. There more than three eigenvalues above the threshold, indicating that the cell contained more than one target. The fast-decaying curves illustrate that the targets have thin walls or are small.....	99
Figure 61: SLO TEMTADS test Cell #444. <i>Left</i> : All 25 eigenvalues vs. time. <i>Right</i> : Above-threshold eigenvalues vs. time. There more than three eigenvalues above the threshold, indicating that the cell contained several targets. In addition, the curves decay fast, illustrating that the targets are small.....	100
Figure 62: SLO TEMTADS test Cell #748. <i>Left</i> : All 25 eigenvalues vs. time. <i>Right</i> : Above-threshold eigenvalues vs. time. More than three fast-decaying above-threshold eigenvalues indicate the presence of several small targets.....	100
Figure 63: SLO TEMTADS test Cell #1285. <i>Left</i> : All 25 eigenvalues vs. time. <i>Right</i> : Above-threshold eigenvalues vs. time. Again, the eigenvalues indicate that there are several small targets in the cell.....	100
Figure 64: TEMTADS multi-static response matrix eigenvalues versus time for some samples of requested anomalies.....	102
Figure 65: TEMTADS multi-static response matrix eigenvalues versus time for a 105-mm HE projectile and a 105-mm HEAT round (top row), an M-48 Fuze and a 37-mm munition (center row), and two clutter scenarios, one with two items (left) and another with several (right) (third row). .....	103
Figure 66: Inverted total ONVMS time-decay profiles for four Camp Butner targets: (top row) 105-mm HE munition and 105-mm HEAT round, and (bottom) M-48 Fuze and 37-mm projectile with copper band.....	105
Figure 67: Inverted total ONSMS time decay profiles for a 37-mm projectile without copper band.....	105
Figure 68: ROC curve for the Camp Butner TEMTADS test data.....	106
Figure 69: <i>Left</i> : Scatter plot for all MM anomalies based on the extracted total ONVMS. <i>Right</i> : Probability function for all MM anomalies.....	107

Figure 70: Inverted magnetic dipole polarizability (left) and total ONVMS (right) time-decay profiles for MM anomaly #2504. The thin red lines show a library sample, while the thick blue and green lines show the inversion results. ....	107
Figure 71: Result of the supervised clustering classification for the Camp Butner MM anomalies using the logarithms of $M_{zz}(t_1)$ and $M_{zz}(t_1)/M_{zz}(t_{30})$ . The supervised clustering was trained with calibration data. The red markers correspond to clutter and the green ones to TOI. ....	108
Figure 72: ROC curve for Camp Butner MetalMapper test data. ....	109
Figure 73: <i>Left</i> : Total ONVMS time-decay curves for a 105 mm projectile in the camp Butner, NC study. <i>Right</i> : Principal elements of the polarizability tensor versus time for the same case. ....	109
Figure 74: ROC curve for Camp Butner live site classification. 100% UXO were identified correctly, with only 295 false positive rate. The total number of anomalies is 2291. The blue dot corresponds to a threshold in the dig list, when the boundary between UXO and clutter was assumed after scoring. The cyan dot specifies the actual position of this boundary. In ideal circumstances the blue and cyan points will coincide. Performing extra digs, however, helps maintain better statistics and improve the results. ....	114
Figure 75: Camp Butner single-object inverted data clustering. <i>Left</i> : Results of weighted-linkage clustering using Mahalanobis distances for single-object inverted EMI features. <i>Right</i> : All four identified UXO (black) after a second clustering within a smaller domain ( $\log k \in [2;8]$ , $b \in [0.05;2]$ , $g \in [0.05;2]$ ) using Ward linkage and Euclidean distances. ....	114
Figure 76: Camp Butner clusters used to train the first GM classifier and its results. <i>Left</i> : Assumed UXO clusters used to generate the 3-component GM classifier. <i>Right</i> : Score histogram showing the number of anomalies scored within a particular range of the log(probability density) in arbitrary units. The ground truth was requested based on thresholding the log(score) at the externally selected value of ~0.5. ....	116
Figure 77: Updated GMM classifier after confirming 118 UXO in the Camp Butner data. <i>Left</i> : GM-classifier score iso-surfaces in the classification case based on all currently identified UXO targets (118 items), in the feature space corresponding to 3-object EMI inversion. <i>Right</i> : Updated score histogram showing the number of anomalies scored within a particular range of the log(probability density) in arbitrary units. An additional 20 items were requested for statistics to probe the region corresponding to log(score) within $[-6; -5]$ (this region was identified with external input from an expert by observing the corresponding score iso-surfaces and the histogram behavior). ....	116
Figure 78: GMM classifier results for 37-mm targets. <i>Left</i> : 1-component GM-classifier score iso-surfaces in the classification case based solely on identified 37-mm UXO targets, in the feature space corresponding to 3-object EMI inversion. <i>Right</i> : Score histogram showing the number of anomalies scored within a particular range of the log(probability density) in arbitrary units. A total of 174 anomalies were requested (with 118 being already known) based on the log(score) cut-off value of about $-6$ (specified externally by an expert to allow enough statistics). ....	116
Figure 79: GMM classifier for 48-mm targets. <i>Left</i> : 1-component GM-classifier score iso-surfaces in the classification case based solely on identified 48-mm UXO targets, in the feature space corresponding to 3-object EMI inversion. <i>Right</i> : Score histogram showing the number of anomalies scored within a particular range of the log(probability density) in arbitrary units. A total of 53 anomalies were requested (with 27 being already known) based on the log(score) cut-off value of about $-5$ (specified externally by an expert to allow enough statistics). ....	117

Figure 80: GMM classifier for 105-mm targets. *Left*: 1-component GM-classifier score iso-surfaces in the classification case based solely on identified 105-mm UXO targets, in the feature space corresponding to 3-object EMI inversion. *Right*: Score histogram showing the number of anomalies scored within a particular range of the log(probability density) in arbitrary units. A total of 36 anomalies were requested (with 18 being already known) based on the log(score) cut-off value was about  $-20$  (specified externally by an expert to allow enough statistics)..... 117

Figure 81: Final GMM classifier for Camp Butner. *Left*: 3-component GM-classifier score iso-surfaces in the classification case based on all identified UXO targets, in the feature space corresponding to 3-object EMI inversion. *Right*: Score histogram showing the number of anomalies scored within a particular range of the log(probability density) in arbitrary units. A total of 377 anomalies were scored as UXO based on the log(score) cut-off value of about  $-10$  (specified externally by an expert to allow enough statistics and iso-surface separation from identified UXO clusters)..... 117

## List of Tables

Table 1: MetalMapper receiver locations with respect to the center of the Z transmitter loop.....	55
Table 2: Inverted location and orientation for TEMTADS data .....	61
Table 3: BUD receiver locations with respect to the origin.....	68
Table 4: SVM classification of Camp Sibert anomalies using k and R with C = 10 .....	80
Table 5: SVM classification of Camp Sibert anomalies using $\gamma$ and k with C = 9 .....	81
Table 6: SVM classification of Camp Sibert anomalies using $\beta$ and $\gamma$ with C = 105 .....	83
Table 7: SVM classification of Camp Sibert anomalies using the complete NSMS time decay .....	83

## List of Acronyms

3D	Three-Dimensional
AIC	Akaike Information Criterion
APG	Aberdeen Proving Ground
BIC	Bayesian Information Criterion
BOR	Body of Revolution
BUD	Berkeley UXO Discriminator
cm	Centimeter
CRREL	Cold Regions Research and Engineering Laboratory
DE	Differential Evolution
DGPS	Differential Global Positioning System
DoD	Department of Defense
DOE	Department of Energy
EM	Expectation Maximization
EMI	Electromagnetic Induction
ESTCP	Environmental Security Technology Certification Program
FD	Frequency Domain
GSEA	Generalized Standardized Excitation Approach
HAP	(1) magnetic field vector <b>H</b> , (2) vector potential <b>A</b> , (3) scalar magnetic Potential $\psi$
Hz	Hertz
ID	Identification
LS	Least Squares
m	Meter
MAS	Method of Auxiliary Sources
MD	Multi-Dipole

MDL	Minimum Description Length
MEG	Magnetoencephalographic
ML	Maximum Likelihood
mm	Millimeter
ms	Millisecond
$\mu$ s	Microsecond
MM	MetalMapper
MNM	Multivariate Normal Mixture
MPV	Man-Portable Vector
MT	Mixed Theory
MUSIC	Multiple Signal Classification
NMMS	Non-metric Multidimensional Scaling
NRL	Naval Research Laboratory
NSMC	Normalized Surface Magnetic Charge
NSMS	Normalized Surface Magnetic Source
ONVMS	Ortho-Normalized Volume Magnetic Source Model
PCA	Principal Component Analysis
PNN	Probabilistic Neural Network
RBF	Radial Basis Function
ROC	Receiver Operating Characteristic
RSS	Residual Sum of Squares
RTS	Robotic Total Station
SEA	Standard Excitation Approach
SFS	Scattered Field Singularities
SLO	San Luis Obispo
SNR	Signal-to-Noise Ratio

SS	Sum of Squares
SVM	Support Vector Machine
TD	Time Domain
TEM	Time Domain Electromagnetic
TEMTADS	Time Domain Electromagnetic Towed Array Detection System
TNLL	Twice-Negative Log-Likelihood Function
TOI	Target Of Interest
TSA	Thin Skin Approximation
UXO	Unexploded Ordnance
VRM	Viscous Magnetic Remanence

## Abstract

The research described in this report was conducted in fulfillment of Project MM-1572, “A Complex Approach to UXO Discrimination: Combining Advanced EMI Forward and Statistical Signal Processing,” submitted to the Strategic Environmental Research and Development Program (SERDP) in response to the Munitions Management Statement of Need MMSON-07-04 “Advanced Technologies for Detection, Discrimination, and Remediation of Munitions and Explosives of Concern (MEC): UXO Technology”.

The primary objective of the project MM-1572 was to develop and validate innovative, robust, and practical approaches for UXO localization and classification under realistic (noisy, cluttered background) field conditions by combining advanced electromagnetic induction (EMI) forward and statistical signal processing methodologies. In a real field the electromagnetic signals become convoluted with noise due to the instrument, magnetic soil and widespread background clutter. Therefore, the rationale for a statistical approach is to use an advanced statistical approach to reduce the impact of these noises to minimum. This project provides mathematical fundamentals, physical meanings and practical realizations of forward, inverse and statistical signal processing approaches for unexploded ordnance (UXO) detection and discrimination at live-UXO sites. Namely, under this project first we developed and implemented advanced, physically complete forward EMI models such as, the normalized surface magnetic source (charge/dipole) model (NSMS), and ortho-normalized volume magnetic source (ONVMS) technique for accurately representing the EMI responses of subsurface metallic targets, then we combined these advanced models with EMI data inversion approaches, such as the gradient search, direct search-differential evolution and etc, for advanced EMI sensor data inversion; third we extended the advanced statistical signal processing approaches, i.e. support vector machines, Gaussian mixture models, for discriminating UXO targets from non-hazardous anomalies. Finally, the combined advanced EMI forward and statistical models were applied to ESTCP live site UXO data sets. Live site discrimination studies showed the excellent discrimination performance of the advanced models when applied to next-generation-sensor data collected at various live sites, such as Camp Sibert, AL, San Luis Obispo (SLO), CA, and Camp Butner, NC as well as APG test sites. The technology was able to single out UXO ranging in caliber from 25 mm up to 155 mm. In addition, the ONVMS technique was seen to provide excellent classification in both single- and multiple-target scenarios when combined with advanced multi-axis/transmitter/receiver sensors data.

## Acknowledgements

The Principal Investigator, Dr. Fridon Shubitidze of Sky Research and Dartmouth College, conceived, implemented, and tested most of the approaches presented in this report. He developed advanced forward and inverse EMI models, combined them with advanced statistical signal processing, and successfully applied them to live-site UXO data sets.

Mrs. Irma Shamatava of Sky Research, an expert in forward and inverse EMI problems, adapted the advanced models to next-generation sensor data and conducted various inversion and discrimination studies.

Dr. Eugene Demidenko implemented and extended the mixed model approach to UXO discrimination starting with the NSMS technique.

Dr. Juan Pablo Fernández of Dartmouth College combined the SVM technique with advanced EMI techniques and conducted Camp Sibert, AL discrimination studies.

Dr. Alex Bijamov implemented statistical clustering algorithms for ONVMS and performed inversion and discrimination studies for Camp Butner TEMTADS data.

Dr. David Karkashadze, visiting professor at Dartmouth College, developed the mathematical basis of the ONVMS technique.

Dr. Benjamin Barrowes and Dr. Kevin O'Neill of the US Army ERDC-CRREL participated in the development and testing of advanced forward EMI models.

Funding for this project was provided by the Strategic Environmental Research and Development Program Office. We wish to express our sincere appreciation to Dr. Jeffrey Marqusee, Dr. Anne Andrews, Dr. Herb Nelson, and the staff of the SERDP Office for their support.

# 1 Introduction

## 1.1 Background and objectives

The research described in this report was conducted in fulfillment of Project MM-1572, “A Complex Approach to UXO Discrimination: Combining Advanced EMI Forward and Statistical Signal Processing,” submitted to the Strategic Environmental Research and Development Program (SERDP) in response to the Munitions Management Statement of Need MMSON-07-04, “Advanced Technologies for Detection, Discrimination, and Remediation of Munitions and Explosives of Concern (MEC): UXO Technology.”

The well-known and prohibitive cost of carefully excavating all geophysical anomalies detected at lands contaminated with unexploded ordnance (UXO) is one of the greatest impediments to performing an efficient and thorough cleanup of former battlefields and of Department of Defense (DoD) and Department of Energy (DOE) sites. Innovative discrimination techniques are required that can quickly and reliably distinguish between hazardous UXO and non-hazardous metallic items. The key to success lies in the development of advanced processing techniques that can analyze and process sophisticated magnetic or electromagnetic induction data, with its novel waveforms, ever improving quality, and vector or tensor character, so as to maximize the probability of correct classification and minimize the false-alarm rate.

The main objective of the proposed work was to combine physically complete forward models and state-of-the-art statistical signal processing methodologies to carry out dependable and robust UXO discrimination in difficult and noisy sites starting from data provided by current electromagnetic induction (EMI) sensors. Specifically, our objectives were to

- Extend physically complete forward approaches like the normalized surface magnetic source model and the orthonormalized volume magnetic source model to treat realistic data sets.
- Formulate and develop an inversion framework featuring robust regularization and parameter-determination methodologies (for both linear intrinsic signatures and non-linear extrinsic particulars) based on advanced signal processing algorithms.
- Combine EMI models and statistical methodologies to process complex, heterogeneous geophysical data.
- Demonstrate the discrimination capability of the combined approach by applying it to blind live-site UXO discrimination studies.

## 1.2 Report structure

Chapter 2 outlines the theoretical basis of the advanced EMI forward models that we use to represent the EMI response of obscured targets, the workhorses at the core of our whole procedure. We first present the single-dipole model, which is usually insufficient in itself, but undergirds the others. We then introduce and study in detail the NSMS model, which distributes dipoles on a closed surface surrounding a target of interest. After that we derive and describe the ONVMS technique, which infuses dipoles throughout the subsurface volume illuminated by a sensor. We end by describing a data-preprocessing technique based on joint diagonalization that estimates the number of targets in a measurement with no need for data inversion; the method, moreover, can provide initial estimates of target locations and perform rudimentary discrimination.

Chapter 3 discusses inverse models: the methods used to harness the forward models so they provide relevant intrinsic and extrinsic information starting from measured data. After presenting some traditional gradient-search based methods and pointing out some of their limitations we describe differential evolution, a state-of-the-art global-search method, similar in character to genetic algorithms, that has shown remarkable flexibility and usefulness. We end by describing the HAP method, a semi-analytic non-iterative procedure to locate buried targets.

Chapter 4 introduces the theory and application of various statistical techniques for UXO classification. First, the Mixed Models for UXO discrimination is presented and the discrimination based on NSMS data in discussed. Finally, some other supervised (SVM) and unsupervised classification techniques are discussed in application for UXO discrimination.

Chapter 5 presents and describes the next-generation EMI sensors—the MetalMapper, the TEMTADS array, the MPV portable instrument, and the BUD system—that took all the data we use and that represent the state of the art in UXO remediation hardware. We present the results of several testing and validation studies carried out on laboratory, test stand and US army standardized Aberdeen Proving Ground in Maryland test-site data from these devices.

Finally, Chapter 6 provides a detailed account of the discrimination and classification studies performed on data from actual UXO sites—the Camp Sibert in Alabama, Camp San Luis Obispo in California, and Camp Butner in North Carolina—in which several combinations of the techniques presented in the previous chapters were used. We describe our solution strategies and the results we obtained.

## 2 Forward models

### 2.1 Introduction

UXO discrimination is an inverse problem that demands a fast and accurate representation of a target's EMI response. Much of our research in this project has had to do with the development, implementation, and honing of models that provide such representations in a physically complete, noise-tolerant way that allows them to perform adequately in realistic settings and to set the stage for dependable live-site UXO discrimination. In this section we provide an overview of the theoretical basis and implementation details of several models of increasing usefulness and sophistication, starting with the standard point-dipole approach, continuing with the generalized standardized excitation approach (GSEA) and the normalized surface magnetic source (NSMS) model, and culminating with the orthonormalized volume magnetic source (ONVMS) model. We finish the section by describing a fast, inversion-free method to estimate the number of buried targets.

The most frequently used method for representing the EMI response of a metallic target in both frequency and time domains approximates the whole object with a set of orthogonal co-located point dipoles that fire up in response to the primary field; the induced dipole moment is related to the primary field through a symmetric polarizability tensor. The use of this dipole approximation is motivated by its speed and simplicity; this simplicity, however, rests on assumptions that often become problematic and limit the model's usefulness. One such assumption is that the buried target of interest is either far enough from the transmitter loop, or small enough, that the primary field is essentially uniform throughout its extent. Usually, complex targets composed of different materials and different sections that contribute appreciably to the response—and, in the case of UXO, containing such complicating features as fins and rings—simply cannot be modeled accurately with a single point dipole. Such cases require more advanced methods that will capture the underlying physics correctly. One such technique is the NSMS model.

The NSMS method [1-4] can be considered as a generalized surface dipole model, and indeed reduces to the point dipole model in a special limiting case. The NSMS approach models an object's response to the primary field of a sensor by distributing a set of equivalent elementary magnetic sources—normally oriented dipoles in this case—over an auxiliary surface that surrounds it. Such a surface distribution can be hypothetically generated by spreading positive magnetic charge over the outer side of the equivalent surface (usually a prolate spheroid) and an identical distribution of opposite sign on its inner side [5], resulting in a double layer of magnetic charge separated by an infinitesimal distance. This double layer introduces the proper discontinuities in the tangential components of the magnetic flux

density vector  $\mathbf{B}$  but does not affect the transition of its normal component, which must always be continuous given the lack of free magnetic charges in nature. The resulting magnetic-moment distribution radiates a field that by construction satisfies the governing EMI equations and can thus account for the secondary field outside the object. The particulars of location and orientation are divided out by normalizing the dipole density at every point with the component of the primary magnetic field normal to the surface. The resulting surface amplitude  $\Omega$  of the NSMS distribution is a property of the object, and its integral  $Q$  over the surface constitutes a sort of global magnetic polarizability that is independent of the computational constructs—primary field, surrounding surface, object location and orientation, etc.—introduced for its determination. The surface amplitude can be determined directly for library-matching purposes by minimizing the difference between measured and modeled data for a known combination of object and sensor at a given relative location and orientation.

The NSMS technique has demonstrated good computational speed and superior classification performance when applied to EMI datasets consisting of well-isolated single targets, but is found to degrade quickly on both counts when confronted with multi-target cases. This has forced us to generalize the model further and develop the ONVMS procedure.

The ONVMS model, a further extension of NSMS, is based on the assumption that a collection of subsurface objects can be replaced with a set of magnetic dipole sources, distributed over a volume. Since all actual radiating sources are located within the scatterers—rather than in the soil or air—the spatial distribution of these fictitious dipoles (their amplitudes scaled by the primary field) indicates the locations and orientations of any targets present inside the computational volume. The great advantage of the ONVMS technique over the other models discussed above is that it takes into account mutual couplings between different sections of the different targets while simultaneously avoiding the appearance of singular matrices in multi-target situations. It is thus gracefully indifferent to the number of targets: Once the amplitudes and the locations of the corresponding dipoles are determined, one need only look at their clustering patterns, compute the time-dependent total polarizability tensor for each group, and subsequently diagonalize each such tensor using joint diagonalization (see immediately below for another application). The resulting diagonal elements have been found to be intrinsic to the objects they represent, and can be used, on their own or combined with other quantities, in discrimination analysis. Recent ESTCP live-site discrimination studies have clearly indicated the superior discrimination performance (illustrated in chapter 6) of the ONVMS method in combination with the statistical processing approaches described in Chapter 4.

One of the main challenges one faces when attempting multi-target inversion and classification is the inability to estimate the number of targets. Under this project we implemented a technique based on

joint diagonalization that estimates the number of targets present in the field of view of the sensor as it takes a data shot, in real time and without requiring a forward model, and, in a good number of cases, even provides the capability to perform a quick inversion-free characterization and classification of these targets. JD determines the eigenvalues and eigenvectors of a square time- or frequency-dependent multi-static response (MSR) matrix synthesized directly from measured data. The number of nonzero eigenvalues of the matrix (i.e., those above a noise threshold) is related to the number of elementary sources in the illuminated cell; moreover, the time-decay patterns of these non-vanishing eigenvalues are intrinsic properties of the targets to which the sources correspond and can ultimately provide dependable classification features.

## 2.2 The single-dipole approximation

According to the Huygens Equivalence Principle, an object's entire response to a given excitation can be approximated as the summation of magnetic fields produced by elementary magnetic dipoles/charges placed on a closed surface surrounding the target. Using the superposition principle, this set of dipoles can be approximated as one independent aggregate dipole. In the simple dipole model, the secondary magnetic field at  $\mathbf{r}$  due to a dipole of moment  $\mathbf{m}$  is:

$$\mathbf{H} = \frac{1}{4\pi R^3} (3\hat{\mathbf{R}}\hat{\mathbf{R}} - \bar{\bar{\mathbf{I}}}) \cdot \mathbf{m} \equiv \bar{\bar{\mathbf{G}}} \cdot \mathbf{m} \quad (1)$$

where  $\hat{\mathbf{R}}$  is the unit vector along  $\mathbf{R} = \mathbf{r}' - \mathbf{r}_d$ ,  $\mathbf{r}_d$  is the dipole's position, and  $\bar{\bar{\mathbf{I}}}$  is the identity dyad (see Figure 1). The dipole moment  $\mathbf{m}$  induced by the primary magnetic field  $\mathbf{H}^{pr}$  is given by

$$\mathbf{m} = \bar{\bar{\mathbf{M}}} \cdot \mathbf{H}^{pr}(\mathbf{r}', \mathbf{r}_d), \quad (2)$$

where  $\bar{\bar{\mathbf{M}}}$ , the target's magnetic polarizability tensor, is a symmetric matrix:  $\mathbf{M}_{\alpha\beta} = \mathbf{M}_{\beta\alpha}$ ,  $\alpha, \beta = x, y, z$ . This tensor depends on the scatterer's shape, size, and material properties. In a coordinate system aligned with the scatterer's principal axes for different primary magnetic fields  $\mathbf{H}^{pr}(\mathbf{r}, \mathbf{r}_d)$ , (2) can be written in matrix form as

$$[\mathbf{m}] = \bar{\bar{\mathbf{M}}} \cdot [\mathbf{H}^{pr}]. \quad (3)$$

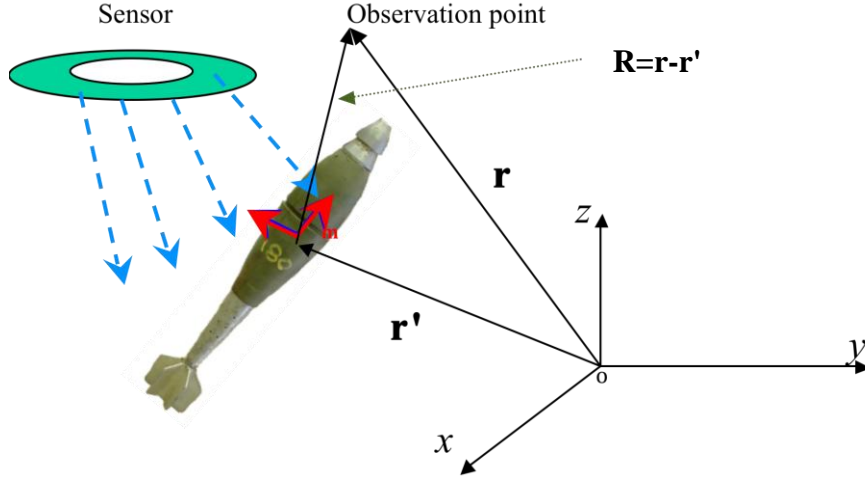


Figure 1: A dipole's location in a global coordinate system.

Thus the secondary magnetic field is

$$\mathbf{H} = \bar{\mathbf{G}} \cdot \bar{\mathbf{M}} \cdot [\mathbf{H}^{\text{pr}}] \equiv [\bar{\Upsilon}] \cdot [\mathbf{M}]^T, \quad (4)$$

where  $[\mathbf{M}]$  is a  $1 \times 6$  dimensional vector whose components  $(M_{xx}, M_{xy}, M_{xz}, M_{yy}, M_{yz}, M_{zz})$  correspond to the elements of the target's magnetic polarizability tensor  $\bar{\mathbf{M}}$  and  $[\Upsilon]$  is a  $3 \times 6$  matrix,

$$\bar{\Upsilon} = \frac{1}{4\pi R^5} \begin{pmatrix} \Upsilon_{11} & \Upsilon_{12} & \Upsilon_{13} & \Upsilon_{14} & \Upsilon_{15} & \Upsilon_{16} \\ \Upsilon_{21} & \Upsilon_{22} & \Upsilon_{23} & \Upsilon_{24} & \Upsilon_{25} & \Upsilon_{26} \\ \Upsilon_{31} & \Upsilon_{32} & \Upsilon_{33} & \Upsilon_{34} & \Upsilon_{35} & \Upsilon_{36} \end{pmatrix}, \quad (5)$$

whose elements are as follows:

$$\Upsilon_{11} = H_x^{\text{pr}} (3R_x^2 - R^2) \quad \Upsilon_{12} = 3R_x (R_x H_y^{\text{pr}} + R_y H_x^{\text{pr}}) - H_y^{\text{pr}} R^2 \quad \Upsilon_{13} = 3R_x (R_x H_z^{\text{pr}} + R_z H_x^{\text{pr}}) - H_z^{\text{pr}} R^2$$

$$\Upsilon_{14} = 3R_x R_y H_y^{\text{pr}} \quad \Upsilon_{15} = 3R_x (R_y H_z^{\text{pr}} + R_z H_y^{\text{pr}}) \quad \Upsilon_{16} = 3R_x R_z H_z^{\text{pr}}$$

$$\Upsilon_{21} = 3R_y R_x H_x^{\text{pr}} \quad \Upsilon_{22} = 3R_y (R_x H_y^{\text{pr}} + R_y H_x^{\text{pr}}) - H_x^{\text{pr}} R^2 \quad \Upsilon_{23} = 3R_y (R_x H_z^{\text{pr}} + R_z H_x^{\text{pr}})$$

$$\Upsilon_{24} = H_y^{\text{pr}} (3R_y^2 - R^2) \quad \Upsilon_{25} = 3R_y (R_y H_z^{\text{pr}} + R_z H_y^{\text{pr}}) - H_z^{\text{pr}} R^2 \quad \Upsilon_{26} = 3R_y R_z H_z^{\text{pr}}$$

$$\begin{aligned}
Y_{31} &= 3R_z R_x H_x^{\text{pr}} & Y_{32} &= 3R_z (R_x H_y^{\text{pr}} + R_y H_x^{\text{pr}}) & Y_{33} &= 3R_z (R_x H_z^{\text{pr}} + R_z H_x^{\text{pr}}) - H_x^{\text{pr}} R^2 \\
Y_{34} &= 3R_z R_y H_y^{\text{pr}} & Y_{35} &= 3R_z (R_y H_z^{\text{pr}} + R_z H_y^{\text{pr}}) - H_y^{\text{pr}} R^2 & Y_{36} &= H_z^{\text{pr}} (3R_z^2 - R^2)
\end{aligned}$$

Once the vector  $\mathbf{M}$  is determined the magnetic polarizability tensor  $\bar{\bar{\mathbf{M}}}$  is constructed as

$$\bar{\bar{\mathbf{M}}} = \begin{pmatrix} M_{xx} & M_{xy} & M_{xz} \\ M_{xy} & M_{yy} & M_{yz} \\ M_{xz} & M_{yz} & M_{zz} \end{pmatrix}, \quad (6)$$

and finally the  $\bar{\bar{\mathbf{M}}}$  tensor's principal polarizability elements are determined in the target frame coordinate system, which is related to the global coordinate system via the Euler rotation tensor  $\bar{\bar{\mathbf{A}}}(\psi, \theta, \phi)$ , as

$$\bar{\bar{\mathbf{M}}} = \bar{\bar{\mathbf{A}}} \bar{\bar{\beta}} \bar{\bar{\mathbf{A}}}^T \equiv \bar{\bar{\mathbf{A}}} \begin{pmatrix} \beta_{xx} & 0 & 0 \\ 0 & \beta_{yy} & 0 \\ 0 & 0 & \beta_{zz} \end{pmatrix} \bar{\bar{\mathbf{A}}}^T. \quad (7)$$

Body-of-revolution (BOR) symmetry (which most UXO possess) dictates that  $\beta_{xx} = \beta_{yy}$  and that the third Euler angle  $\psi$  is zero. We thus obtain

$$\bar{\bar{\mathbf{A}}} = \begin{bmatrix} \cos \theta \cos \phi & \cos \theta \sin \phi & -\sin \theta \\ -\sin \phi & \cos \phi & 0 \\ \sin \theta \cos \phi & \sin \theta \sin \phi & \cos \theta \end{bmatrix}, \quad (8)$$

where  $\theta$  and  $\phi$  are the angles between the local and global axes. Note that the tensor  $\bar{\bar{\mathbf{M}}}$  depends on time or frequency while the Euler tensor does not. This suggests that one could apply joint diagonalization (along the lines of the procedure introduced in Section 2.5) to separate the polarizability eigenvalues from the rotational eigenvectors; the attitude angles can in turn be extracted from the latter.

## 2.3 Normalized surface magnetic source model

### 2.3.1 Governing equations

Outside the objects of interest, both the primary and the secondary magnetic fields in air and ground ( $\mathbf{H}^{\text{pr}}$  and  $\mathbf{H}^{\text{sc}}$  respectively, both measured in A/m) are irrotational and can be represented by scalar magnetic potentials (with dimensions of current) through

$$\mathbf{H}^{\text{out}} \equiv \mathbf{H}^{\text{pr}} + \mathbf{H}^{\text{sc}} = -\nabla \psi^{\text{out}} = -\nabla \psi^{\text{pr}} - \nabla \psi^{\text{sc}}. \quad (9)$$

Inside a metallic target the EMI field is governed by a diffusion equation and can be expressed as

$$\mathbf{H}^{\text{in}} = \frac{1}{\mu^{\text{in}}} \nabla \times \mathbf{A}^{\text{in}}, \quad (10)$$

where the vector potential  $\mathbf{A}$  (also with dimensions of current) obeys

$$\nabla \times \left( \frac{1}{\mu^{\text{in}}} \nabla \times \mathbf{A}^{\text{in}} \right) + \sigma^{\text{in}} \frac{\partial \mathbf{A}^{\text{in}}}{\partial t} = 0, \quad (11)$$

and  $\mu^{\text{in}} = \mu_r^{\text{in}} \mu_0$ ;  $\mu_0 = 4\pi \cdot 10^{-7}$  [H/m] and  $\sigma^{\text{in}}$  are respectively the magnetic permeability and the electric conductivity of the object.

The total interior and exterior magnetic fields are connected at the surface of an object by the customary boundary conditions

$$\begin{aligned} \hat{\mathbf{n}} \times (\mathbf{H}^{\text{pr}} + \mathbf{H}^{\text{sc}}) &= \hat{\mathbf{n}} \times \mathbf{H}^{\text{in}}, \\ \hat{\mathbf{n}} \cdot \mu_r^{\text{out}} (\mathbf{H}^{\text{pr}} + \mathbf{H}^{\text{sc}}) &= \hat{\mathbf{n}} \cdot \mu_r^{\text{in}} \mathbf{H}^{\text{in}}, \end{aligned} \quad (12)$$

where  $\hat{\mathbf{n}}$  is a unit vector normal to the surface and  $\mu_r^{\text{in}}$  and  $\mu_r^{\text{out}}$  are the relative magnetic permeabilities of the target and the surrounding medium respectively. Dividing the scatterer's surface into subsurfaces (patches) allows us to rewrite the boundary conditions in the following convenient form:

$$[\bar{\bar{G}}] [P] = [V], \quad (13)$$

where

$$\begin{bmatrix} \bar{\bar{G}} \end{bmatrix} = \begin{bmatrix} G_n^{P_n} & \mu_r G_n^{P_u} & \mu_r G_n^{P_v} \\ G_u^{P_n} & G_u^{P_u} & G_u^{P_v} \\ G_v^{P_n} & G_v^{P_u} & G_v^{P_v} \end{bmatrix}, \quad [P] = \begin{bmatrix} P_n \\ P_u \\ P_v \end{bmatrix}, \quad \text{and} \quad [V] = - \begin{bmatrix} H_n^{\text{pr}} \\ H_u^{\text{pr}} \\ H_v^{\text{pr}} \end{bmatrix}. \quad (14)$$

The vector  $[P]$  contains the amplitudes of induced magnetic dipoles oriented along the  $\hat{\mathbf{n}}$ ,  $\hat{\mathbf{u}}$  and  $\hat{\mathbf{v}}$  directions, where  $\hat{\mathbf{n}}$  is normal to the surface and  $\hat{\mathbf{v}} = \hat{\mathbf{n}} \times \hat{\mathbf{u}}$  and  $\hat{\mathbf{u}} = \hat{\mathbf{v}} \times \hat{\mathbf{n}}$  are tangential to it. The impedance matrix  $[\bar{\bar{G}}]$  depends only on the target's geometry and electromagnetic parameters and not on its location and orientation; its elements represent the exterior and interior solutions, expressed in terms of dipole sources distributed over the surface using a Green function of the form  $e^{jkR}/4\pi R$ . More explicit

forms of the  $G_{\xi}^{P_{\xi}}$  matrices, where  $\hat{\xi} = \hat{\mathbf{n}}, \hat{\mathbf{u}}, \hat{\mathbf{v}}$ , are presented in [4]. Finally,  $[V]$  is the primary magnetic field that can be considered as a driving/forcing vector for the  $[P]$ . Since most actual UXO are heterogeneous objects, numerical methods may require tens or even hundreds of thousands of unknowns for magneto quasi static boundary-value problems. This makes rigorous 3D-EMI numerical models impractical for UXO discrimination. To achieve the goal of reproducing EMI responses of realistic objects quickly, accurately, and with only a few model parameters we developed the normalized surface magnetic source model.

### 2.3.2 Theoretical basis of NSMS

The NSMS model is based upon the assumption that the entire scatterer can be replaced with an auxiliary very thin surface shell. The primary magnetic field strikes the shell and induces on it a surface magnetization, in terms of which the secondary scalar potential can be written as [5]

$$\psi^{sc}(\mathbf{r}) = \frac{1}{4\pi} \oint_S \mathbf{M}(\mathbf{r}') \cdot \nabla' \frac{1}{R} ds' \quad (15)$$

Here  $\mathbf{R} = \mathbf{r} - \mathbf{r}'$ , where  $\mathbf{r}$  is the observation point and  $\mathbf{r}'$  is on the surface  $S$ , and  $\mathbf{M}(\mathbf{r}')$  is a surface density of magnetization, which can be defined as the induced magnetic moment per unit surface:  $\mathbf{m} = \oint_S \mathbf{M}(\mathbf{r}') ds'$ . The surface density  $\mathbf{M}$  of magnetic polarization may be resolved at every point on  $S$  into normal and tangential components by means of the identity

$$\mathbf{M} = (\hat{\mathbf{n}} \cdot \mathbf{M}) \hat{\mathbf{n}} + (\hat{\mathbf{n}} \times \mathbf{M}) \times \hat{\mathbf{n}}, \quad (16)$$

and combining (16), (15) and (9) we get for the total scattered magnetic field

$$\begin{aligned} \mathbf{H}^{sc}(\mathbf{r}) = & -\frac{1}{4\pi} \nabla \oint_S (\hat{\mathbf{n}}' \cdot \mathbf{M}(\mathbf{r}')) \hat{\mathbf{n}}' \cdot \nabla' \frac{1}{R} ds' \\ & -\frac{1}{4\pi} \nabla \oint_S (\hat{\mathbf{n}}' \times \mathbf{M}(\mathbf{r}')) \times \hat{\mathbf{n}}' \nabla' \frac{1}{R} ds'. \end{aligned} \quad (17)$$

The first integral in (17) may be interpreted as a scalar potential due to a double layer of moment

$$\tau(\mathbf{r}') = (\hat{\mathbf{n}}' \cdot \mathbf{M}(\mathbf{r}')) \hat{\mathbf{n}}' = \sigma_m(\mathbf{r}') \hat{\mathbf{n}}', \quad (18)$$

and the second may be interpreted as a scalar potential due to a “free” magnetic charge distribution proportional to a discontinuity in the normal components of magnetic flux. Since the normal component of the magnetic field is always continuous across a boundary between two media, the total scattered magnetic field can thus be written as

$$\mathbf{H}^{sc}(\mathbf{r}) = -\nabla \oint_S \sigma_m(\mathbf{r}') g(\mathbf{r}, \mathbf{r}') ds' \quad (19)$$

where

$$g(\mathbf{r}, \mathbf{r}') = \frac{1}{4\pi} \hat{\mathbf{n}}' \cdot \nabla' \frac{1}{|\mathbf{r} - \mathbf{r}'|}. \quad (20)$$

Thus the EMI response of a permeable and conducting metallic object can be represented using a surface density  $\sigma_m(s')$ . At every point, the magnetic flux density  $\mathbf{B}$  is

$$\mathbf{B} = \mu_0(\mathbf{H} + \mathbf{M}). \quad (21)$$

Using Gauss's law for the magnetic flux density in the volume enclosed by  $S$  and using the divergence theorem we obtain

$$\begin{aligned} \int_V \nabla \cdot \mathbf{B} dv &= \mu_0 \oint_S (\mathbf{H} \cdot \hat{\mathbf{n}}' + \mathbf{M} \cdot \hat{\mathbf{n}}') ds' \\ &= \mu_0 \oint_S (H_n(\mathbf{r}') + \sigma_m(\mathbf{r}')) ds' = 0, \end{aligned} \quad (22)$$

and it follows that the magnetization density at a given point on the surface equals

$$\begin{aligned} \sigma_m(s') &= -H_n(s') = -(H_n^{pr}(s') + H_n^{sc}(s')) \\ &= -H_n^{pr}(s') (1 + P(s')), \end{aligned} \quad (23)$$

where  $P(s')$  is in general position-dependent on  $S$  surface. In other words, the surface magnetic charge is proportional to the normal component  $H_n^{pr}(s')$  of the primary magnetic field. This motivates us to introduce a normalized surface distribution  $\Omega(s')$  through

$$\sigma_m(s') \equiv -\Omega(s') [\mathbf{H}^{pr}(s') \cdot \hat{\mathbf{n}}'], \quad (24)$$

which would result from exciting each patch of the surface  $S$  with a nonphysical unit primary magnetic field in the normal direction. After combining (19) and (24), the total scattered magnetic field can be expressed as

$$\begin{aligned} \mathbf{H}^{sc}(\mathbf{r}) &= \oint_S \Omega(\mathbf{r}') [\mathbf{H}^{pr}(\mathbf{r}') \cdot \hat{\mathbf{n}}'] \nabla g(\mathbf{r}, \mathbf{r}') ds' \\ &= \oint_S \Omega(\mathbf{r}') [\mathbf{H}^{pr}(\mathbf{r}') \cdot \hat{\mathbf{n}}'] \frac{3\mathbf{R}(\mathbf{R} \cdot \hat{\mathbf{n}}') - R^2 \hat{\mathbf{n}}'}{4\pi R^5} ds'. \end{aligned} \quad (25)$$

In the following we will argue that  $\Omega$ , and in particular its integral over the surface,

$$Q = \oint_S \Omega ds', \quad (26)$$

contains all the information about an object that could be of need in the UXO discrimination problem, incorporating the effects of heterogeneity, interaction with other objects, and near- and far-field effects. We note that  $Q$  has dimensions of volume, which makes it comparable to the polarizability tensor elements of the point dipole model [6-13].

### 2.3.3 Formulation for bodies of revolution; determining NSMS amplitudes from data

Most UXO are bodies of revolution (BOR), and the simplicity and efficiency afforded by this simplification motivates specializing the above analysis to scatterers with BOR symmetry. The best choice for auxiliary surface is a prolate spheroid, since it has BOR symmetry but at the same time has the elongated shape of UXO and can be made to have a definite orientation. We take a spheroid of semiminor and semimajor axes  $a$  and  $b \equiv ea$  with  $e > 1$ . In the prolate spheroidal coordinate system  $(\xi, \eta, \varphi)$  we can write (25) in the form (see Figure 2)

$$\mathbf{H}^{\text{sc}}(\mathbf{r}) = \int_{-1}^1 h_\eta' d\eta' \int_0^{2\pi} h_\varphi' d\varphi' \Omega(\eta', \xi_0, \varphi') [\mathbf{H}^{\text{pr}}(\mathbf{r}') \cdot \hat{\xi}'] \nabla g(\mathbf{r}, \mathbf{r}'), \quad (27)$$

where the prolate spheroidal coordinates obey  $-1 \leq \eta \leq 1$ ,  $0 \leq \xi < \infty$ ,  $0 \leq \varphi \leq 2\pi$ ,  $\mathbf{r}$  is the observation point,  $h_\eta$  and  $h_\varphi$  are the metric coefficients

$$h_\eta = \frac{d}{2} \sqrt{\frac{\xi_0^2 - \eta^2}{1 - \eta^2}} \quad \text{and} \quad h_\varphi = \frac{d}{2} \sqrt{(1 - \eta^2)(\xi_0^2 - 1)}, \quad (28)$$

the spheroid is characterized by  $\xi_0 = e / \sqrt{e^2 - 1}$ , and  $d = 2\sqrt{b^2 - a^2}$  is the focal distance.

For a body with BOR symmetry the NSMS amplitude is azimuthally constant, and moreover the variation of the induced magnetic charge density  $\sigma$  is accounted for by the normal component of the primary magnetic field. This implies that  $\Omega(\eta', \xi_0, \varphi') = \Omega(\eta')$ . For convenience we define

$$\mathbf{H}^{\text{sc}}(\mathbf{r}) = \int_{-1}^1 \Omega(\eta') \mathbf{K}(\eta', \mathbf{r}) d\eta', \quad (29)$$

where

$$\mathbf{K}(\eta', \mathbf{r}) = \int_0^{2\pi} [\mathbf{H}^{\text{pr}}(\mathbf{r}') \cdot \hat{\xi}'] \nabla g(\mathbf{r}, \xi_0, \eta', \varphi') h_\eta h_\varphi d\varphi', \quad (30)$$

and assume that the NSMS can be approximated by a series of expansion functions  $F_m(\eta')$  such that

$$\Omega(\eta') = \sum_{m=1}^M \Omega_m F_m(\eta') \quad (31)$$

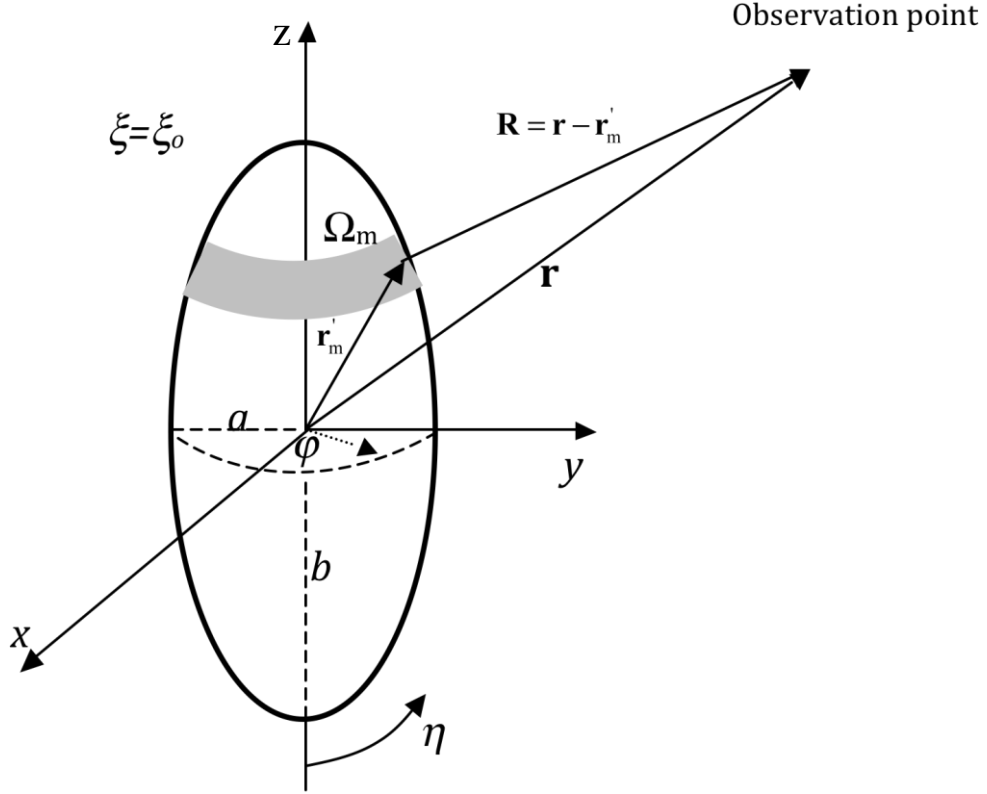


Figure 2: The NSMC that are distributed on a prolate spheroidal surface is implemented for a body of revolution. The prolate spheroidal coordinate system is specified by  $(\xi, \eta, \varphi)$ .

For computational simplicity, in the subsequent analysis we assume the expansion functions  $F_m(\eta)$  are a set of orthogonal pulse functions given by

$$F_m(\eta') = \begin{cases} 1, & \eta' \in \Delta\eta_m \\ 0, & \text{otherwise.} \end{cases} \quad (32)$$

The expansion in terms of pulse functions is a “stairstep” approximation to the NSMS distribution on the spheroid along  $\eta'$ , where the spheroidal surface is divided into  $M$  belts. The expansion coefficient  $\Omega_m$  thus corresponds to the NSMS amplitude at the  $m$ -th belt. Substituting into (29) we obtain

$$\mathbf{H}^{sc}(\mathbf{r}) = \int_{-1}^1 \sum_{m=1}^M \Omega_m F_m(\eta') \mathbf{K}(\eta', \mathbf{r}) d\eta', \quad (33)$$

and the use of (32) in (33) enables us to write

$$\begin{aligned} \mathbf{H}^{sc}(\mathbf{r}) &= \sum_{m=1}^M \Omega_m \int_{\Delta\eta_m} \mathbf{K}(\eta, \mathbf{r}) d\eta \equiv \sum_{m=1}^M \Omega_m \mathbf{f}(\eta_m, \mathbf{r}) \\ &= \Omega_1 \mathbf{f}(\eta_1, \mathbf{r}) + \Omega_2 \mathbf{f}(\eta_2, \mathbf{r}) + \dots + \Omega_M \mathbf{f}(\eta_M, \mathbf{r}). \end{aligned} \quad (34)$$

The physical interpretation of this equation is as follows. The spheroid has been divided up to  $M$  belts, each of surface  $\Delta s_m = 2\pi h_\eta^m h_\phi^m \Delta \eta_m$ , as shown in Figure 2, with the NSMS being an unknown constant over each belt. At the center of each segment, the sum of the scattered fields from all  $M$  belts is set to equal the measured field  $\mathbf{H}^{\text{data}}(\mathbf{r})$  at point  $\mathbf{r}$  that is a known field arising from the scatterer. For a point  $\mathbf{r}_n$  the latter equation leads to

$$\sum_{m=1}^M \Omega_m \mathbf{f}(\eta_m, \mathbf{r}_n) = \mathbf{H}^{\text{data}}(\mathbf{r}_n) \quad (35)$$

So far we have only generated one equation (or three if we have access to the full vector field) with  $M$  unknowns. We can obtain additional independent equations by using data collected at different points  $\mathbf{r}_n$  with  $n = 1, 2, \dots, N$ . Matching the modeled scattered magnetic field to the data at these  $N$  points results in the linear system

$$[\mathbf{Z}_{mn}] [\boldsymbol{\Omega}_m] = [\mathbf{H}^{\text{data}}(\mathbf{r}_n)], \quad (36)$$

with

$$\begin{aligned} [\mathbf{Z}_{mn}] &= \begin{bmatrix} \mathbf{f}(\eta_1, \mathbf{r}_1) & \mathbf{f}(\eta_2, \mathbf{r}_1) & \cdots & \mathbf{f}(\eta_M, \mathbf{r}_1) \\ \mathbf{f}(\eta_1, \mathbf{r}_2) & \mathbf{f}(\eta_2, \mathbf{r}_2) & \cdots & \mathbf{f}(\eta_M, \mathbf{r}_2) \\ \vdots & \vdots & \ddots & \vdots \\ \mathbf{f}(\eta_1, \mathbf{r}_N) & \mathbf{f}(\eta_2, \mathbf{r}_N) & \cdots & \mathbf{f}(\eta_M, \mathbf{r}_N) \end{bmatrix}, \\ [\boldsymbol{\Omega}_m] &= [\Omega_1 \ \Omega_2 \ \dots \ \Omega_M]^T, \\ [\mathbf{H}^{\text{data}}(\mathbf{r}_n)] &= [\mathbf{H}^{\text{data}}(\mathbf{r}_1) \ \mathbf{H}^{\text{data}}(\mathbf{r}_2) \ \mathbf{H}^{\text{data}}(\mathbf{r}_N)]^T, \end{aligned} \quad (37)$$

and  $\mathbf{f}(\eta_m, \mathbf{r}_n)$  given by (34), whose solution can be written symbolically as

$$[\boldsymbol{\Omega}_m] = \frac{[\mathbf{Z}_m]^T [\mathbf{H}^{\text{data}}(\mathbf{r}_n)]}{[\mathbf{Z}_m]^T [\mathbf{Z}_m]}. \quad (38)$$

Once  $[\boldsymbol{\Omega}_m]$  is determined the object's EMI response can be computed readily. The resulting discrete NSMS distribution can then be used to compute the total NSMS amplitude, which is a global measure of  $\Omega$  for the entire object and can be used for discrimination:

$$Q = \sum_{m=1}^M \Omega_m \Delta S_m. \quad (39)$$

In the following sections we study some features of this global measure of response.

### 2.3.4 The dipole model as a limiting case of NSMS

Here we show that NSMS reduces in the limit to the point dipole model [6-11] of Section 2.2. Recall that the magnetic field due to a dipole of moment  $\mathbf{m}$  is

$$\mathbf{H}^{\text{sc}}(\mathbf{r}) = \frac{1}{4\pi R^3} \mathbf{m} \cdot (3\hat{\mathbf{R}}\hat{\mathbf{R}} - \bar{\mathbf{I}}), \quad (40)$$

where  $\hat{\mathbf{R}}$  is the unit vector along  $\mathbf{R} = \mathbf{r} - \mathbf{r}_d$  and  $\mathbf{r}_d$  and  $\mathbf{r}$  are respectively the location of the dipole and the observation point, as seen in Figure 3, while  $\bar{\mathbf{I}}$  is the identity dyad. The relation between the induced dipole moment  $\mathbf{m}$  and the primary magnetic field  $\mathbf{H}^{\text{pr}}$  at the dipole location is given by

$$\mathbf{m} = \bar{\mathbf{M}} \cdot \mathbf{H}^{\text{pr}}(\mathbf{r}_d), \quad (41)$$

where the magnetic polarizability tensor  $\bar{\mathbf{M}}$  depends on the scatterer's shape, size, and material properties. For a body of revolution, the polarizability tensor in a coordinate system aligned with the scatterer's principal axes can be written as

$$\bar{\mathbf{M}} = \begin{bmatrix} \beta_{\rho\rho} & 0 & 0 \\ 0 & \beta_{\rho\rho} & 0 \\ 0 & 0 & \beta_{zz} \end{bmatrix} \quad (42)$$

where the degeneracy in the “radial” element  $\beta_{\rho\rho}$  displays the BOR symmetry explicitly. The target's principal axes and the global coordinate system are related by the Euler rotation tensor.

Now let us prove that in the dipole model is a limited case of the NSMS. To do that, first let us divide the surrounding spheroidal surface into three belts and assume that on the  $m$ -th belt the NSMS density follows a Dirac delta distribution (see Figure 3). With these assumptions the scattered magnetic field (40) becomes

$$\mathbf{H}^{\text{sc}}(\mathbf{r}) = \frac{1}{4\pi} \sum_{m=1}^3 \frac{1}{R_m^3} \Omega_m H_m^{\text{pr}}(\mathbf{r}_m) \hat{\mathbf{n}}_m \cdot (3\hat{\mathbf{R}}_m \hat{\mathbf{R}}_m - \bar{\mathbf{I}}) \quad (43)$$

where now  $\mathbf{R} = \mathbf{r} - \mathbf{r}_m$  points from  $\mathbf{r}_m$  on the  $m$ -th belt to the observation point. As  $S \rightarrow 0$  we have that  $\mathbf{r}_m \rightarrow \mathbf{r}_d$ , and  $H_n^{\text{pr}}(\mathbf{r}_m) = H_n^{\text{pr}}(\mathbf{r}_d)$ , and because  $\hat{\mathbf{n}}_2 = \hat{\mathbf{p}} = \alpha_1 \hat{\mathbf{x}} + \alpha_2 \hat{\mathbf{y}}$ , and  $\hat{\mathbf{n}}_1 = -\hat{\mathbf{n}}_3 = \hat{\mathbf{z}}$ , ( $\alpha_1 = \cos \alpha$  and  $\alpha_2 = \sin \alpha$ , where  $\alpha$  is the angle between  $\hat{\mathbf{p}}$  and  $\hat{\mathbf{x}}$ ) then (43) reduces to

$$\mathbf{H}^{\text{sc}}(\mathbf{r}) = \frac{3\hat{\mathbf{R}}\hat{\mathbf{R}} - \bar{\mathbf{I}}}{4\pi R^3} \cdot (2\Omega_1 H_z^{\text{pr}}(\mathbf{r}_d) \hat{\mathbf{z}} + \Omega_2 (H_x^{\text{pr}}(\mathbf{r}_d) \alpha_1 \hat{\mathbf{x}} + H_x^{\text{pr}}(\mathbf{r}_d) \alpha_2 \hat{\mathbf{y}})) \quad (44)$$

in terms of the Cartesian unit vectors  $\hat{\mathbf{x}}$ ,  $\hat{\mathbf{y}}$ , and  $\hat{\mathbf{z}}$ . After introducing a diagonal tensor

$$\bar{\bar{\mathbf{M}}}_n = \begin{bmatrix} \Omega_2 & 0 & 0 \\ 0 & \Omega_2 & 0 \\ 0 & 0 & 2\Omega_1 \end{bmatrix} \quad (45)$$

and the vector  $\mathbf{m}_n = \bar{\bar{\mathbf{M}}}_n \cdot \mathbf{H}^{pr}(\mathbf{r}_d)$ , (44) can be written as

$$\begin{aligned} \mathbf{H}^{sc}(\mathbf{r}) &= \frac{1}{4\pi R^3} \mathbf{m}_n \cdot (3\hat{\mathbf{R}}\hat{\mathbf{R}} - \bar{\bar{\mathbf{I}}}) \\ &= \frac{1}{4\pi R^3} [\bar{\bar{\mathbf{M}}}_n \cdot \mathbf{H}^{pr}(\mathbf{r}_d)] \cdot (3\hat{\mathbf{R}}\hat{\mathbf{R}} - \bar{\bar{\mathbf{I}}}), \end{aligned} \quad (46)$$

which proves that in the limit the NSMS model is identical to the infinitesimal dipole approximation.

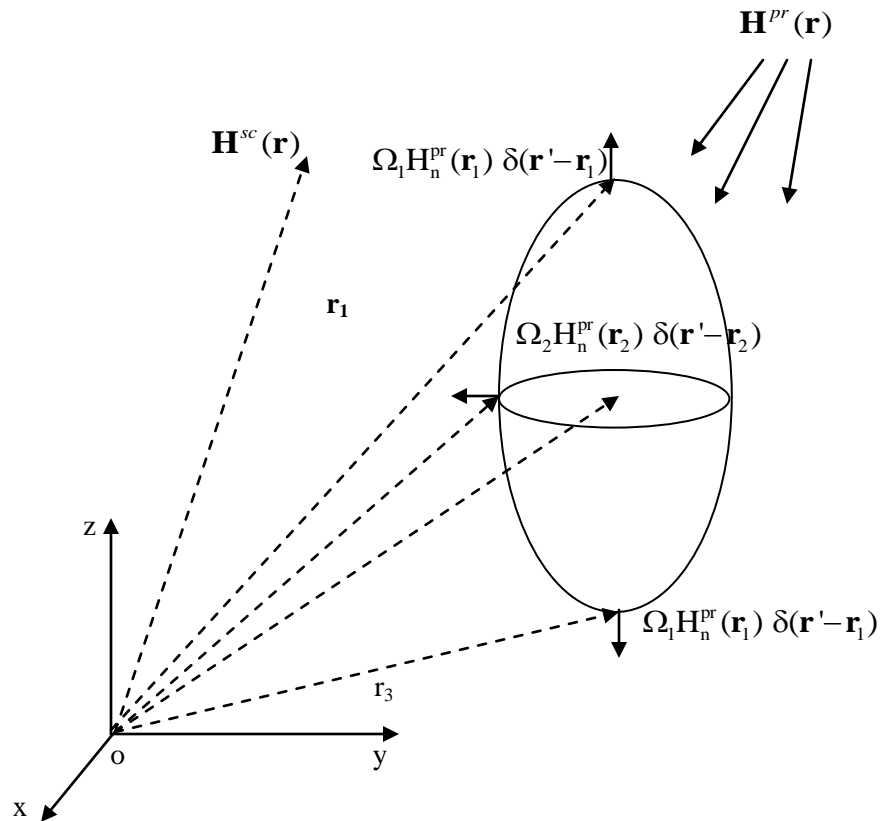


Figure 3: A schematic diagram for a dipole model.

### 2.3.5 Invariance properties of the total NSMS

One of the distinguishing features of the NSMS model is that the total NSMS amplitude is a global characteristic of the object and is independent of the size of the surrounding spheroidal surface. To illustrate this feature let us consider a sphere of radius  $a$ , conductivity  $\sigma$ , and permeability  $\mu = \mu_r \mu_0$  illuminated with a time-varying uniform magnetic field  $\mathbf{H}^{\text{pr}} = \hat{\mathbf{z}}$ . The scattered magnetic field at any point outside the sphere can be written in analytic form as

$$\mathbf{H}_{\text{sph}} = \frac{1}{4\pi R^3} \mathbf{m}_{\text{sph}} \cdot (3\hat{\mathbf{R}}\hat{\mathbf{R}} - \bar{\mathbf{I}}), \quad (47)$$

where  $\mathbf{m}_{\text{sph}} = \beta \mathbf{H}^{\text{pr}}$  is the magnetic dipole moment of the sphere, and the polarizability  $\beta$  can be expressed in terms of the induction number  $k = \sqrt{j\omega\mu_r\mu_0\sigma}$  through

$$\beta = 2\pi a^3 \frac{(2\mu_r + 1)(ka \coth ka - 1) - (ka)^2}{(\mu_r - 1)(ka \coth ka - 1) + (ka)^2}. \quad (48)$$

The scattered field due to the NSMS density in the spherical coordinate system is

$$\mathbf{H}^{\text{sc}}(\mathbf{r}) = \nabla \int_0^{2\pi} a^2 d\varphi \int_0^\pi \Omega(\theta) \cos\theta \frac{\hat{\mathbf{n}}' \cdot \mathbf{R}}{R^3} \sin\theta d\theta, \quad (49)$$

where

$$\begin{aligned} \hat{\mathbf{n}}' &= \hat{\mathbf{r}}' = \sin\theta \cos\varphi \hat{\mathbf{x}} + \sin\theta \sin\varphi \hat{\mathbf{y}} + \cos\theta \hat{\mathbf{z}}, \\ \hat{\mathbf{n}}' \cdot \mathbf{R} &= \hat{\mathbf{n}}' \cdot (\mathbf{r} - \hat{\mathbf{r}}) = z_0 \cos\theta - a, \\ R &= \sqrt{a^2 + z_0^2 - 2az_0 \cos\theta}. \end{aligned} \quad (50)$$

For a homogeneous sphere the amplitude of NSMS density  $\Omega = \Omega_0$  is constant over the spherical surface and is the only unknown to be determined. This can be achieved by matching the secondary magnetic field of the NSMS with the dipole field (40) at an observation point; for convenience we take  $\mathbf{r} = z_0 \hat{\mathbf{z}}$ .

The closed-form solution for the sphere becomes

$$H_z^{\text{sph}} = \frac{m_z}{4\pi} \left[ \frac{3z_0^2}{z_0^5} - \frac{1}{z_0^3} \right] = \frac{2m_z}{4\pi z_0^3} \quad (51)$$

and the scattered NSMS magnetic field due to a uniform source density  $\Omega_0$  simplifies to

$$\begin{aligned}
H_z^{\text{sc}} &= 2\pi a^2 \Omega_0 \frac{\partial}{\partial z_0} \int_0^\pi \sin \theta d\theta \frac{\cos \theta (z_0 \cos \theta - a)}{(a^2 + z_0^2 - 2az_0 \cos \theta)^{3/2}} \\
&= 2\pi a^2 \Omega_0 \frac{\partial}{\partial z_0} \left( \frac{2}{3z_0^2} \right) = -\frac{8\pi a^2 \Omega_0}{3z_0^3} = -\frac{2Q}{3z_0^3}
\end{aligned} \tag{52}$$

where  $Q = 4\pi a^2 \Omega_0$  is the total NSMS of the sphere. Comparing (51) and (52) we find that

$$Q = -\frac{3}{8\pi} m_z. \tag{53}$$

The total NSMS is thus independent of the size of the surrounding surface and is an intrinsic property of the scatterer.

### 2.3.6 Interpretation of the total NSMS

The total NSMS (and its time evolution) depends on the size, geometry, and material composition of the object in question. Early time gates bring out the high-frequency response to the shutdown of the exciting field; the induced eddy currents in this range are superficial, and a large NSMS amplitude at early times correlates with large objects whose surface stretches wide. At late times, where the eddy currents have diffused completely into the object and low-frequency harmonics dominate, the EMI response relates to the metal content (*i.e.*, the volume) of the target. Thus a smaller but compact object has a relatively weak early response that dies down slowly, while a large but thin or hollow object has a strong initial response that decays quickly. These features can be neatly summarized by the parameters of an empirical decay-law model like the Pasion-Oldenburg law see (57).

### 2.3.7 The parameterized NSMS

During APG standardized test-site discrimination studies (see Chapter 6) we use a parameterized version of NSMS to encapsulate the electromagnetic signature of a target [14]. In this version of the model—which provides at least three independent polarizability-like parameters for use in discrimination and thus in a sense extracts further information from the same data—the scatterer is associated with a surrounding sphere  $S$  on which a set of dipoles are distributed. The secondary field is expressed as

$$\mathbf{H}^{\text{sc}}(\mathbf{r}, t) = \oint_S \frac{3\hat{\mathbf{R}}_{s'} \hat{\mathbf{R}}_{s'} - \mathbf{1}}{4\pi R_{s'}^3} \cdot \begin{bmatrix} \Omega_{xx}(\mathbf{r}_{s'}, t) & \Omega_{xy}(\mathbf{r}_{s'}, t) & \Omega_{xz}(\mathbf{r}_{s'}, t) \\ \Omega_{yx}(\mathbf{r}_{s'}, t) & \Omega_{yy}(\mathbf{r}_{s'}, t) & \Omega_{yz}(\mathbf{r}_{s'}, t) \\ \Omega_{zx}(\mathbf{r}_{s'}, t) & \Omega_{zy}(\mathbf{r}_{s'}, t) & \Omega_{zz}(\mathbf{r}_{s'}, t) \end{bmatrix} \begin{bmatrix} H_x^{\text{pr}}(\mathbf{r}_{s'}) \\ H_y^{\text{pr}}(\mathbf{r}_{s'}) \\ H_z^{\text{pr}}(\mathbf{r}_{s'}) \end{bmatrix} ds' \equiv \vec{\mathbf{Z}} \cdot \boldsymbol{\Omega}, \tag{54}$$

where  $\mathbf{R}_{s'}$  points from the location  $\mathbf{r}_{s'}$  of the  $s'$ -th patch on the sphere to the observation point  $\mathbf{r}$  and the response amplitude of each patch is a combination of the primary field piercing it and the tensor of normalized strengths  $\Omega_{ij}(\mathbf{r}_{s'}, t)$ , which, as usual [15], is symmetric:  $\Omega_{ij} = \Omega_{ji}$ . The  $z$ -axis is dictated by the direction of  $\mathbf{m}$  from HAP or from the dipole model, and the  $x$ - and  $y$ -axes are arbitrarily chosen to be perpendicular to  $\hat{\mathbf{z}}$  and to each other. The integral is again transformed to a matrix-vector product through numerical quadrature. The amplitude array  $\Omega$  is determined by minimizing in a least-squares sense the difference between measured data with a known object-sensor configuration and the predictions of equation (54). Once the tensor elements  $\Omega_{ij}(s')$  are found one can define “total polarizabilities” by integrating over the sphere,

$$Q_{ij}(t) = \oint_S \Omega_{ij}(\mathbf{r}_{s'}, t) ds', \quad (55)$$

and these can in turn be used to find “principal elements” through joint diagonalization:

$$\begin{bmatrix} Q_{xx}(t) & Q_{xy}(t) & Q_{xz}(t) \\ Q_{yx}(t) & Q_{yy}(t) & Q_{yz}(t) \\ Q_{zx}(t) & Q_{zy}(t) & Q_{zz}(t) \end{bmatrix} = \Lambda \begin{bmatrix} Q_x(t) & 0 & 0 \\ 0 & Q_y(t) & 0 \\ 0 & 0 & Q_z(t) \end{bmatrix} \Lambda', \quad (56)$$

where the matrix  $\Lambda$  is orthogonal and the prime denotes transposition. The information contained in the diagonal tensor can be summarized further by incorporating the empirical decay law of Pasion and Oldenburg [16]:

$$M_{\alpha\alpha}(t) \equiv Q_{\alpha}(t) = B_{\alpha\alpha} t^{-\beta_{\alpha\alpha}} e^{-\gamma_{\alpha\alpha} t}, \quad \alpha = x, y, z, \quad (57)$$

where  $t$  is the time,  $B_{\alpha\alpha}$ ,  $\beta_{\alpha\alpha}$ , and  $\gamma_{\alpha\alpha}$  are the fitting parameters, and  $M_{\alpha\alpha}(t)$  is the total NSMS along the  $x$ ,  $y$ , and  $z$  directions in the body frame. The principal NSMS elements and the Pasion-Oldenburg parameters are intrinsic to the object and can be used, on their own or in combination with other quantities, in discrimination processing.

## 2.4 The orthonormalized volume magnetic source model

Most EMI sensors are composed of separate transmitting and receiving coils. When the operator activates the sensor, a current runs through the transmitter coils, which results in the establishment of a (“primary” or “principal”) magnetic field in the surrounding space (Figure 4). According to the elementary atomic model of matter, all materials are composed of atoms, each with a positively charged nucleus and a number of orbiting negatively charged electrons. The orbiting electrons cause circulating

currents and form microscopic magnetic dipoles. In the absence of an external magnetic field the magnetic dipoles of atoms of most materials have random orientations, resulting in no magnetic moment. The application of an external time varying magnetic field, by Faraday's law, induces eddy currents in highly conducting bodies by an alignment of the magnetic moments of the spinning electrons and a magnetic moment due to a change in the orbital motion of electrons. These currents and magnetization in turn generate a ("secondary" or "scattered") magnetic field that also varies with time and induces measurable currents in the receiving coils. The induced magnetic dipoles/eddy currents are distributed inside the object and produce a magnetic field intensity  $\mathbf{H}$  outside. The magnetic field due to the  $i$ -th source can then be expressed at any observation point  $\mathbf{r}$  as the matrix-vector product

$$\mathbf{H}_i(\mathbf{r}) = G_i(\mathbf{r})\mathbf{m}_i, \quad (58)$$

where the Green function  $G_i$  is given in detail in equation (1). When there are several such sources, the total field can be expressed as a superposition:

$$\mathbf{H}(\mathbf{r}) = \sum_{i=1}^M G_i(\mathbf{r})\mathbf{m}_i = \begin{bmatrix} G_1 & G_2 & \dots \end{bmatrix} \begin{bmatrix} \mathbf{m}_1 \\ \mathbf{m}_2 \\ \vdots \end{bmatrix}. \quad (59)$$

Before going further we note that our method takes as input the (in principle unknown) number  $M$  of radiating sources. For advanced EMI sensors such as the MetalMapper and  $2 \times 2$  and  $5 \times 5$  TEMTADS arrays we have developed a procedure based on joint diagonalization, sketched in Section 2.5, that estimates  $M$  starting from raw data and with no need for inversion. For other sensors one may proceed by letting  $M$  vary as part of an optimization routine.

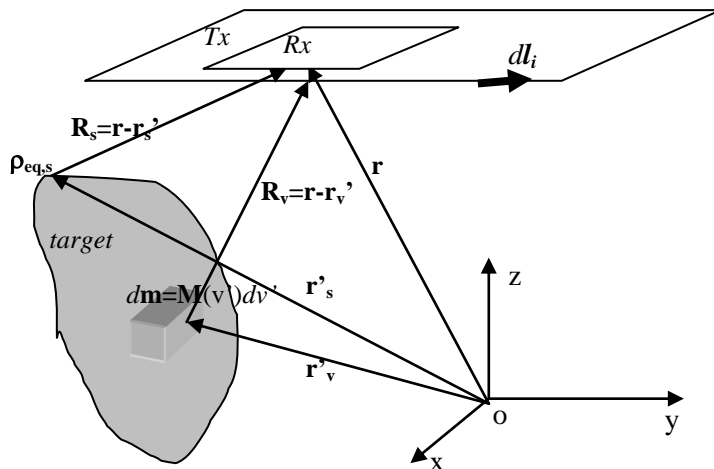


Figure 4: A metallic object under the transmitter. The target's EMI response at the receiver coil can be calculated from the equivalent surface or volume magnetic dipole moment  $d\mathbf{m}$ .

The superposition (59) can be used (and often has) to carry out one- and multi-object inversions starting from data taken at an ensemble of points. All the measured  $\mathbf{H}$ -values—which can pertain to multiple transmitters, multiple receivers, and different vector components—are strung together in a one-dimensional array, while the corresponding Green functions are stacked as matrix rows. The resulting composite  $G$  matrix can then be (pseudo)inverted to find the strengths of the sources. This procedure, which is nothing other than the dipole model if each body is taken to be represented by one source only, works well for one or two sources, but for larger numbers becomes very time-consuming (since the Green matrix becomes very large) and increasingly ill-posed, usually requiring regularization. The ONVMS method is designed to circumvent these difficulties.

### 2.4.1 Orthonormal Green functions

The method starts from the realization that the matrix-vector product (58) is valid at any observation point  $\mathbf{r}$  and, in particular, at every point  $\mathbf{r}_s$ . If we introduce the inner product

$$\langle A, B \rangle = \int_S A^T B ds = \int_{Rx_0} A^T B ds + \int_{Rx_1} A^T B ds + \dots, \quad (60)$$

where the integral is computed over the “sensitive” surfaces of the sensor, and if furthermore we can find a basis of Green functions orthogonal under this measure,

$$\mathbf{H}(\mathbf{r}_s) = \sum_{j=1}^M \Psi_j(\mathbf{r}_s) \mathbf{b}_j \quad \text{such that} \quad \langle \Psi_j, \Psi_k \rangle = F_j \delta_{jk}, \quad (61)$$

where  $\delta_{jk}$  is a Kronecker delta, then it is possible to find the source amplitudes  $\mathbf{b}_j$  without costly and ill-conditioned inversions simply by exploiting the sifting property of the orthogonal basis:

$$\langle \Psi_k, \mathbf{H} \rangle = \sum_{j=1}^M \langle \Psi_k, \Psi_j \rangle \mathbf{b}_j = \sum_{j=1}^M F_j \delta_{kj} \mathbf{b}_j = F_k \mathbf{b}_k \quad (62)$$

and thus

$$\mathbf{b}_k = F_k^{-1} \langle \Psi_k, \mathbf{H} \rangle, \quad (63)$$

which clearly does not involve solving a linear system of equations; it is necessary to invert only the  $6 \times 6$  matrix  $F_k$ . Moreover, this definition of the coefficients  $\mathbf{b}_j$  guarantees that they are “optimal” in the sense that the expansion (61) yields the least mean-square error  $\langle \mathbf{H} - \sum_{j=1}^M \Psi_j \mathbf{b}_j, \mathbf{H} - \sum_{j=1}^M \Psi_j \mathbf{b}_j \rangle$  [17].

To construct the set of orthonormal Green functions we resort to a generalization of the Gram-Schmidt procedure [18]. Assuming that the Green matrices are linearly independent—i.e., that we cannot have a collection of distinctly located dipole sources combining to produce no measurable field unless their amplitudes all vanish—we define

$$\begin{aligned}\Psi_1 &= G_1, \\ \Psi_2 &= G_2 - \Psi_1 A_{21}, \\ &\vdots \\ \Psi_m &= G_m - \sum_{k=1}^{m-1} \Psi_k A_{mk}, \\ &\vdots \\ \Psi_M &= G_M - \sum_{k=1}^{M-1} \Psi_k A_{Mk},\end{aligned}\tag{64}$$

where the  $6 \times 6$  matrices  $A_{jk}$  obey  $A_{jk} = 0$  for  $j \leq k$ . Enforcing the orthogonality relation (61) is equivalent to setting  $\langle \Psi_n, G_m \rangle = F_n A_{mn}$  for  $n < m$ , and using this relation twice in definition (64) we find

$$A_{mn} = F_n^{-1} \left( C_{nm} - \sum_{k=1}^{n-1} A_{nk}^T F_k A_{mk} \right),\tag{65}$$

where the overlap integral  $C_{mn} = \langle G_m, G_n \rangle$ .

At the end of the process it is necessary to recover an expansion expressed, like (58), in terms of the actual Green functions, in part because the functions  $\Psi_j$  are orthogonal (and defined) only at points on the receivers, and in part because of the non-uniqueness of the coefficients  $\mathbf{b}_j$  due to the arbitrary order in which the  $G_j$  enter the recursion (64). To that end, we express

$$\Psi_m = \sum_{k=1}^m G_k B_{mk},\tag{66}$$

and to find the coefficients  $B_{mk}$  we compare expansion (66) term by term to the definition (64) and use the rule that  $A_{jk} = 0$  for  $j \leq k$  to find

$$\begin{aligned}B_{mm} &= I, \text{ the identity,} \\ B_{m(m-1)} &= -A_{m(m-1)}, \\ B_{mq} &= -\sum_{l=q}^{m-1} B_{lq} A_{ml} \text{ for } 1 \leq q \leq m-2,\end{aligned}\tag{67}$$

in terms of which we recover the physical polarizability elements:

$$\mathbf{H} = \sum_{k=1}^M \Psi_k \mathbf{b}_k = \sum_{k=1}^M \left( \sum_{l=1}^k G_l B_{kl} \right) \mathbf{b}_k = \sum_{l=1}^M G_l \left( \sum_{k=l}^M B_{kl} \mathbf{b}_k \right) = \sum_{l=1}^M G_l \mathbf{m}_l. \quad (68)$$

### 2.4.2 ONVMS procedure

With all the pieces in place, we can sketch an algorithm to invert EMI data using the ONVMS model:

- 1) Given a number of sources and their tentative locations, find the Green tensors  $G_i \equiv \bar{\bar{Y}}$  using equation (5) and compute the overlap integrals  $G_{mn}$  using the inner product (60).
- 2) Determine the first normalization factor,  $F_1 = \langle G_1, G_1 \rangle$ , and use it to find all the Gram-Schmidt coefficients  $A_{mn}$  with  $n=1$ :  $A_{m1} = F_1^{-1} C_{1m}$ .
- 3) Set  $m=2$ ; compute, in sequence,
  - a) The coefficients  $A_{mn}$  with  $n=2, \dots, m-1$  using equation (65);
  - b) The function  $\Psi_m$  using the expansion (64);
  - c) The normalization factor  $F_m = \langle \Psi_m, \Psi_m \rangle$ ;

increase  $m$  by 1 and iterate until all sources have been included.

- 4) Once all the  $A_{mn}$ ,  $F_m$ , and  $\Psi_m$  are known, find  $B_{mq}$  using (67).
- 5) Use the orthonormality of the new Green functions to determine the source amplitudes using  $\mathbf{b}_q = F_q^{-1} \langle \Psi_q, \mathbf{H}^{\text{data}} \rangle$ , as in (63). Take the measured field to be piecewise constant—i.e., constant throughout each receiver—when evaluating the integrals.
- 6) Use the computed  $\mathbf{b}_q$ ,  $B_{mq}$ , and  $G_m$ , along with the expansion (68), to generate the secondary field prescribed by the given number of sources at the given locations.
- 7) Compare the model prediction with the measured data, vary the source locations, and iterate until the least-squares discrepancy between prediction and measurement attains a suitable minimum.

The procedure as written applies to only one time gate, but the extension to fully time-dependent functions is straightforward: we need only substitute the vectors  $\mathbf{b}_q$  and  $\mathbf{H}^{\text{data}}$  for two-dimensional arrays

where the columns denote time. The relations between the two, namely (63) and (68), acquire multiple right-hand-sides, and the optimization mentioned on Step 7 of the algorithm is constrained further. As a final remark we note that rigorously speaking the coefficients  $\mathbf{b}_q$  (and, for that matter, the amplitudes  $\mathbf{m}_k$ ) are *not* the polarizabilities themselves but relate more closely to their time derivatives [19-20].

The great advantage of the ONVMS technique is that it takes into account mutual couplings between different parts of targets and avoids matrix singularity problems in cases with multiple objects. Once the polarizability tensor elements and the locations of the elemental responding dipoles are determined one can group them according to their volume distribution. For each group a total polarizability tensor can be computed and diagonalized using joint diagonalization, the topic of Section 2.5. The resulting time-dependent diagonal elements have been shown to be intrinsic to the objects and can be used, on their own or combined with other quantities, in discrimination processing.

## 2.5 Joint diagonalization for multi-target data pre-processing

In real life situations the targets of interest are usually surrounded by natural and artificial debris with metallic content, including, for instance, the remains of ordnance that did explode. Thus it is usually not clear how many objects are producing a given detected signal; all sensing methods, including EMI, are fraught with detection rates that overwhelm cleanup efforts and hike their cost. Here we introduce a data pre-processing technique based on joint diagonalization (JD) that estimates the number of targets present in the field of view of the sensor as it takes a data shot, and, in a good number of cases, even provides the capability to perform real-time characterization and classification of the targets without the need for a forward model.

Joint diagonalization has become an important tool for signal processing and inverse problems, used as part of independent component analysis [21], blind source separation or BSS [22], common principal component analysis, and, more recently, kernel-based nonlinear BSS [23]. We further extend the applicability of the method by using it to detect and locate buried targets without the need for inversion. As we say above, a variation of the method can be used to extricate time-dependent electromagnetic signatures from attitude information. Here we will outline the detailed procedure as applied to the TEMTADS sensor array, a time-domain device with 25 transmitter/receiver pairs that provides 625 measurements over  $N_g = 123$  time gates at each sensor location.

### 2.5.1 The multi-static response matrix

JD estimates the eigenvalues and eigenvectors of a square time- or frequency-dependent multi-static response (MSR) matrix synthesized directly from measured values. To construct the MSR matrices

one just has to stack the 625 readings at each time gate in a  $25 \times 25$  array so that each column stands for one of  $N_t$  transmitters and each row represents one of  $N_r$  receivers:

$$\mathbf{S}(t_k) = \begin{bmatrix} H_{11} & H_{12} & \dots & H_{1N_t} \\ H_{21} & H_{22} & \dots & H_{2N_t} \\ \mathbf{M} & \mathbf{M} & \mathbf{O} & \mathbf{M} \\ H_{N_r 1} & H_{N_r 2} & \mathbf{L} & H_{N_r N_t} \end{bmatrix}, \quad k = 1, K, N_g, \quad (69)$$

where the element  $H_{ij}$  is the field measured by the  $i$ -th receiver when the  $j$ -th transmitter is fired. The second step of the procedure is to diagonalize the 123 matrices at one stroke so they all share a single set of orthonormal eigenvectors. In other words, given the MSR matrix  $\mathbf{S}(t_k)$  at the  $k$ -th time gate, we look for a unitary matrix  $\mathbf{V}$  such that the products

$$\mathbf{D}_k = \mathbf{V}^T \mathbf{S}(t_k) \mathbf{V} \quad (70)$$

are “as diagonal as possible” (i.e., their off-diagonal elements vanish within a preset tolerance). By diagonalizing all the matrices simultaneously we separate the time-dependent intrinsic features of the responding sources (and hence the interred objects), which get encapsulated in the eigenvalues, from the other factors—notably the location and orientation of the target with respect to the sensor—that influence the signal but do not change as the data are being taken; these get bundled into the eigenvectors. (The fact that the locations and orientations can be dissociated in this way from the electromagnetic signatures is an upside of the low frequencies of the quasistatic EMI range, because the relevant Green functions are time-independent.) Thus the measured data can be resolved as a superposition of “elemental” sub-signals, each corresponding to an elementary dipolar source, whose combination corresponds to the buried objects. Each source—and the corresponding field singularity—can moreover be localized numerically: the TEMTADS geometry is such that the diagonal of the unprocessed MSR matrix mimics a set of monostatic measurements, akin to those taken with a handheld sensor, which peak sharply when there is a target directly underneath. The maxima in the diagonal thus point to the transmitter/receiver pairs closest to any responding sources. These location estimates can be grouped and correlated to the eigenvalue distributions to estimate target locations.

### 2.5.2 Interpretation and diagonalization of the MSR matrix

We now proceed to express our above considerations quantitatively. Initially we consider the transmitter assembly, which in TEMTADS consists of a set of coplanar square loops forming a regular grid. The Biot-Savart law gives the primary magnetic induction established at the location  $\mathbf{r}_i$  of the  $i$ -th

source when the  $j$ -th transmitter antenna (whose area is  $\sigma_{\text{Tx}_j}$ ) is excited immediately before shutdown by a current  $I_j$ :

$$\mathbf{B}_{jl}^{\text{pr}} = \frac{\mu_0 I_j}{4\pi} \sigma_{\text{Tx}_j} \frac{1}{\sigma_{\text{Tx}_j}} \oint \frac{d\mathbf{l}' \times (\mathbf{r}_l - \mathbf{r}')}{|\mathbf{r}_l - \mathbf{r}'|^3} = \mathbf{g}_{jl}^{\text{pr}} \sigma_{\text{Tx}_j} I_j. \quad (71)$$

This primary field induces in the  $l$ -th source a dipole moment given by

$$\mathbf{m}_{jl} = \mathbf{U}_l \mathbf{\Lambda}_l \mathbf{U}_l^T \mathbf{B}_{jl}^{\text{pr}}, \quad (72)$$

where the Euler rotation matrix  $\mathbf{U}$  relates the instrument's coordinate axes to the principal axes of the source, and the diagonal polarizability matrix  $\mathbf{\Lambda}_i$ , the only quantity intrinsic to the source, measures the strength with which the primary field induces a moment along each of those axes.

According to Faraday's law, the signal measured by a receiver coil is the electromotive force given by the negative of the time derivative of the secondary magnetic flux through the coil. Since the field at point  $\mathbf{r}$  of a dipole of moment  $\mathbf{m}$  placed at  $\mathbf{r}_0$  is given by

$$\mathbf{B} = \frac{\mu_0}{4\pi} \nabla \times \left( \mathbf{m} \times \frac{\mathbf{r} - \mathbf{r}_0}{|\mathbf{r} - \mathbf{r}_0|^3} \right), \quad \text{and thus} \quad \int \mathbf{B} \cdot d\mathbf{s} = -\mathbf{m} \cdot \frac{\mu_0}{4\pi} \oint d\mathbf{l} \times \frac{\mathbf{r} - \mathbf{r}_0}{|\mathbf{r} - \mathbf{r}_0|^3} \quad (73)$$

by straightforward application of Stokes's theorem, one obtains that the signal sampled at time  $t_k$  by the  $i$ -th receiver (of area  $\sigma_{\text{Rx}_i}$ ) when the  $l$ -th source is excited by the  $j$ -th transmitter is

$$\begin{aligned} H_{ij}^l(t_k) \sigma_{\text{Rx}_i} \sigma_{\text{Tx}_j} I_j &= \frac{\mu_0}{4\pi} \sigma_{\text{Rx}_i} \frac{1}{\sigma_{\text{Rx}_i}} \oint \frac{d\mathbf{l}' \times (\mathbf{r}' - \mathbf{r}_l)}{|\mathbf{r}' - \mathbf{r}_l|^3} \cdot \dot{\mathbf{m}}_{jl}(t_k) = \mathbf{g}_{li}^{\text{sc}} \sigma_{\text{Rx}_i} \cdot \dot{\mathbf{m}}_{jl}(t_k) \\ &= \mathbf{g}_{li}^{\text{sc}} \sigma_{\text{Rx}_i} \cdot [\mathbf{U} \dot{\mathbf{\Lambda}}_l(t_k) \mathbf{U}^T] \cdot \mathbf{g}_{jl}^{\text{pr}} \sigma_{\text{Tx}_j} I_j, \end{aligned} \quad (74)$$

where a dot over a variable indicates its time derivative. In equations (71) and (74) the line element  $d\mathbf{l}'$  lies on the  $x$ - $y$  plane, and as a consequence the Green functions are similar in structure to those of the simple model presented in Section 2.2. Note that we have included the exciting current  $I_j$  and the transmitter and receiver areas in the definition of the signal; we have explicit knowledge of these quantities and can factor them out. If only the  $l$ -th source is illuminated, we construct the MSR matrix for the complete transmitter/receiver array by tiling  $N_r \times N_t$  instances of the expression (74):

$$\mathbf{S} = \mathbf{G}^{\text{sc}} \mathbf{U}_l \mathbf{\Lambda}_l \mathbf{U}_l^T (\mathbf{G}^{\text{pr}})^T, \quad (75)$$

where the primary (or transmitter) dyad  $\mathbf{G}^{\text{pr}}$  is of size  $N_t \times 3$ , the secondary (or receiver) dyad  $\mathbf{G}^{\text{sc}}$  is of size  $N_r \times 3$ , and the response matrix  $\mathbf{U}\Lambda\mathbf{U}^T$  is  $3 \times 3$ . When there is more than one source present, the MSR matrix of equation (75) is readily generalized:

$$\begin{aligned} \mathbf{S} &= \begin{bmatrix} \mathbf{G}_1^{\text{sc}} & \mathbf{G}_2^{\text{sc}} & \dots \end{bmatrix} \begin{bmatrix} \mathbf{U}_1 \dot{\mathbf{A}}_1 \mathbf{U}_1^T & 0 & \dots \\ 0 & \mathbf{U}_2 \dot{\mathbf{A}}_2 \mathbf{U}_2^T & \dots \\ \vdots & \vdots & \ddots \end{bmatrix} \begin{bmatrix} (\mathbf{G}_1^{\text{pr}})^T \\ (\mathbf{G}_2^{\text{pr}})^T \\ \vdots \end{bmatrix} \\ &= \begin{bmatrix} \mathbf{G}_1^{\text{sc}} \mathbf{U}_1 & \mathbf{G}_2^{\text{sc}} \mathbf{U}_2 & \dots \end{bmatrix} \begin{bmatrix} \dot{\mathbf{A}}_1 & 0 & \dots \\ 0 & \dot{\mathbf{A}}_2 & \dots \\ \vdots & \vdots & \ddots \end{bmatrix} \begin{bmatrix} (\mathbf{G}_1^{\text{pr}} \mathbf{U}_1)^T \\ (\mathbf{G}_2^{\text{pr}} \mathbf{U}_2)^T \\ \vdots \end{bmatrix}, \end{aligned} \quad (76)$$

where we see that the features intrinsic to the targets can be separated formally from the particulars of the measurement—that is, from the geometry and dimensions of the sensor and the sensor-target attitude. The array  $\mathbf{S}$  has size  $N_r \times N_t$  and is square if  $N_r = N_t$ , as is the case with TEMTADS. This allows us to diagonalize the matrix but does not suffice to guarantee that the extracted information is useful—i.e., that the eigenvalues and eigenvectors are real, and that the latter are orthonormal. For that to hold we must have a real, symmetric matrix, which requires  $\mathbf{G}_l^{\text{sc}} = \mathbf{G}_l^{\text{pr}} \equiv \mathbf{G}_l$ . This cannot be rigorously true, because the receivers cannot coincide exactly with the transmitters, but holds approximately for TEMTADS if we factor the exciting current and the coil areas out of  $\mathbf{S}$ , as we did in equation (74). The diagonalization we perform is thus a particular case of a singular value decomposition (SVD), and in what follows we use “diagonalization” as shorthand for “SVD of a symmetric matrix.”

The decomposition (76) exhibits the actual polarizability elements but is not directly available to us because the Green tensors are not orthogonal. To see what we do get when we diagonalize  $\mathbf{S}$  we can perform the SVD on  $\mathbf{G}$ :

$$\mathbf{S} = \mathbf{G} \mathbf{U} \Lambda \mathbf{U}^T \mathbf{G}^T = \mathbf{W} \left[ \mathbf{\Sigma} \mathbf{V}^T \mathbf{U} \Lambda \mathbf{U}^T \mathbf{V} \mathbf{\Sigma} \right] \mathbf{W}^T = \mathbf{W} \mathbf{Z} \Delta \mathbf{Z}^T \mathbf{W}^T = \mathbf{Y} \Delta \mathbf{Y}^T \quad (77)$$

In the intermediate step we have used the fact that the matrix within the brackets is real and symmetric and thus has a purely real eigendecomposition. Result (77) shows that the eigenvalue matrix  $\Delta$ , though time-dependent, is not solely composed of source responses, but also contains location and orientation information extracted from the Green tensors. The eigenvectors, likewise, include information from both the polarizabilities and the measurement particulars.

We also see in the decomposition (77) that  $\mathbf{S}$  contains an unknown “hidden dimension”— $3N$ , where  $N$  is the number of sources—in the size of the block-diagonal response matrix. Numerical diagonalization (or, in general, the SVD) of  $\mathbf{S}$  will impose this middle dimension to be  $N_r = N_t$ . Ideally,

the method should be able to resolve up to  $\lfloor N_r / 3 \rfloor$  responding sources, or eight for TEMTADS, but the actual number is lower. For one, the procedure will resolve targets only when they are spatially separated: two distinct dipoles sharing one location decrease the rank of the  $\mathbf{G}$  matrices, and hence of  $\mathbf{S}$ , by 3. In any case, diagonalization of  $\mathbf{S}$  can again let us estimate the number of targets illuminated by the sensor; since the only time-dependent quantities are the intrinsic polarizabilities of the sources, we expect the additional information provided by the time decay of the eigenvalues to be useful for classification.

The development outlined above corresponds to each time gate taken separately. To make sense of the time-dependent information we have to find a way to “follow” each of the eigenvalues as the signal decays. (A similar process must be carried out when using the dipole model for inversion.) One could in principle diagonalize the MSR matrix at each time channel, and the eigenvectors, which depend only on geometry and pose, should stay constant; however, it is not possible to know a priori the order in which the eigenvalues will be given by the diagonalization; this fact—not to mention noise and experimental uncertainty—makes it inevitable to have to disentangle the tensor elements by hand, which is easily done wrong. Instead, we explicitly look for an orthogonal matrix of eigenvectors that diagonalizes all the MSR matrices simultaneously. The procedure we employ is a generalization of the method for single matrices, and is well-known; it is sketched in next Section.

### 2.5.3 Algorithm for joint diagonalization

The joint diagonalization algorithm we use [22, 24-25] is a generalization of Jacobi’s procedure to find the eigenvalues of a single matrix. Formally we set out to solve the optimization problem

$$\begin{aligned} \min_V \quad & \frac{1}{2} \sum_{q=1}^{N_g} \sum_{i \neq j} ([VA(t_q)V^T]_{ij})^2 \\ \text{s.t.} \quad & V^T V = I, \end{aligned} \tag{78}$$

which we accomplish by making repeated Givens-Jacobi similarity transformations designed to gradually accumulate the “content” of the matrices on their diagonals until a certain tolerance level is reached. The transformations are of the form  $A(t_q) \rightarrow A'(t_q) = V_{rs} A(t_q) V_{rs}^T$ , with the matrix  $V_{rs}$  being the identity but with the four elements  $V_{rr}$ ,  $V_{rs}$ ,  $V_{sr}$ , and  $V_{ss}$  replaced by the two-dimensional rotation array

$$\begin{bmatrix} \cos \phi_{rs} & \sin \phi_{rs} \\ -\sin \phi_{rs} & \cos \phi_{rs} \end{bmatrix}, \quad \text{with} \quad \tan 2\phi_{rs} = \frac{f_{rs}}{n_{rs} + \sqrt{f_{rs}^2 + n_{rs}^2}}, \tag{79}$$

where

$$n_{rs} = \sum_q \left\{ [a_{rr}(t_q) - a_{ss}(t_q)]^2 - [a_{rs}(t_q) + a_{sr}(t_q)]^2 \right\}, \quad (80)$$

$$f_{rs} = 2 \sum_q [a_{rr}(t_q) - a_{ss}(t_q)][a_{rs}(t_q) + a_{sr}(t_q)]. \quad (81)$$

The indices are swept systematically, and the procedure is repeated until convergence is reached. The computational burden is equivalent to that of diagonalizing the matrices one by one. The resulting eigenvalues and eigenvectors are all real because all the MSR matrices are symmetric.

## 3 Inverse Models

### 3.1 Introduction

Several EMI sensing and data-processing techniques [1-4, 7, 13, 19, 26-38] have been recently developed for detecting and discriminating between UXO and non-UXO items. Typically the first step of these methods is the recovery of a set of parameters that specify a physics-based model representing the object under interrogation. For example, in EMI sensing, the recovered parameters consist of the object's location and spatial orientation in addition to "intrinsic" parameters such as the polarizability tensor (along with some parameterization of its time-decay curve) in dipole models or the amplitudes of responding magnetic sources in the NSMS and ONVMS models. EMI responses depend nonlinearly on the subsurface object's location and orientation, therefore determining the buried object's orientation and location is a non-linear problem. In this section several inverse scattering approaches are described for EMI data inversion.

Most EMI sensors are composed of separate transmitting and receiving coils. When the operator activates the sensor, a current runs through the transmitter coils, resulting in the establishment of a ("primary" or "principal") magnetic field in the surrounding space. By Faraday's law, this time-varying magnetic field induces eddy currents in highly conducting bodies (ferromagnetic bodies also have their magnetization affected by the impinging field). These currents and magnetization in turn generate a ("secondary" or "scattered") magnetic field that also varies with time and induces measurable currents in the receiving coils. At the end, the electromagnetic data are inverted using different forward models. The procedure for estimating the location, orientation, and electromagnetic parameters of a buried object (linked in a "model vector"  $\mathbf{v}$ ) is carried out by defining an objective function that quantifies the goodness-of-fit between the measured data and the predictions of the forward model. Routinely, a least-squares (LS) approach is taken to recover  $\mathbf{v}$ : formally, if  $\mathbf{d}^{\text{obs}}$  is the vector of the measured scattered field and  $\mathbf{F}(\mathbf{v})$  is the solution to the forward problem, the least-squares criterion assumes the form

$$\text{minimize } \phi(\mathbf{v}) = \left\| \mathbf{d}^{\text{obs}} - \mathbf{F}(\mathbf{v}) \right\|^2. \quad (82)$$

A simple way to determine the model vector  $\mathbf{v}$  is to use the Gauss-Newton method, which starts with an initial guess  $\mathbf{v}_0$  and updates it iteratively through

$$\mathbf{v}_{k+1} = \mathbf{v}_k + \mathbf{s}_k \quad (83)$$

where  $k$  denotes the iteration number and  $\mathbf{s}_k$  is a perturbation direction; we solve for the  $\mathbf{s}_k$  that minimizes  $\phi$ . In many cases the LS approaches suffer from an abundance of local minima that often leads them to

make incorrect predictions of location and orientation. Global search procedures, such as differential evolution (DE) [33-34] and genetic algorithms [37], have been recently developed to avoid this problem. We have combined the DE algorithm with the NSMS model [2] (or with the dipole model [37]) to recover locations and orientations of buried objects. Once these extrinsic properties are found we perform classification using Mixed Models (MM) and standard Matlab built-in classifiers based on maximum likelihood methods or on linear, quadratic, or Mahalanobis distances. Both gradient and global search approaches are computationally intensive because they require a massive number of forward-model evaluations and because the determination of the nonlinear elements of  $\mathbf{v}$ —the location and orientation of the object—is a nontrivial and time-consuming problem in itself. To avoid non-linear, time-consuming inversions, and by so doing streamline the inversion process, we recently developed a new physics-based approach called the HAP method and applied it to various UXO discrimination problems. The HAP method exploits an analytic relationship between the magnetic field vector  $\mathbf{H}$ , the vector potential  $\mathbf{A}$ , and the scalar magnetic potential  $\psi$  (Psi) of a hypothetical point dipole to determine the location of a visually obscured object. Of these quantities only the magnetic field (and often only one of its components) is available, and as part of this project we developed a numerical procedure based on the 2D NSMS model that replaces the measurement surface around the scatterer with a flat plane of dipoles at a (known) location intermediate between the instrument and the target. The amplitudes of these responding sources can be computed starting from high-spatial-coverage geophysical data by solving a linear system of equations and can then be used to reconstruct  $\mathbf{H}$ ,  $\mathbf{A}$ , and  $\psi$  at any point on or above the measurement surface and thus to solve for the relative location  $\mathbf{R}$  and the polarizability  $\bar{\bar{\mathbf{M}}}$  of the hypothetical dipole.

This chapter briefly overviews gradient-based optimization, differential evolution, and the HAP method.

### 3.2 Gradient-based methods of optimization

One of the most popular approaches for solving inverse problems is the gradient method [39-41]. The gradient method requires the system's Jacobian, which contains the gradients of the scattered field with respect to the unknown parameters of interest. In many cases it is impossible to determine the scattered EM field's derivatives analytically; this, however, is not a problem with either the dipole model or the NSMS model. Further, the NSMS-based inverse approach always results in an over-determined system and thus does not suffer from the ill-conditioning that usually afflicts finite-element or finite-difference time-domain methods. The EM scattering problem can be written in compact matrix form as:

$$[Z]\{\Omega\} = \{H^d\} \quad (84)$$

where  $[Z]$  is the scattering matrix,  $\{\Omega\}$  is a vector containing the amplitudes of responding dipoles (normalized by the primary field), and  $\{H^d\}$  is a vector containing the measured data over a set of points. The important point to note is that  $[Z]$  in the NSMS contains explicit expressions for the responding source amplitudes  $\{\Omega\}$  in terms of the object's location and orientation that can be differentiated analytically and that contain no singularities in the regions where they must be evaluated. Let us assume that  $\alpha$  is a set of parameters (orientation, depth, etc.) that must be determined from a set of measured data [42]. A convenient way to view the problem is to define a forward map as one that associates a given  $\alpha$  with an initial value  $\alpha_0$  (which serves to kick-start the inversion process). A least-squares formulation of the problem identifies a minimum of the error function by solution of the equation

$$\left[ \frac{\partial H^{\text{mod}}}{\partial \alpha} \right]_{\alpha_{\beta-1}} \{\delta\alpha_{\beta}\} = [J]_{\alpha_{\beta-1}} \{\delta\alpha_{\beta}\} = \min \left( \{H^{\text{meas}}\} - \{H^{\text{mod}}(\{\alpha_{\beta-1}\})\} \right), \quad (85)$$

where  $[J]_{\alpha_{\beta-1}}$  is a Jacobian matrix based on  $\{\alpha_{\beta-1}\}$ ,  $\beta$  is the iteration number, the modeled values  $\{H^{\text{mod}}(\{\alpha_{\beta-1}\})\}$  are predicted based on  $\{\alpha_{\beta-1}\}$ , and the solution  $\{\delta\alpha_{\beta}\}$  is a vector of incremental steps in the unknown parameters, which are updated via

$$\{\alpha_{\beta}\} = \{\alpha_{\beta-1}\} + \{\delta\alpha_{\beta}\}. \quad (86)$$

For a case in which the EMI response from a body of revolution (BOR) is approximated using five NSMS sources, the solution vector contains 10 numbers: five describe its location and orientation,  $\Theta = (x_0, y_0, z_0, \theta, \varphi)$ , and five more are the source amplitudes ("omega parameters"). These parameters are recovered from measurements  $H^{\text{data}}$  of the secondary magnetic field at the center of the sensor. Specifically, the parameters are found from minimization of the sum of squares (SS),

$$\text{SS} = \frac{1}{2} \sum_{i=1}^{N_{\text{exp}}} (H_i - H_i^{\text{data}})^2 \quad (87)$$

where  $H_i$ , the theoretical scattered magnetic field at each of  $N_{\text{exp}}$  measurement points, is a function of 10 parameters,

$$H_i = H_i(\Theta; \Omega_1, \Omega_2, \Omega_3, \Omega_4, \Omega_5) = \sum_{k=1}^5 \Omega_k \tilde{H}_k(\Theta), \quad (88)$$

assuming five belts of sources. Our model in vector notation is expressed as

$$\mathbf{h} = \mathbf{F}(\boldsymbol{\theta}) + \boldsymbol{\varepsilon}, \quad (89)$$

where  $\mathbf{h} \in \mathbb{R}^{L \times 1}$  is the vector of scattered magnetic field measurements at the center of the sensor ( $L$  is the total number of measurements on the grid),  $\mathbf{H} = \mathbf{H}(\boldsymbol{\theta})$  is the  $L \times 5$  matrix as a function of  $\boldsymbol{\theta}$  and  $\boldsymbol{\Omega} \in \mathbb{R}^{L \times 1}$  is the vector of normalized magnetic charges.

Below we describe three gradient-based methods for the minimization of the sum of squares.

### 3.2.1 Stepwise optimization

This is a traditional way to recover  $\boldsymbol{\theta}$  and  $\boldsymbol{\Omega}$  in alternating fashion. We start by specifying a starting value,  $\boldsymbol{\theta}_0$ , and compute an estimate for  $\boldsymbol{\Omega}$  from linear least squares by solving the corresponding normal equations,

$$\tilde{\boldsymbol{\Omega}} = (\mathbf{H}' \mathbf{H})^{-1} \mathbf{H}' \mathbf{h}, \quad (90)$$

where the primes denote transposition. We then keep  $\boldsymbol{\Omega}$  fixed at  $\tilde{\boldsymbol{\Omega}}$  and perform a nonlinear regression to obtain a new estimate for  $\boldsymbol{\theta}$ , which we then use to find a new  $\tilde{\boldsymbol{\Omega}}$  using (90), iterating until we attain convergence.

### 3.2.2 Simultaneous optimization

In simultaneous optimization we treat the linear  $\boldsymbol{\Omega}$  parameters on the same footing as the nonlinear  $\boldsymbol{\theta}$ ; the Jacobian thus takes the form of an  $L \times 10$  matrix:

$$\mathbf{J} = \begin{bmatrix} \frac{\partial \mathbf{F}}{\partial \boldsymbol{\theta}} & \frac{\partial \mathbf{F}}{\partial \boldsymbol{\Omega}} \end{bmatrix} = \begin{bmatrix} \frac{\partial \mathbf{F}}{\partial x} & \frac{\partial \mathbf{F}}{\partial y} & \frac{\partial \mathbf{F}}{\partial z} & \frac{\partial \mathbf{F}}{\partial \varphi} & \frac{\partial \mathbf{F}}{\partial \theta} & \frac{\partial \mathbf{F}}{\partial \Omega_1} & \frac{\partial \mathbf{F}}{\partial \Omega_2} & \frac{\partial \mathbf{F}}{\partial \Omega_3} & \frac{\partial \mathbf{F}}{\partial \Omega_4} & \frac{\partial \mathbf{F}}{\partial \Omega_5} \end{bmatrix}. \quad (91)$$

### 3.2.3 Condensed algorithm

In this method, we use a closed-form formula to reduce the number of model parameters from 10 to one:

$$\mathbf{h} = \mathbf{F}(\boldsymbol{\theta}) + \boldsymbol{\varepsilon}, \quad (92)$$

where

$$\mathbf{F}(\boldsymbol{\theta}) = \mathbf{H}(\mathbf{H}' \mathbf{H})^{-1} \mathbf{H}' \mathbf{h}. \quad (93)$$

We need the derivatives of  $\mathbf{F}$  with respect to all five components of  $\boldsymbol{\theta}$ ; to compute them we use a matrix chain rule. Using a formula for matrix derivatives we get the derivative for a specific component of  $\boldsymbol{\theta}$  as

$$\frac{\partial \mathbf{F}}{\partial \boldsymbol{\theta}} = \frac{\partial \mathbf{H}}{\partial \boldsymbol{\theta}} (\mathbf{H}' \mathbf{H})^{-1} \mathbf{H}' \mathbf{h} - \mathbf{H} (\mathbf{H}' \mathbf{H})^{-1} \left( \frac{\partial \mathbf{H}'}{\partial \boldsymbol{\theta}} \mathbf{H} + \mathbf{H}' \frac{\partial \mathbf{H}}{\partial \boldsymbol{\theta}} \right) (\mathbf{H}' \mathbf{H})^{-1} \mathbf{H}' \mathbf{h} + \mathbf{H} (\mathbf{H}' \mathbf{H})^{-1} \frac{\partial \mathbf{H}'}{\partial \boldsymbol{\theta}} \mathbf{h} \quad (94)$$

Combining the five derivatives we get the  $L \times 5$  total Jacobian

$$\mathbf{J} = \left[ \frac{\partial \mathbf{F}}{\partial x}, \frac{\partial \mathbf{F}}{\partial y}, \frac{\partial \mathbf{F}}{\partial z}, \frac{\partial \mathbf{F}}{\partial \varphi}, \frac{\partial \mathbf{F}}{\partial \theta} \right] \quad (95)$$

and the Gauss-Newton algorithm takes the form

$$\boldsymbol{\theta}_{s+1} = \boldsymbol{\theta}_s + (\mathbf{J}' \mathbf{J}_s)^{-1} \mathbf{J}' \mathbf{h} \quad (96)$$

to be iterated until reaching convergence.

### 3.3 Differential evolution

Differential evolution (DE) [33-34], one of the global-search algorithms recently developed to bypass the local-minima problem that often leads standard gradient-search approaches to make incorrect predictions for location and orientation, is a heuristic, parallel, direct-search method for minimizing nonlinear functions of continuous variables. Similar in concept to the genetic algorithms that have been used with much success on problems with discrete variables, DE is easy to implement and has good convergence properties.

We have combined the DE algorithm with the above-discussed dipole, NSMS, and ONVMS techniques to invert digital geophysical EMI data following a procedure reminiscent of the stepwise optimization described in the previous section. The scattered field from any object whose location and orientation are known depends linearly on the magnitudes of its responding sources, and the procedure starts by giving initial values of the attitude parameters and using these estimates, along with the measured data, to determine the source amplitudes by solving a linear system of equations. The amplitudes thus found are fed into a nonlinear objective function that quantifies the mismatch between measured data and model predictions and whose (DE-determined) minimum serves to refine the estimates for location and orientation. The procedure continues to alternate between these linear and nonlinear stages until it reaches convergence (or a preset maximum number of iterations). The responding amplitudes are then stored and used in a later classification step, while the location and orientation parameters are used during target excavation.

Differential evolution uses  $N_p$ -dimensional parameter vectors  $\mathbf{v}$ ,

$$\mathbf{v}_{p,G}, p = 1, 2, \dots, N_p \quad (97)$$

where  $G$  is a generation/iteration index. In our case  $\mathbf{v} = \{x_0, y_0, z_0, \theta, \phi\}$ ; the first three are the object's location and the other two are the polar ( $\theta$ ) and azimuthal ( $\phi$ ) Euler angles that define its orientation (by using only two angles we are assuming that UXO are effectively BOR). The objective function to be minimized is defined as

$$F(\mathbf{v}) = \frac{1}{(MN_f)^2} \sum_{m=1}^M \sum_{f=1}^{N_f} |H_{m,f}^{\text{sc}}(\mathbf{v}) - H_{m,f}^{\text{data}}(\mathbf{v})|^2, \quad (98)$$

where  $H_{m,f}^{\text{sc}}(\mathbf{v})$  and  $H_{m,f}^{\text{data}}$  are respectively the theoretical prediction (for vector  $\mathbf{v}$ ) and the measured magnetic field data at the  $m$ -th measurement point (of  $M$ ) and the  $f$ -th frequency or time point (of  $N_f$ ). The DE optimization process itself can be subdivided into three steps:

- 1) The first step creates random initial populations  $\mathbf{v}_{p,G}, p = 1, 2, \dots, N_p$ , that span the entire parameter space. For a given  $\mathbf{v}_{p,G}$  in the generation, a linear system of equations is constructed by matching measured data to the secondary magnetic field from (88). This system is linear in  $\Omega_i$  and is solved directly for those parameters.
- 2) The second step, which requires the most execution time, is the calculation of the secondary magnetic field (88) for each of the  $\mathbf{v}_{p,G}$ . When the NSMS (or ONVMS) model is used, the calculation for each  $\mathbf{v}_{p,G}$  requires a fraction of the time required to execute any other proposed 3D forward model; this relative computational efficiency makes NSMS (or ONVMS) an attractive alternative for performing real-time inversion.
- 3) Next comes the evaluation of the cost function for each population member and the storage of the best sets of parameters. At each step, the DE algorithm produces an estimate of position and orientation. By examining and sorting the cost function at each step, the best-half of the population is chosen as the next generation's parameters, whereas the bottom half is discarded. Thereafter the next generation is created by taking the parameters in the previous generation and applying crossover and mutation operations on them. The three steps are repeated until the maximum number of generations has been reached or until the objective function reaches a desired value. Rules for using DE are discussed in more detail elsewhere [33-34].

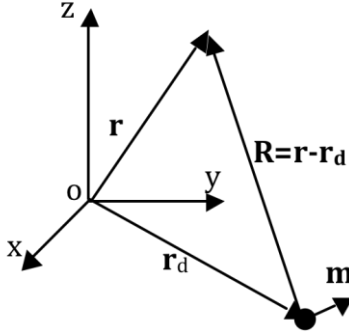


Figure 5: The HAP approach for a dipole.

### 3.4 The HAP method

#### 3.4.1 Estimating the location and orientation of buried objects

In the EMI regime, the secondary magnetic fields measured by the EMI receivers are induced by eddy currents or magnetic dipoles which are distributed non-uniformly inside the scatterer. There are some particular points, named “scattered field singularities” (SFS), where most of these sources are concentrated. Recent studies show that under certain conditions the entire scatterer can be replaced with several responding elementary sources by putting them at SFS points [43-50]. The mathematical and physical properties of SFS and its applications to EM scattering problems are very well documented, and their study is known in the literature as “*Catastrophe Theory*” [43-44]. Our objective has been to determine the locations of the SFS from data without solving traditional ill-posed inverse-scattering problems. We have found a new analytic expression for estimating the location, orientation, and polarizability elements of a buried object starting from measured EMI data. The algorithm (dubbed “HAP” [51]) is based on the fact that a target’s response can be approximated by dipole sources concentrated at SFS points. It utilizes three global values at a single location in space: (1) the magnetic field vector  $\mathbf{H}$ , (2) the vector potential  $\mathbf{A}$ , and (3) the scalar magnetic potential  $\psi$ . Since among these quantities only the  $\mathbf{H}$  field (and sometimes only one of its components) is measurable, we employ a variation of the NSMS model to obtain  $\mathbf{A}$  and  $\psi$  we distribute elementary sources on an auxiliary planar layer, located between the sensor and the object, and find their amplitudes by fitting measured data.

The magnetic field  $\mathbf{H}$  and the scalar ( $\psi$ ) and vector ( $\mathbf{A}$ ) potentials of a magnetic dipole are

$$\mathbf{H} = \frac{e^{jkR}}{4\pi R^3} \left[ \left( \frac{3\mathbf{R}(\mathbf{R} \cdot \mathbf{m})}{R^2} - \mathbf{m} \right) (1 - jkR) - k^2 (\mathbf{R} \times (\mathbf{R} \times \mathbf{m})) \right], \quad (99)$$

$$\psi = \frac{(\mathbf{R} \cdot \mathbf{m})}{4\pi R^3} (1 - jkR) e^{jkR}, \quad (100)$$

$$\mathbf{A} = -\mu_0 \frac{\mathbf{m} \times \mathbf{R}}{4\pi R^3} (1 - jkR) e^{jkR} \equiv -\mu_0 \frac{\mathbf{m} \times \mathbf{R}}{R^3} G(R), \quad \text{where} \quad G(R) = \frac{e^{jkR}}{4\pi} (1 - jkR) \quad (101)$$

where  $k$  is the wave number in the surrounding medium,  $\mathbf{R} = \mathbf{r} - \mathbf{r}_d$ ,  $\mathbf{r}$  is an observation point, and  $\mathbf{r}_d$  is the location of the dipole [49] (Figure 5). Note that the magnetic field (99) has terms that decay as  $R^{-1}$ ,  $R^{-2}$ , and  $R^{-3}$ . The range  $kR \gg 1$  is referred to as the far zone, and fields in this range are referred to as being in the far field. Similarly, fields in the near zone  $kR \ll 1$  are referred to as being in the near field, and the zone  $kR \approx 1$  is called intermediate zone. Typically, UXO detection and discrimination are conducted in the near zone. In addition, in the EMI regime displacement currents are considered irrelevant, which means that the contribution of the  $k^2$  term in equation (99) can be set to zero. Making this assumption, taking the dot product of (99) with  $\mathbf{R}$ , and using (100) we get that

$$\mathbf{H} \cdot \mathbf{R} = \mathbf{H} \cdot (\mathbf{r} - \mathbf{r}_d) = \frac{1}{R^3} \left( \frac{3\mathbf{R}(\mathbf{R} \cdot \mathbf{m})}{R^2} - \mathbf{m} \right) \cdot \mathbf{R} G(R) = 2 \frac{\mathbf{R} \cdot \mathbf{m}}{R^3} G(R) = 2\psi. \quad (102)$$

Similarly, taking the cross product of (99) and  $\mathbf{R}$  and using (101) we obtain

$$\mathbf{H} \times \mathbf{R} = G(R) \frac{1}{R^3} \left( \frac{3\mathbf{R}(\mathbf{R} \cdot \mathbf{m})}{R^2} - \mathbf{m} \right) \times \mathbf{R} = -G(R) \frac{\mathbf{m} \times \mathbf{R}}{R^3} = \frac{\mathbf{A}}{\mu_0}. \quad (103)$$

Now, the cross product of  $\mathbf{H}$  and (103) gives

$$\left[ \mathbf{H} \times \frac{\mathbf{A}}{\mu_0} \right] = \mathbf{H} \times [\mathbf{H} \times \mathbf{R}] = \mathbf{H}(\mathbf{H} \cdot \mathbf{R}) - \mathbf{R} |\mathbf{H}|^2 = 2\mathbf{H} \psi - \mathbf{R} |\mathbf{H}|^2, \quad (104)$$

which allows us to solve for  $\mathbf{R}$ :

$$\mathbf{R} = \frac{2\mathbf{H} \psi - [\mathbf{H} \times \mathbf{A} / \mu_0]}{|\mathbf{H}|^2}. \quad (105)$$

The location  $\mathbf{R}$  of the responding dipole is seen to be independent of the frequency. In other words, as long as MQS assumptions hold, equation (105) is valid when the dipole is in free space and equally well when it is embedded in a conducting medium such as seawater. Also note that  $\mathbf{R}$  is determined as a ratio, which makes the expression (105) partially tolerant to noise due to scaling arguments, since  $\mathbf{A}$  and  $\psi$  are dependent on the  $\mathbf{H}$  field (see equations (102) and (103)). Taking the

cross product of  $\mathbf{R}$  and (103) from the left side and using equation (102) we obtain an expression for the dipole moment  $\mathbf{m}$ :

$$\mathbf{m} = \frac{R}{G(\mathbf{R})} \left( \mathbf{R} \psi + \left[ \mathbf{A} / \mu_o \times \mathbf{R} \right] \right) \quad (106)$$

with  $\mathbf{R}$  previously determined from equation (105).

### 3.4.2 A simplified HAP method

It is possible to simplify the HAP method by eliminating the need for the vector potential. We rewrite equation (102) as

$$\mathbf{H} \cdot \mathbf{r}_d = -2\psi + \mathbf{H} \cdot \mathbf{r}, \quad (107)$$

which provides a least-squares estimate of  $\mathbf{r}_d$  when evaluated at  $N$  distinct observation points:

$$\begin{bmatrix} H_x(\mathbf{r}_1) & H_y(\mathbf{r}_1) & H_z(\mathbf{r}_1) \\ H_x(\mathbf{r}_2) & H_y(\mathbf{r}_2) & H_z(\mathbf{r}_2) \\ \vdots & & \\ H_x(\mathbf{r}_N) & H_y(\mathbf{r}_N) & H_z(\mathbf{r}_N) \end{bmatrix} \begin{bmatrix} x_d \\ y_d \\ z_d \end{bmatrix} = \begin{bmatrix} -2\psi(\mathbf{r}_1) + \mathbf{H}(\mathbf{r}_1) \cdot \mathbf{r}_1 \\ -2\psi(\mathbf{r}_2) + \mathbf{H}(\mathbf{r}_2) \cdot \mathbf{r}_2 \\ \vdots \\ -2\psi(\mathbf{r}_N) + \mathbf{H}(\mathbf{r}_N) \cdot \mathbf{r}_N \end{bmatrix}. \quad (108)$$

### 3.4.3 Determining the HAP amplitudes

To construct the potentials (and the other field components, if unavailable) we assume that the field is produced by a surface distribution of magnetic charge  $q(s')$  spread on a fictitious plane located just below the ground (Figure 6). The positions  $\mathbf{r}_{s'}$  of the sources are fixed and known by construction, and the field can be expressed as the matrix-vector product

$$H_z(\mathbf{r}) = \int \frac{q(s')}{4\pi} \frac{z - z_{s'}}{|\mathbf{r} - \mathbf{r}_{s'}|^3} ds' \equiv \tilde{\mathbf{Z}}_z \cdot \mathbf{q} \quad (109)$$

by employing a quadrature scheme. To determine the array  $\mathbf{q}$  of charges we minimize the difference between model predictions and collected data  $\mathbf{H}^{\text{meas}}$  at a set of known points:

$$\mathbf{q} = \arg \min \frac{1}{2} \left( \tilde{\mathbf{Z}}_z \cdot \mathbf{q} - \mathbf{H}_z^{\text{meas}} \right)^2 = \left[ \tilde{\mathbf{Z}}_z^T \cdot \tilde{\mathbf{Z}}_z \right]^{-1} \left[ \tilde{\mathbf{Z}}_z^T \cdot \mathbf{H}_z^{\text{meas}} \right], \quad (110)$$

where each matrix row corresponds to a different measurement point and each column to a subsurface of the underground virtual source layer. The potential is then found from

$$\psi(\mathbf{r}) = \int \frac{q(s')}{4\pi|\mathbf{r} - \mathbf{r}_{s'}|} ds' \equiv \tilde{\mathbf{Z}}_\psi \cdot \mathbf{q}. \quad (111)$$

Current EMI sensors operate in both monostatic and multistatic modes. Monostatic sensors, such as the Geophex frequency-domain GEM-3 instrument [48] and the Geonics EM-61 and EM-63 time-domain instruments [47] have collocated transmitter and receiver coils, whereas multistatic sensors like the MPV time-domain instrument [28] and the Berkeley UXO Discriminator (BUD) [52] have multiple transmitters or multiple receiver coils or both. We have implemented numerical procedures to estimate the vector and scalar magnetic potentials starting from multi-static or mono-static EMI data. For bistatic data we determine the potentials as described above; for the monostatic case we normalize the amplitudes of the responding auxiliary sources by the primary magnetic field. The procedure is discussed in further detail in [51].

It is worth reiterating that the HAP method replaces the scatterer with a point dipole, and is thus based on a rather drastic simplification; yet it provides acceptable location estimates because the sources within the target that produce the scattered field tend to concentrate at a set of “scattered field singularities” [46, 50]. The locations of these singularities change at every measurement point, since the primary field of the sensor also changes; the HAP method takes these variations into account and outputs an average location as a result.

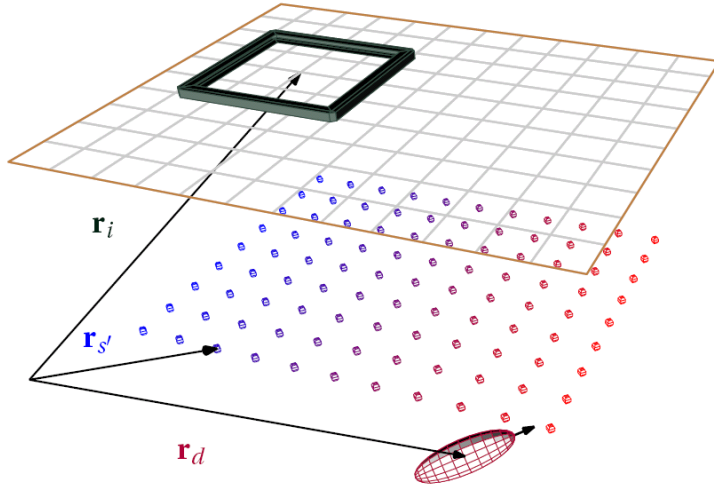


Figure 6: Determining the location and orientation of a buried target. The method assumes the object is a point dipole and exploits an analytic relation between the field measured at  $\mathbf{r}_i$  and the scalar potential at the same point to find the location  $\mathbf{r}_d$ . The potential is constructed using a layer of equivalent magnetic sources placed between the sensor and the object;  $\mathbf{r}_{s'}$  is a typical location on the layer.

### 3.4.4 The HAP method with gradient information

The HAP technique can be simplified further by reducing the formulation such that it only requires the magnetic field and its gradient, both of which are measurable by current sensors. After taking the gradient of equation (102) with respect to the  $x$ -,  $y$ -, and  $z$ -coordinates, we obtain

$$\begin{cases} x_d \frac{\partial H_x}{\partial x} + y_d \frac{\partial H_y}{\partial x} + z_d \frac{\partial H_z}{\partial x} = 3H_x + x \frac{\partial H_x}{\partial x} + y \frac{\partial H_y}{\partial x} + z \frac{\partial H_z}{\partial x} \\ x_d \frac{\partial H_x}{\partial y} + y_d \frac{\partial H_y}{\partial y} + z_d \frac{\partial H_z}{\partial y} = 3H_y + x \frac{\partial H_x}{\partial y} + y \frac{\partial H_y}{\partial y} + z \frac{\partial H_z}{\partial y} \\ x_d \frac{\partial H_x}{\partial z} + y_d \frac{\partial H_y}{\partial z} + z_d \frac{\partial H_z}{\partial z} = 3H_z + x \frac{\partial H_x}{\partial z} + y \frac{\partial H_y}{\partial z} + z \frac{\partial H_z}{\partial z} \end{cases} \quad (112)$$

Thus, in order to determine the target's location we need only the magnetic field  $\mathbf{H}$  and its gradient at a given point in space.

## 4 Statistical approaches

### 4.1 Introduction

UXO discrimination is a three-step process that comprises data collection, parameter inversion, and target classification. The classification step requires robust statistical approaches that will dependably separate UXO from innocuous items. As inputs to these procedures one needs inverted intrinsic parameters that encapsulate relevant features of the targets in question (like the time decay of their response, any symmetries they may possess, etc.) in such a way that the parameters remain as consistent as possible between samples of the same type of target and vary significantly enough from type to type. In other words, one needs to find parameters that cluster well. One can then create feature libraries and, given an unknown target, compare its features to those in the library and ascribe it to the class or cluster that better assimilates it. There are several clustering techniques available, such as K-means clustering [53], principal-component analysis (PCA) [21-25, 54], or the support vector machine (SVM) algorithm [55-56], that are largely heuristically motivated and do not require an underlying statistical model. A possible alternative is model-based clustering, which assumes that the samples of each type of target in an inverted feature data set follow identical multivariate statistical distributions (Gaussians, for example) but with different parameters, and that the complete set is a mixture of a finite number of such distributions. This model-based approach has the desirable traits (1) that it permits the use of objective statistical criteria—like the Akaike Information Criterion (AIC) or the Bayesian Information Criterion (BIC)—to choose the optimal number of clusters and (2) that there are several available distributions that can be varied until one is found that best fits the data; for “heuristic” algorithms, on the other hand, choosing the “correct” number of clusters and the best clustering method is not a settled question and has to be dealt with on an ad hoc basis.

Clustering methods can be either unsupervised or supervised. Supervised clustering uses parameters derived from training/calibration samples, whereas unsupervised clustering applies the same classification criteria to all targets, regardless of size, composition, and decay curves. Supervised clustering has the obvious advantage that it utilizes additional information from the training data as prior knowledge and the obvious drawback that it completely ignores potentially valuable information from the blind data. Several supervised clustering techniques (like SVM [57-58] and template matching) have been applied to UXO discrimination. A straightforward approach to implement the model-based supervised clustering algorithm is to (a) estimate the parameters from the training samples and (b) use the estimated values of the parameters to classify blind data.

This chapter introduces and analyzes several such methods from a UXO discrimination point of view, including mixed modeling, supervised and unsupervised Gaussian mixture models, and the SVM technique. We first introduce and discuss mixed modeling, then give an overview of the unsupervised multivariate normal mixture model, and end by presenting the SVM approach to target classification.

## 4.2 Mixed modeling applied to advanced EMI features

Mixed modeling may be viewed as a compromise between a frequentist and a Bayesian approach. As in a Bayesian approach, it formulates the problem in a hierarchical fashion. The first stage is a conditional model that describes the measurements as a function of the signal, assuming that the distribution of the true signal is known. The second stage specifies the distribution of the true signal using a distribution given *a priori*. In mixed modeling, as in the frequentist approach, the *a priori* distribution is given but the parameters are unknown. These parameters are further estimated using maximum likelihood or an approximation, especially when the dimension is high, to avoid ill-posedness. Under this project we investigated (1) the applicability of mixed modeling to regularize the inversion of EMI data and (2) the possibility of expanding the procedure to incorporate target discrimination.

In general, the determination of intrinsic features of targets (dipole polarizabilities, NSMS, ONVMS, or the like) is an ill-posed problem that often results in instability of inversion. One may improve this instability by incorporating *a priori* information about the properties of the relevant objects. The method we suggest here uses the total NSMS of Section 2.3 for illustration purposes; the total ONVMS of Section 2.4 works just as well. We start by writing down an expression for the secondary field due to a set of discrete sources

$$\mathbf{H}^{\text{sc}}(\mathbf{r}_j) = \sum_i^{N_s} \Omega_i G(\mathbf{r}_i, \mathbf{r}_j), \quad \text{where} \quad G(\mathbf{r}_i, \mathbf{r}_j) = H_n^{\text{pr}}(\mathbf{r}_o, \mathbf{r}_i) \frac{1}{4\pi} \left\{ \frac{1}{r_{ji}^5} (3\mathbf{r}_{ji}(\mathbf{r}_{ji} \cdot \mathbf{n}_i) - r_{ji}^2 \mathbf{n}_i) \right\} \quad (113)$$

is the Green function,  $\mathbf{r}_o$ ,  $\mathbf{r}_j$ , and  $\mathbf{r}_i$  are respectively the locations of the  $o$ -th transmitter, the  $j$ -th receiver, and the  $i$ -th NSMS source,  $\mathbf{r}_{ji} = \mathbf{r}_j - \mathbf{r}_i$ , and  $N_s$  is the total number of NSMS sources. The total NSMS (or ONVMS) is the main classification parameters; we will focus directly on estimating the total NSMS using the average amplitude  $\bar{\Omega}$ . Mixed modeling relates the average  $\bar{\Omega}$  to the actual amplitude at each  $k$ -th point through

$$\Omega_i = \bar{\Omega} + \varepsilon_i, \quad (114)$$

where the  $\varepsilon_i$  are random deviations from the average with mean  $E(\varepsilon_i) = 0$  and variance  $\text{var}(\varepsilon_i) = \sigma_\varepsilon^2$ . After combining equations (113) and (114), and matching modeled field to the data we have that

$$d_j = \bar{\Omega} \sum_i^{N_s} G(\mathbf{r}_i, \mathbf{r}_j) + \eta_j, \quad (115)$$

where  $d_j$  is the data collected at the  $j$ -th point,  $j = 1, 2, 3, \dots, N_d$ , and  $\eta_j$  is a random variable with zero mean and variance

$$\text{var}(\eta_j) = \sigma_\delta^2 + \sigma_\varepsilon^2 \sum_i^{N_s} G^2(\mathbf{r}_i, \mathbf{r}_j). \quad (116)$$

where  $\sigma_\delta^2$  is a parameter that is determined using the mixed model approach. This is the fundamental principle of mixed modeling, which assumes that, in the same way that data can be contaminated with random noise, the *model* used to process and invert it can also contain random statistical errors. The error statistics for both data and model are estimated using the mixed model, which belongs to the family of nonlinear marginal models (Chapter 6, [59]). The average  $\bar{\Omega}$  can be estimated from actual data  $d_j$  using a regularized nonlinear least squares minimization:

$$\sum_{i,j} \left( d_j - \sum_i^{N_s} \Omega_i G(\mathbf{r}_i, \mathbf{r}_j) \right)^2 + \rho \sum_{i=1}^{N_s} (\Omega_i - \bar{\Omega})^2. \quad (117)$$

The regularization parameter  $\rho$  is found by regressing the squared residuals on the variance  $\text{var}(\eta_j)$  as a linear function of  $\sigma_\delta^2$ . The magnitudes  $\Omega$  of the NSMS are determined by solving

$$\Omega = (\rho \mathbf{I} + \mathbf{H}' \mathbf{H})^{-1} (\rho \bar{\Omega} \mathbf{I} + \mathbf{H}' \mathbf{y}). \quad (118)$$

Note that we use matrix notation (boldface type for vectors and matrices, regular roman type for scalars, and primes to denote transposition). The mixed model (MM) algorithm for finding  $\Omega$  can be summarized as follows:

1. Estimate the NSMS from (118) using standard nonlinear least squares and taking  $\rho = 0$ .
2. Obtain  $\bar{\Omega}$  from  $\bar{\Omega} = \frac{1}{N_s} \sum_i^{N_s} \Omega_i$ .
3. Obtain the squared residuals  $e_{ij}^2$  and regress them on  $\sum_i^{N_s} G^2(\mathbf{r}_i, \mathbf{r}_j)$  to determine estimates of  $\sigma_\varepsilon^2$  and  $\sigma_\delta^2$ . Let  $\rho = \sigma_\delta^2 / \sigma_\varepsilon^2$ .
4. Estimate the NSMS from (118) and repeat steps 2, 3, and 4 until  $\Omega$  converges.

We now proceed to describe an algorithm to obtain estimates of  $\bar{\Omega}$ ,  $\sigma_\varepsilon^2$ , and  $\sigma_\delta^2$  using a maximum-likelihood approach. We rewrite the NSMS model (115) as:

$$\mathbf{d} = \mathbf{G}\boldsymbol{\Omega} + \boldsymbol{\eta}, \quad \boldsymbol{\Omega} = \bar{\Omega}\mathbf{1} + \boldsymbol{\varepsilon}, \quad (119)$$

where  $\mathbf{d} = (d_1, d_2, \dots, d_{N_d})'$  is the vector of all  $N_d$  measurements,  $\mathbf{G} \in R^{N_d \times N_s}$  is a matrix,  $\boldsymbol{\Omega}$  and  $\mathbf{1} = (1, 1, \dots, N_s)'$  are vectors of size  $N_s \times 1$ , and the average amplitude  $\bar{\Omega}$  is a scalar. We assume that the errors are normally distributed:

$$\mathbf{y} \sim N(\bar{\Omega} \mathbf{h}_1, \sigma_\varepsilon^2 \mathbf{I}_{N_d} + \sigma_\delta^2 \mathbf{G}\mathbf{G}'), \quad (120)$$

where  $\mathbf{N}$  denotes a multivariate normal distribution and

$$\mathbf{h}_1 = \mathbf{G}\mathbf{1}, \quad (121)$$

which implies that

$$E(\mathbf{y}) = \bar{\Omega} \mathbf{h}_1, \quad \text{and} \quad \text{cov}(\mathbf{d}) = \sigma_\varepsilon^2 \mathbf{I}_{N_d} + \sigma_\delta^2 \mathbf{G}\mathbf{G}'. \quad (122)$$

In previous studies we used weighted least squares and estimated the regularization parameter using the method of moments. Here we apply the method of maximum likelihood, which is more complex but more precise. To obtain the log-likelihood we use the following fact of the multivariate statistics: if  $\mathbf{d} \sim N(\boldsymbol{\mu}, \boldsymbol{\Omega})$ , then the density function is [60]

$$p(\mathbf{d}; \boldsymbol{\mu}, \boldsymbol{\Omega}) = (2\pi)^{-n/2} |\boldsymbol{\Omega}|^{-1/2} \exp\left[-\frac{1}{2}(\mathbf{d} - \boldsymbol{\mu})' \boldsymbol{\Omega}^{-1} (\mathbf{d} - \boldsymbol{\mu})\right]. \quad (123)$$

The likelihood function is the density function with data and parameters exchanged,

$$L(\boldsymbol{\mu}, \boldsymbol{\Omega}) = (2\pi)^{-n/2} |\boldsymbol{\Omega}|^{-1/2} \exp\left[-\frac{1}{2}(\mathbf{d} - \boldsymbol{\mu})' \boldsymbol{\Omega}^{-1} (\mathbf{d} - \boldsymbol{\mu})\right] \quad (124)$$

The twice-negative log-likelihood (TNLL) function  $-2 \ln L$  takes the form

$$\ln |\sigma_\varepsilon^2 \mathbf{I}_{N_d} + \sigma_\delta^2 \mathbf{G}\mathbf{G}'| + (\mathbf{d} - \bar{\Omega}\mathbf{h}_1)' (\sigma_\varepsilon^2 \mathbf{I}_{N_d} + \sigma_\delta^2 \mathbf{G}\mathbf{G}')^{-1} (\mathbf{d} - \bar{\Omega}\mathbf{h}_1). \quad (125)$$

Minimizing the TNLL yields maximum-likelihood estimates of  $\sigma_\varepsilon^2$  and  $\sigma_\delta^2$ , and once these are known we obtain

$$\bar{\Omega} = \frac{\mathbf{d}' (\sigma_\varepsilon^2 \mathbf{I}_{N_d} + \sigma_\delta^2 \mathbf{G}\mathbf{G}')^{-1} \mathbf{h}_1}{\mathbf{h}_1' (\sigma_\varepsilon^2 \mathbf{I}_{N_d} + \sigma_\delta^2 \mathbf{G}\mathbf{G}')^{-1} \mathbf{h}_1} \quad (126)$$

from the weighted least squares. This follows from the fact that the minimum of

$$(\mathbf{d} - \bar{\Omega} \mathbf{h}_1)' \mathbf{W} (\mathbf{d} - \bar{\Omega} \mathbf{h}_1) \quad (127)$$

with respect to  $\bar{\Omega}$ , where  $\mathbf{W}$  is the weight matrix, occurs at

$$\bar{\Omega} = \frac{\mathbf{d}' \mathbf{W} \mathbf{h}_1}{\mathbf{h}_1' \mathbf{W} \mathbf{h}_1}. \quad (128)$$

Note that for  $\mathbf{W} = \mathbf{I}$  we obtain the regular LS. Assuming that  $\bar{\Omega}$  is fixed and letting  $\mathbf{r} = \mathbf{d} - \bar{\Omega} \mathbf{h}_1$  we come to minimization over  $\sigma_\varepsilon^2$  and  $\nu = \sigma_\delta^2 / \sigma_\varepsilon^2$ :

$$N_d \ln \sigma_\varepsilon^2 + \ln \left| \mathbf{I}_{N_d} + \nu \mathbf{G} \mathbf{G}' \right| + \frac{1}{\sigma_\varepsilon^2} \mathbf{r}' (\mathbf{I}_{N_d} + \nu \mathbf{G} \mathbf{G}')^{-1} \mathbf{r}, \quad (129)$$

where  $N_d$  is the number of locations/observations. Differentiating with respect to  $\sigma_\varepsilon^2$  we obtain

$$\frac{N_d}{\sigma_\varepsilon^2} - \frac{1}{\sigma_\varepsilon^4} \mathbf{r}' (\mathbf{I}_{N_d} + \nu \mathbf{G} \mathbf{G}')^{-1} \mathbf{r} = 0, \quad \text{which implies that} \quad (130)$$

which implies

$$\sigma_\varepsilon^2 = \frac{1}{N_d} \mathbf{r}' (\mathbf{I}_{N_d} + \nu \mathbf{G} \mathbf{G}')^{-1} \mathbf{r}. \quad (131)$$

Plugging this back into previous equation we arrive at the equivalent minimization problem

$$N_d \ln \mathbf{r}' (\mathbf{I}_{N_d} + \nu \mathbf{G} \mathbf{G}')^{-1} \mathbf{r} + \ln \left| \mathbf{I}_{N_d} + \nu \mathbf{G} \mathbf{G}' \right|. \quad (132)$$

The straightforward minimization of this problem may be prohibitive because matrix  $\mathbf{I}_{N_d} + \nu \mathbf{G} \mathbf{G}'$  has dimension  $N_d \times N_d$ , so we use a reduced-dimension matrix inverse [59]

$$(\mathbf{I}_{N_d} + \nu \mathbf{G} \mathbf{G}')^{-1} = \mathbf{I}_{N_d} - \mathbf{G} (\rho \mathbf{I}_{N_s} + \mathbf{G}' \mathbf{G})^{-1} \mathbf{G}', \quad (133)$$

where  $\rho = \sigma_\varepsilon^2 / \sigma_\delta^2 = 1 / \nu$  is the regularization parameter [61-65]. Thus we do not have to invert a  $N_d \times N_d$  matrix but only one of size  $N_s \times N_s$ . Similarly, we can reduce the computation of Eq. (132):

$$\ln \left| \mathbf{I}_{N_d} + \nu \mathbf{G} \mathbf{G}' \right| = \ln \left| \rho \mathbf{I}_{N_s} + \mathbf{G}' \mathbf{G} \right| - N_s \ln \rho. \quad (134)$$

Finally we come to the one-dimensional minimization (one-variable function):

$$f(\rho) = N_d \ln \left( \|\mathbf{r}\|^2 - \mathbf{g}'(\rho \mathbf{I}_{N_s} + \mathbf{G}'\mathbf{G})^{-1} \mathbf{g} \right) + \ln |\rho \mathbf{I}_{N_s} + \mathbf{G}'\mathbf{G}| - N_s \ln \rho \quad (135)$$

where  $\mathbf{g} = \mathbf{H}'\mathbf{r}$  for  $\rho > 0$ . Equivalently one can solve the equation

$$\frac{df}{d\rho} = \frac{N_d}{\|\mathbf{r}\|^2 - \mathbf{g}'(\rho \mathbf{I}_{N_s} + \mathbf{G}'\mathbf{G})^{-1} \mathbf{g}} \mathbf{g}'(\rho \mathbf{I}_{N_s} + \mathbf{G}'\mathbf{G})^{-2} \mathbf{g} + \text{tr}(\rho \mathbf{I}_{N_s} + \mathbf{G}'\mathbf{G})^{-1} - \frac{N_s}{\rho} = 0, \quad (136)$$

which can be expressed as  $H(\rho) = 0$ , where

$$H(\rho) = N_d \rho \mathbf{g}'(\rho \mathbf{I}_{N_s} + \mathbf{G}'\mathbf{G})^{-2} \mathbf{g} + \left[ \rho \text{tr}(\rho \mathbf{I}_{N_s} + \mathbf{G}'\mathbf{G})^{-1} - N_s \right] \left[ \|\mathbf{r}\|^2 - \mathbf{g}'(\rho \mathbf{I}_{N_s} + \mathbf{G}'\mathbf{G})^{-1} \mathbf{g} \right] \quad (137)$$

But

$$\begin{aligned} \frac{dH}{d\rho} &= n \mathbf{g}'(\rho \mathbf{I}_{N_s} + \mathbf{G}'\mathbf{G})^{-2} \mathbf{g} - 2n \rho \mathbf{g}'(\rho \mathbf{I}_{N_s} + \mathbf{G}'\mathbf{G})^{-3} \mathbf{g} \\ &+ \left[ \text{tr}(\rho \mathbf{I}_{N_s} + \mathbf{G}'\mathbf{G})^{-1} - \rho \text{tr}(\rho \mathbf{I}_{N_s} + \mathbf{G}'\mathbf{G})^{-2} \right] \left[ \|\mathbf{r}\|^2 - \mathbf{g}'(\rho \mathbf{I}_{N_s} + \mathbf{G}'\mathbf{G})^{-1} \mathbf{g} \right] \\ &+ \left[ \rho \text{tr}(\rho \mathbf{I}_{N_s} + \mathbf{G}'\mathbf{G})^{-1} - K \right] \mathbf{g}'(\rho \mathbf{I}_{N_s} + \mathbf{G}'\mathbf{G})^{-2} \mathbf{g} \end{aligned} \quad (138)$$

Therefore, the Newton's gradient search algorithm takes the form

$$\rho_{s+1} = \rho_s - \frac{H(\rho_s)}{dH/d\rho|_{\rho=\rho_s}} \quad (139)$$

starting from  $\rho_0 = 0$ . Finally, the algorithm is as follows:

1. Obtain the least-squares  $\bar{\Omega}$  as  $\mathbf{y}'\mathbf{h}_1 / \mathbf{h}_1'\mathbf{h}_1$ .
2. Compute  $\mathbf{r} = \mathbf{d} - \bar{\Omega}\mathbf{h}_1$  and  $\mathbf{g} = \mathbf{G}'\mathbf{r}$ .
3. Find the minimum of  $f(\rho)$  using Newton's  $\rho$ -iterations above.
4. Compute the new  $\bar{\Omega}$  as

$$\bar{\Omega} = \frac{\mathbf{d}' \left[ \mathbf{I}_n - \mathbf{G}(\rho \mathbf{I}_{N_s} + \mathbf{G}'\mathbf{G})^{-1} \mathbf{G}' \right] \mathbf{h}_1}{\mathbf{h}_1' \left[ \mathbf{I}_n - \mathbf{G}(\rho \mathbf{I}_{N_s} + \mathbf{G}'\mathbf{G})^{-1} \mathbf{G}' \right] \mathbf{h}_1} = \frac{\mathbf{d}'\mathbf{h}_1 - \mathbf{d}'\mathbf{G}(\rho \mathbf{I}_{N_s} + \mathbf{G}'\mathbf{G})^{-1} \mathbf{G}'\mathbf{h}_1}{\mathbf{h}_1'\mathbf{h}_1 - \mathbf{h}_1'\mathbf{G}(\rho \mathbf{I}_{N_s} + \mathbf{G}'\mathbf{G})^{-1} \mathbf{G}'\mathbf{h}_1} \quad (140)$$

and go to step 2. Incidentally, this is the same formula (126) but expressed in terms of

$\rho = \sigma_e^2 / \sigma_\delta^2$ . Indeed, we have:

$$\bar{\Omega} = \frac{\mathbf{d}'(\mathbf{I}_{N_d} + \sigma_\delta^2 / \sigma_\varepsilon^2 \mathbf{G}\mathbf{G}')^{-1}\mathbf{h}_1}{\mathbf{h}_1'(\mathbf{I}_{N_d} + \sigma_\delta^2 / \sigma_\varepsilon^2 \mathbf{G}\mathbf{G}')^{-1}\mathbf{h}_1} = \frac{\mathbf{d}'(\mathbf{I}_{N_d} + \nu \mathbf{G}\mathbf{G}')^{-1}\mathbf{h}_1}{\mathbf{h}_1'(\mathbf{I}_{N_d} + \nu \mathbf{G}\mathbf{G}')^{-1}\mathbf{h}_1}. \quad (141)$$

5. Iterate until convergence, and at the end compute the amplitudes:

$$\mathbf{\Omega} = (\rho \mathbf{I}_{N_s} + \mathbf{G}'\mathbf{G})^{-1}(\mathbf{G}'\mathbf{d} + \rho \bar{\Omega} \mathbf{1}). \quad (142)$$

## 4.3 Gaussian mixture models

### 4.3.1 Model-based supervised clustering

Targets of interest (TOI) with similar features (i.e., dipole polarizabilities or total NSMS or ONVMS) are likely to show similar power-law/exponential time decay patterns under various conditions, and as a result these patterns form clusters when plotted in a convenient and pertinent space. It is possible to identify an unknown target by comparing its time-decay parameters to those of a set of previously characterized, previously clustered objects and assigning it to the category where its profile fits best. Such “supervised” clustering allows the use of additional information from the training data as prior knowledge; on the other hand, it uses only the training set to estimate the parameters and completely ignores the blind data, which is potentially quite useful. The test data set, moreover, is usually much larger than the training sample, implying that the unused information may be substantially richer than what is contained in the training sample.

Let us assume that there are  $K$  clusters and that each cluster is mathematically described by a parametric continuous or discrete distribution function (usually a Gaussian, as in this case). The classification parameters (extracted for example by fitting the total NSMS or ONVMS with a Pasion-Oldenburg time-decay law) can then be arranged in an  $n \times m$  matrix denoted by  $\mathbf{Y} = [\mathbf{Y}_1, \mathbf{Y}_2, \dots, \mathbf{Y}_m]$ , where  $\mathbf{Y}_i$ ,  $i = 1, 2, \dots, n$ , is a vector,  $n$  is the number of anomalies, and  $m$  is the number of parameters. Each  $\mathbf{Y}_i$  can be considered to follow an  $m$ -dimensional mixture of normal distributions expressed as

$$F(\mathbf{Y}_i) = \sum_{k=1}^K w_k f_i(\mathbf{Y}_i | \boldsymbol{\mu}_k, \boldsymbol{\sigma}_k), \quad (143)$$

where  $w_k$  is the mixing weight of cluster  $k$  (defined as the proportion of anomalies that belong to it),

$\sum_{k=1}^K w_k = 1$ , and

$$f_i(\mathbf{Y}_i | \boldsymbol{\mu}_k, \boldsymbol{\sigma}_k) = \frac{1}{\sqrt{\boldsymbol{\sigma}_k (2\pi)^m}} \exp\left(-\frac{1}{2}(\mathbf{Y}_i - \boldsymbol{\mu}_k)' \boldsymbol{\sigma}_k^{-1} (\mathbf{Y}_i - \boldsymbol{\mu}_k)\right) \quad (144)$$

is the probability density of the  $k$ -th normal distribution with the  $m \times 1$  mean vector  $\mu_k$  and the  $m \times m$  variance-covariance matrix  $\sigma_k$ . The parameters  $\mu_k$ ,  $\sigma_k$ , and  $w_k$  are estimated by the maximum likelihood (ML) criterion using the Expectation Maximization (EM) algorithm.

This simple and intuitive supervised method usually performs well if the number of TOI within each known cluster in the training sample is sufficiently large to ensure high accuracy of the estimates of  $\mu_k$  and  $\sigma_k$ . For small training samples these estimates are subject to large errors—in some cases, if the number of targets within a cluster is smaller than the number of parameters, the estimated variance-covariance matrices may not even be positive definite. Furthermore, much information from the test dataset has not been fully utilized. The test dataset is usually much larger than the training sample, implying that the unutilized information may be substantially more than that contained in the training sample. To overcome this problem we use unsupervised clustering and derive  $\mu_k$  and  $\sigma_k$  from blind-test data using an iterative EM algorithm.

### 4.3.2 Unsupervised classification using the multivariate normal mixture approach

Mixture distribution is perhaps the only model-based approach among existing methods of clusterization and pattern recognition. Its attractive features are that (a) it is not necessary to specify what class each observation belongs to (i.e., the classification is “unsupervised”) and that (b) the method estimates the membership probability which results in *confusion matrix*  $\pi$ .

Let  $\mathbf{x}_1, \dots, \mathbf{x}_n$  be  $m$ -dimensional feature vectors that we want to split into  $K$  classes. It is assumed that each  $\mathbf{x}_i$  belongs to one of  $K$  classes that are described by densities  $\varphi_1(\mathbf{x}), \dots, \varphi_K(\mathbf{x})$ . If  $\pi_k \geq 0$  denotes the probability of  $\mathbf{x}$  belonging to class  $k$ , then the mixture density is the linear combination

$$\varphi(\mathbf{x}) = \sum_{k=1}^K \pi_k \varphi_k(\mathbf{x}), \quad (145)$$

where

$$\sum_{k=1}^K \pi_k = 1. \quad (146)$$

In the case of a normal distribution we have

$$\sum_{k=1}^K \pi_k N(\mathbf{x}; \mu_k, \Omega_k) \quad (147)$$

for the mixture, where the mean  $\boldsymbol{\mu}_k$  and the covariance matrix  $\boldsymbol{\Omega}_k$  are different for the different clusters and subject to estimation along with probabilities  $\pi_k$ . Since the density of  $N(\mathbf{x}; \boldsymbol{\mu}_k, \boldsymbol{\Omega}_k)$  is

$$\varphi_k(\mathbf{x}; \boldsymbol{\mu}_k, \boldsymbol{\Omega}_k) = (2\pi)^{-m/2} |\boldsymbol{\Omega}_k|^{-1/2} \exp\left[-\frac{1}{2}(\mathbf{x} - \boldsymbol{\mu}_k)' \boldsymbol{\Omega}_k^{-1} (\mathbf{x} - \boldsymbol{\mu}_k)\right], \quad (148)$$

the method of maximum likelihood prescribes the maximization of a nonlinear function:

$$L(\boldsymbol{\mu}_k, \boldsymbol{\Omega}_k, \pi_k) = (2\pi)^{-m/2} \sum_{k=1}^K \pi_k |\boldsymbol{\Omega}_k|^{-1/2} \exp\left[-\frac{1}{2}(\mathbf{x} - \boldsymbol{\mu}_k)' \boldsymbol{\Omega}_k^{-1} (\mathbf{x} - \boldsymbol{\mu}_k)\right] \Rightarrow \max_{\boldsymbol{\mu}_k, \boldsymbol{\Omega}_k, \pi_k} \quad (149)$$

This task is not easy because the function is unbounded (it may go to  $+\infty$ ), and this creates numerical obstacles.

A penalized version of the multivariate normal mixture method was recently developed [66]. The idea of penalization is based on the fact that the problem of mixture maximization is not difficult when all  $\boldsymbol{\Omega}_k$  are the same, and thus it would make sense to penalize for variation among the  $\boldsymbol{\Omega}_k$ . Moreover, when  $\boldsymbol{\Omega}_k = \boldsymbol{\Omega}$  then they should be equal to the sample covariance matrix

$$\boldsymbol{\Omega}_k = \mathbf{S}_x = \frac{1}{n} \sum_{i=1}^n (\mathbf{x}_i - \bar{\mathbf{x}})(\mathbf{x}_i - \bar{\mathbf{x}})'. \quad (150)$$

Specifically Chen and Tan suggest to penalize the log of (148) with:

$$p = -a_n \sum_{k=1}^K \left[ \text{tr}(\mathbf{S}_x \boldsymbol{\Omega}_k^{-1}) + \ln |\boldsymbol{\Omega}_k| \right]. \quad (151)$$

The justification of this penalization is that it reaches an extremum if and only if  $\boldsymbol{\Omega}_k = \mathbf{S}_x$  so its addition to (148) tends to keep the  $\boldsymbol{\Omega}_k$  close to  $\mathbf{S}_x$ . The authors suggest using either  $a_n = 1/n$  or  $a_n = 1/\sqrt{n}$  for the weight coefficients. Once penalization is in place we apply the expectation-maximization (EM) algorithm to find the maximum of

$$l(\boldsymbol{\mu}_k, \boldsymbol{\Omega}_k, \boldsymbol{\pi}) + p \quad (152)$$

over  $\boldsymbol{\pi}_k, \boldsymbol{\mu}_k, \boldsymbol{\Omega}_k$ , where the log-likelihood  $l = \ln L$ . Specifically, the EM algorithm for the multivariate normal mixture (MNM) is as follows:

1. Let the initial estimates of  $\boldsymbol{\pi}_k, \boldsymbol{\mu}_k, \boldsymbol{\Omega}_k$  be given (for example, we can take  $\pi_k = 1/K$ ,  $\boldsymbol{\Omega}_k = \mathbf{S}_x$ , and  $\boldsymbol{\mu}_k$  from  $K$ ).

2. Compute the elements of the confusion matrix  $\pi$  as the probability that a given observation  $\mathbf{x}_i$  belongs to class  $k$ :

$$\pi_{ik} = \frac{\pi_k \varphi_k(\mathbf{x}; \boldsymbol{\mu}_k, \boldsymbol{\Omega}_k)}{\sum_{j=1}^K \varphi_j(\mathbf{x}; \boldsymbol{\mu}_j, \boldsymbol{\Omega}_j)}. \quad (153)$$

3. Adjust the probabilities accordingly:

$$\pi_k = \frac{1}{n} \sum_{i=1}^n \pi_{ik}. \quad (154)$$

4. Recompute the means

$$\boldsymbol{\mu}_k = \frac{\sum_{i=1}^n \pi_{ik} \mathbf{x}_i}{n \pi_k} \quad (155)$$

and covariance matrices

$$\boldsymbol{\Omega}_k = \frac{2a_n \mathbf{S}_x + \mathbf{S}_k}{2a_n + n\pi_k}, \quad (156)$$

where:

$$\mathbf{S}_k = \sum_{i=1}^n \pi_{ik} (\mathbf{x}_i - \boldsymbol{\mu}_k)(\mathbf{x}_i - \boldsymbol{\mu}_k)'. \quad (157)$$

5. If the values are different from the previous iteration return to Step 1 and continue until reaching convergence.

#### 4.4 Support vector machines for subsurface object classification

The Support Vector Machine (SVM) [38] is a machine-learning methodology based on statistical learning theory that has been used to perform binary classification [67] and regression [68] and has recently been adapted for multi-category classification [69]. The method has been employed in UXO research, either to classify or regress, in combination with the point-dipole model [7, 70-71], the Standardized Excitation Approach [56, 72-73], and finite elements [74-75], and has shown to be competitive in its discrimination ability in relation to neural networks [73-74] and other statistical methods [57, 76].

A support vector machine learns from data: when fed a series of answered training examples it attempts to make sense of them by weighing the available empirical evidence, with no need for an underlying model, and applies this knowledge to make predictions about unseen cases. The examples can be any combination of model parameters expected to contain evidence of the essence of an object. In the simplest instance of binary classification each  $n$ -dimensional example  $\mathbf{x}_i$  has an associated yes/no attribute  $y_i = \pm 1$ ; the SVM performs the classification by finding a hyperplane that divides the parameter space into two distinct regions, each of which ideally contains points from only one of the categories. During the learning or training process the machine readjusts the hyperplane parameters to accommodate every training vector until it strikes an optimal balance between fitting accuracy and model simplicity. All information about the hyperplane is contained in a subset of the examples—the support vectors that give the method its name—which are then combined to specify a predicting function.

The SVM algorithm uses two different strategies to tackle the nonseparability of realistic data. On the one hand it projects the examples into a space of higher dimensionality by means of a kernel function [77]. The separating surface thus found is flat by construction in the new space but can be curved and even multiply connected in the original. On the other hand, the technique tries to control overfitting—and thus concentrate on essentials rather than on details, resulting in better generalization—by having an adjustable penalty on misclassifications. This penalty is represented by a single scalar parameter, the capacity of the machine [78].

During training an SVM solves the constrained quadratic optimization problem [79]

$$\begin{aligned} \max_{\alpha} \quad & \sum_i \alpha_i - \frac{1}{2} \sum_{i,j} \alpha_i y_i \mathbf{x}_i^T \mathbf{x}_j y_j \alpha_j \\ \text{s.t.} \quad & \sum_i \alpha_i y_i = 0, \quad 0 \leq \alpha_i \leq C, \end{aligned} \tag{158}$$

whose solution is a vector of coefficients  $\alpha_i$  that measure the information content of the examples and are nonzero only for the support vectors. The coefficients are prescribed not to exceed the capacity  $C$ , which limits the influence of potentially problematic points on the final result.

The projection to higher dimensions occurs by substituting the scalar products:

$$\mathbf{x}_i^T \mathbf{x}_j \rightarrow K(\mathbf{x}_i, \mathbf{x}_j) \equiv \mathbf{f}(\mathbf{x}_i)^T \mathbf{f}(\mathbf{x}_j) \tag{159}$$

for some mapping  $\phi(\mathbf{x})$ . The function  $K$  is the kernel we mentioned earlier. It is not necessary to know  $\phi(\mathbf{x})$  to find  $K$ : any function that combines two vectors into a scalar and fulfills the (not very restrictive) set of conditions spelled out in Mercer's theorem [80] can be used as a kernel. Some kernels stretch out

the examples into the added dimensions in such a way that gaps open up between the examples which permit a flat separating surface to pass through. In this chapter we use the radial basis function (RBF) kernel:

$$K(\mathbf{x}_i, \mathbf{x}_j) = \exp(-(\mathbf{x}_i - \mathbf{x}_j)^T(\mathbf{x}_i - \mathbf{x}_j)/2\sigma^2), \quad (160)$$

which surrounds every example with a surface that in a sense “repels” the separating hyperplane. The Gaussian width  $\sigma$  is a second adjustable parameter and usually has a scale on the order of the average separation between points. In [81] it was found that polynomial kernels may outperform the RBF kernel in some electromagnetic inverse problems. We find that the linear kernel makes similar predictions and runs faster than the RBF, though the difference in run time is negligible for the number of training data and example features that we typically use. Once  $\alpha$  is known the SVM can predict the attribute of an unknown example using the function [78, 82]

$$f(\mathbf{x}) = \text{sgn}\left(\sum_{i \in \text{SV}} \alpha_i y_i K(\mathbf{x}_i, \mathbf{x})\right) \quad (161)$$

There are several ways to generalize the SVM procedure to perform multi-class categorization. These have been reviewed in [69], whose authors conclude that the methods more suitable for practical use perform several binary classifications instead of attempting to separate all classes at once. In this

work we adopt a one-against-one approach [82] in which the system carries out  $\binom{k}{2} = \frac{k(k-1)}{2}$

optimizations and obtains the same number of decision functions of the form (161). When given an example to predict the algorithm proceeds by ballot: it evaluates the decision functions one by one on the example and adds a vote to the one category (out of two) in which it is predicted to be. At the end the example is assigned to the category with the most votes; should there be a tie between two classes, the program arbitrarily selects that with the smallest label.

## 5 Advanced models applied to next-generation sensors: Modeling and validation

### 5.1 Introduction

A wide range of different electromagnetic induction sensing technologies, with novel waveforms, multi-axis transmitters, and scalar/vector receivers have been recently developed under SERDP-ESTCP programs. These advanced EMI sensors—including the MetalMapper, the TEMTADS array, the Berkeley UXO discriminator (BUD), and the man-portable vector (MPV) sensor—provide measurements that feature a combination of high spatial diversity, different viewpoints, and a very wide dynamic range and which do full justice to the vector character of the electromagnetic field. Current state-of-the-art EMI systems thus offer data of unprecedented richness for use by discrimination processing algorithms. We have adapted our advanced EMI models and data-interpretation and -processing schemes to all these innovative EMI systems in order to take advantage of the quality of the data they provide.

This chapter overviews these advanced EMI sensors, their geometries and sensing modalities, and the procedures we have in place to model the way they establish primary fields and measure subsurface responses. We validate our methods by making comparisons between measured and modeled data for single- and multi-target scenarios. We initially describe the MetalMapper, continue with TEMTADS and BUD, and finish with a look at the MPV.

### 5.2 MetalMapper

The MetalMapper (MM) is an advanced EMI system for UXO detection and discrimination developed primarily by G&G Sciences and commercialized by Geometrics. The system has three mutually orthogonal transmitter rectangular loops. It is able to illuminate a target with primary fields from three independent directions from a single spatial field point. The  $1\text{ m} \times 1\text{ m}$   $Z$  transmitter loop is located at ground level. The  $Y$  transmitter loop, also  $1\text{ m} \times 1\text{ m}$ , is centered 56 cm above the  $Z$  loop, as is the  $0.98\text{ m} \times 0.98\text{ m}$   $X$  transmitter (Figure 7). The targets are illuminated from different directions depending on the geometry between a particular transmitting loop and the target. The system has seven 10-cm-side receiver cubes placed at seven unique spatial points on the plane of the  $Z$  transmitter loop. The receivers measure the vector  $d\mathbf{B}/dt$  at each of the seven points, thus providing 63 independent readings of the transient secondary magnetic field for each instrument location. The positions of the receiver cubes' centers with respect to the  $Z$  transmitter loop (whose center we consider as the local origin of coordinates for the system) are given in Table 1.



Figure 7: The MetalMapper during SLO site deployment (left) and its schematic diagram (right).

Table 1: MetalMapper receiver locations with respect to the center of the Z transmitter loop.

Rx #	X [cm]	Y [cm]	Z [cm]
0	39	39	5
1	-26	26	5
2	13	13	5
3	0	0	5
4	-13	-13	5
5	26	-26	5
6	-39	-39	5

The MM transmitters are modeled as infinitely thin rectangular wires. The primary magnetic induction produced at any observation point  $\mathbf{r}$  by the  $T$ -th loop is determined simply from the Biot-Savart law,

$$\mathbf{B}_T(\mathbf{r}) = \frac{\mu_0}{4\pi} \sum_{i=1}^{N_{Tx}} \frac{I_T [\Delta\ell_{T,i} \times \mathbf{R}_{T,i}]}{R_{T,i}^3}, \quad T = 1, 2, 3, \quad (162)$$

where,  $\mathbf{R}_{T,i} = |\mathbf{r} - \mathbf{r}'_{T,i}|$ ,  $\mathbf{r}'_{T,i}$  is the location of the  $i$ -th current element, and  $\Delta\ell_{T,i}$  is the tangential length vector for the  $i$ -th subsection of the loop. In what follows, and unless we note otherwise, we divide each transmitter coil into  $N_{Tx} = 40$  subsections whenever we calculate the primary magnetic induction using Eq. (162).

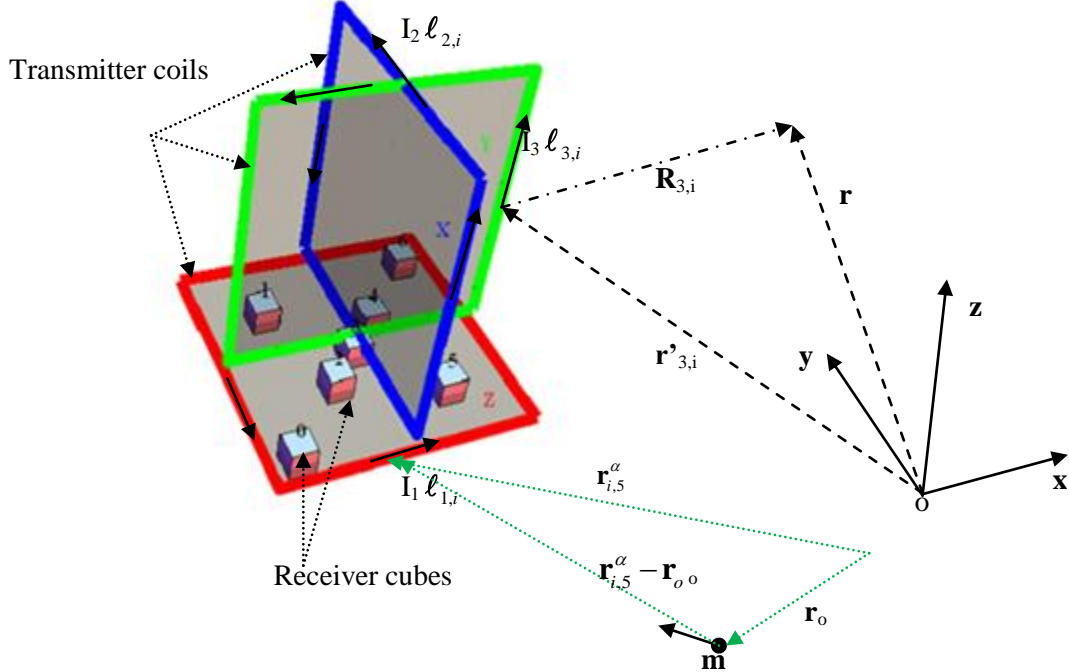


Figure 8. The MetalMapper geometry. The observation point  $\mathbf{r}$  is defined with respect to the global Cartesian coordinate system XYZO;  $\mathbf{r}'_{3,i}$  is the location of the  $i$ -th current element on (in this case) the  $T = 3$  transmitter, which carries a current  $I_3$  in the direction  $\ell_{3,i}$ .

The MM receiver assembly consists of seven cube sensors. Each of these measures along three orthogonal directions the induced voltages that, from Faraday's law, correspond to the negative of the time derivative of the secondary magnetic flux through the area spanned by the different coils. The induced voltage in the  $R$ -th sensor along the  $\alpha$ -th direction, where  $R = 0, \dots, 6$  and  $\alpha = z, y, x$ , is computed using

$$V_R^\alpha = - \int_{S_R^\alpha} \frac{\partial \mathbf{B}}{\partial t} \cdot d\mathbf{s}_R^\alpha = \sum_{i=1}^{N_{Rx}} \frac{\partial \mathbf{B}_i(\mathbf{r}_{i,R}^\alpha - \mathbf{r}_o)}{\partial t} \cdot \hat{\mathbf{n}}_\alpha \Delta s_{i,R}^\alpha, \quad (163)$$

where  $s_R^\alpha$  is the area of the relevant coil (all of which are  $10 \text{ cm} \times 10 \text{ cm}$  squares in MetalMapper) and  $\hat{\mathbf{n}}_\alpha$  is the unit vector perpendicular to it,  $\Delta s_{i,R}^\alpha$  and  $\mathbf{r}_{i,R}^\alpha$  are respectively the  $i$ -th sub-area and vector location point on  $s_R^\alpha$ ,  $\mathbf{B}_i(\mathbf{r}_{i,R}^\alpha) = \mu_o \mathbf{H}_i(\mathbf{r}_{i,R}^\alpha)$  is the magnetic induction (proportional to the magnetic field  $\mathbf{H}_i(\mathbf{r}_{i,R}^\alpha)$ ) produced at  $\mathbf{r}_{i,R}^\alpha$  by a source placed at  $\mathbf{r}_o$ . Within the ONVMS model,  $\mathbf{H}_i(\mathbf{r}_{i,R}^\alpha)$  is calculated using equation (68). In what follows we always divide  $s_R^\alpha$  into  $N_{Rx} = 4$  sub-areas.

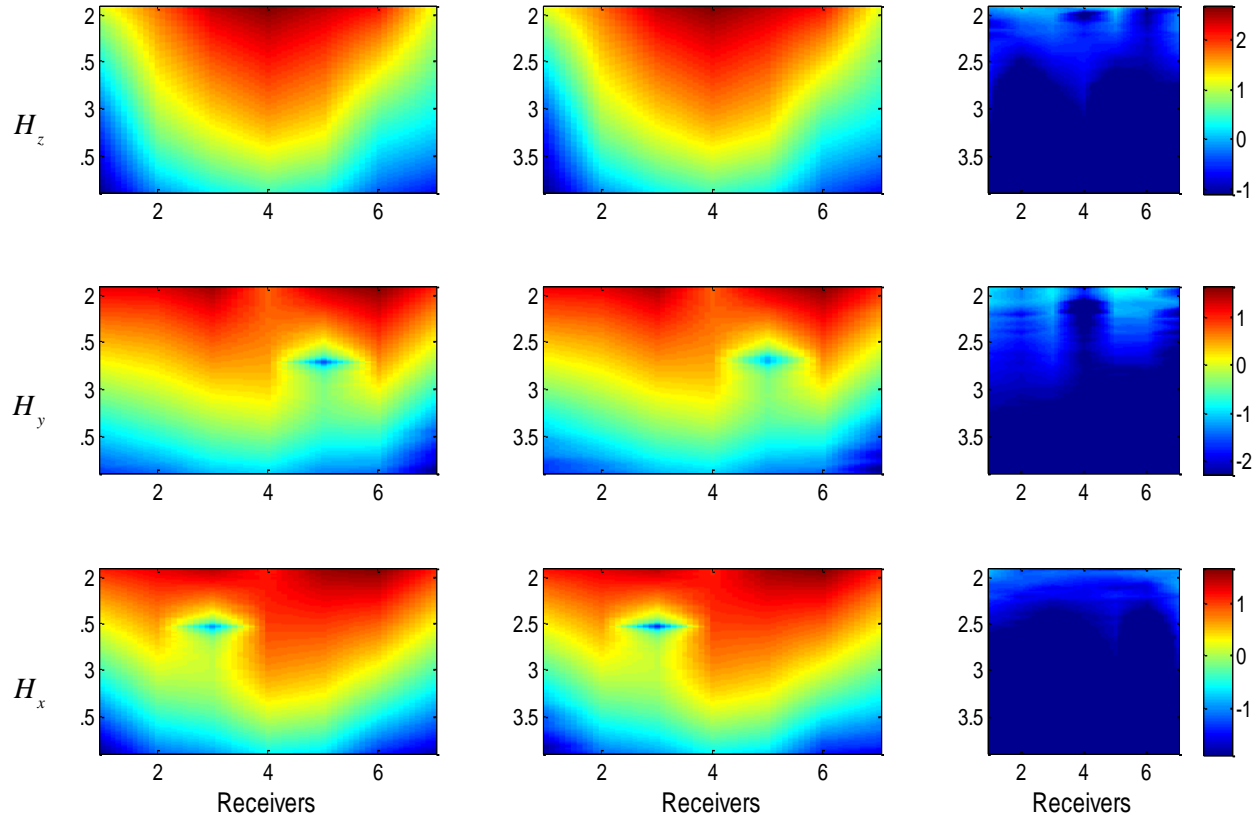


Figure 9. Response of an 81-mm mortar illuminated by the MM Z-transmitter: measured (left), ONVMS prediction (center), and mismatch between modeled and actual data (right). The mortar is placed 35 cm below the sensor center and oriented 45 degrees nose down. The data are plotted in  $\log_{10}$  scale.

To validate the MetalMapper versions of our advanced EMI codes we conducted comparisons between actual and measured data for different targets. Figure 9 through Figure 11 compare measured and ONVMS-modeled data for an 81-mm mortar placed 35 cm below the sensor center, oriented 45 degrees nose-down and illuminated in turn by the  $Z$ ,  $Y$ , and  $X$  transmitters. We use three responding ONVMS sources whose locations are determined with the combined ONVMS-DE algorithm. The inverted location matches the actual target location very well. The model is seen to predict target EMI responses very accurately.

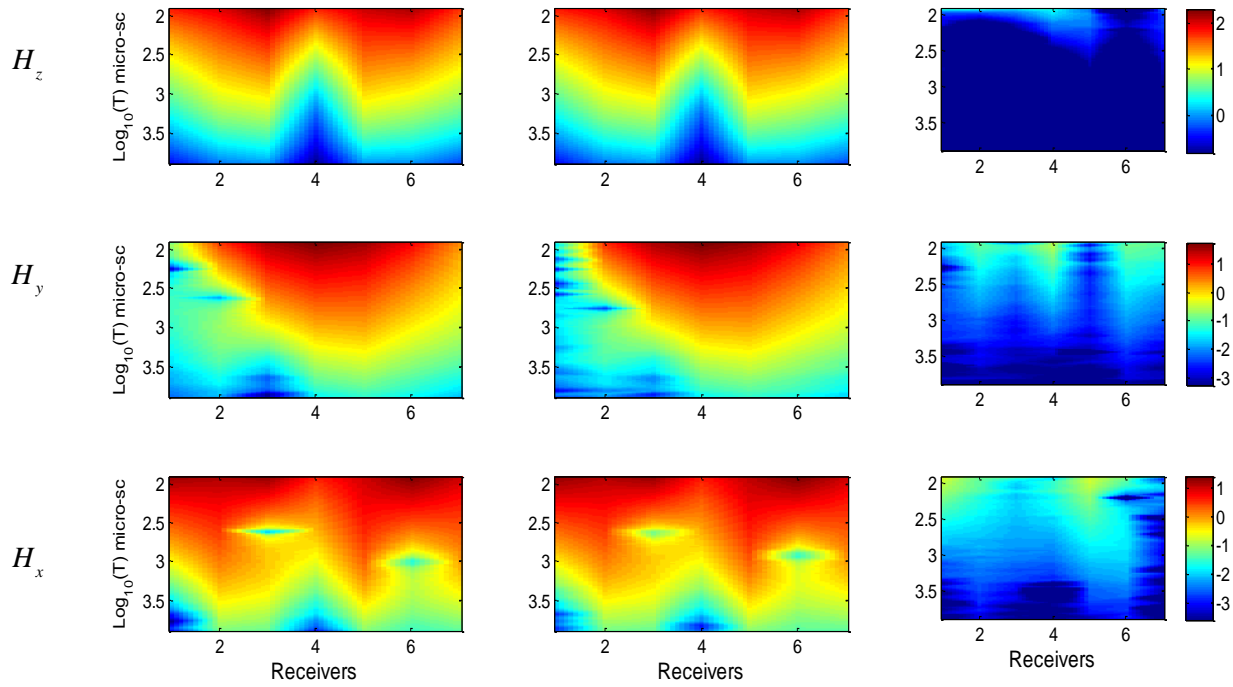


Figure 10. Response of an 81-mm mortar illuminated by the MM Y-transmitter: measured (left), ONVMS prediction (center), and mismatch between modeled and actual data (right). The mortar is placed 35 cm below the sensor center and oriented 45 degrees nose down. The data are plotted in  $\log_{10}$  scale.

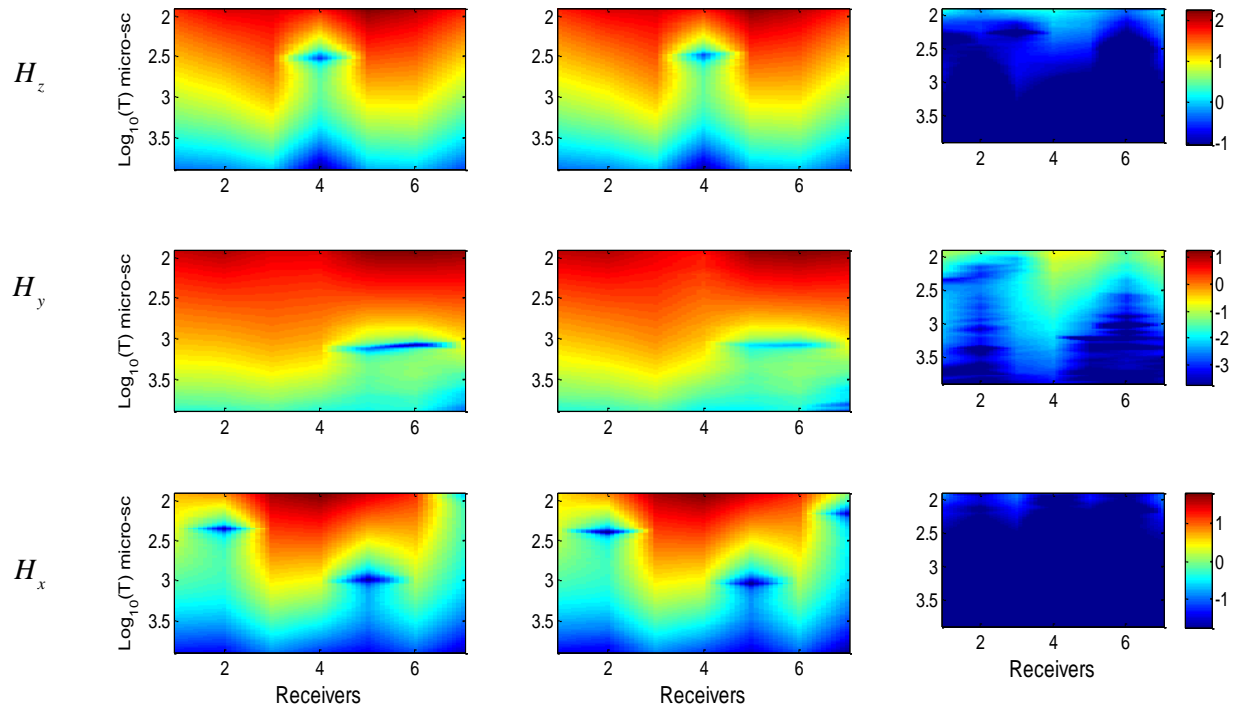


Figure 11. Response of an 81-mm mortar illuminated by the MM X-transmitter: measured (left), ONVMS prediction (center), and mismatch between modeled and actual data (right). The mortar is placed 35 cm below the sensor center and oriented 45 degrees nose down. The data are plotted in  $\log_{10}$  scale.

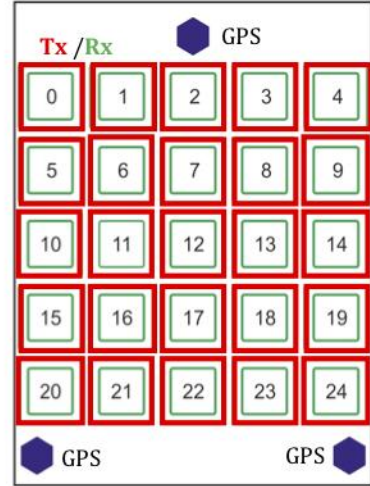


Figure 12: Photo of the TEMTADS in deployment at Blossom Point Test Site (left) and a schematic diagram of its Tx/Rx sensors (right).

## 5.3 TEMTADS

### 5.3.1 TEMTADS modeling

The NRL time-domain EMI sensor array TEMTADS is a next-generation system designed for subsurface target discrimination. The sensor consists of 25 transmit/receive pairs, each composed of a 35-cm square transmitter loop surrounding a 25-cm square receiver loop, arranged in a rectangular  $5 \times 5$  grid with 40-cm neighbor-to-neighbor separation [83] (Figure 12). The sensor activates the transmitter loops in sequence, one at a time, and for each transmitter all receivers receive, measuring the complete transient response over a wide dynamic range of time going approximately from 100 microseconds ( $\mu\text{s}$ ) to 25 milliseconds (ms) and distributed in 123 time gates. The sensor thus provides 625 spatial data points at each location, with unprecedented positional accuracy.

In modeling for TEMTADS, the transmitter loops are idealized as infinitesimally thin  $35 \text{ cm} \times 35 \text{ cm}$  square loops. The primary field produced at any observation point by a given transmitter loop is determined from equation (162). We use  $N_{Tx} = 20$  for TEMTADS unless we note otherwise. The TEMTADS measured signal is modeled using equation (163), assuming  $\alpha = z$  throughout and receiver sizes of  $25 \text{ cm} \times 25 \text{ cm}$  and dividing each receiver into  $N_{Rx} = 9$  sub-areas. We compare actual and ONVMS modeled data for a 105-mm projectile in Figure 13 and find very good agreement.

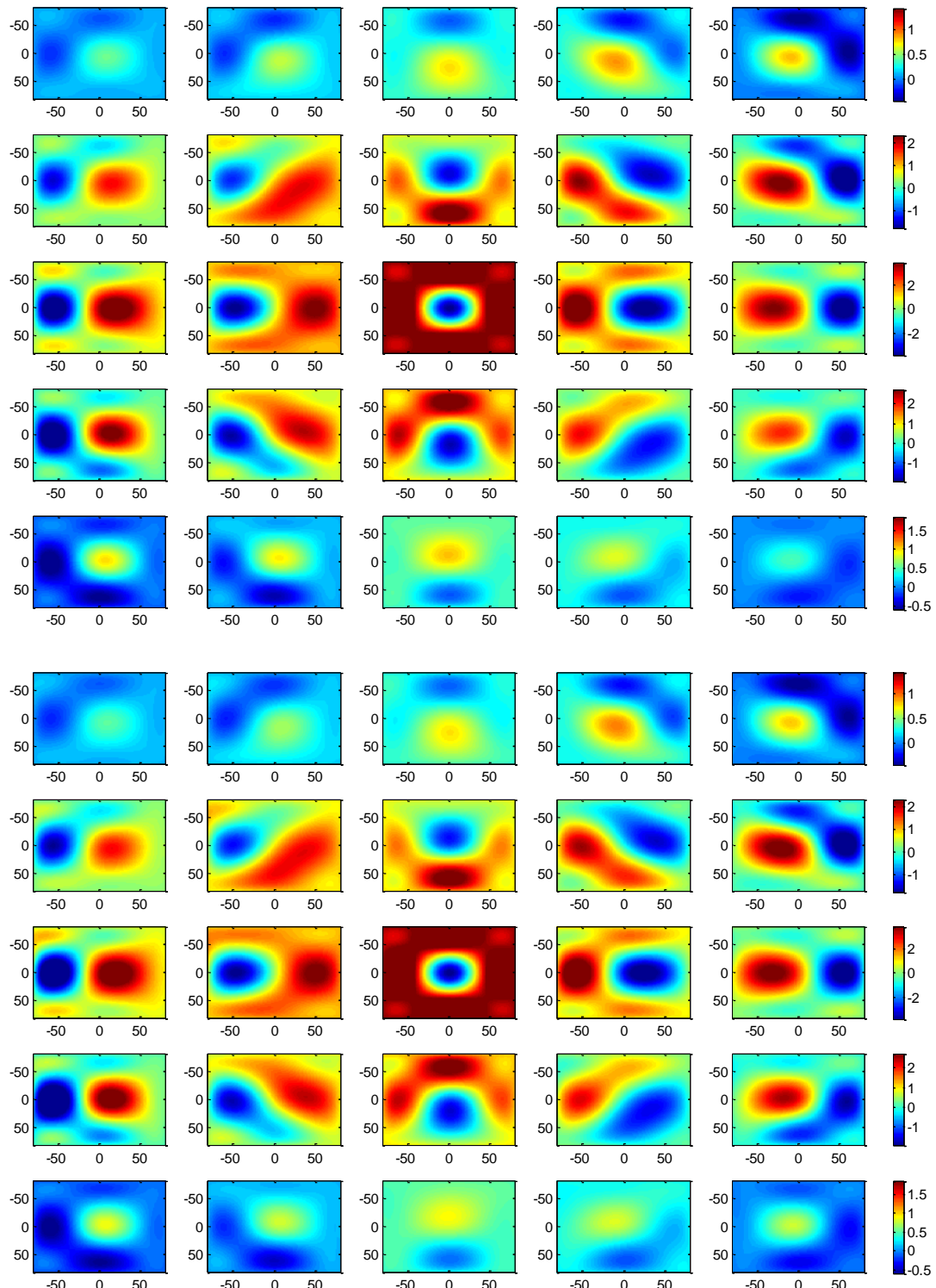


Figure 13. Measured (top five rows) and ONVMS-modeled (bottom five) TEMTADS data for a 105-mm projectile at the 25th time channel. The target is buried at a depth of 30 cm and oriented horizontally relative to the TEMTADS system.



Figure 14: The APG TOI.

Table 2: Inverted location and orientation for TEMTADS data

Case #	Ground truth /estimated for a 37 mm UXO				
	Xo [m]	Yo [m]	Zo [m]	Azimuth [Degree]	Dip [Degree]
1	0.0/(0.03)	0.0/(0.02)	-0.35/(-0.39)	0/(3)	0/(5)
2	0.0/(0.013)	0.0/(0.007)	-0.34/(-0.369)	0/(3)	90/(88)
3	0.0/(0.001)	0.0/(0.02)	-0.38/(-0.41)	0/(5)	-90/(85)
4	0.0/(0.04)	0.0/(0.05)	-0.37/(-0.405)	0/(5)	45/(35)

### 5.3.2 APG test-site classification

To demonstrate the classification performance of the advanced EMI models we conducted discrimination studies at the APG test site. We applied a combined HAP/NSMS approach to TEMTADS data sets. The main objective of the study was to discriminate TOI from non-TOI targets and further to indicate the type and caliber of each TOI. The TOI at APG varied in size from 25 mm up to 155 mm and are depicted in Figure 14.

There were three types of data sets: 1) Test stand data set collected for 14 UXO items placed in air for different depths and orientations; 2) Calibration grid data sets collected over the same targets and over some clutter items; 3) Blind grid data sets collected over 214 buried items. According to a preliminary data analysis by ESTCP, soil responses were insignificant at this site, and they were thus subsequently neglected. The test-stand and calibration grid data sets were used to test data inversion and discrimination algorithms. Object depths were inverted for each grid using the HAP method. The results for a 37-mm UXO are tabulated in Table 2. Since, TEMTADS half thickness is 5cm, the inverted depths were in very good agreement (between 1=(-4+5) and 2=(-3+5) cm) with the actual depths for test-stand UXO items.

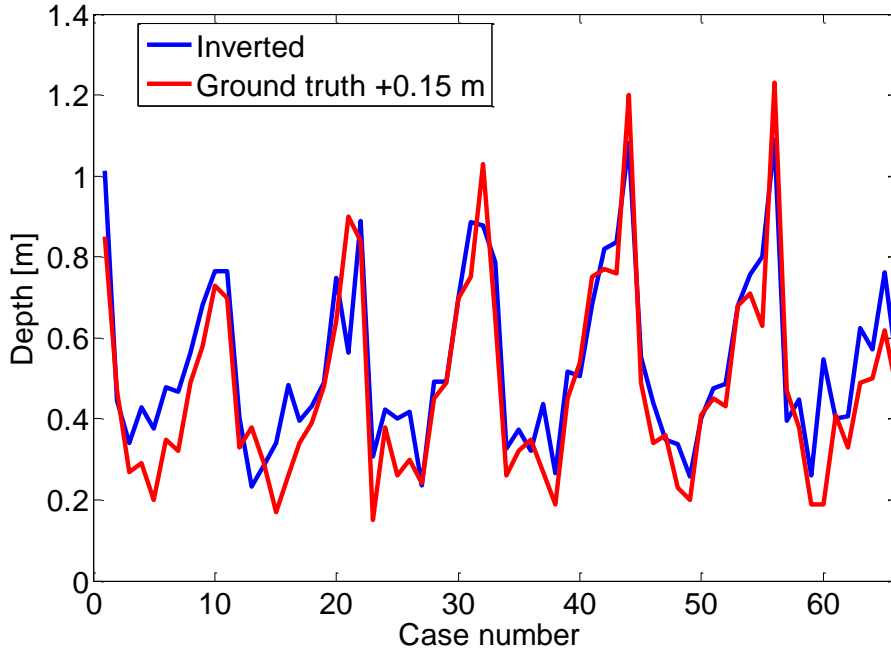


Figure 15: Comparison between the inverted and actual depth for all 65 APG calibration targets.

We also used the HAP method to invert for the depths of all 65 calibration targets. The results are depicted in Figure 15. The inverted depth differed by up to 15 cm from the ground truth, a difference due to the fact that HAP estimates the distance from the sensor center to the target center, as was recorded for test-stand cases, while for calibration items the depths were measured from the ground surface. The sensor is 4" (10.1 cm) above the ground and the transmitters are about 10 cm thick, and therefore the method provides reasonably accurate depth estimates.

Once we established that the HAP method estimates depths accurately for test-stand and calibration items we proceeded to estimate the total NSMS for all items and used it for discrimination. Figure 16 shows the inverted total NSMS as a function of time from test-stand TEMTADS data sets with the 105-mm projectile and the 81-mortar as targets. Each set of test-stand measurements comprised six different depths and target orientations. The total NSMS is seen to be unique for all cases and, for both test-stand and calibration data. We then determined the best NSMS classification features. We fit the total  $M_{zz}$  NSMS curves with the Pasion-Oldenburg expression  $M_{zz}(t) = kt^{-\beta}e^{-\gamma t}$ , where  $t$  is time, and  $k$ ,  $\beta$  and  $\gamma$  are the fitting parameters for each anomaly. We studied different combinations of  $\ln k$ ,  $\beta$ , and  $\gamma$  using test-stand data. The results for  $\beta$  vs.  $\ln k$  appear in Figure 17, and those for  $\gamma$  vs.  $\ln k$  and  $\gamma$  vs.  $\beta$  appear in Figure 16. We see that the best classification performance is achieved using  $\ln k$  and  $\beta$ .

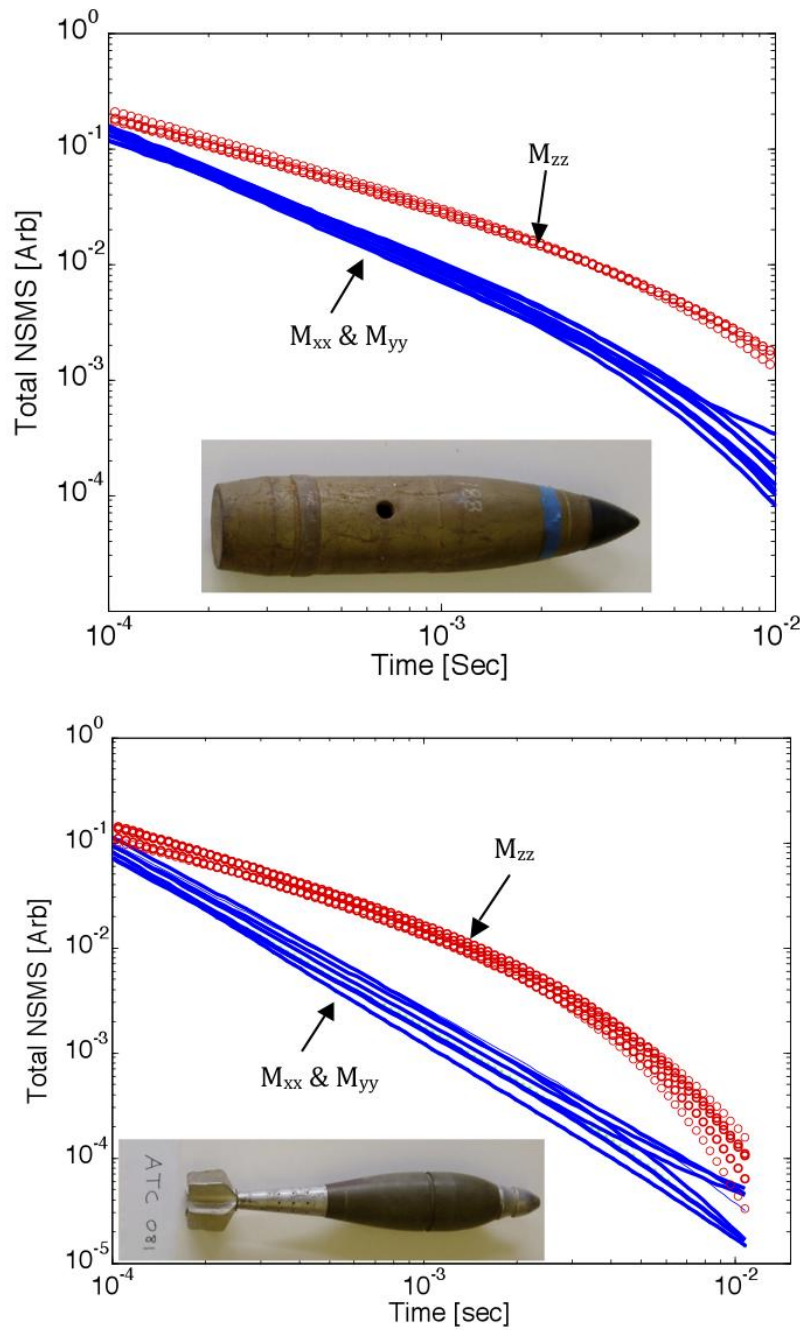
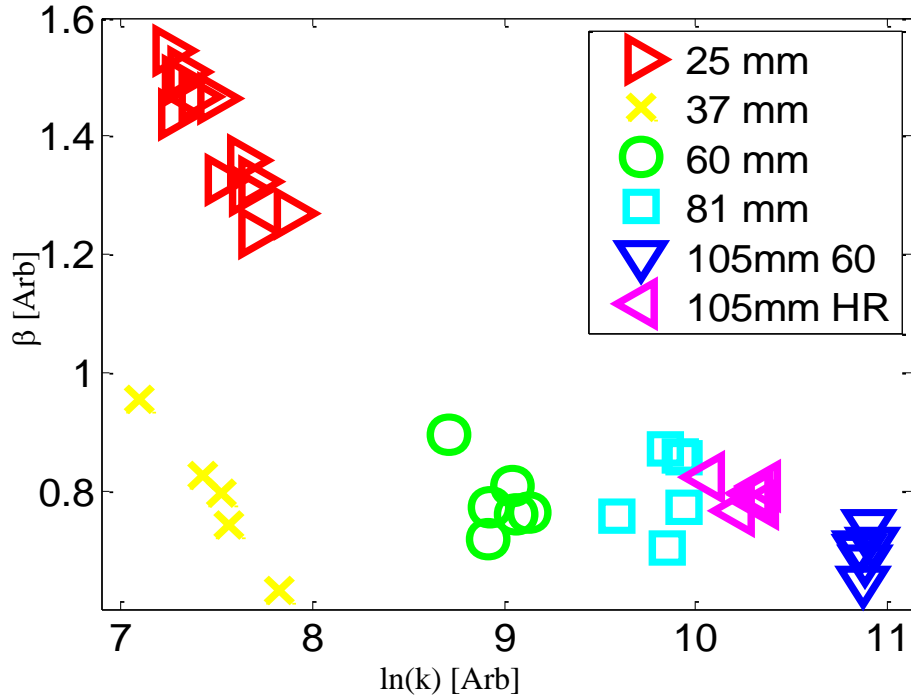
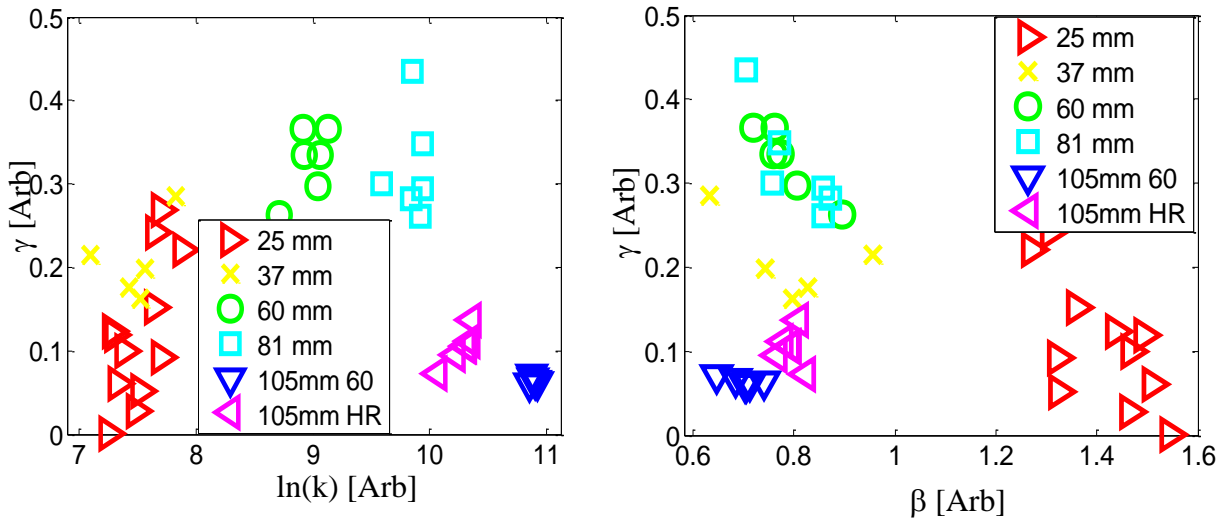


Figure 16: Inverted total NSMS for APG test-stand 105 mm projectile and 81 mm mortar.

Figure 17: Scatter plot of inverted  $\beta$  vs.  $\ln k$  classification features for APG test-stand TOI.Figure 18: Scatter plot of inverted  $\gamma$  vs  $\ln k$  (left) and  $\beta$  (right) parameters for APG test-stand TOI.

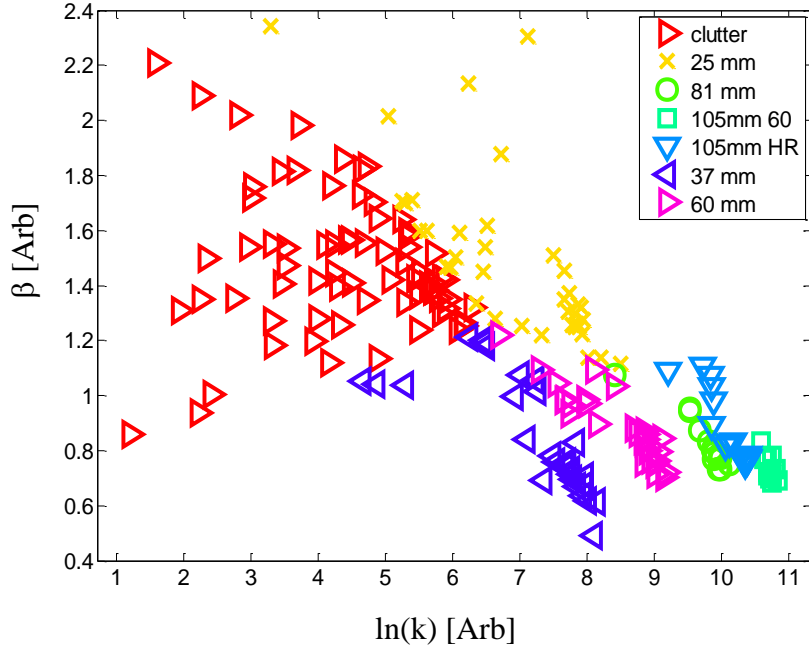


Figure 19: Scatter plot of inverted  $\beta$  vs.  $\ln k$  classification features for all 214 APG blind-test anomalies.

Finally, the described data inversion and classification schemes were applied to the 214 blind grid-data cells. These were also first inverted to determine the total NSMS, from which time-decay-history curves were synthesized, discrimination features were extracted, and classification was performed vis-à-vis test-stand UXO items. A scatter plot of inverted and classified  $\ln k$  and  $\beta$  features for all 214 APG test anomalies is shown in Figure 19. The result illustrates that the inverted features for 60-mm, 81-mm, and 105-mm TOI are clustered tightly, while those for 37-mm and 25-mm TOI s are scattered and mixed with those of clutter items. This complicates classification.

To overcome this problem, in addition classification/clustering approach, the entire time decay history of the total NSMS were also examined and compared to the total NSMS of the test-stand TOI case-by-case as a check on the classification. The comparisons are summarized in Figure 20 and Figure 21. For all APG test anomalies a ranked list was created in which the anomalies were ranked as clutter or TOI and TOI were further ranked by caliber and type. This list was submitted to the Institute for Defense Analyses (IDA) for independent scoring. The scores showed that the advanced model was able to identify all UXO as TOI and classified all UXO correctly by type and caliber. The false-positive rate was 5%.

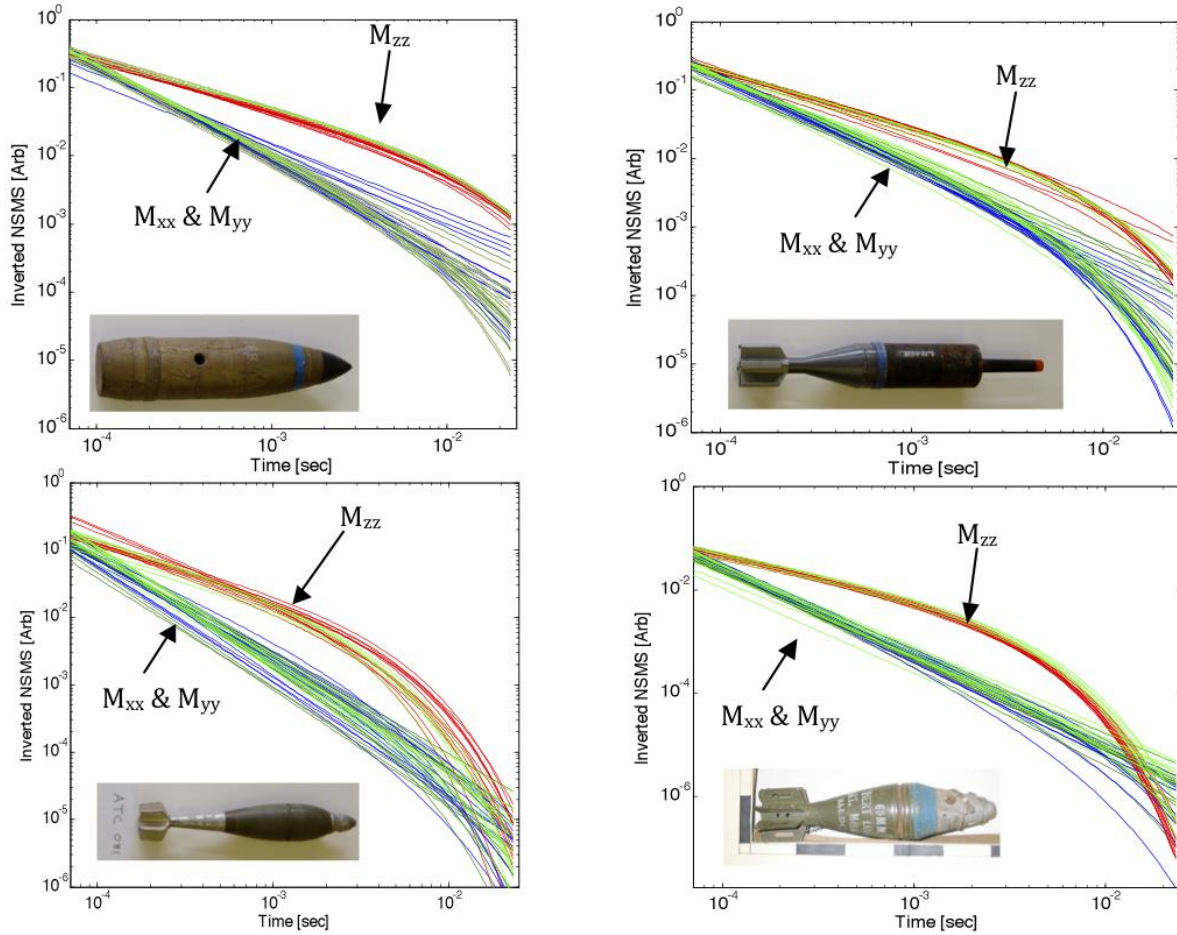


Figure 20: Comparison between library (green lines) and inverted (red and blue lines) blind-test total NSMS for 105-mm projectiles, 81-mm munitions, and 60-mm mortars.

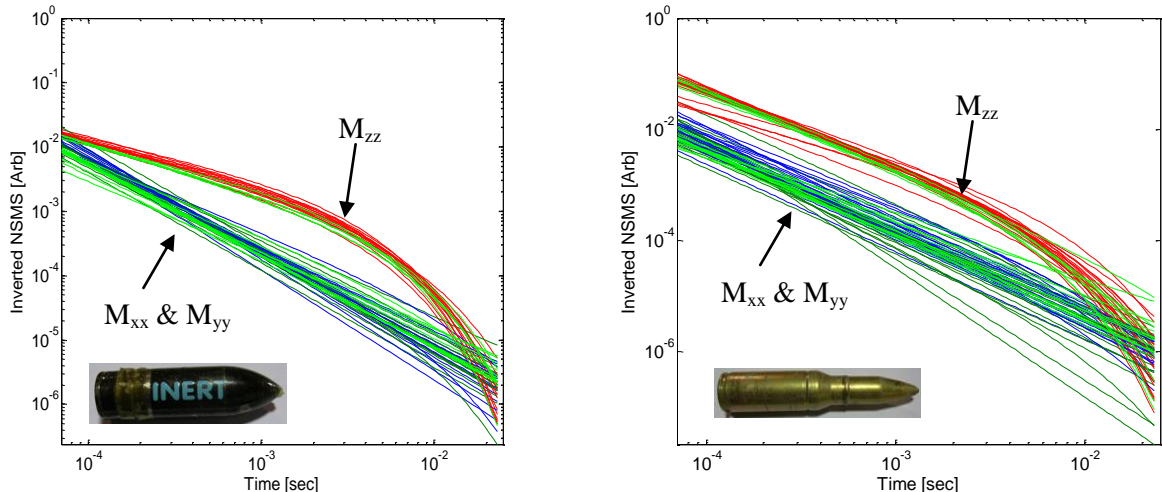


Figure 21: Comparisons between library (green lines) and inverted (red and blue lines) blind-test total NSMS for 37-mm and 25-mm mortars.

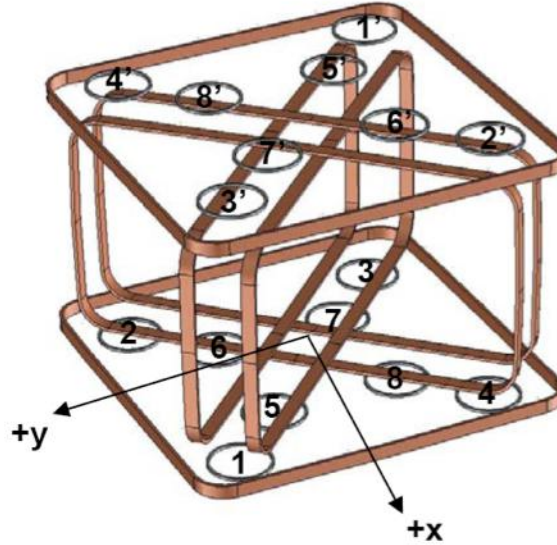


Figure 22: Schematic diagram of the BUD system.

## 5.4 BUD

The Berkeley UXO discriminator (BUD) is an advanced standalone time-domain system developed at the University of California to detect and discriminate UXO in the 20-mm to 155-mm size range, and consists of three orthogonal coil transmitters. The horizontal Z-coils are vertically separated by 26" and have a 39"  $\times$  39" footprint. The Y- and X-vertical coils are mounted on the diagonals between the Z-coils (see Figure 22): the X-coils are 45.5"  $\times$  23.5" while the Y-coils are 45.5"  $\times$  22.5" in size, and both are separated by 6". The BUD illuminates targets in three independent directions, which induce eddy currents in all three modes. BUD has eight pairs of differenced receiver coils placed horizontally along the two diagonals of the upper and lower planes of the Z-transmitter loops. The pairs are located on symmetry lines through the center and are wired in opposition so as to cancel the primary magnetic field during transmission. Figure 22 shows the BUD system in operation.

The BUD transmitter loops were modeled as idealized infinitely thin square loops. The primary fields produced at any observation point by the transmitters are determined using a suitable modification of equation. (162), again with  $N_{Tx} = 40$ . The BUD measured signals are modeled using equation (163) as

$$\mathbf{V}_R = -\sum_{i=1}^{N_{Rx}} \frac{\partial \mathbf{B}_i(\mathbf{r}_{i,R} - \mathbf{r}_0)}{\partial t} \cdot \Delta \mathbf{s}_{i,R} + \sum_{i=1}^{N_{Rx}} \frac{\partial \mathbf{B}_i(\mathbf{r}'_{i,R} - \mathbf{r}_0)}{\partial t} \cdot \Delta \mathbf{s}_{i,R}, \quad \Delta \mathbf{s}_{i,R} = \Delta s_{i,R} \hat{\mathbf{z}} \quad (164)$$

where  $\mathbf{r}_{i,R}$  and  $\mathbf{r}'_{i,R}$  are the locations of the Rx and Rx' receivers, given in Table 3. For the case of BUD we divide the receivers into  $N_{Rx} = 9$  sub-areas.

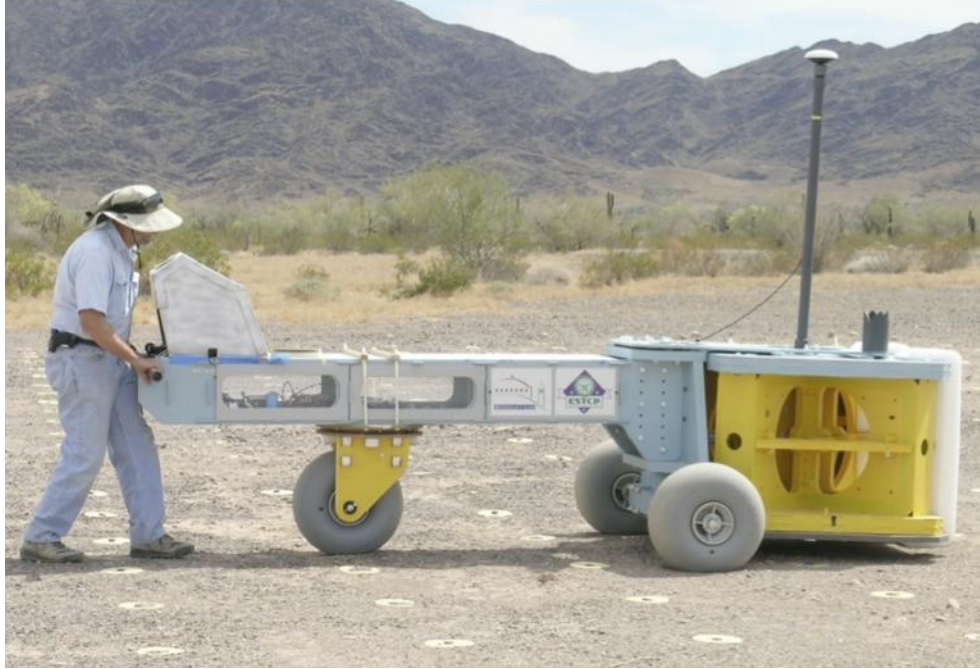


Figure 23: The BUD system in operation.

Table 3: BUD receiver locations with respect to the origin.

Rx #	X [cm]	Y [cm]	Z [cm]	Rx' #	X'[cm]	Y'[cm]	Z'[cm]
1	35.48	35.48	0	1'	-35.48	-35.48	66
2	-35.48	35.48	0	2'	35.48	-35.48	66
3	-35.48	-35.48	0	3'	35.48	-35.48	66
4	35.48	-35.48	0	4'	-35.48	35.48	66
5	19.29	19.29	0	5'	-19.29	-19.29	66
6	-19.29	19.29	0	6'	19.29	-19.29	66
7	-19.29	-19.29	0	7'	19.29	19.29	66
8	19.29	-19.29	0	8'	-19.29	19.29	66

All data presented here were collected by personnel from the Berkeley UXO team at Yuma Proving Ground in Arizona over objects at different orientations and depths. The response of each object was represented with only five NSMS. Figure 24, Figure 25, and Figure 26 show comparisons between modeled and actual data for all transmitters and receivers and for all time channels. The results clearly show that the NSMS very well predicts the EMI response of a M-75 mm UXO. Total NSMS amplitudes were determined for three samples each of M-75, 60-mm, and M-37 UXO and are depicted in Figure 27. The result demonstrates that the NSMS is applicable to the BUD system and is a good discriminator.

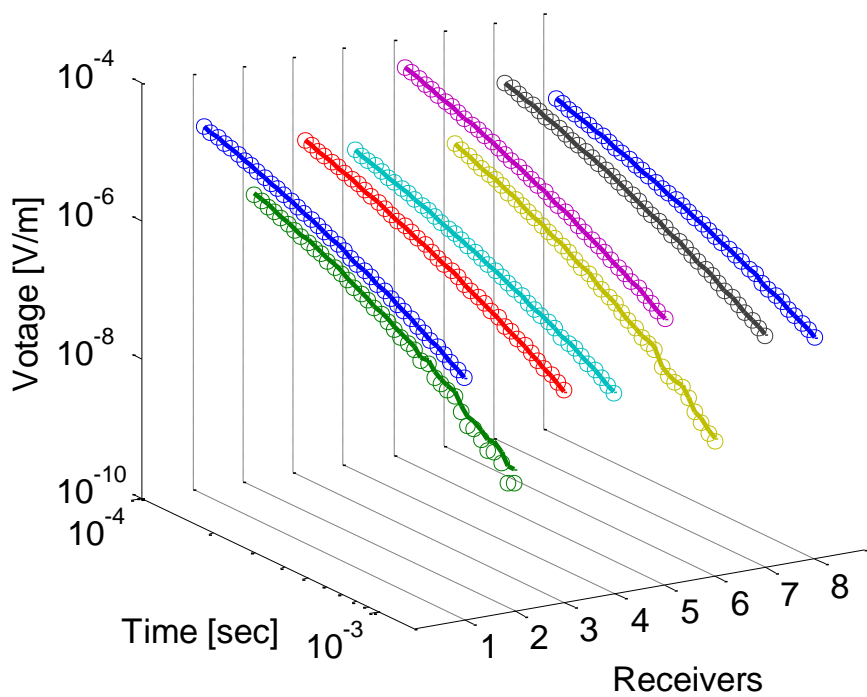


Figure 24: Comparisons between actual and predicted data for an M75 UXO illuminated by the BUD Z transmitter. Solid lines are actual data, circles stand for NSMS predictions.

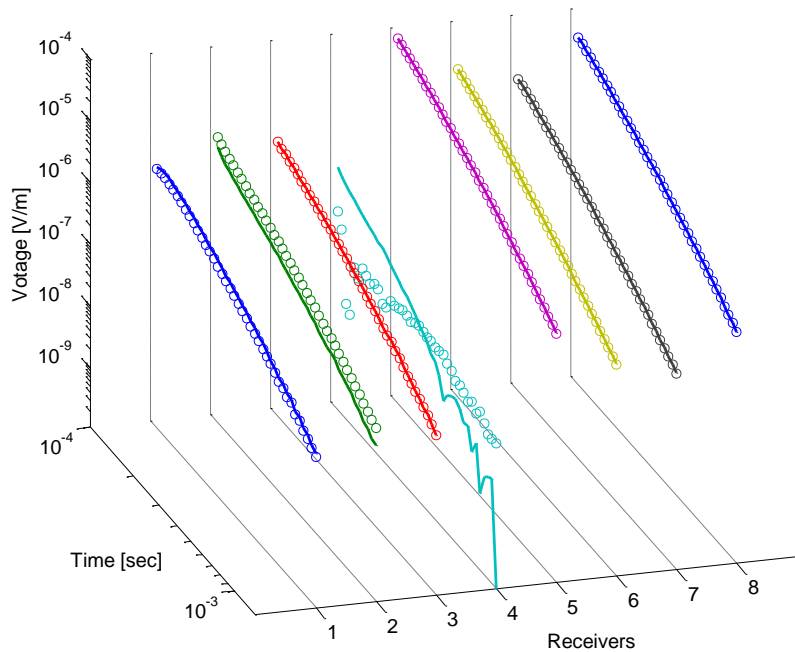


Figure 25: Comparisons between actual and predicted data for an M75 UXO illuminated by the BUD X transmitter. Solid lines are actual data, circles stand for NSMS predictions.

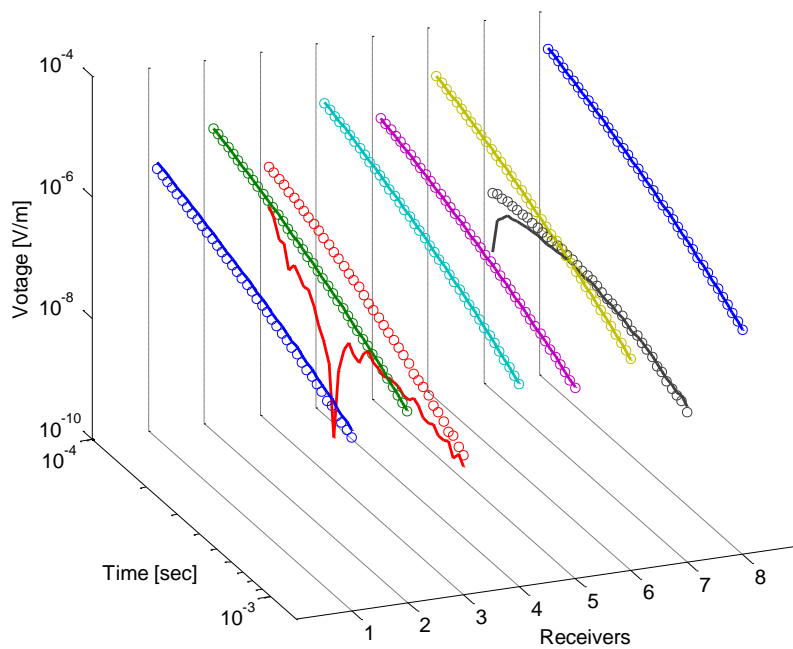


Figure 26: Comparisons between actual and predicted data for an M75 UXO illuminated by the BUD  $Y$  transmitter. Solid lines are actual data, circles stand for NSMS predictions.

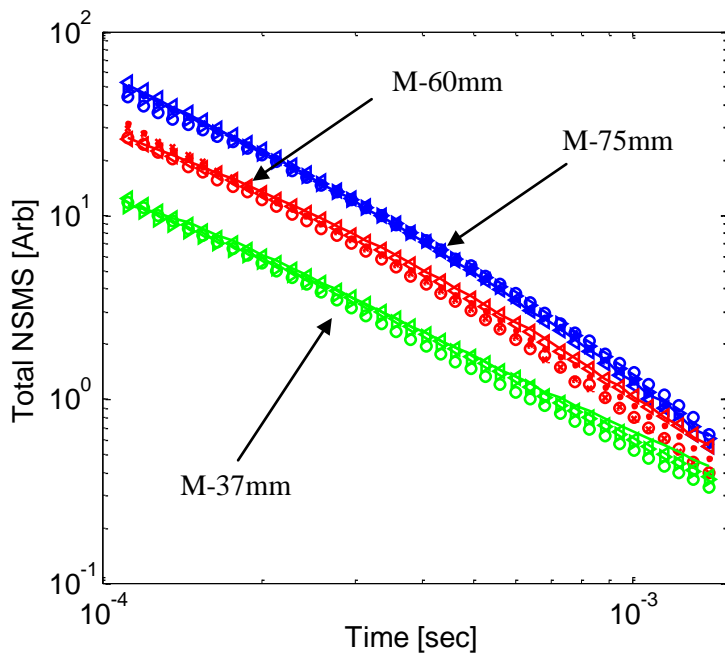


Figure 27: Recovered total NSMS from calibration BUD measurements for M-75 (blue), 37-mm (green), and M-60 (red) UXO.

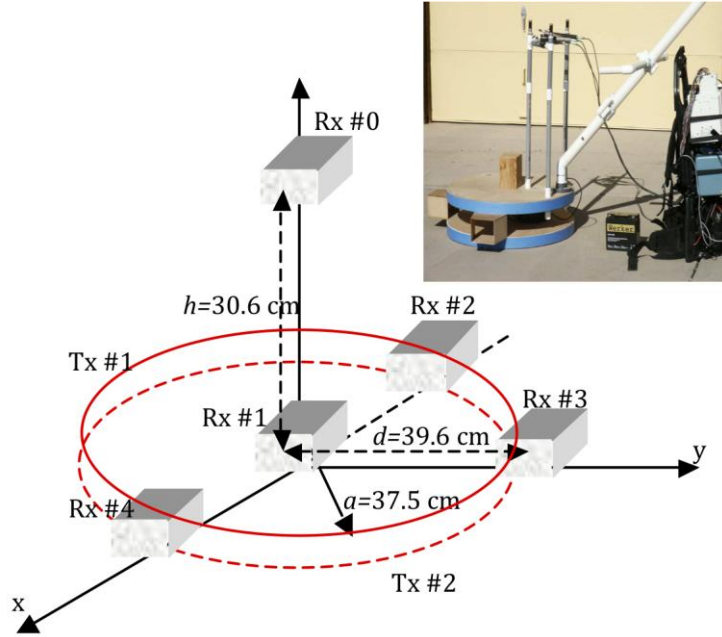


Figure 28. Photo and schematic diagram of the MPV sensor.

## 5.5 MPV

The MPV sensor, developed by G&G Sciences, Inc., consists of two transmitter loops and five triaxial receiver cubes. The receivers are located as follows: Cube #0 above center ( $z = 30.6$  cm); Cube #1 at the origin; Cube #2 left of center ( $x = -39.6$  cm); Cube #3 forward of center ( $y = 39.6$  cm); and Cube #4 right of center ( $x = 39.6$  cm). These receivers accurately measure the complete transient response over a wide dynamic range of time going from 100  $\mu$ s to 25 ms. In numerical models we assume that the transmitter loops are idealized as infinitely thin circular loops with 37.5 cm radii, and separated by 12 cm. The complete primary field produced at any observation point by the transmitter loop is determined from equation (162) as

$$\mathbf{B}(\mathbf{r}) = \frac{\mu_0}{4\pi} \sum_{t=1}^2 \sum_{i=1}^N \frac{I \Delta \ell_{t,i} \times \mathbf{R}_{t,i}}{R_{t,i}^3} \quad (165)$$

where, for the  $t$ -th transmitter loop,  $t = 1, 2$ ,  $\mathbf{R}_{t,i} = |\mathbf{r} - \mathbf{r}'_{t,i}|$ ,  $\mathbf{r}'_{t,i}$  is the location of the  $i$ -th current element on  $t$ -transmitter, and  $\Delta \ell_{t,i}$  is the tangential length vector for the  $i$ -th subsection. We use  $N = 20$  unless we note otherwise. The MPV measured signal is modeled using equation (163) with each loop having area  $10 \times 10$  cm<sup>2</sup> and divided into 4 sub-areas.

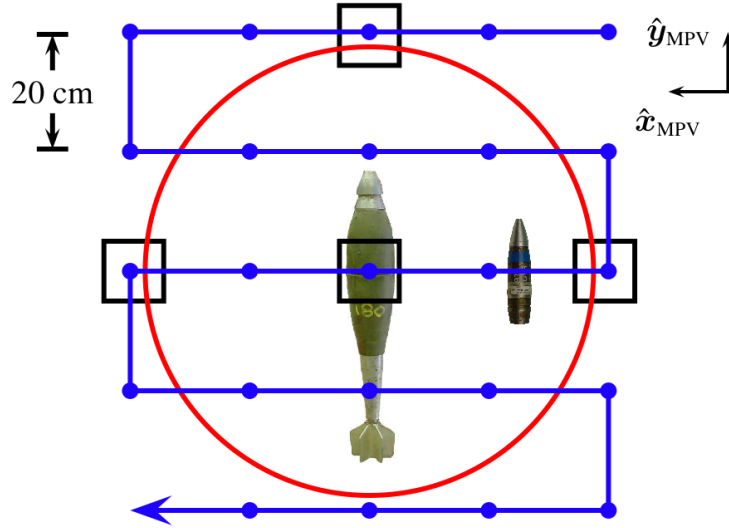


Figure 29: Multi-object MPV data collection setup (right). The red circle corresponds to the MPV head, which was placed stationary; the targets were moved along the blue line. The center of the first target (the 81-mm) was placed at the blue points, and the distance between the first and second targets was kept fixed.

To illustrate the applicability of the ONVMS for MPV data we conducted studies in multi-target inversion and discrimination. The measurements reported here were conducted at the SKY Research office in Hanover, New Hampshire. The sensor was placed stationary, and data were collected for two objects with different separations and orientations placed on  $5 \times 5$  grid points. The separation between the grids points was 20 cm. The targets were an 81-mm munition and a 40-mm round. The data were inverted using the simple dipole model with DE and the ortho-normalized volume magnetic source model (ONVMS). The number was assumed given in the simple dipole model, while in the ONVMS four arbitrarily distributed interacting dipoles were used. The dipoles' positions were determined using DE. The inverted polarizability tensor principal elements for the projectiles are depicted in Figure 30 for three different target-to-target separation vectors:  $(-25, 0, 0)$  cm (blue),  $(-40, 0, 0)$  cm (red), and  $(-25, 0, 25)$  (green). The single-dipole/DE algorithm accurately inverts the polarizability elements for the shallow 81-mm projectile but fails to identify the 40 mm projectile when the distance between the two is 25 cm (blue) and when the 40-mm is placed deeper (green). When the distance between the targets increases and they both have the same depth the algorithm identifies the 40-mm projectile correctly. The same data sets were inverted using the combined ONVMS-DE technique. The inverted locations showed the ONVMS dipoles grouped around the locations of the projectiles, and for discrimination we summed the ONVMS amplitudes for each group. The results for the two targets, which appear in Figure 31, show that the inverted ONVMS is consistent for all cases and both munitions. The ONVMS technique is seen to be a robust algorithm for discriminating not only single well-isolated targets but also multi-target scenarios.

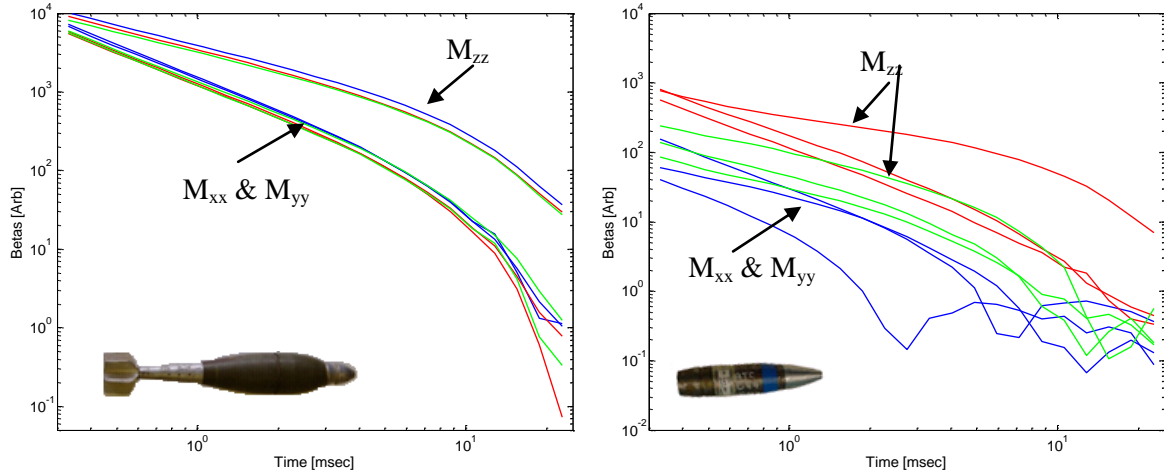


Figure 30: Inverted polarizability principal elements for two targets in three different setups; results for the 81-mm projectile at left and for the 40-mm munition at right. In all three cases the targets were horizontal, and the vertical distance between the MPV center and the 81-mm was 40 cm. The center to the center coordinate differences between the 81-mm and 40-mm projectiles are  $(-25, 0, 0)$  cm,  $(-40, 0, 0)$  cm, and  $(-25, 0, 25)$  cm.

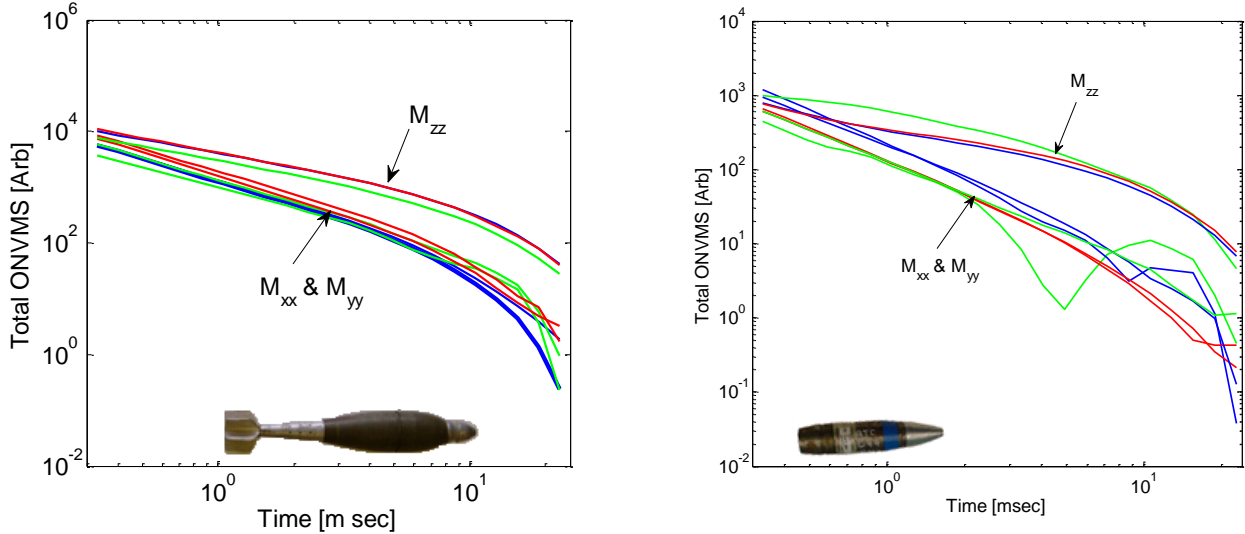


Figure 31: Inverted total ONVMS for 81 mm (left) and 40 mm (right) projectiles for three different cases.

We have just compared the single-dipole and ONVMS model for UXO discrimination. (We do note that in all cases we used DE to perform the crucial task of determining object locations). The dipole model is sufficient for inversion when the different targets are well separated but breaks down when they are placed close to each other or when the EMI response from one item dominates. In contrast, the physically complete model is able to predict target EMI responses accurately for these situations, making the ONVMS method our preferred tool for the live-site UXO classification studies we present next.

## 6 ESTCP live-site classification studies using advanced models

### 6.1 Introduction

The Environmental Security Technology Certification Program (ESTCP) recently launched a series of live-site UXO classification blind tests at increasingly challenging and complex sites [84-86] aiming to demonstrate the performance of advanced EMI detection technologies and UXO discrimination and classification algorithms. The first test was conducted in 2007 at the UXO live site at the former Camp Sibert in Alabama using first-generation EMI sensors (the commercially available EM61-MK2 and EM-63, both developed by Geonics Ltd.). The Sibert test was relatively simple: one had to discriminate well-isolated large intact 4.2" mortars from smaller range scrap, shrapnel, and cultural debris. The second ESTCP discrimination study to demonstrate the applicability of EMI classification technologies was set up in 2009 at the live UXO site in San Luis Obispo (SLO) in California and featured a more challenging topography and a wider mix of TOI [84-85]. Magnetometers and first-generation EMI sensors were deployed on the site and used in survey mode. Two advanced EMI sensing systems—the Berkeley UXO Discriminator (BUD) of Section 5.4 and the Naval Research Laboratory's TEMTADS EMI array, presented in Section 5.3—were used to perform cued interrogation of the anomalies detected. A third advanced system, the Geometrics MetalMapper of Section 5.2, was used in both survey and cued modes for identifying and classifying anomalies. Among the munitions buried at SLO were 60-mm and 81-mm projectiles, 4.2" mortars, and 2.36" rockets; three additional munition types were discovered during the course of the demonstration. The third site chosen was the former Camp Butner in North Carolina. That demonstration was designed to investigate evolving classification methodologies at a site contaminated with 37-mm projectiles, adding yet another layer of complexity into the process [87-89]. In this chapter we describe the work we performed when we participated in those studies and summarize the results we obtained.

### 6.2 Camp Sibert

In 2006, researchers affiliated with Sky Research, Inc. collected data at Camp Sibert using the EM-63, a cart-based step-off time-domain EMI sensor produced by Geonics Ltd. [90]. The targets buried in 216 cells—some of which were empty—included unexploded 4.2" mortar shells, mortar explosion byproducts like base plates and partial mortars (i.e., stretched-out half-shells), smaller shrapnel, and unrelated metallic clutter; some examples appear in Figure 32. The different items were distributed as shown in Figure 32(d).

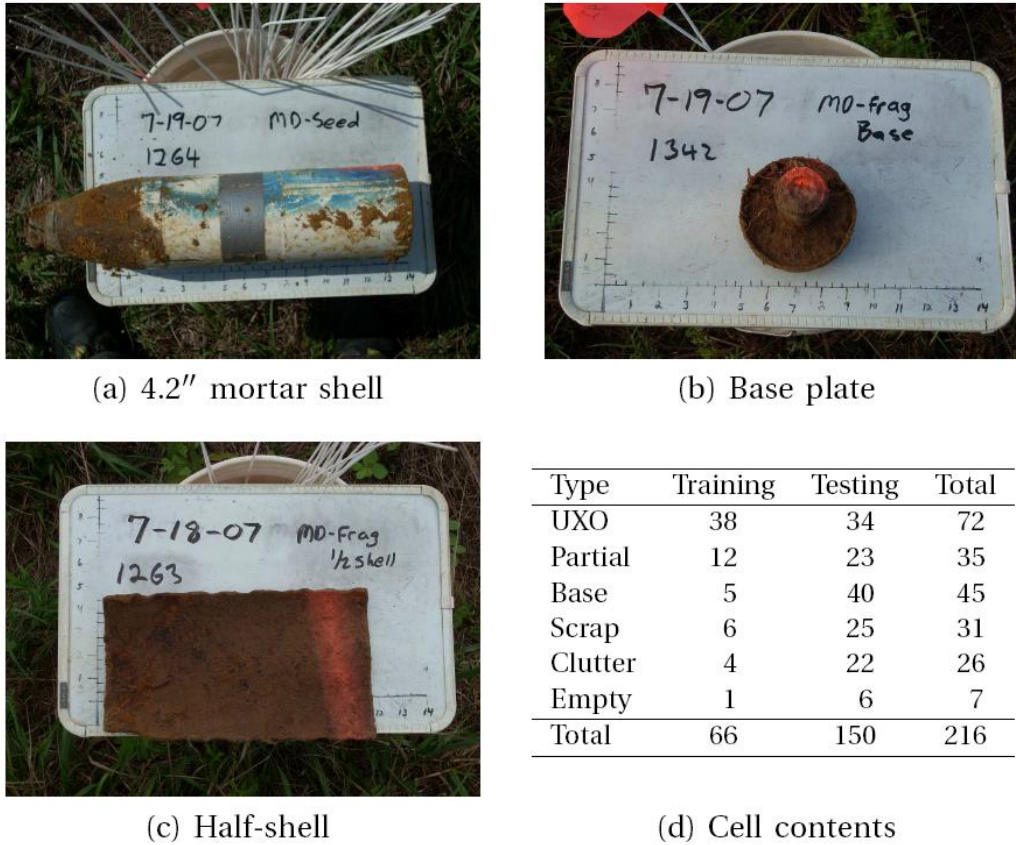


Figure 32: Camp Sibert anomalies: 4.2 inch, base plates and partial mortars.

We analyzed the Sibert data using HAP and NSMS. By combining those two techniques we made sure our method of analysis [82, 91] avoided the tendency of inversion algorithms to linger in local minima. We performed the localization step independently at the outset and then used its results to help in the characterization, allowing for fast and accurate determination of the total NSMS for each target. We classified these NSMS values using a heuristic pattern-matching method (Section 6.2.1), an open-source implementation [92] of SVM (Section 6.2.3), and mixed modeling (Section 6.2.4). The SVM-based classification improved upon template-matching [93-94] in that it required less human intervention and was thus faster to run and easier to adapt to other sets of observations. On the other hand, the semi-supervised Gaussian mixture model provided a classification performance exceeding that of SVM, which made it our preferred statistical classification procedure for use in all subsequent classification tasks.

### 6.2.1 Target location and characterization; preliminary pattern-matching classification

We started the procedure by applying HAP to determine the target location for each cell. Figure 33 compares actual and inverted data at the first and 20th time channels (top and bottom rows

respectively) for one cell. To find the target we take a fictitious  $5\text{ m} \times 5\text{ m}$  flat square surface concentric with the plot and located 30 cm below the sensor (i.e., at ground level) and divide it into  $11 \times 11$  patches, each of which is assumed to contain a magnetic-charge distribution of uniform density. We take the measured field data (seen on the left column of Figure 33) and use Eq. (109) to determine  $q$ , which in turn allows us to determine  $\psi(\mathbf{r})$  using Eq. (111) and construct the matrices of Eq. (108) to find the location. We do this separately for every time channel and get consistent location estimates from gate to gate, which lends credence to their precision. The depths thus determined are also acceptably close to the ground truth.

After finding the locations we run a fully three-dimensional orientation-free NSMS code to determine the time-dependent total NSMS amplitude for all cells. To compute  $Q(t)$  we surround the target with a prolate spheroid of semiminor axis  $a = 5\text{ cm}$  and elongation  $e \equiv b/a = 4$ . This spheroid is divided into seven azimuthal belts, each of which is assumed to contain a radial-magnetic-dipole distribution of constant density. The spheroid is placed at the location estimated by the HAP method and the orientation given by the dipole moment  $\mathbf{m}$  obtained from Eqs. (106) and (99)-(101). With all the pieces in place, we apply Eq. (25) to find  $\Omega$  and Eq. (26) to extract  $Q(t)$  for the target. The inverted total NSMS for all anomalies, and for 4.2" mortars, base plates, and partial mortars are depicted in Figure 34.

It is evident that there are distinguishable differences between the total NSMS for the 4.2" mortars, the base plates, and the partial mortars. Particularly at late times, each target has different natural decay characteristics that depend on its geometry and material properties. It is also important to notice that the total NSMS for the 4.2" mortars is very well grouped. To further simplify the classification task we used the Pasion-Oldenburg law to fit the time-dependent NSMS curves, obtaining as a result the amplitudes ( $k$ ), the power-law exponents ( $\beta$ ), and the exponential-decay inverse time constants ( $\gamma$ ), all of which we tested as classification features. We obtained the parameters by direct nonlinear least-squares fit of (57) and by linear (pseudo)inversion of its logarithm (166); both procedures gave consistent results. In general we obtain good fits to the measured fields [94]; Figure 33 shows that the discrepancy between the actual data and the model prediction runs only to a few percent.

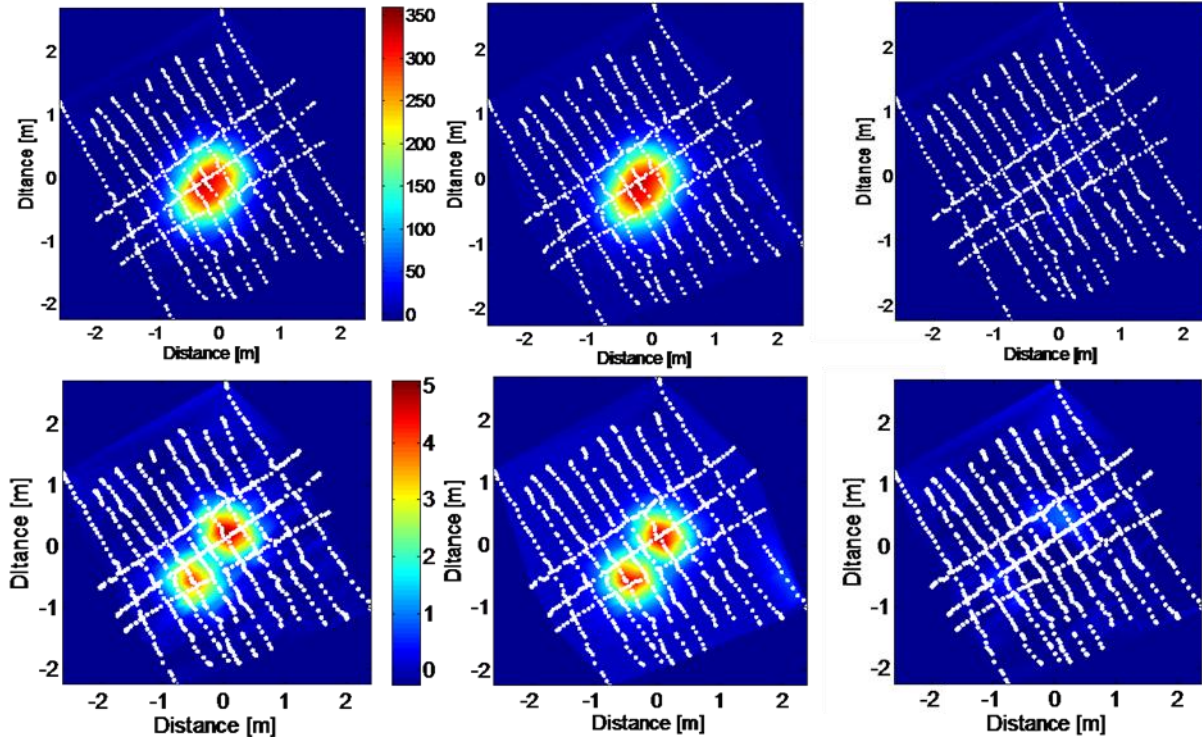


Figure 33: Camp Sibert EM-63 near field distributions: Left and middle columns: actual and modeled data respectively. Right column: misfits.

After investigating different combinations of these feature-space parameters we found that  $k$  in conjunction with the ratio  $Q(t_{15})/Q(t_1)$  which involves a fixed superposition of  $\beta$  and  $\gamma$ , worked best: the left panel of Figure 35 depicts this winning combination for all items and clearly shows the tight clustering and generous cluster-to-cluster separation that generally lead to reliable classification. (The 15th time channel, centered at about 2.7 ms, was chosen because it takes place late enough to show the behavior described above but early enough that all targets still have an acceptable signal-to-noise ratio; nearby time channels produce similar results.) When we received the ground truth for all targets we proceeded to construct the ROC curve that appears in the right panel of Figure 35. We see that only one excavation out of 130 anomalies is necessary before all UXO are identified correctly.

We obtain similar results using the SVM algorithm.

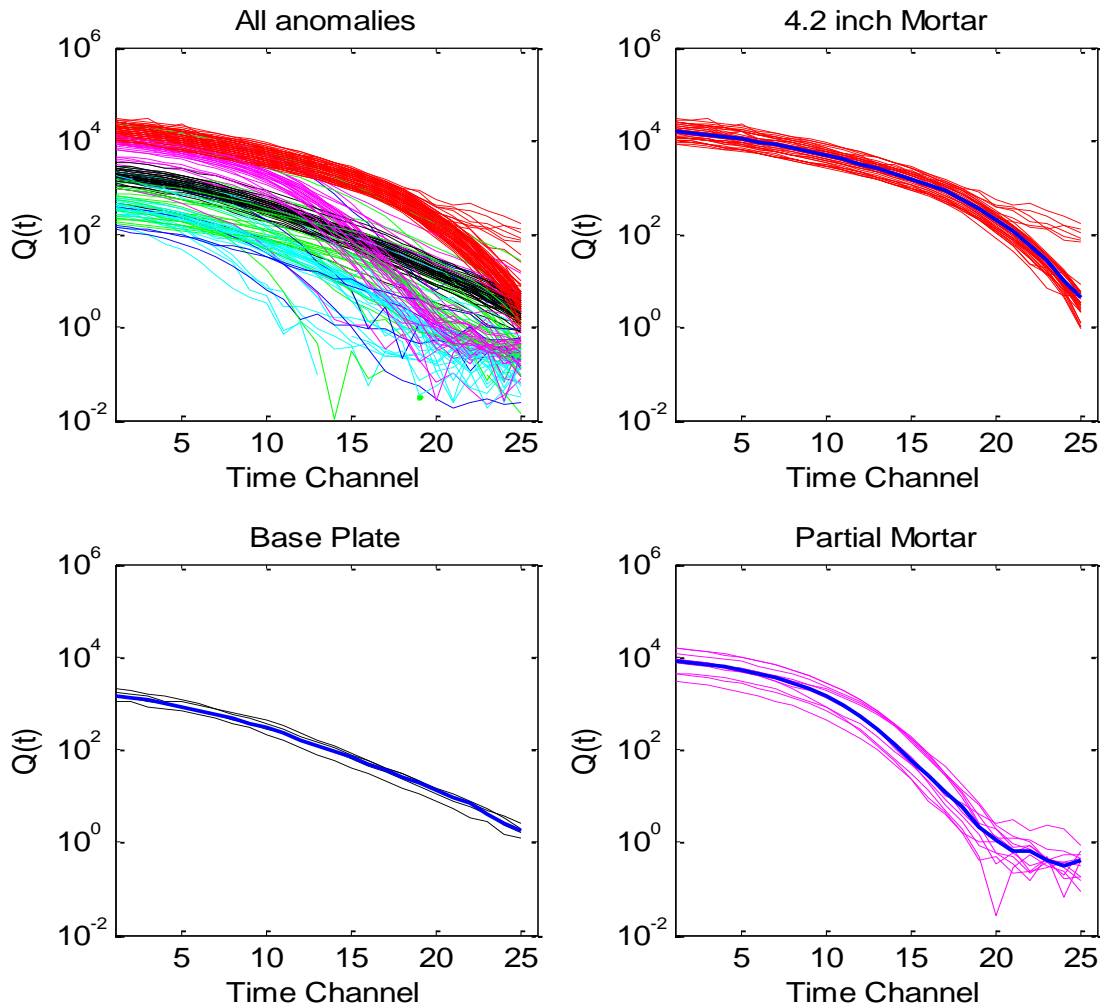


Figure 34: Inverted total NSMS for all anomalies: 4.2" mortars, base plates, and partial mortars.

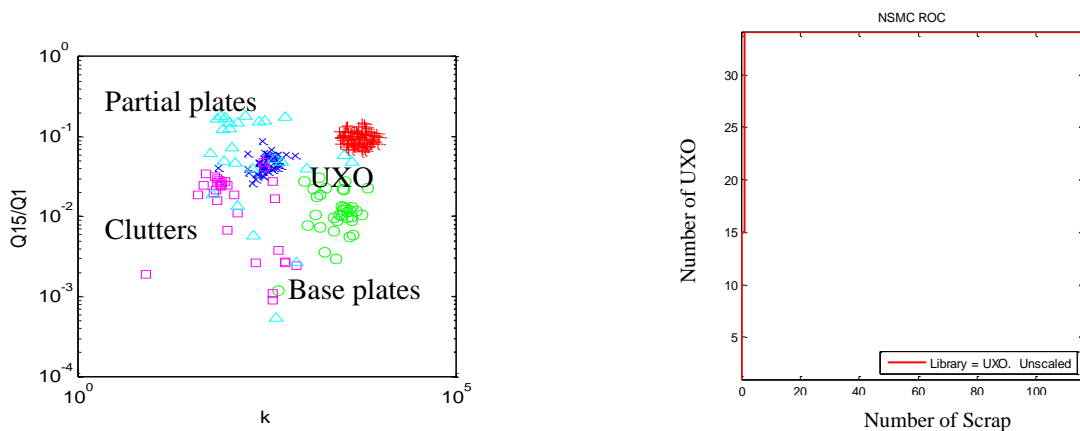


Figure 35: *Left:* Classification features. *Right:* ROC curve of NSMS performance.



Figure 36: a) Unexploded shell from Cell No. 7 and (b,c) the two false alarms obtained by the SVM classifier using  $k$  and  $Q(t_{15})/Q(t_1)$  as discriminators.

### 6.2.2 SVM classification

We use a Gaussian RBF kernel for the SVM analysis. The kernel width turns out not to have much influence on the outcome; we usually set it so that a unit in a typical  $x$ - or  $y$ -axis in a log plot (for example, Figure 37) comprises  $100\Delta$  Gaussian widths, where  $\Delta$  is the dimensionality of the feature space. To find the capacity  $C$  we train the SVM with a subset of the training data and a given  $C$ , scramble the training set, and use a new subset of the data for testing. We then vary  $C$ , setting it to a high value initially and then lowering it, and keep the lowest capacity with which the machine identifies all dangerous items in the test. The procedure is rather ad hoc but effective for the data at hand, given the small sample sizes, the low dimensionality of the feature spaces, and the speed of the SVM implementation. A more systematic search for  $C$  and  $\gamma$  using five-fold cross-validation [92] recommends slightly higher capacities that result in identical predictions.

For  $R$  and  $k$  as features we find the best SVM performance using  $C = 10$ . The results are displayed (for testing data only) in Table 4 and shown pictorially (for both training and testing) in Figure 37. The matrix element  $c_{ij}$  in the table denotes an item of category  $i$  that was identified by the SVM as belonging to category  $j$ ; in other words, the rows of this contingency table correspond to the ground truth and the columns to predictions. The small markers in the plot show the ground truth (hollow for training data and filled for the tests), while the large markers point out the items for which the SVM makes wrong predictions. For example, a small yellow upright triangle surrounded by a large cyan square is a piece of scrap (clutter unrelated to UXO) incorrectly identified as a base plate. The UXO, with their high initial amplitudes and slow decay, are clustered at the top right corner. We see that there are only two false alarms (i.e., objects identified with UXO that were in fact something else) and that all potentially dangerous items have been identified correctly.

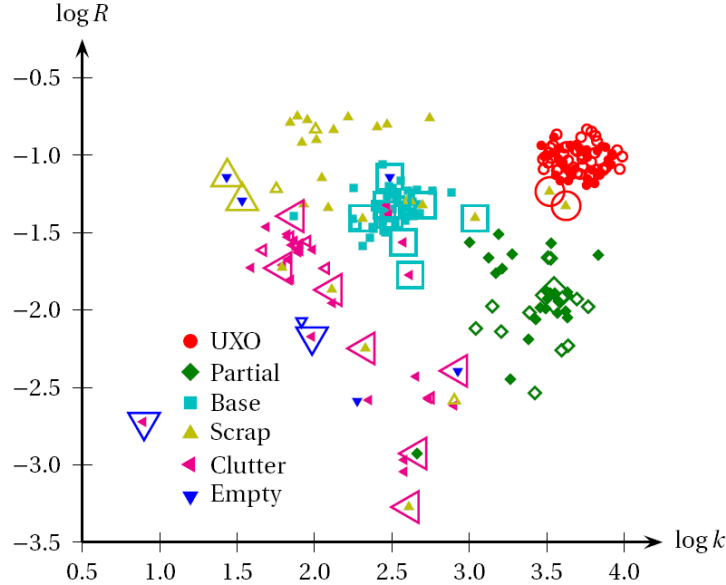


Figure 37: Result of the SVM classification for the Camp Sibert anomalies using the logarithms of  $k$  and  $R = Q(t_{15})/Q(t_1)$ . The SVM has been trained with capacity  $C = 10$  and kernel width  $\sigma = 1/200$ . The small markers denote the ground truth for both training (hollow) and testing (solid) cells. The larger markers highlight the cases where there is disagreement between the ground truth and the SVM prediction.

Table 4: SVM classification of Camp Sibert anomalies using  $k$  and  $R$  with  $C = 10$

$k, R; C = 10$	SVM prediction					
	UXO	Partial	Base	Clutter	Scrap	Empty
Ground truth	UXO	34	0	0	0	0
	Partial	0	22	0	1	0
	Base	0	0	39	1	0
	Clutter	0	0	4	19	0
	Scrap	2	0	3	4	13
	Empty	0	1	1	1	2

The false alarms, two pieces of non-UXO clutter, appear in Figure 36(b) and Figure 36(c). They are seen to be similar to the 4.2" mortars in size and metal content (cf. Figure 36 (a)), which makes their  $k$  and  $R$  values lie closer to the tight UXO cluster than to any other anomaly. Here we note that, as can be seen in Figure 32(d), the training data provided by the examiners was somewhat biased toward UXO, while clutter and scrap samples were underrepresented (this was not the case with the testing data and should not be expected in future tests). If we switch training and testing data in the SVM analysis we can achieve perfect discrimination without varying the capacity—though in this case we have more training data than tests. This highlights the importance of having a diverse collection of representative samples to use during the training stage.

Table 5: SVM classification of Camp Sibert anomalies using  $\gamma$  and  $k$  with  $C = 9$ 

$\gamma, k; C = 9$	SVM prediction					
	UXO	Partial	Base	Clutter	Scrap	Empty
Ground truth	UXO	34	0	0	0	0
	Partial	5	17	0	1	0
	Base	0	0	39	0	1
	Clutter	0	0	4	15	5
	Scrap	2	1	3	5	11
	Empty	1	1	2	2	0

We can repeat the analysis using other two-dimensional combinations of the Pasion-Oldenburg parameters. Combining  $k$  and  $\gamma$  yields results similar to those of  $k$  and  $R$ , as Figure 38 and Table 5 show. Figure 39 and Table 6 show the classification resulting from the use of  $\beta$  and  $\gamma$  as discriminators. The table shows that we can obtain reasonable discrimination, with all the UXO once again correctly identified, but the increased number of false alarms and the very high capacity needed (four orders of magnitude larger than the previous ones) indicate that this combination of parameters may not be optimal and that this machine is prone to overfitting. A glance at the figure shows the clustering is much less clear-cut than in the previous cases, partly because the range of  $\beta$  is rather small. In fact, combining  $k$  and  $\beta$  greatly reduces the performance, since the small  $\beta$ -range and the close similarity in  $k$  of the UXO and the partial mortars cause an overlap between the two categories that cannot be disentangled.

It is helpful and straightforward to increase the dimensionality of the feature space. Figure 40 shows the discrimination obtained by running the SVM using all three Pasion-Oldenburg features. The capacity  $C = 9$  here, and increasing it changes the results only slightly. The number of false alarms increases: we get the same two pieces of scrap from before, and now a few of the partial mortars are identified as UXO by the algorithm, due in part to the small range of  $\beta$  and in part to the large gap between the UXO and the other anomalies, clearly visible in the figure, which again calls out for more and more-diverse training information.

Finally, it is possible to dispense with the Pasion-Oldenburg model altogether and run an SVM using the “raw”  $Q(t)$  as input. The feature space has dimensionality  $\Delta = 25$ . We scale the values by  $Q(t_1)$  and take the logarithm. We find  $C = 20$  to be the optimal value. Table 4 shows the results. The performance is slightly inferior to that of  $R$  vs.  $k$ ; the usual two false alarms are there, along with a few new ones. All the UXO are identified correctly. We can also use the logarithm of  $Q$  without any scaling (though the SVM internally rescales the feature space to  $[0,1]^\Delta$ ). A capacity  $C = 1$  suffices here. The results appear on Table 5. All dangerous items are once more identified as such.

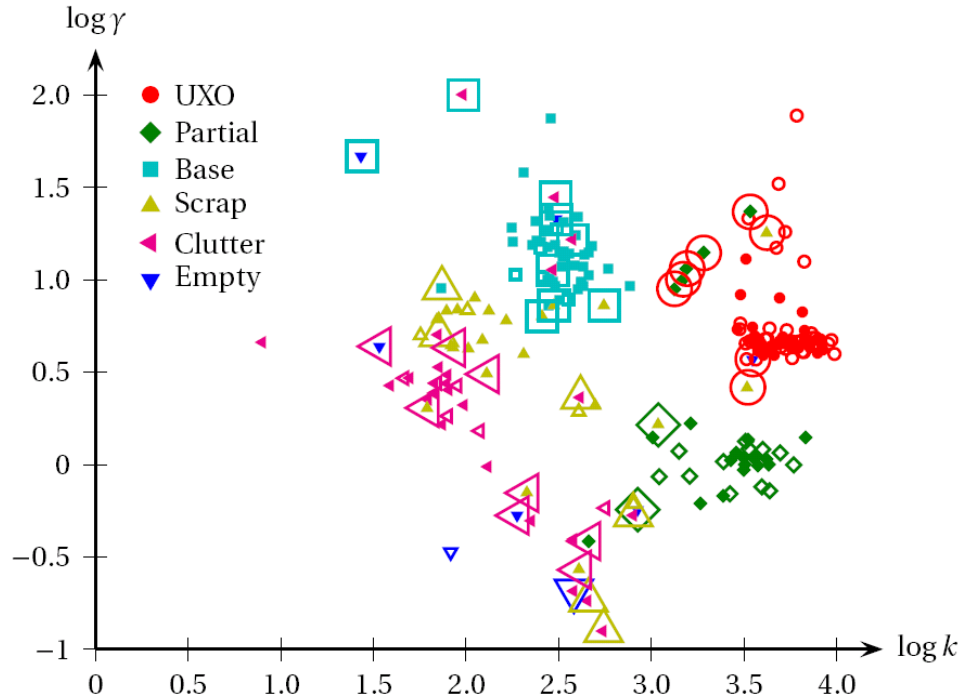


Figure 38: Result of the SVM classification for the Camp Sibert anomalies using the logarithms of the Pasion-Oldenburg parameters  $k$  and  $\gamma$ . The SVM here has a capacity  $C = 9$ . The small markers denote the ground truth for both training (hollow) and testing (solid) cells. The larger markers show the wrong SVM predictions.

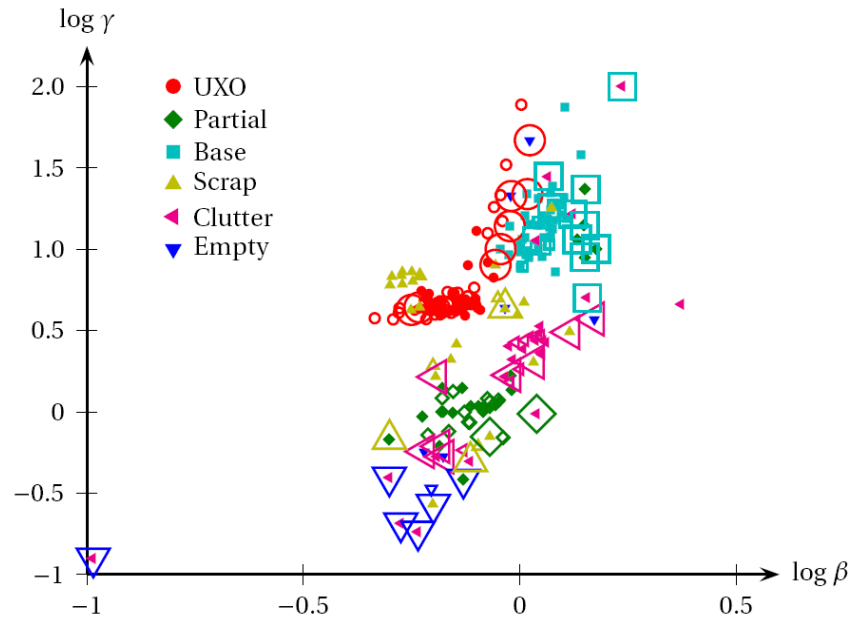


Figure 39: Result of the SVM classification for the Camp Sibert Anomalies using the logarithms of the Pasion-Oldenburg parameters  $\beta$  and  $\gamma$ . The SVM capacity  $C = 10^5$ . The small markers denote the ground truth for both training (hollow) and testing (solid) cells. The larger markers highlight the wrong predictions made by the SVM.

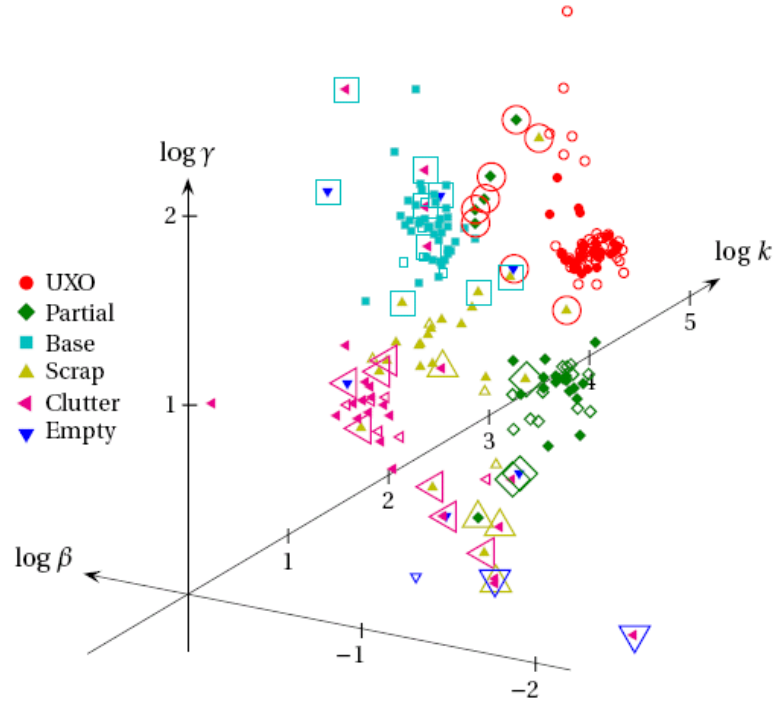


Figure 40: SVM classification of the Camp Sibert Anomalies using the logarithms of  $k$ ,  $b$ , and  $g$ . The SVM has  $C = 9$ . The small markers denote the ground truth for both training and testing cells. The larger markers highlight the cases where there is disagreement between the ground truth and the SVM prediction.

Table 6: SVM classification of Camp Sibert anomalies using  $\beta$  and  $\gamma$  with  $C = 105$

		SVM prediction					
		UXO	Partial	Base	Clutter	Scrap	Empty
Ground truth	UXO	34	0	0	0	0	0
	Partial	0	14	5	2	1	1
	Base	3	0	37	0	0	0
	Clutter	0	1	5	14	1	4
	Scrap	3	1	1	3	13	1
	Empty	2	0	0	3	1	0

Table 7: SVM classification of Camp Sibert anomalies using the complete NSMS time decay

		SVM prediction					
		UXO	Partial	Base	Clutter	Scrap	Empty
Ground truth	UXO	34	0	0	0	0	0
	Partial	0	15	0	7	1	0
	Base	3	0	34	3	0	0
	Clutter	0	2	3	14	4	2
	Scrap	3	1	3	3	12	0
	Empty	2	2	1	0	1	0

### 6.2.3 SVM analysis of Camp Sibert data: summary

In this section we applied the NSMS model to EM-63 Camp Sibert discrimination data. First the locations of the objects were inverted for by the fast and accurate dipole-inspired HAP method. Subsequently each anomaly was characterized at each time channel through its total NSMS strength. Discrete intrinsic features were selected and extracted for each object using the Pasion-Oldenburg decay law and then used as input for a support vector machine that classified the items.

Our study reveals that the ratio of an object's late response to its early response can be used as a robust discriminator when combined with the Pasion-Oldenburg amplitude  $k$ . Other mixtures of these parameters also result in good classifiers. Moreover, we can use  $Q$  directly, completely obviating the need for the Pasion-Oldenburg fit. In each case the classifier runs by itself and does not require any human intervention. The SVM can be trained very quickly, even when the feature space has more than 20 dimensions, and it is a simple matter to add more training data on-the-fly. It is also possible to use already processed data to classify examples as yet unseen.

We should stress that none of our classifications yielded false negatives: all UXO were identified correctly in every instance. (This is due in part to the clean, UXO-intensive training data provided by the examiners and may change under different conditions.) The number of false alarms (false positives) varies with the classification features, but is in general low and can be as low as 2 out of 36 reported positives. Figure 37, Figure 38 and Figure 39 show, among others, how these false alarms occur: Some of the clutter items have a response that closely resembles that of UXO. While this will inevitably arise, it may still be possible to make the SVM more effective—and perhaps approach 100% accuracy—by including some of these refractory cases during the training. That said, there will certainly be cases in the field where the non-uniqueness inherent to noisy inverse scattering problems will cause the whole procedure to fail and yield dubious estimates. In those cases it will be necessary to assume the target is dangerous and dig it up.

In a completely realistic situation, where in principle no training data are given and the ground truth can be learned only as the anomalies are excavated, one can never be sure that the data already labeled constitute a representative sample containing enough of both hazardous and non-hazardous items. This difficulty is mitigated by two facts: 1) Usually at the outset we have some idea of the type of UXO present in the field, and 2) The (usually great) majority of detected anomalies will not be UXO and thus random digging will produce a varied sampling of the clutter present. Methods involving semi-supervised learning exploit this gradual revealing of the truth and have been found to perform better at UXO discrimination than supervised learning methods like SVM when starting from the point dipole model

[91, 95]. (Active learning methods, which try to infer which anomalies would contain the most useful information and could thus serve to guide the anomaly unveiling, show further, though fairly minor, improvement.) Combining this more powerful learning procedure with the excellent performance of the HAP/NSMS method may enhance the discrimination protocol and should be the subject of further research.

In summary, the results presented here show that our search and characterization procedure, whose effectiveness is apparent from several recent studies [14, 93-94, 96], can be combined with an SVM classifier to produce a UXO discrimination system capable of correctly identifying dangerous items from among munitions-related debris and other natural and artificial clutter.

We repeated the analysis using the semi-supervised Gaussian mixture approach. The solution process and results are presented in Section 6.2.4. We found that the method provides excellent classification performance and has the advantage over SVM that it is less dependent on training data. This made it our preferred statistical classification model, and we have continued to prefer it.

#### 6.2.4 Mixed model approach applied to Camp Sibert data

We also tested the mixed model approach of Section 4.2 on the 216-sample Camp Sibert data. Initially we took the time decay of the total NSMS over 25 time channels for all targets and parameterized it using the Pasion-Oldenburg law of equation (57). Taking the logarithm of that equation we arrive at the linear model

$$\ln Q(t) = \ln k - \beta \ln t - \gamma t. \quad (166)$$

As features we use  $k$  and the ratio  $Q(t_{15})/Q(t_1)$ . Figure 41 is a log-log plot of  $Q(t_{15})/Q(t_1)$  vs.  $k$ . Initially we used  $K$ -means clustering to estimate the number of target types; the algorithm found five clusters (see Figure 41). Then we proceeded to classify the targets. The resulting classification into the five classes is depicted in Figure 42 and the corresponding ROC curves are presented in Figure 43.

The results illustrated that the semi-supervised Gaussian mixture model provides excellent classification performance over the SVM. This made the semi-supervised Gaussian mixture our preferred statistical classification model, and was used in the consequence classification studies.

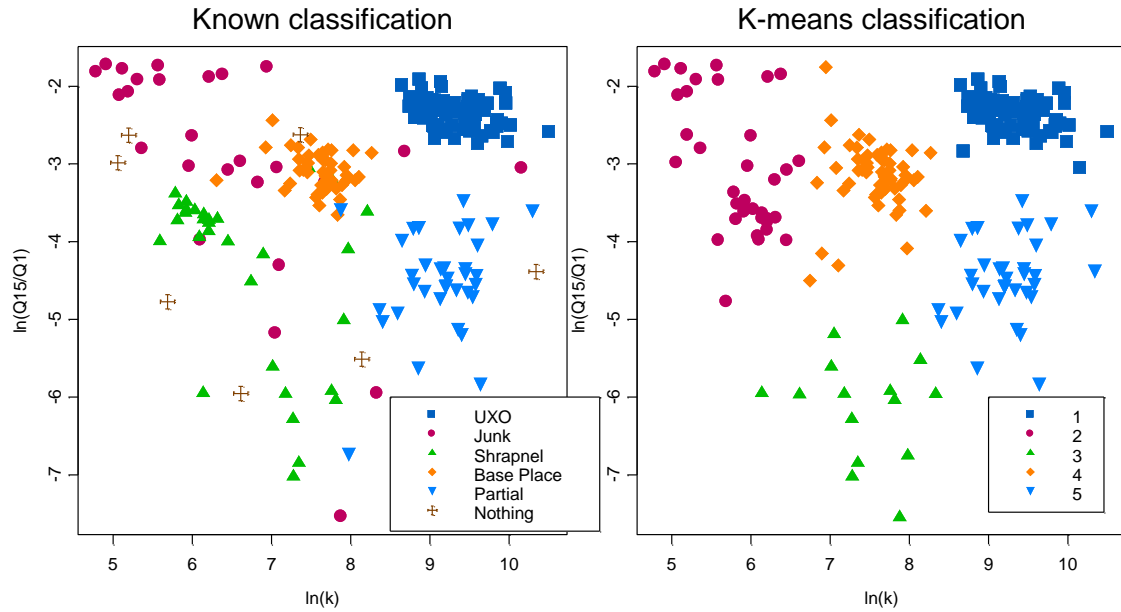


Figure 41: Log-scale plot of  $Q(t_{15})/Q(t_1)$  vs.  $k$  for Camp Sibert data classification. *Left:* Ground truth. *Right:* K-means clustering result.

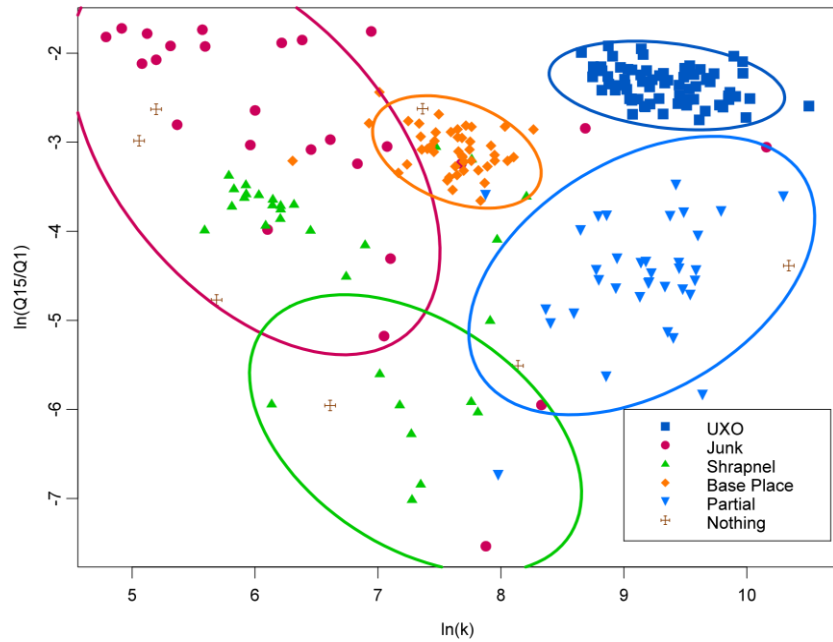


Figure 42: Classification of 216 targets into five classes using a bivariate normal mixture. Also shown are the 95% confidence ellipses.

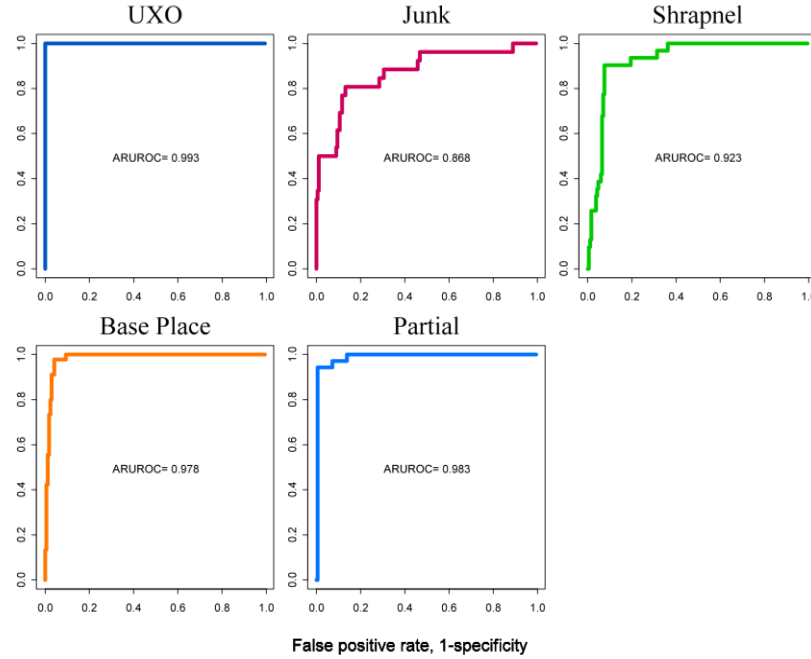


Figure 43: Five ROC curves that indicate the performance of the mixed model approach to Camp Sibert data.

### 6.3 Camp San Luis Obispo (TEMTADS, MM, BUD)

The discrimination test at Camp Sibert UXO site was relatively simple: it involved discrimination of large intact ordnance from smaller clutter using data from using first-generation EMI sensors. Real sites, however contain assorted types of ordnance, many smaller than 4.2", and the need to tackle this more forbidding condition has prompted significant developments in both detection and discrimination technologies. Acceptance of these technologies requires demonstrating that they can achieve 100% discrimination confidence in terms of the range of ordnance types and their overlap with clutter, while taking into account the terrain/vegetation at the site and the effects of the geological setting on EMI sensors [2, 7, 16, 91, 94, 97-98].

To demonstrate the applicability of the classification technologies for a live-UXO site with more challenging topography and a wider mix of targets-of-interest, in 2009 ESTCP conducted a second discrimination study at the SLO live UXO site in California. Magnetometers and first-generation EMI sensors were deployed to the site and used in survey mode. Then the BUD and TEMTADS systems were used to perform cued interrogation of the detected anomalies. Simultaneously, the MetalMapper was used in both survey and cued modes. The collected data were preprocessed by data collection demonstrators, who performed background subtraction, drift correction, and sensor positioning.

The classification demonstrators were provided with calibration data sets for algorithm testing and classification performance analysis. The goal was not only to identify if the target was harmful, but

also to classify it completely; i.e., to identify its type, size, and caliber. The blind data sets contained one or more buried objects that could be either one of four ordnance items used at the site—60-mm mortar shells, 2.76" rockets, 81-mm projectiles, and 4.2" mortars—or a piece of clutter. The clutter items found on the site are UXO explosion byproducts like partial mortars (i.e., stretched-out half-shells), smaller shrapnel, and man-made metallic clutter; some examples appear in Figure 44.

This section presents the discrimination studies carried out on 1282 TEMTADS and 1407 MetalMapper cued blind data sets. The total parameterized NSMS amplitudes were used to discriminate TOI from metallic clutter and to classify the different hazardous objects. First we used the combined NSMS/DE algorithm to determine the total NSMS for each TOI from the training data provided by SERDP. We used the HAP method and a combined dipole/Gauss-Newton approach to validate the location and orientation estimates given by NSMS/DE. We then used the inverted total NSMS to extract time-decay classification features for all cases and input these to several multi-class statistical classification procedures to perform discrimination. Once our inversion and classification algorithms were tested on calibration data we repeated the procedure on the blind data sets. The inverted targets were ranked by target ID and submitted to SERDP for independent scoring.



Figure 44: Found Clutter Items on SLO UXO live sites.

### 6.3.1 The total NSMS for discrimination

The reader may recall from Section 2.3.6 that the initial amplitude and the decay rate of the total NSMS depend on the size, the geometry, and the material composition of the object it represents. Early-time responses are associated with surface eddy currents and the associated early-time NSMS is directly proportional to the object's surface; at later times the currents diffuse gradually into the object and the response is related to the target's volume. Thus a small and thin target like the partial 2.36" rocket (Figure 45) has a relatively small initial NSMS that decays quickly, while a large object like the 4.2" mortar of Figure 46 has a strong immediate response that decays slowly, particularly along its axis of symmetry.

These considerations may be put on a more quantitative footing through discrimination features that summarize these characteristics for the different NSMS curves. To that end we employ the Pasion-Oldenburg law in its parameterized form (see Section 2.3.7). We tried different combinations of  $B_{\alpha\alpha}$ ,  $\beta_{\alpha\alpha}$ , and  $\gamma_{\alpha\alpha}$  for discrimination and in the end settled for  $\log[M_{zz}(t_{82})/M_{zz}(t_1)]$  and  $M_{zz}(t_1)$  as features for use with the model-based supervised clustering of Section 4.3.1 (Figure 47).

### 6.3.2 SLO discrimination results

The SERDP Program Office provided us with 188 TEMTADS calibration data sets for the inversion and classification algorithms testing performance analysis. Our objective here was not only to identify if a given target was a UXO or not, but also to classify it completely; *i.e.*, to identify TOI type, size, and caliber. We had the same number of calibration data sets for the MetalMapper sensor, but we used only two data sets for each TOI, for a total of ten data sets. The blind data sets contained a single or multiple buried objects that could be either one or more TOI.

We used the 188 TEMTADS calibration data to build a catalog of expected total NSMS values that were then tested on the 1282 other cells. The TEMTADS took data over 115 channels that span in approximately logarithmic fashion a lapse of time between 100  $\mu$ s and 24 ms. The TEMTADS was always placed 30 cm above the ground. For each data set we run the combined NSMS-DE and NSMS-HAP method [3] to determine object locations.

The target response was approximated with set of magnetic dipoles distributed on a spherical surface of radius 5 cm. This sphere is divided into 17 subsurfaces, each of which is assumed to contain a magnetic-dipole distribution of constant density. Once the location of the sphere's center is determined then the magnitude of each responding source is obtained and the total NSMS is calculated. The inverted total NSMS curves for SLO TEMTADS calibration (green lines) and blind data sets (red lines) are depicted in Figure 45 and Figure 46 for partial 2.36" rockets, 4.2" mortars, 81-mm projectiles, 2.36"

rockets, and 60-mm mortars. The results indicate that the inverted and calibration total NSMS time decay curves are similar and are good discriminators. Also, as the size of the TOI decreases the inverted total NSMS time decay curves show a larger spread, making them more difficult harder to discriminate.

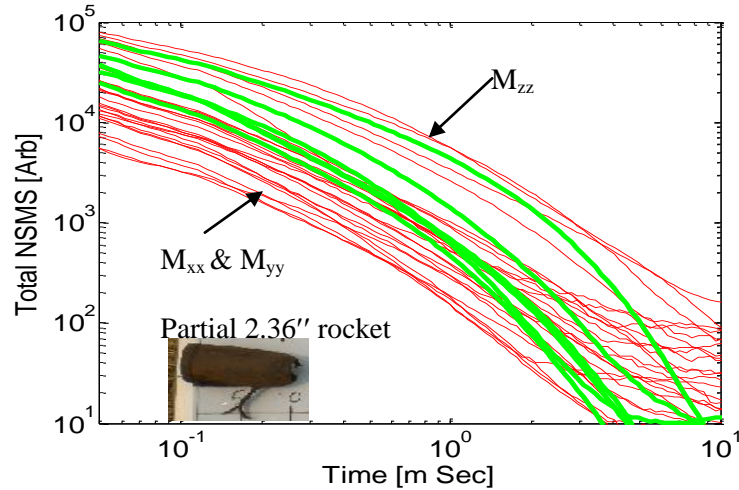


Figure 45: Inverted total NSMS time decay profiles for the 2.36'' partial rocket. The green lines depict calibration data and the red lines correspond to blind SLO TEMTADS data sets.

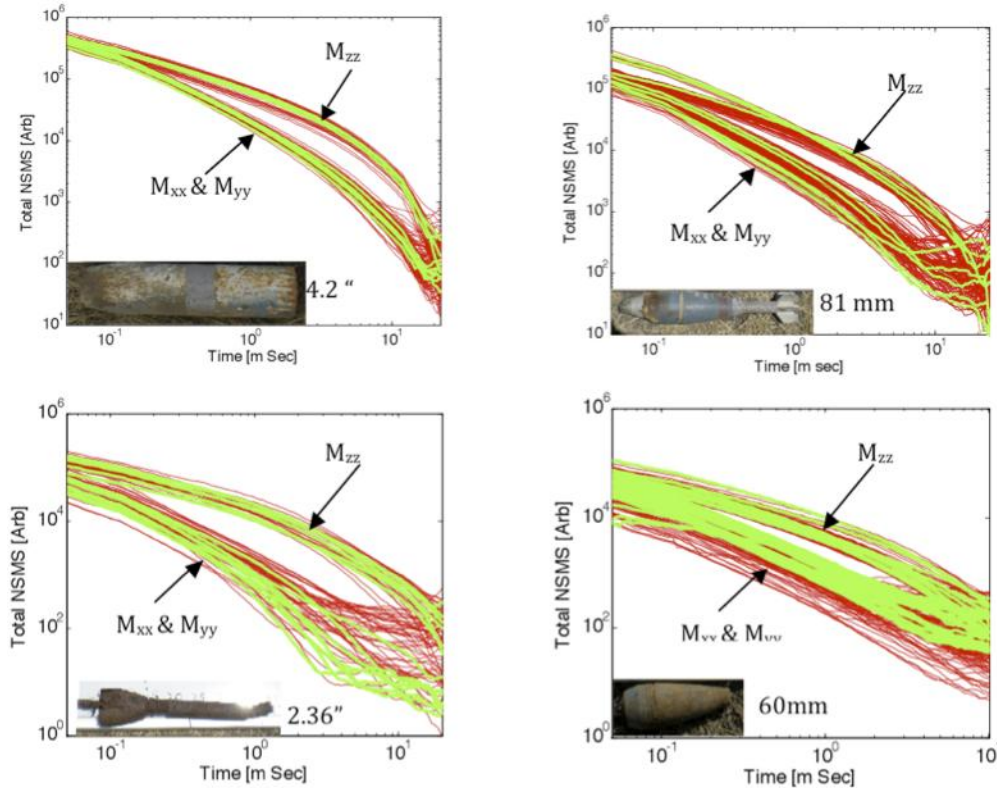


Figure 46: Inverted total NSMS time decay profiles for 4.2'' mortars (top left), 81-mm projectiles (top right), 2.36'' rockets (bottom left), and 60-mm mortars (bottom right) in the SLO TEMTADS test. The green lines depict calibration data and the red lines correspond to blind data sets.

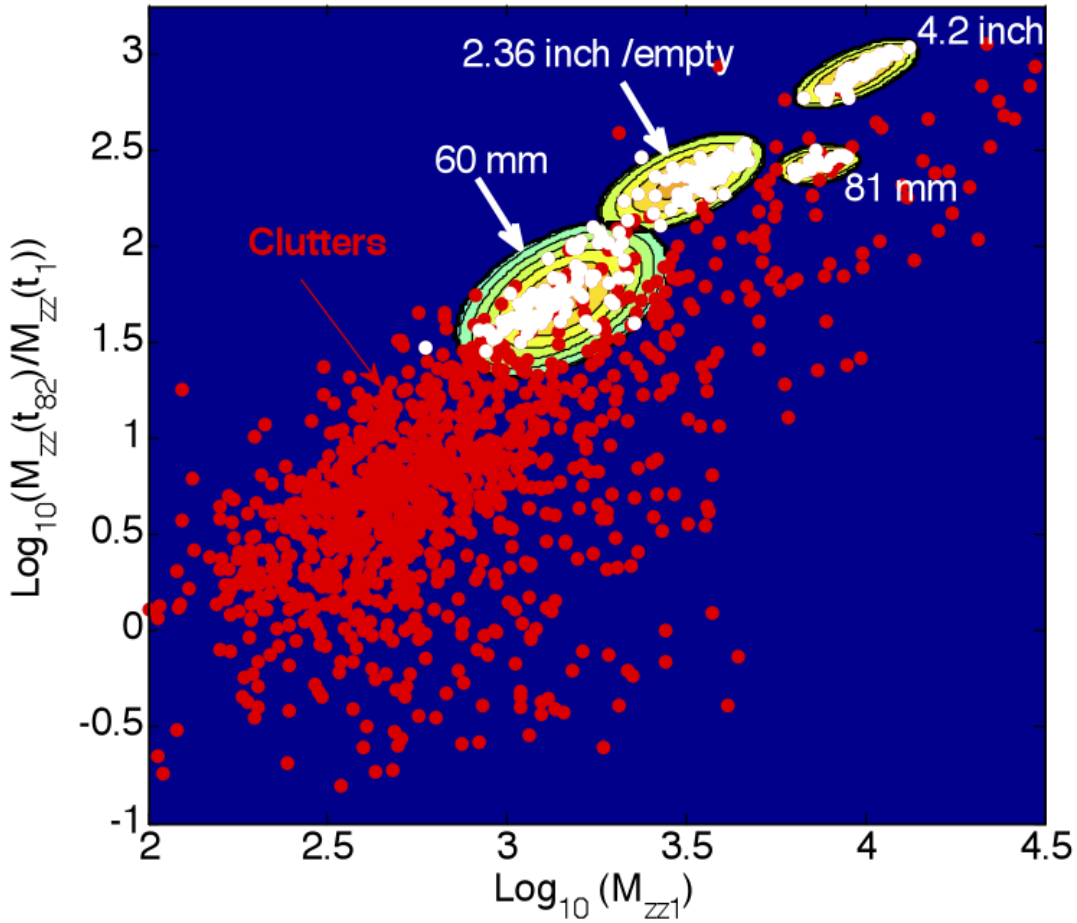


Figure 47: Result of the supervised clustering classification for the SLO-TEMTADS anomalies using the logarithms of  $M_{\alpha\alpha}(t_1)$  and  $M_{\alpha\alpha}(t_1) / M_{\alpha\alpha}(t_{80})$ . The supervised clustering has been trained with calibration data. The red markers correspond to clutters and the white ones to TOI.

We also determine the Pasion-Oldenburg parameters  $k_{\alpha\alpha}$ ,  $\beta_{\alpha\alpha}$ , and  $\gamma_{\alpha\alpha}$  for each anomaly from equation (166); the inverted parameters were used in the supervised clustering algorithm. We have previously found [12,14] that the ratio of the inverted total NSMS at the 82nd time channel to that at the first time channel, which involves a fixed superposition of  $\beta$  and  $\gamma$ , shows discernible clustering for this particular data set when combined with the third parameter. The values of  $\log_{10}(M_{\alpha\alpha}(t_1) / M_{\alpha\alpha}(t_{80}))$  versus  $\log_{10}(M_{\alpha\alpha}(t_1))$  are plotted in Figure 47 for all TEMTADS data sets. We see that the inverted parameters are well clustered, and for the most part noticeably distinct from those of the others, suggesting that this two-dimensional feature space is good for classification purposes. This suggestion is confirmed by the classification results that appear in Figure 48.

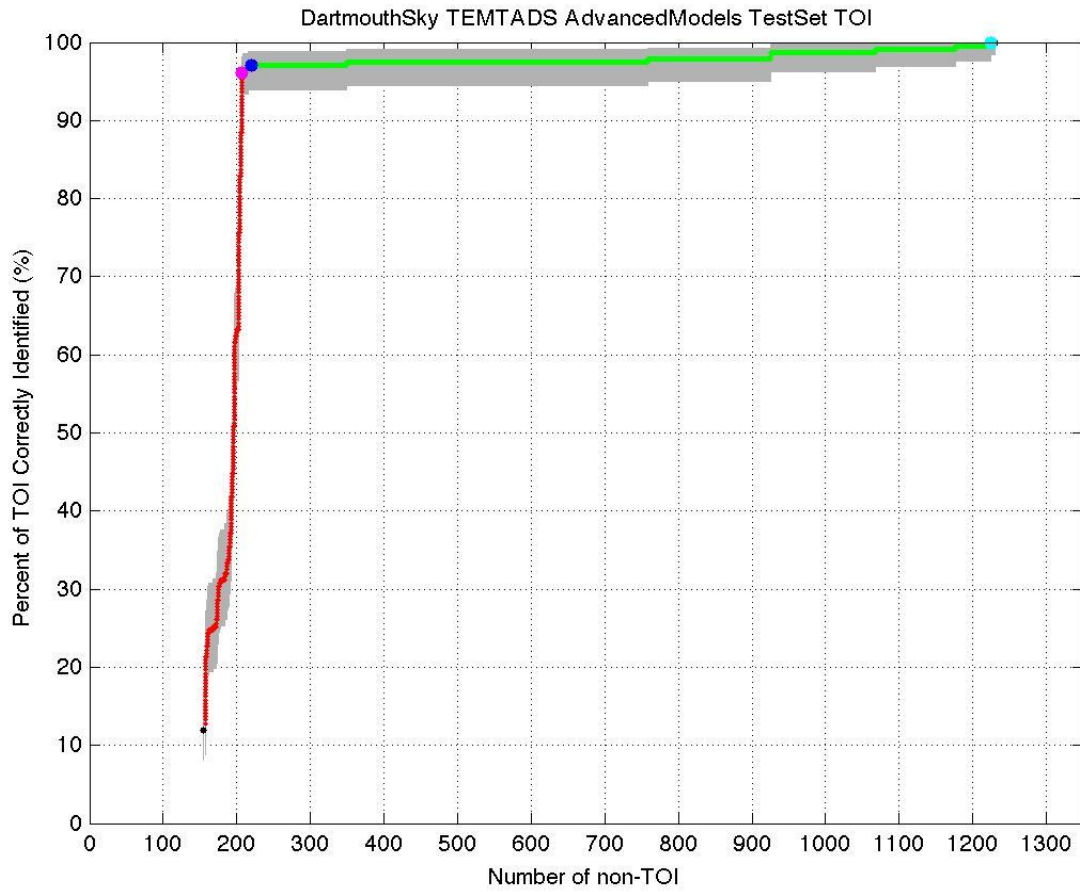


Figure 48: ROC curve for SLO TEMTADS test data.

The inverted SLO TEMTADS and MetalMapper test data were ranked by target type and caliber and submitted to the SERDP office for independent scoring, which was carried out by personnel from the Institute for Defense Analyses (IDA). Our discrimination results are summarized in Figure 49, Figure 50, and Figure 51. Our classification technique was able to correctly identify all big UXO, (the 2.36", 81-mm and 4.2" projectiles) for both TEMTADS and MetalMapper data. The algorithm had only one false negative (a 60-mm mortar) for MetalMapper. In the case of TEMTADS the algorithm missed two 2.36" rockets and five 60-mm mortars. These false negatives were mostly due to small signal-to-noise ratios.

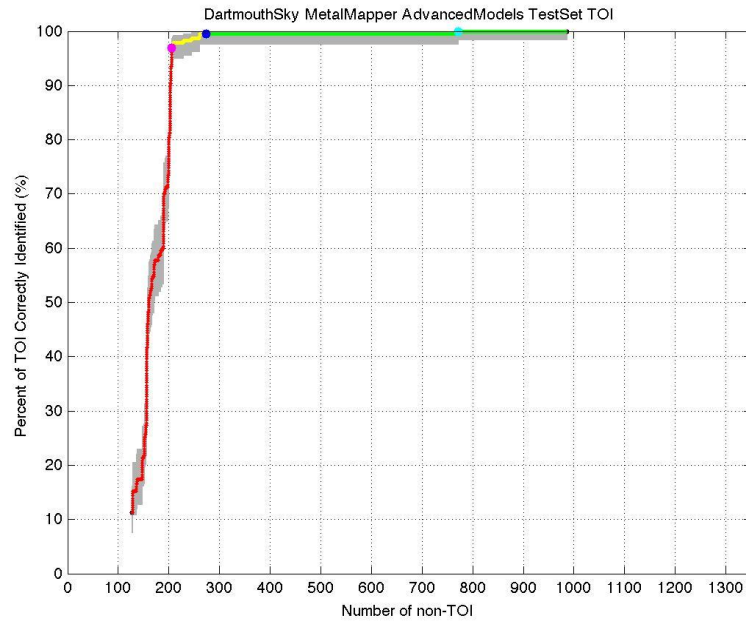


Figure 49: ROC curve for SLO MetalMapper test data.

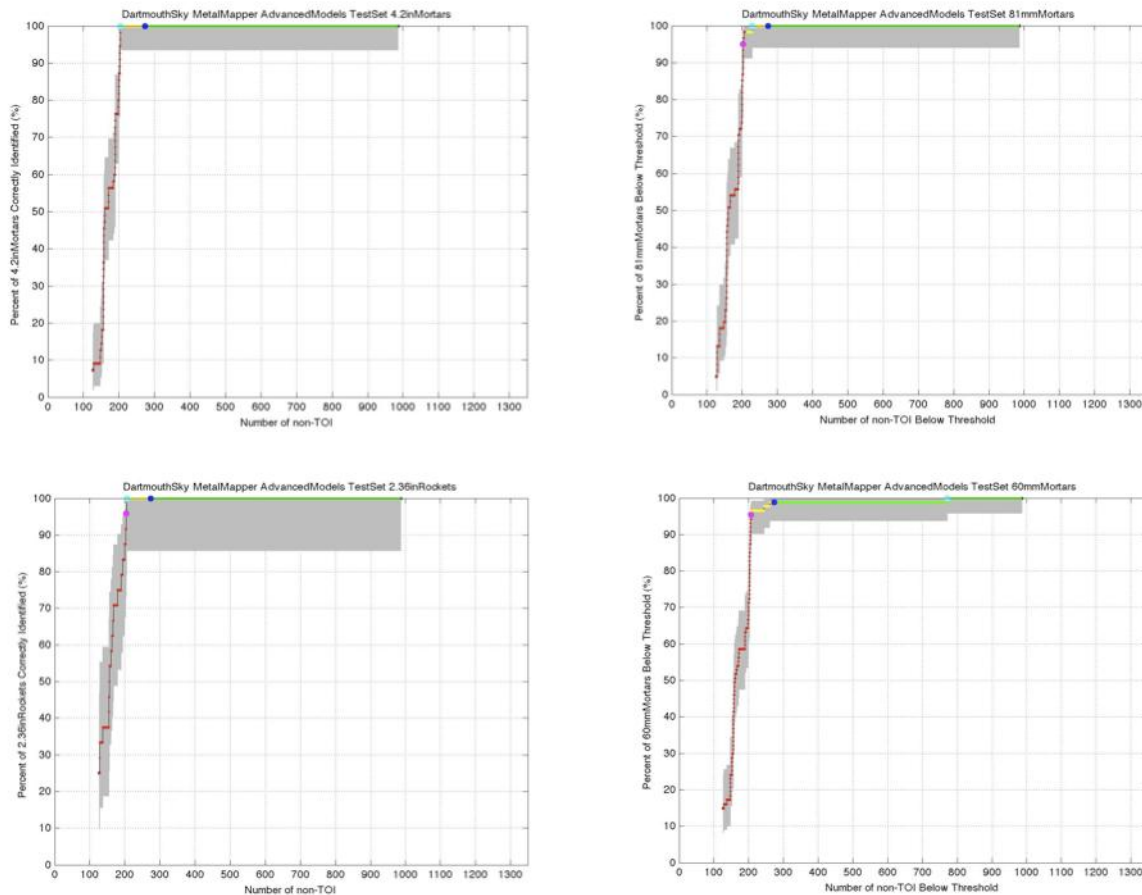


Figure 50: ROC for SLO TEMTADS data for individual TOI.

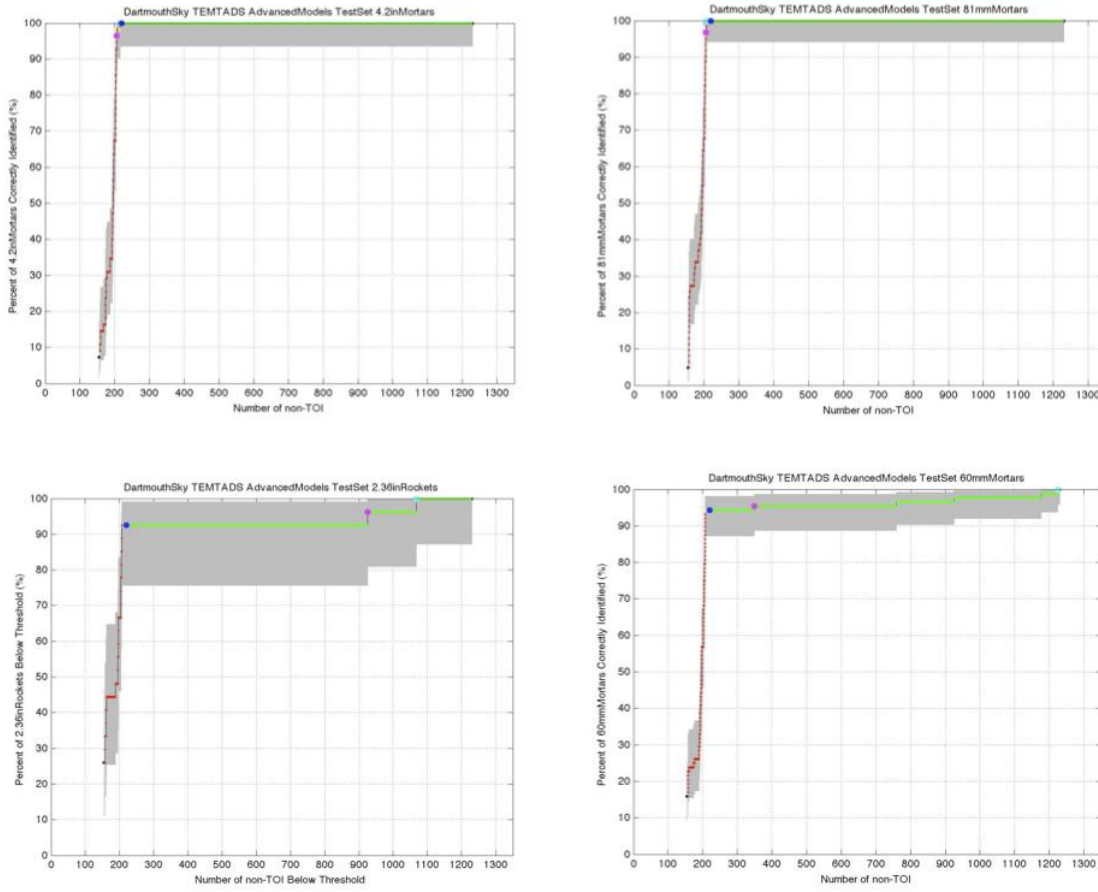


Figure 51: ROC for SLO MetalMapper data sets: individual TOI.

### 6.3.3 Comparisons between NSMS and Dipole models

#### 6.3.3.1 Calibration SLO-TEMTADS data

We now compare the dipole and NSMS models as applied to SLO calibration data. The data were inverted using both gradient search and DE. For the gradient search 100 initial guesses were used to avoid local minima, with 30 iterations for each initial guess to guarantee convergence. For DE 100 iterations were used. Once the targets' locations were determined the dipole polarizability matrix and the total NSMS were determined and diagonalized using JD. The inverted dipole tensor principal elements and total NSMS for two calibration cells (410 and 489, shown in Figure 52) appear in Figure 53. The inverted dipole principal polarizability elements are seen to be totally different for the same 60-mm mortar. For Cell #489 the dipole elements are not symmetric, and their inverted magnitudes are much higher than for the other cell even though the targets and burial depths are the same. The simple dipole model clearly breaks down while the NSMS technique predicts consistent results and is more stable and accurate. It is worth pointing out that other researchers reported the same problem with this cell when using the dipole model and overcame it using multiple dipoles.



Figure 52: 60-mm mortars actually found in calibration cells #410 and #489.

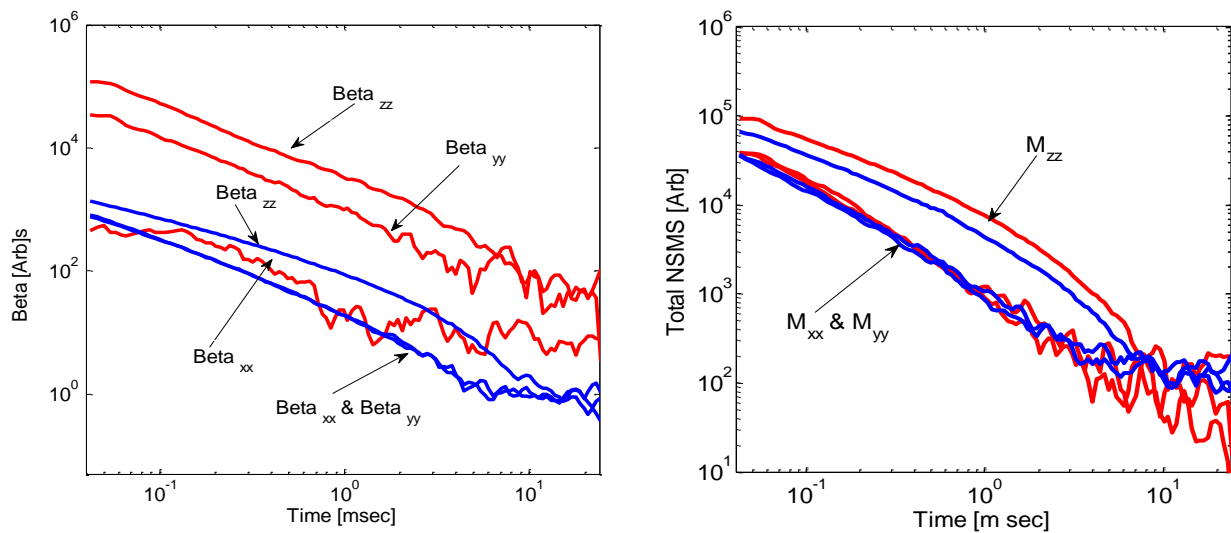


Figure 53: *Left*: Principal elements of the polarizability tensor versus time for a 60mm mortar in the SLO study. *Right*: Total NSMS time-decay curves for the same cases. The red curve corresponds to calibration Cell #489 and the blue curve to calibration Cell #410.

#### 6.3.3.2 Blind SLO-TEMTADS data sets

A similar performance was observed for deep targets in blind-test data. Figure 54 compares library and inverted data using the dipole and NSMS models. In this case a 60-mm mortar was buried 35 cm deep. Due to the low signal-to-noise ratio the dipole model was unable to predict stable, symmetric polarizability tensor elements, but the total extracted NSMS curves show axial symmetry and resemble the 60-mm library curve well.

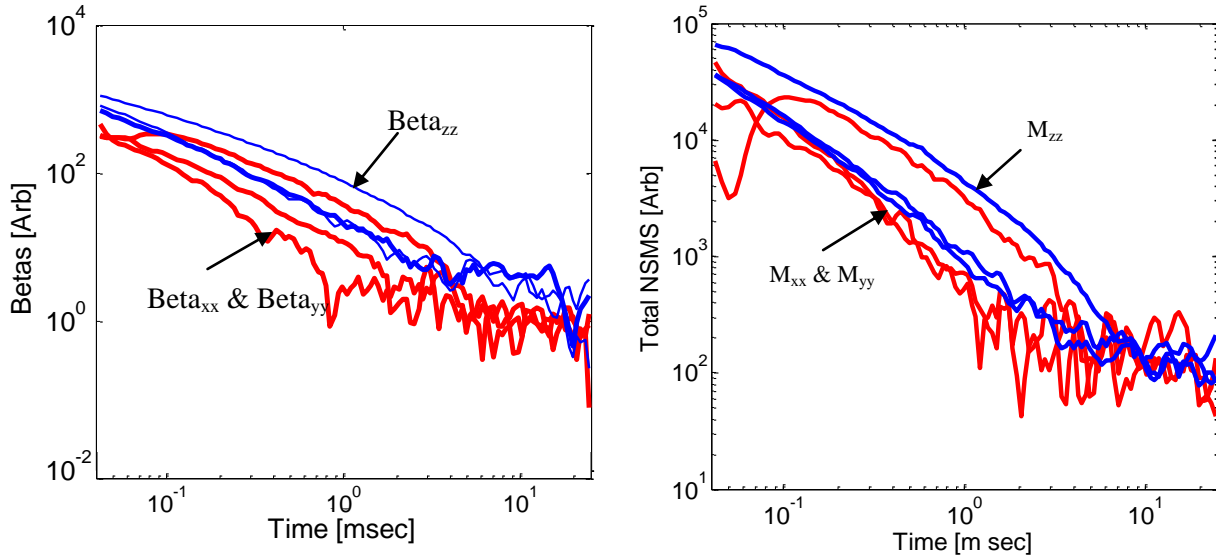


Figure 54: Comparison between library and inverted blind tests for the dipole model (left) and NSMS model (right).

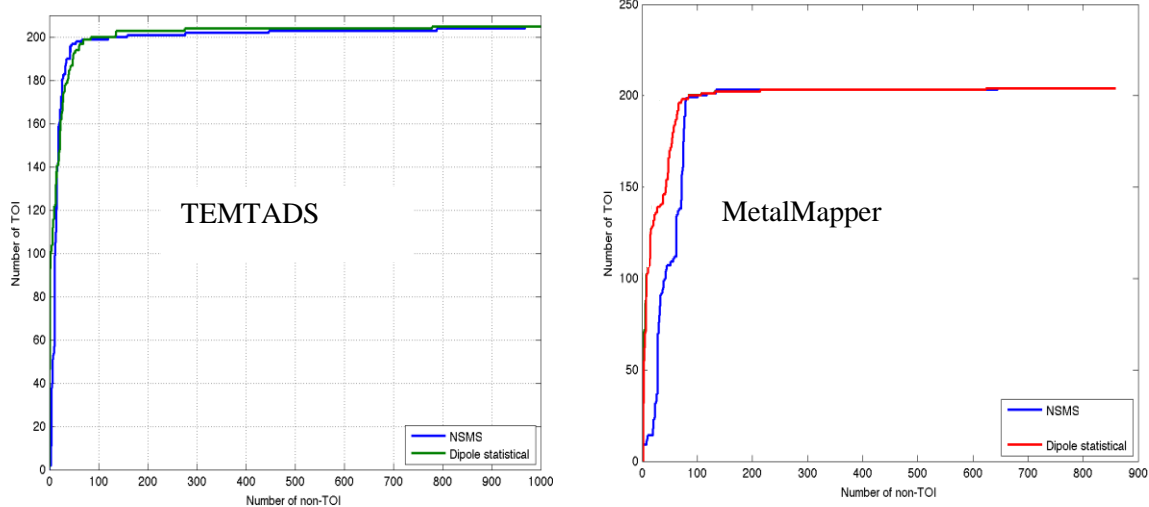


Figure 55: ROC curves for SLO TEMTADS and SLO MetalMapper discrimination studies. Green and red curves: Sky/UBC dipole results; blue curve: NSMS results obtained by our Dartmouth/Sky group.

#### 6.3.3.3 SLO-Discrimination studies

Using NSMS we inverted all SLO blind-test data sets and sorted them by target ID. The same anomalies were inverted by researchers at SKY/UBC using the dipole model. The ROC curves for the SLO TEMTADS and SLO MetalMapper discrimination studies are depicted in Figure 55. The NSMS performs slightly better than the dipole statistical approach for TEMTADS data. For the SLO MetalMapper data sets the NSMS shows higher false positives in comparisons with the dipole model, but overall it has only one false negative, while the dipole model had three false negatives.

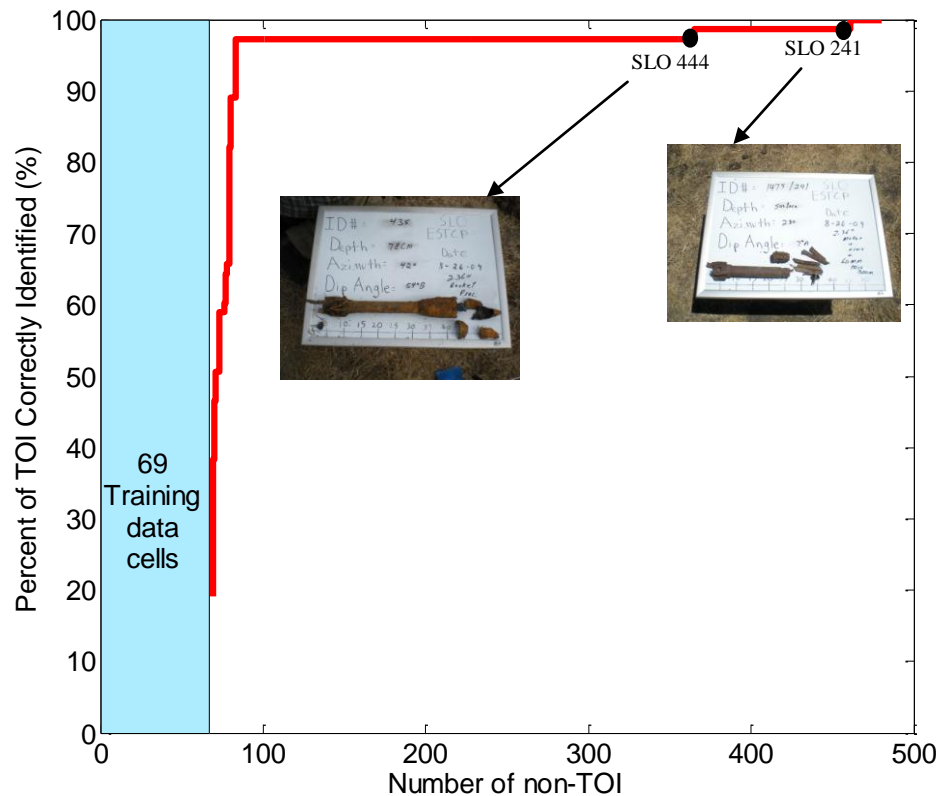


Figure 56: ROC curves for SLO BUD discrimination studies.

#### 6.3.4 SLO BUD data inversion and classification studies

The combined NSMS-DE algorithm was applied to the SLO live site BUD data sets (539 anomalies) and targets intrinsic (total NSMS) and extrinsic parameters were extracted for each anomalies. The discrimination features (size and shape information) were extracted from the total NSMS time decay history curve and anomalies were classified using the provided 69 training data set. In addition, the library matching technique, that uses the entire time decay history of the total NSMS, was also used for the classification. The inverted targets were ranked as TOI and non-TOI items. The ROC for the SLO BUD data sets is shown on Figure 56. The studies showed that only two 2.36 inch rockets were misclassified.

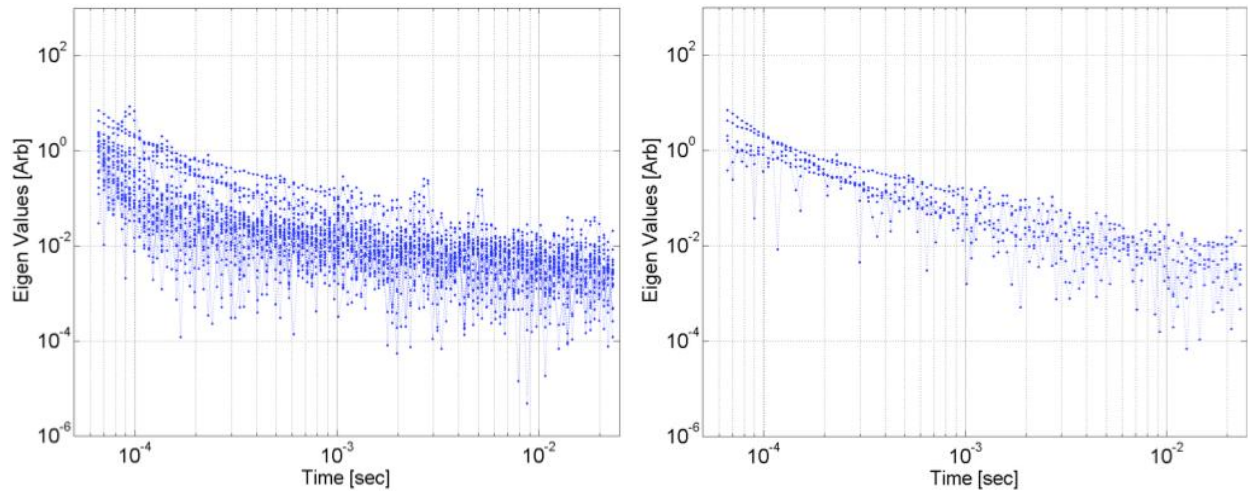


Figure 57: SLO TEMTADS test Cell #16. *Left:* All 25 eigenvalues vs. time. *Right:* Four highest eigenvalues vs. time. The target response is weak and mixed with the sensor's electronic and background noise.

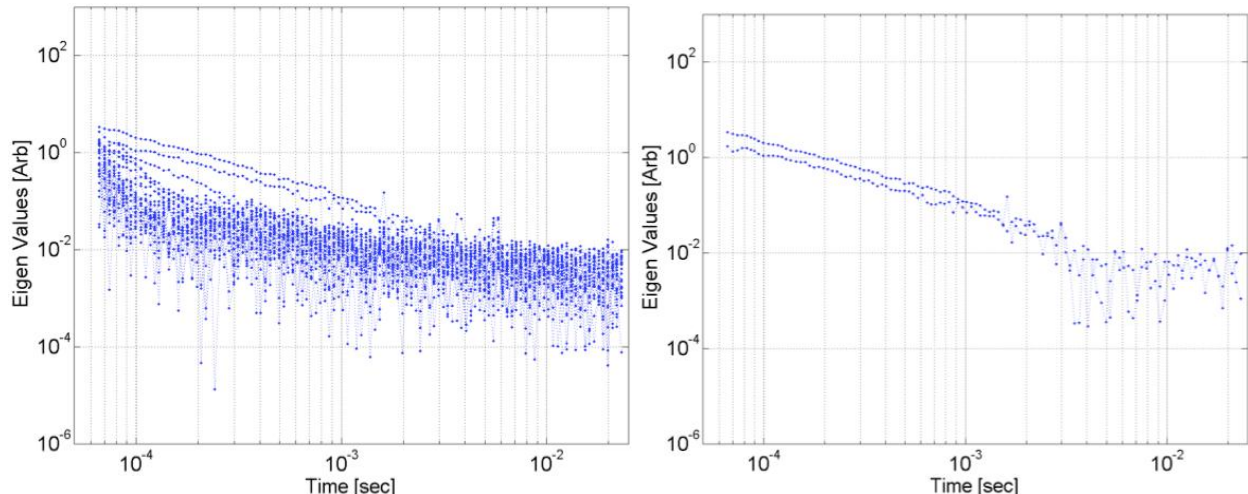


Figure 58: SLO TEMTADS test Cell #103. *Left:* All 25 eigenvalues vs. time. *Right:* Above-threshold eigenvalues vs. time. Only two eigenvalues are above the threshold, indicating a low signal-to-noise ratio.

### 6.3.5 SLO retrospective analysis

During the SLO test our algorithms missed five 60-mm mortars and two 2.36" rockets. The missed anomalies were in Cells #16, 103, 241, 441, 444, 748, and 1285. Figure 57 through Figure 63 present the results for each of these anomalies, along with our comments.

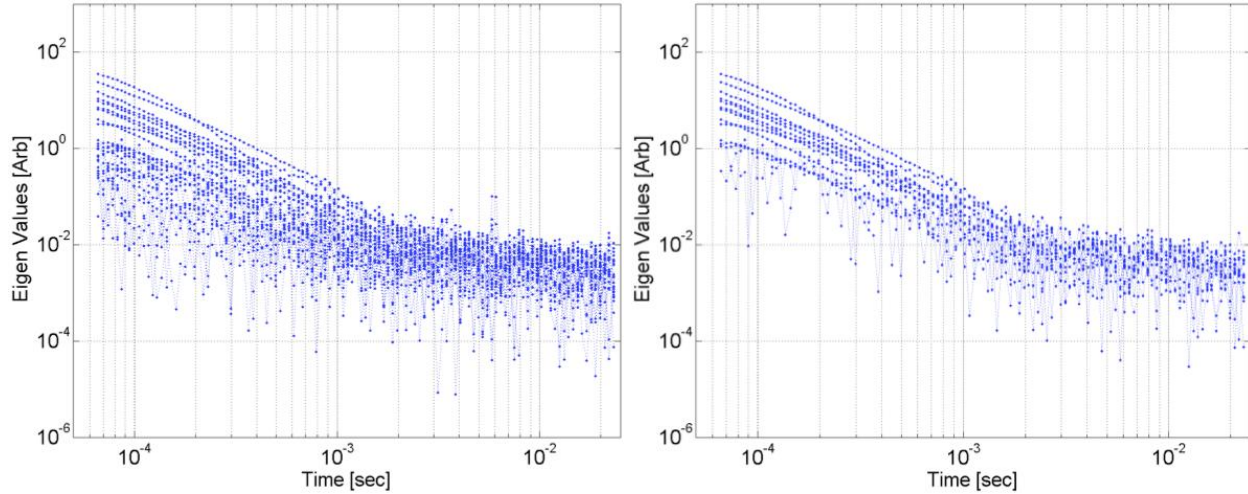


Figure 59: SLO TEMTADS test Cell #241. *Left:* All 25 eigenvalues vs. time. *Right:* Above-threshold eigenvalues vs. time. There are more than three eigenvalues above the threshold, which indicates that the cell contains more than one target. The curves decay fast, illustrating that the targets are small.

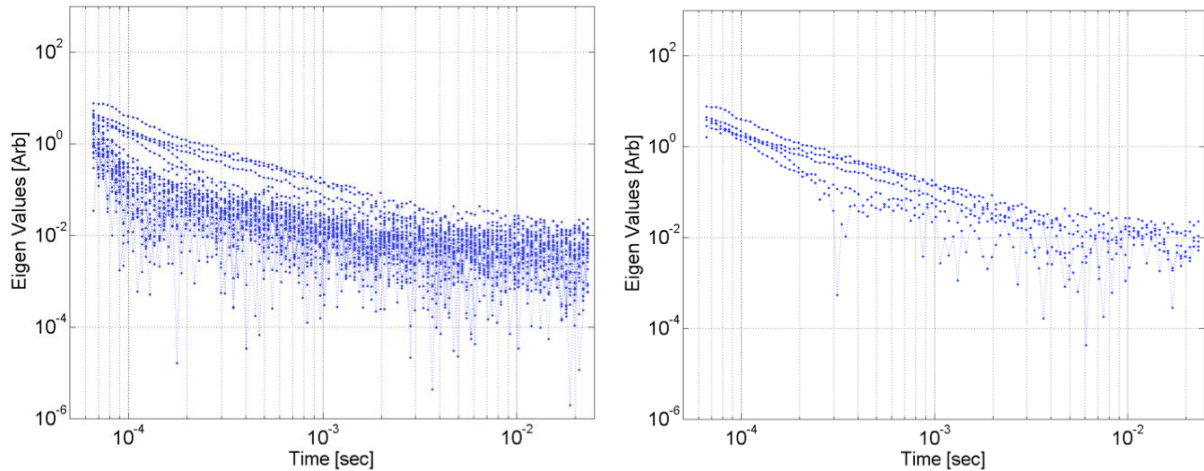


Figure 60: SLO TEMTADS test Cell #441. *Left:* All 25 eigenvalues vs. time. *Right:* Above-threshold eigenvalues vs. time. There are more than three eigenvalues above the threshold, indicating that the cell contained more than one target. The fast-decaying curves illustrate that the targets have thin walls or are small.

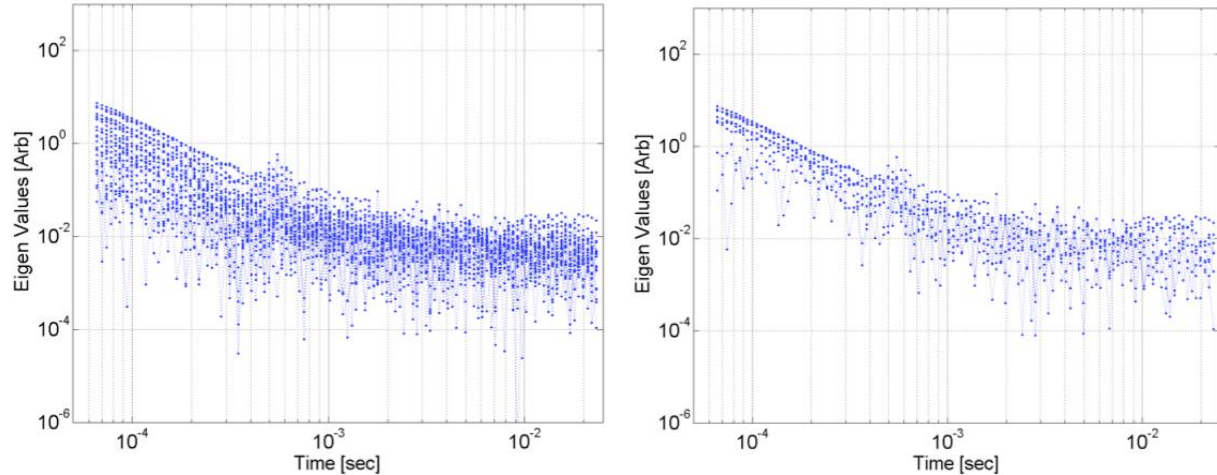


Figure 61: SLO TEMTADS test Cell #444. *Left:* All 25 eigenvalues vs. time. *Right:* Above-threshold eigenvalues vs. time. There are more than three eigenvalues above the threshold, indicating that the cell contained several targets. In addition, the curves decay fast, illustrating that the targets are small.

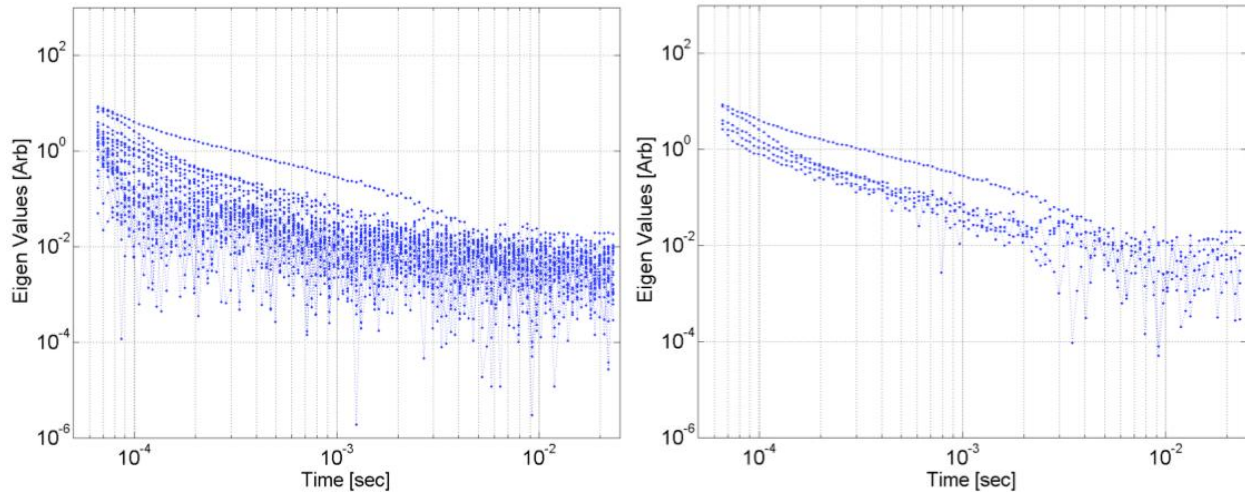


Figure 62: SLO TEMTADS test Cell #748. *Left:* All 25 eigenvalues vs. time. *Right:* Above-threshold eigenvalues vs. time. More than three fast-decaying above-threshold eigenvalues indicate the presence of several small targets.

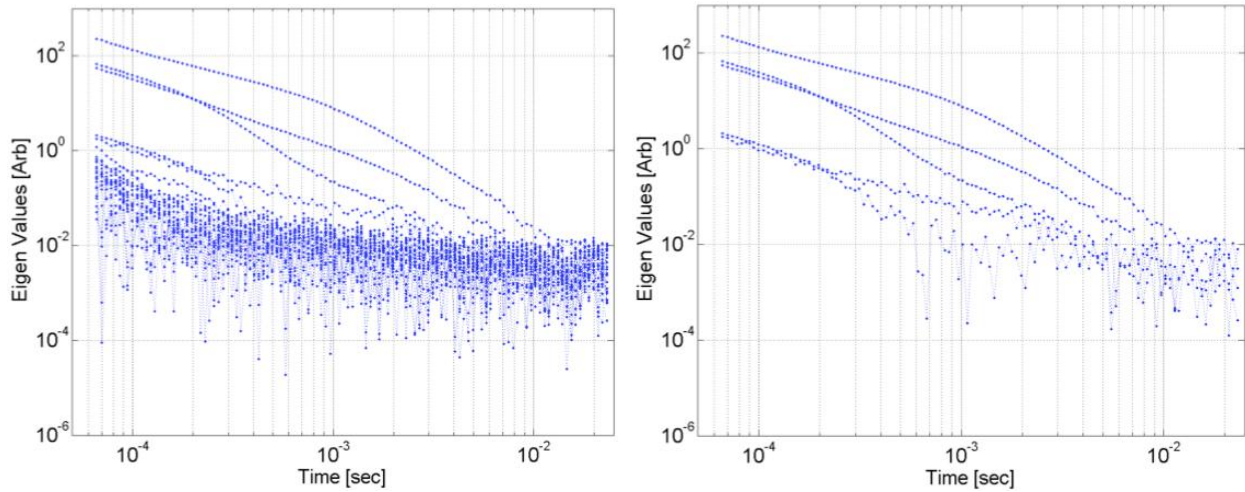


Figure 63: SLO TEMTADS test Cell #1285. *Left:* All 25 eigenvalues vs. time. *Right:* Above-threshold eigenvalues vs. time. Again, the eigenvalues indicate that there are several small targets in the cell.

## 6.4 Camp Butner

The former Camp Butner is a 40,384-acre site located approximately 15 miles north of Durham and straddling Durham, Granville, and Person Counties, all in North Carolina. The War Department acquired the property from private landowners in 1942 for use as a training and cantonment facility during World War II. The camp was primarily established for the training of infantry divisions (including the 78th, 89th, and 4th) and miscellaneous artillery and engineering units [85]. A large variety of munitions have been reported as used at the former Camp Butner, including rifle grenades, 2.36" rockets, 37-mm and 40-mm rounds, 81-mm mortars, and 105-mm, 155-mm, and 240-mm projectiles. Although the historical records are not definitive, it is thought that the targets of interest at the site of the test are mostly 37-mm and 105-mm projectiles; some of the former have a copper band, others do not. The clutter items found on the site are for the most part UXO explosion byproducts like partial mortars (i.e., stretched-out half-shells), smaller shrapnel, and man-made metallic clutter. An initial surface clearance was carried out on the site prior to the collection of digital geophysical data. Then an EM61 survey was conducted on two 100'  $\times$  100' grids for site characterization. A surface clutter analysis and excavation of one of these 100'  $\times$  100' grids confirmed the identities of the targets of interest (TOI), provided an indication of their depth distribution, and gave the demonstrators some information about the clutter environment at the site.

At a live site such as this, the ratio of clutter to TOI is such that only a small number of TOI may be found in a 10-acre area, far from enough to determine any demonstrator's classification performance with acceptable confidence bounds. To avoid this problem, the site was seeded with enough TOI to ensure reasonable statistics. Three types of targets—37-mm and 105-mm projectiles and M48 fuze assemblies—were thus used. The survey data for the study were collected with a line spacing of 50 cm. The detection threshold was set to detect all 37-mm projectiles at a depth of 30 cm [85], which for the EM61-MK2 catted survey corresponds to a threshold of 5.2 mV in the second time gate. Using this detection threshold a first anomaly list was produced. This list was used as a starting point for two detailed cued surveys carried out using TEMTADS and the MetalMapper.

Our team processed both data sets independently using our advanced EMI discrimination techniques and occasionally requesting training data to assist during the classification stage. The main objective of this section is to demonstrate the discrimination performance of the ONVMS model [99] in a live UXO site under realistic field conditions; the method is combined with DE optimization (the two-step approach described in Section 3.3) to determine the locations, orientations, and time-dependent total ONVMS of the subsurface targets. The latter depends on the intrinsic properties of the object in question and can be used for discrimination. To streamline the process we employed JD to estimate the number of

potential targets before inverting. To classify the targets in the MM data sets we performed semi-supervised Gaussian-mixture model-based clustering on the total ONVMS in a process similar to that described in Section 4.3.1. We now present the results of our discrimination and classification strategies when applied to the Camp Butner TEMTADS and MM blind cued data sets. The SERDP office provided us with 2291 cases interrogated with each system. We divided our team into two groups: One group processed TEMTADS data and the other worked on the MM sets; each group worked independently using different classification strategies. Each team constructed a custom training list (amounting to less than 5% of the entire blind data) and requested the ground truth for those anomalies for use during the classification stage.

#### 6.4.1 TEMTADS data discrimination strategy and classification results using supervised clustering

We processed all the TEMTADS data using the JD and ONVMS models. Initially we used JD to estimate the data quality and the number of potential targets. The JD algorithm constructs a multi-static response matrix using TEMTADS data and computes its eigenvectors and eigenvalues, the latter as a function of time. Studies show that these eigenvalues are intrinsic properties of the targets and that each target has at least three eigenvalues above the threshold (noise level). For example, Figure 65 shows the eigenvalues extracted for a 105-mm HE projectile, a 105-mm HEAT round, an M-48 fuze, and a 37-mm UXO. As the number of targets increases (as in Figure 64 and the third row of Figure 65), so does the number of eigenvalues above the noise level. We thus examined the eigenvalues versus time for each case and used them to estimate the number of targets.

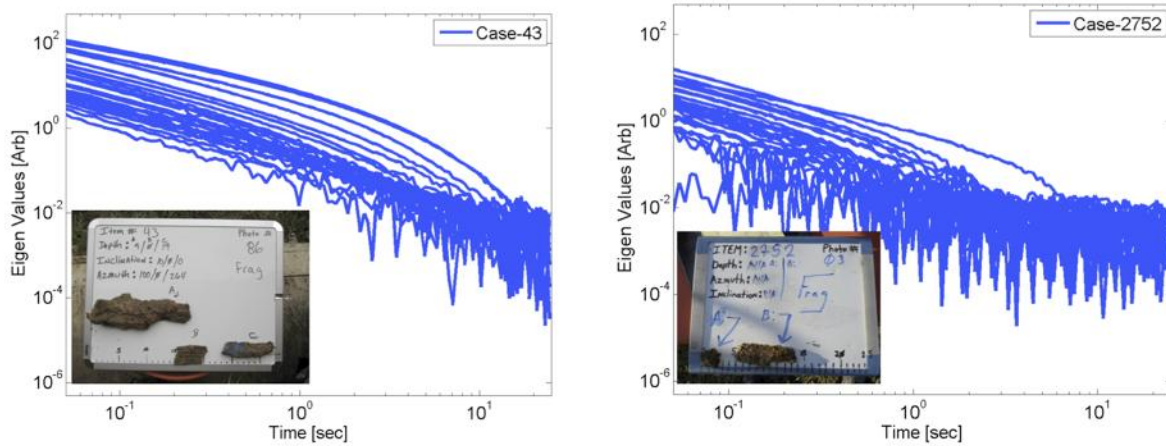


Figure 64: TEMTADS multi-static response matrix eigenvalues versus time for some samples of requested anomalies.

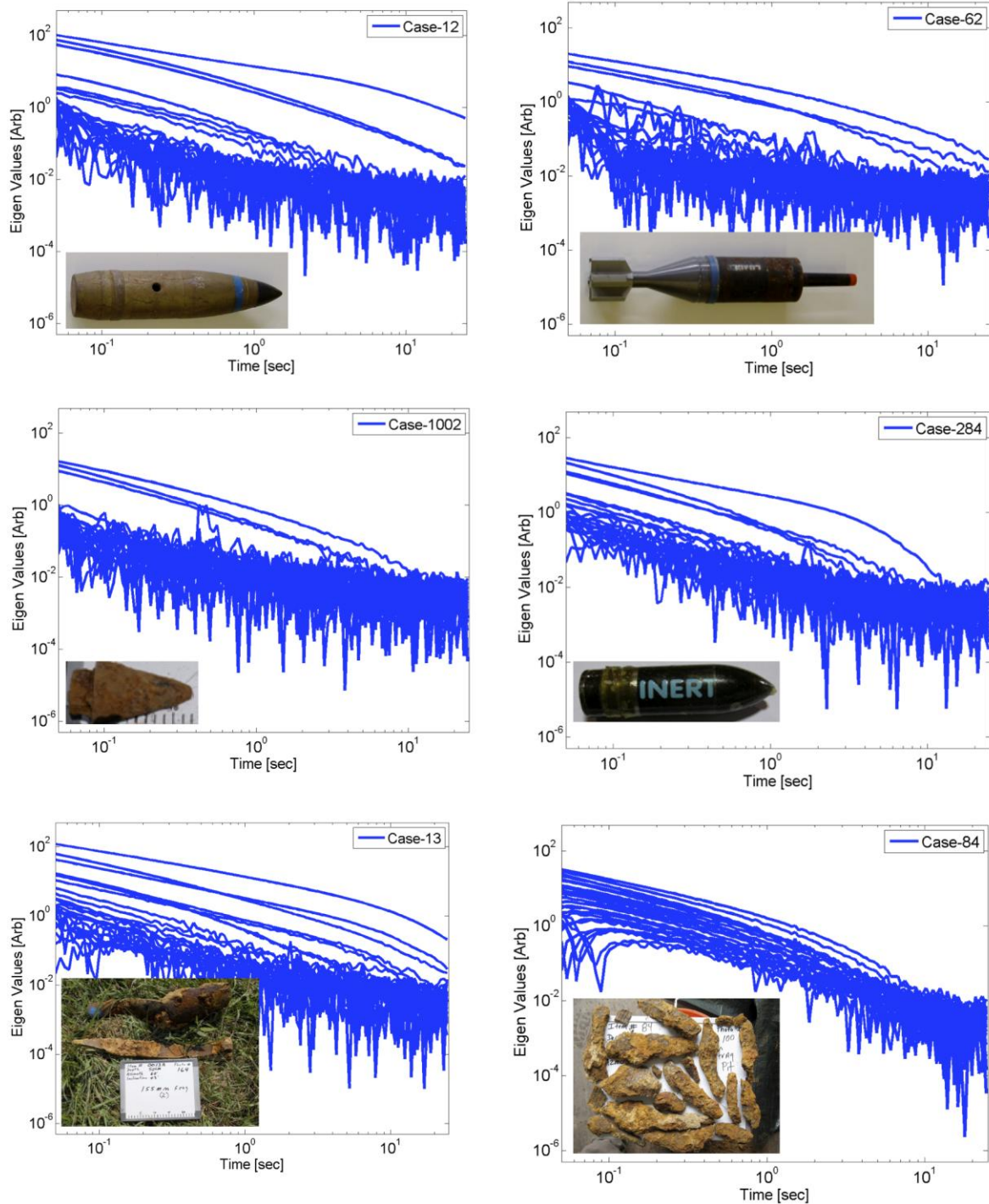


Figure 65: TEMTADS multi-static response matrix eigenvalues versus time for a 105-mm HE projectile and a 105-mm HEAT round (top row), an M-48 Fuze and a 37-mm munition (center row), and two clutter scenarios, one with two items (left) and another with several (right) (third row).

In addition, based on the eigenvalues' time-decay characteristics we built a custom training list. For the most part, the list contained anomalies that had too many above-threshold eigenvalues, like the samples depicted in Figure 64. We requested two batches of training data. The first contained 65 anomalies, all of which were clutter; some had six eigenvalues above the noise level, while others had several eigenvalues mixed with the noise. The second batch consisted mostly of UXO. Once we had the ground truth for all 75 custom identified anomalies we proceeded to invert all TEMTADS data sets using a multi-target ONVMS algorithm combined with DE. We extracted the total ONVMS for every anomaly. Armed with the custom identified training list and the inverted total ONVMS for each case we created a library for M-48 fuzes and 37-mm projectiles without copper band. We did not request training data for either of the 105-mm UXO or for the 37-mm projectile with copper band because we already had TEMTADS test-stand data for these targets. The JD and ONVMS analysis clearly showed the presence of those items at the site. We implemented a library-matching technique in which we quantified the mismatch in total ONVMS between library samples and blind items and used it to classify UXO and non-UXO items. The inverted total ONVMS for the anomalies that were classified as 105-mm HE projectiles, 105-mm HEAT rounds, M-48 fuzes, and 37-mm UXO with and without a copper band are depicted in Figure 66 and Figure 67. All the inverted total ONVMS are seen to cluster well, and each target has a total ONVMS with features—such as its amplitude at the first time channel, its decay rate, or the separation between the primary (blue lines) and secondary (red and green lines) components at different time channels—that make it amenable to identification. (The most difficult differences to discern were between the M-48 fuzes of Figure 66 and the 37-mm projectiles without copper band of Figure 67). These features allowed us to classify targets as UXO or clutter and also let us sort the UXO by caliber. With this knowledge we created a prioritized dig list that we cross-validated using the time-decay curves of the JD eigenvalues.

The final prioritized dig list was submitted to the Institute for Defense Analyses (IDA) for independent scoring. The scored results were sent back in the form of a receiver operating characteristic (ROC) curve, which we depict in Figure 68. We can see that a) of the 75 targets that were dug for training, 68 targets were not TOI (shift along  $x$ -axis) and seven were (shift along  $y$ -axis); b) for 95% TOI classification (the pink dot in Figure 68) only seven extra (false positive) digs are needed; c) to classify all TOI correctly (the light blue dot) only 21 extra (false positive) digs are needed; d) for increased classification confidence the algorithm requested an additional thirty digs after all TOI had been identified correctly.

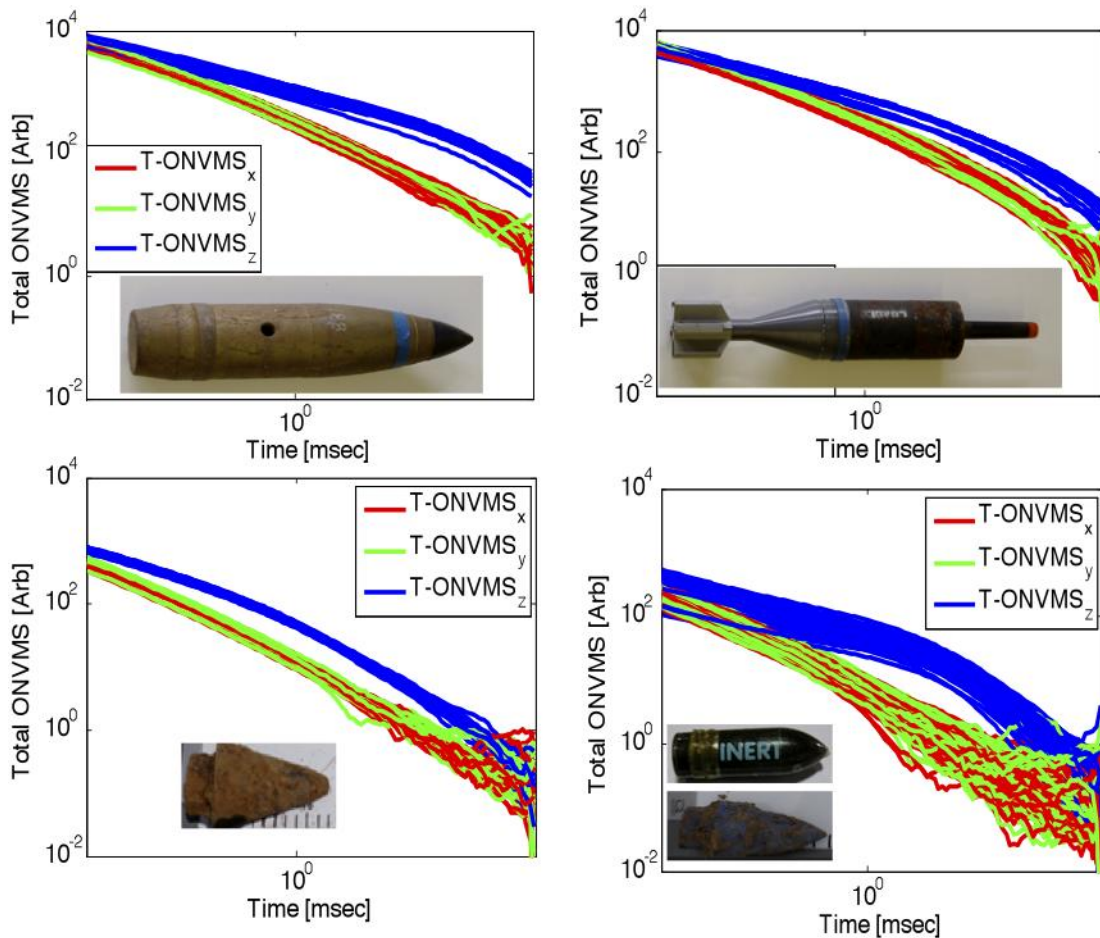


Figure 66: Inverted total ONVMS time-decay profiles for four Camp Butner targets: (top row) 105-mm HE munition and 105-mm HEAT round, and (bottom) M-48 Fuze and 37-mm projectile with copper band.

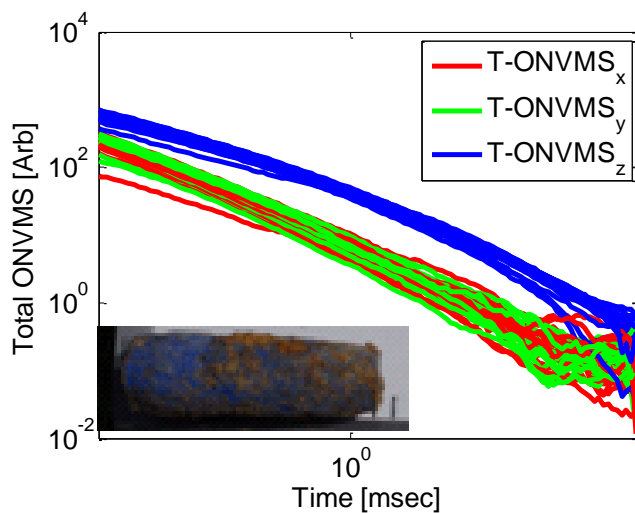


Figure 67: Inverted total ONSMS time decay profiles for a 37-mm projectile without copper band.

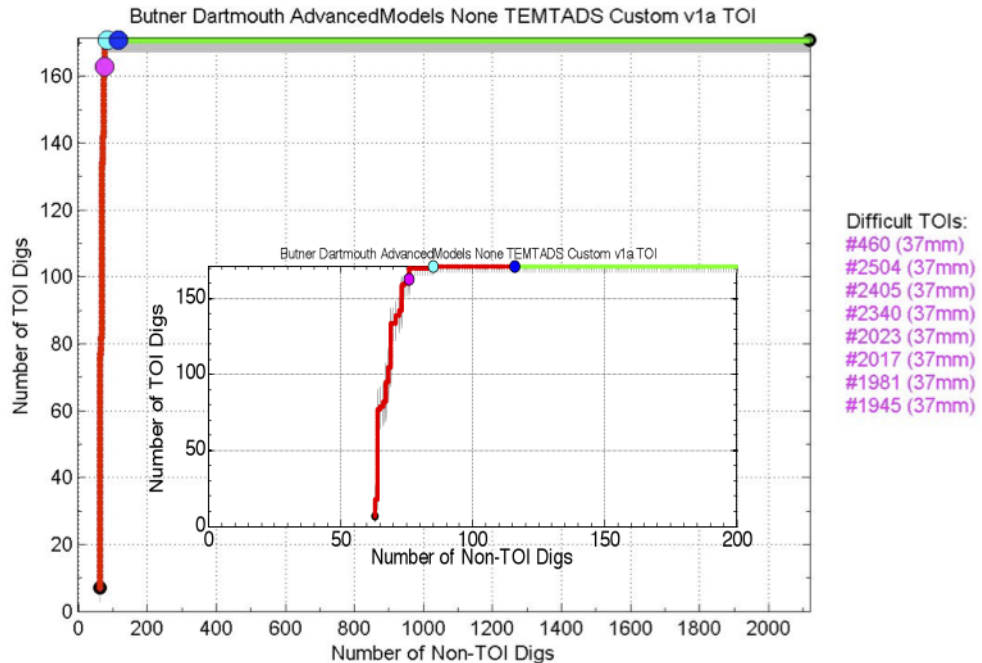


Figure 68: ROC curve for the Camp Butner TEMTADS test data.

#### 6.4.2 MetalMapper data discrimination strategy and classification results using supervised clustering

All Camp Butner MM data sets were processed using a multi-object ONVMS/DE code. The combined procedure yields the total ONVMS for each anomaly, which, like the total NSMS, is intrinsic to the object it represents and can therefore be used for classification (See Section 2.3.6). As with the total NSMS, early-time ONVMS responses are associated with superficial eddy currents and thus directly proportional to the size of the object's surface, while late-time signals are due to volumetric currents and thus proportional to the target's entire volume.

These physics-based features were utilized in the supervised clustering algorithm. We used the ratio of the inverted total ONVMS at the 30th time channel to that at the first. The values of  $\log_{10}[M_{zz}(t_1)/M_{zz}(t_{30})]$  vs.  $\log_{10}[M_{zz}(t_1)]$  are plotted in Figure 69 (left) for all Camp Butner MM data sets. We see that the plotted quantities exhibit a wide spread of values. To use these features for statistical classification, and for determining clusters and a classification probability function, we started by dividing the scatter plot of Figure 69 (left) into subsections. We then applied the Gaussian mixture model to each subsection assuming that there were five clusters. From the Gaussian mixture model we extracted the mean and standard deviations for each cluster and built a global classification probability function, depicted in Figure 69 (right) that depended on the two feature parameters. The figure shows that there are 55 well-separated clusters. We next created a first custom training dig list that contained 55 anomalies,

(i.e., one anomaly for each cluster) and requested the ground truth. The MM data for each scenario were inverted using the combined ONVMS-DE algorithm as though there were one, two, or three targets present, and the resulting total ONVMS amplitudes were compared. Whenever we spotted significant differences we examined the curves visually (a sample case is depicted in Figure 70) and, based on this examination, requested the ground truth for an additional 60 datasets. Once we had the ground truth for a 121 custom training data set, we classified all targets as either TOI or non-TOI items using the probability function of Figure 69. The classification based on the supervised clustering is plotted in Figure 71: the red circles correspond to TOI, and the green dots to clutter.

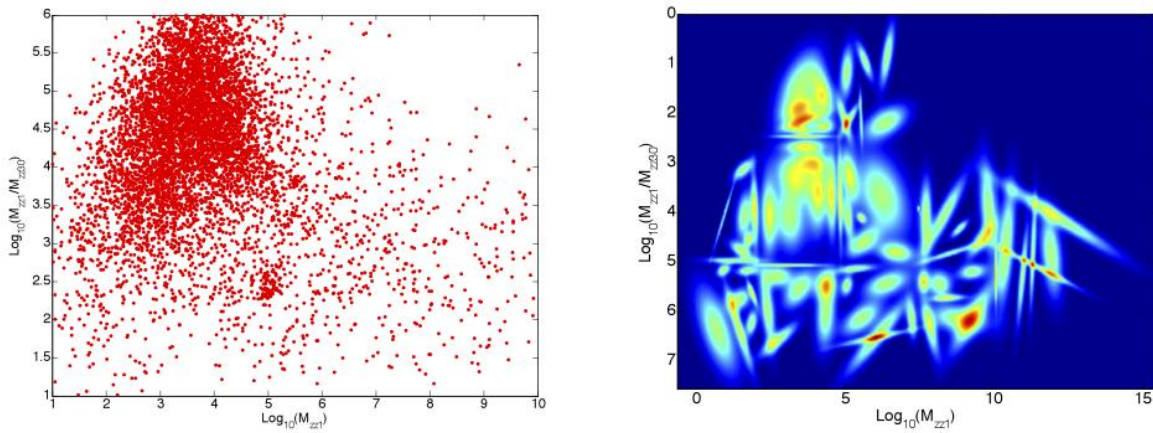


Figure 69: *Left*: Scatter plot for all MM anomalies based on the extracted total ONVMS. *Right*: Probability function for all MM anomalies.

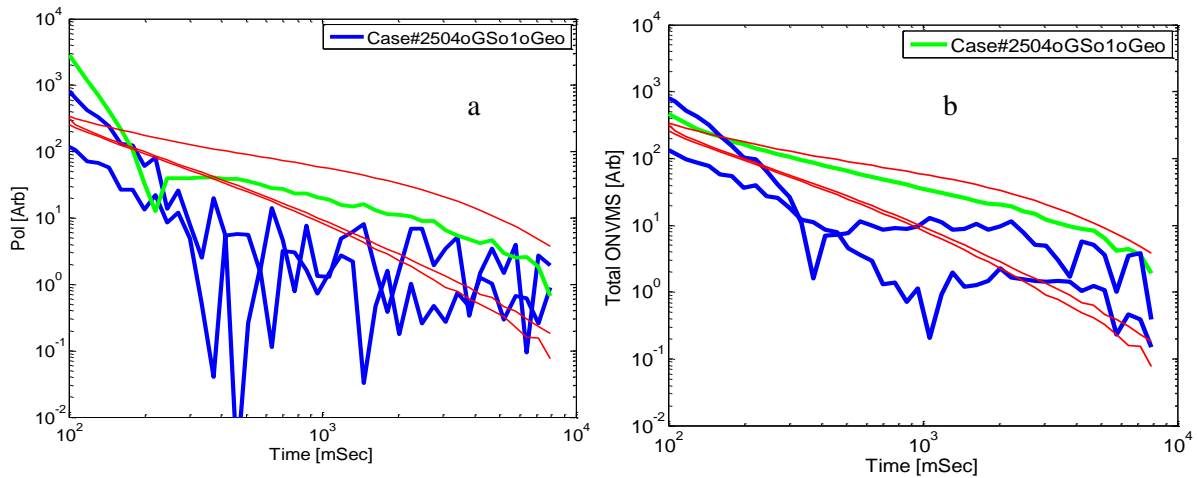


Figure 70: Inverted magnetic dipole polarizability (left) and total ONVMS (right) time-decay profiles for MM anomaly #2504. The thin red lines show a library sample, while the thick blue and green lines show the inversion results.

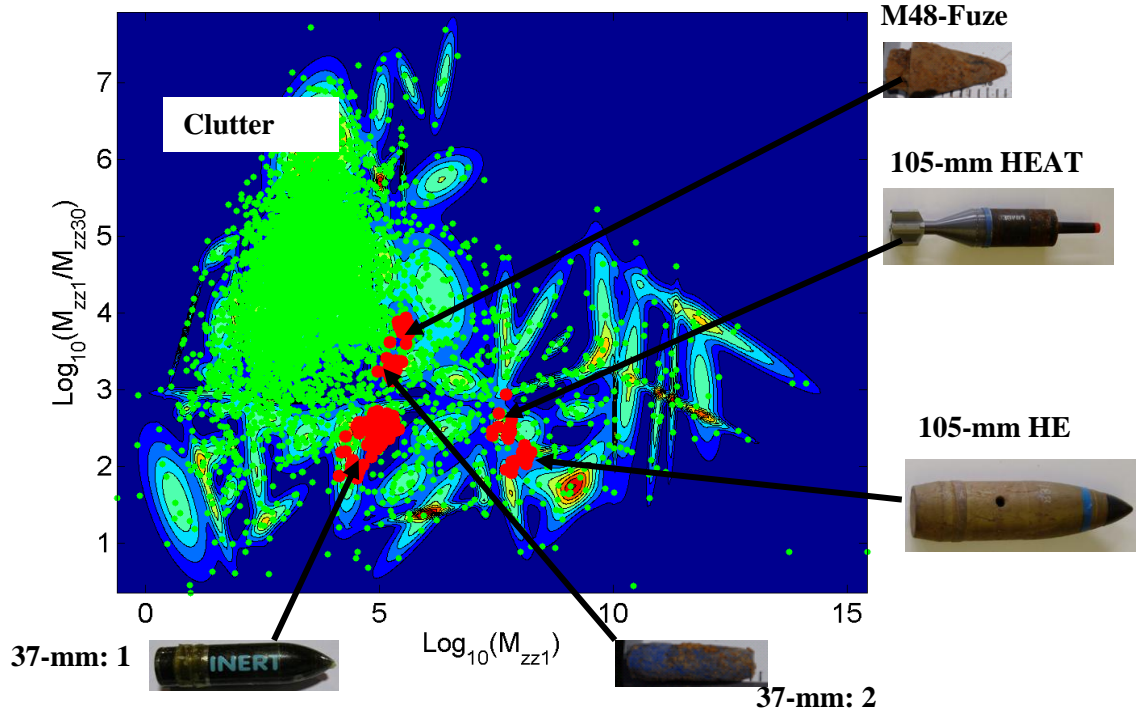


Figure 71: Result of the supervised clustering classification for the Camp Butner MM anomalies using the logarithms of  $M_z(t_1)$  and  $M_z(t_1)/M_z(t_{30})$ . The supervised clustering was trained with calibration data. The red markers correspond to clutter and the green ones to TOI.

We see that the Gaussian mixture model separates and clusters inverted parameters well. The clusters for the TOI are noticeably distinct from those of the others, suggesting that this two-dimensional feature space is appropriate for sound classification.

Using these results we created a prioritized dig list for the Camp Butner MM anomalies and again submitted the list to the Institute for Defense Analyses for scoring. Our classification results are summarized in the ROC curve of Figure 72. We see that a) of the 121 targets that were dug for training, 120 targets were not TOI (shift along  $x$ -axis) and one was (shift along  $y$ -axis); b) for 95% TOI classification (pink dot in Figure 72) eight extra (false positive) digs are needed; c) to classify all TOI correctly (light blue dot) only 32 additional digs are needed; d) for increased classification confidence the algorithm requested 33 additional digs after all the TOI were identified correctly.

Our classification results for both TEMTADS and MM were scored independently by the Institute for Defense Analyses. The scores we obtained reveal that our advanced models produce superb classification in all cases. There were no false negatives, and less than 5% of the anomalies had to be dug to achieve 100% correct classification. This is the third time our advanced EMI and statistical models have shown successful classification performance on a realistic live-site blind test.

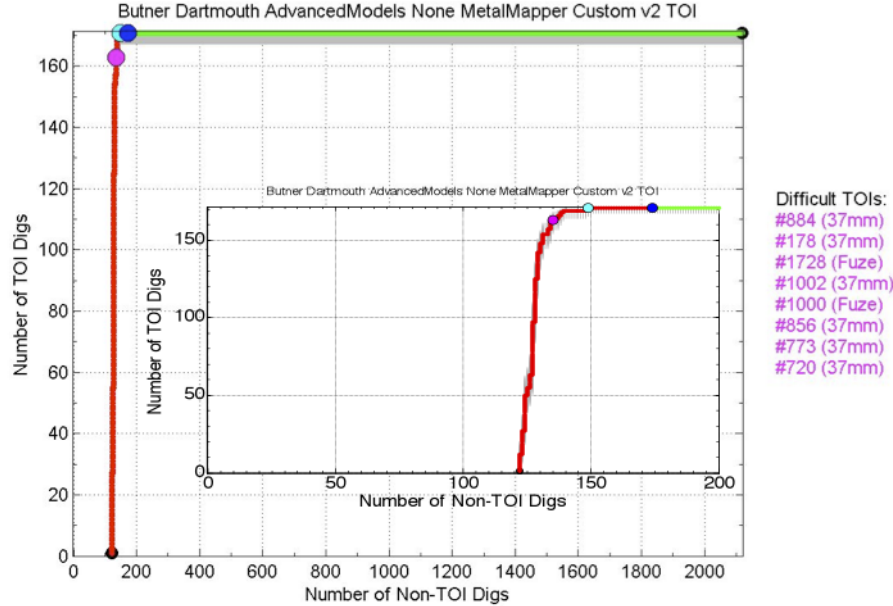
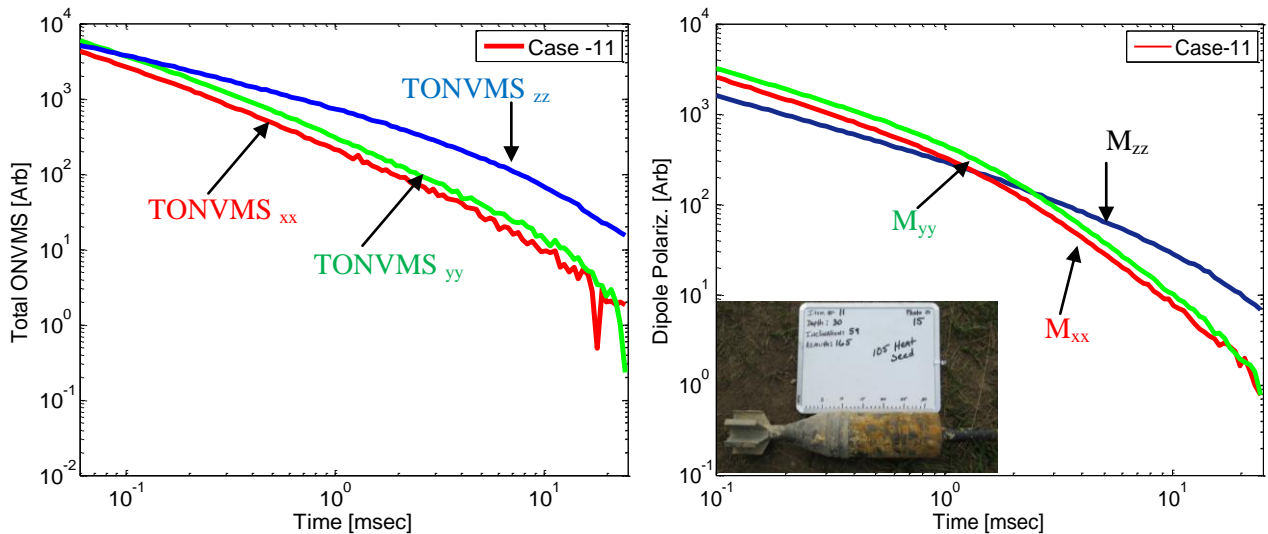


Figure 72: ROC curve for Camp Butner MetalMapper test data.

Figure 73: *Left:* Total ONVMS time-decay curves for a 105 mm projectile in the camp Butner, NC study. *Right:* Principal elements of the polarizability tensor versus time for the same case.

#### 6.4.3 A Comparison between ONVMS and Dipole model

To illustrate the ONVMS superior classification performances over a simple dipole model, here we analyze extracted dipole polarizabilities and total ONVMS for 105 mm projectile. The data were collected at camp Beale, NC using the TEMTADS sensor. The object's intrinsic parameters were inverted

using the ONVMS-DE and the simple dipole model-DE algorithms, with 100 iterations. The target dipole polarizability matrix and the total NSMS were determined and diagonalized using JD, and are illustrated in Figure 73. The results show that magnitudes of extracted dipole principal polarizabilities versus times are out of orders; namely, at early time gates amplitudes of the primary polarizability  $M_{zz}$  are less than the secondary  $M_{xx}$  and tertiary  $M_{yy}$  polarizabilities, while the TONVMS magnitudes have consistent orders for all time channels and provides good classification parameters.

#### 6.4.4 Camp Butner retrospective study using semi-supervised clustering

In this section we discuss an automated classification approach that could provide a rigorous framework for data processing that maximizes both the sensitivity and the specificity and minimizes any other external inputs from the user. Such a method would ideally infer the patterns from the data itself and determine the minimal possible training data set required to correctly identify trends and classify the data. The ground truth could then be requested from the site and further incorporated into the model. The method would internally update for the newly available results and then could either request more ground truth to further refine the classification or provide a final priority-weighted dig list.

Several clustering and statistical signal processing techniques have been applied previously to UXO detection based on magnetometry and EMI data [7-8, 53], where classification was based on features extracted from direct magnetic field observations. In [100], for example, first-generation (single transmitter/single receiver) data collected by the EM61 sensor was treated as an image, with no physical models used for classification, and the results were compared to those using a simple dipole model. Successful applications of Bayesian data fusion, multivariate Gaussian representation of the EMI signals, and semi-supervised learning techniques have also been reported [95, 100-102]. Here we use a simple combination of hierarchical clustering and probabilistic classification approaches to perform unsupervised (or semi-unsupervised) learning for UXO classification using NSMS-extracted Pasion-Oldenburg parameters from TEMTADS Camp Butner data. We first use agglomerative clustering in the feature space to split the entire data set into a finite number of clusters (which is an external parameter, and was assumed to range from 1% to 5% of the number of items in the data set). Then we request the ground truth for the anomalies which lie closest to the geometrical center of each cluster in the feature space. Those clusters which then happen to be centered around a TOI are further labeled as potential UXO clusters and used as a basis to construct a Gaussian Mixture model (fitting either one or more multivariate Gaussian distributions across the suspicious clusters). Any other anomaly can then be assigned a probability of being a particular type of UXO based on its position in the feature space relative to the identified UXO clusters. These probabilities can be used to sort the anomalies and generate a prioritized dig list.

As mentioned previously, the multi-target magnetic field inversion approach often provides better target localization and more precise NSMS decay law, thus yielding more reliable features. In a two-target case, however, this means having total of a factor of three data points in feature space (one for object 1 alone, second for object 2 alone, and third for objects 1 and 2 considered acting as a single object). For every physical anomaly, therefore, there is a triplet of points in feature space describing its contents. If any of these three points is suspected to be a UXO, the whole “anomaly” (the objects buried at that specific location at the UXO site) should be treated as UXO. It turns out that, while it is still possible to perform the data clustering in the feature space, there is no straightforward way to identify which training data to request and how to interpret it. Suppose a training data point is requested from a certain cluster, containing only clutter objects (perhaps even having outlier values as features). While the data point corresponding to this object indeed has features peculiar to clutter, it can happen that this signal is coming from a triplet containing a UXO, which will be revealed in the ground truth. Since it is very difficult to determine which of the points in the triplet belongs to which of the physical items (object 1, object 2, or objects 1 and 2 acting as a single object), one would have to mark all three of the clusters as potential UXO, immediately leading to a large rate of false positives.

To get around this issue we employ a two-step approach. In the first step, the features extracted from an inversion assuming only one target (single-target inversion) are clustered and the ground truth is requested for the data points closest to the cluster centroids. There are several options for clustering, which are taking different criteria into the account. Some of the options we found useful for Camp Butner data classification are

1. Ward linkage criteria with Euclidean distances [103-106]. The Ward technique is based on the minimization of the increase in the total within-cluster sum of squared distances between the members of a cluster and its centroid:  $E = \sum_{k=1}^K \sum_{x_j \in C_k} \|\mathbf{x}_j - \mathbf{m}_k\|^2$ , where  $K$  is the total number of clusters and  $\mathbf{m}_k$  is the centroid of cluster  $C_k$  [105]. In agglomerative hierarchical clustering, therefore, only those clusters are merged which cause the minimal increase in this distance.
2. Weighted Pair Group Method Average (WPGMA) linkage based on Mahalanobis distances. When any two clusters are merged, WPGMA [104-105] uses a recursive approach to update the distances between already existing clusters and a newly formed one by weighting the pairwise-average-distances to original merged clusters with respect to the number of elements in them. The Mahalanobis distance [107] provides a way to measure the separation of a point from a particular statistical distribution described by a given covariance matrix and, therefore, takes into the

account the natural variation and spread of physically different feature values in their own dimensions.

The central elements belonging to each of the clusters then are probed, and those identified as UXO are stored. In the second step, two-target-inversion features are clustered with the same algorithm, with the number of clusters being 3 times greater than that in the first step. After that, the confirmed UXO feature coordinates for a single-target inversion can be imported into the multi-target feature space, and the clusters closest to these points were marked as potential UXO. Such an approach combines the ease of training data interpretation of the single-target-inversion case with the rigor and accuracy of the multi-target inversion. The multivariate Gaussian Mixture model can then be constructed around the identified UXO clusters, and the rest of the anomalies assigned a probability of being UXO.

The combined clustering/Gaussian mixture approach therefore provides a natural way to find intrinsic patterns in noisy feature data and yields a convenient probabilistic measure of class membership for unknown items. It also reduces the amount of required training data, improving both classification sensitivity and specificity.

#### 6.4.4.1 Results

In this section we apply the classification techniques described above to the blind data set from former Camp Butner. This data set contains 2291 anomalies, with no initial training data available. The suspected UXO types are 37-mm and 105-mm projectiles and 48-mm fuzes. The goal of automated classification process is to minimize the involvement of human experts in the learning process. By delegating the routine tasks such as feature extraction, clustering and labeling to the software, it is possible to extract only the key structural information from the complex data, leaving the less cumbersome but more crucial tasks, such as decision-making and quality control, to human experts. With no training data available, only unsupervised learning techniques have to be used at the first stage of the process. Below we report on the progress of the blind test classification study for Camp Butner, which, overall, consisted of the following steps:

- (a) The features  $\log k$ ,  $b$ , and  $g$  were extracted from EMI data sets of all anomalies, corresponding to 1-object, 2-object and 3-object inversions.
- (b) Initial clustering was performed, and, in order to probe the feature space, the ground truth was requested for all targets whose features were located closest to their corresponding cluster centroids (a total of 69 targets).
- (c) Clusters containing at least one UXO were identified and a smaller domain was selected within the feature space for further interrogation.

- (d) Second clustering was performed within the selected domain, and those targets with features closest to the corresponding cluster centroids were probed for ground truth (26 targets). The clusters with at least one identified UXO were marked as *suspicious*.
- (e) All targets whose features (based on 2-object inversion) fell inside any of the *suspicious* clusters were used to train a 3-component Gaussian Mixture model classifier and score all of the unknown targets.
- (f) All targets with a score greater than a specifically selected threshold value of log-likelihood were assumed to be UXO, and the ground truth was requested for them (a total of 131 targets, 3 of which had already been requested previously. Of these targets, 118 were confirmed UXO).
- (g) A new 3-component GMM classifier was then trained based on the features from the 3-object EMI inversion. All the items were re-scored to correct for the changes and adapt for new information. Another 20 targets with consecutively decreasing scores (starting from a specific low value) were then selected for additional verification.

*At this point, if the verification yielded that all these 20 targets are clutter, the algorithm would stop, and the scored values would be used to produce a final dig list.*

- (h) Four out of the 20 items requested happened to be UXO, and the classification continued. *NOTE: the ground truth for three of these 20 items had already been requested in the previous steps, with one being a confirmed UXO.*
- (i) All confirmed UXO were separated into three groups (105-mm, 48-mm, and 37-mm) without further discriminating between the differences within each group. Each of the three groups was used to train a separate 1-component GMM classifier, which was then used to score all of the targets with a separate score for each of the target types (based on the features from the precise 3-object EMI inversion). The ground truth was then selected individually for each of the object types, based on a certain threshold score. This step helped resolve the possible biases arising from simultaneous treatment of all targets.
- (j) A total of 36 items were requested from a 105-mm scored data set, with 18 being already known; 174 items were requested from a 37-mm-scored data set, with 118 being already known; and 53 items were requested from a 48-mm-scored data set, with 27 of them being already known.
- (k) At this stage a total of 322 items were requested, 162 of which were UXO.
- (l) Finally, a 3-component GMM classifier was trained on the confirmed UXO and further used to score all of the unknown targets. A specific threshold was then selected and the final dig list produced. 100% of UXO were identified correctly, with a total of 295 non-TOI items (false positives). Total number of anomalies in the data set was 2291.

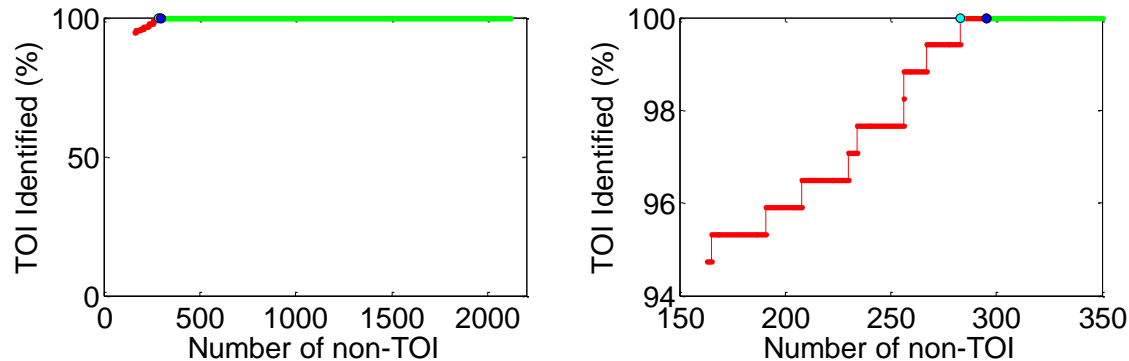


Figure 74: ROC curve for Camp Butner live site classification. 100% UXO were identified correctly, with only 295 false positive rate. The total number of anomalies is 2291. The blue dot corresponds to a threshold in the dig list, when the boundary between UXO and clutter was assumed after scoring. The cyan dot specifies the actual position of this boundary. In ideal circumstances the blue and cyan points will coincide. Performing extra digs, however, helps maintain better statistics and improve the results.

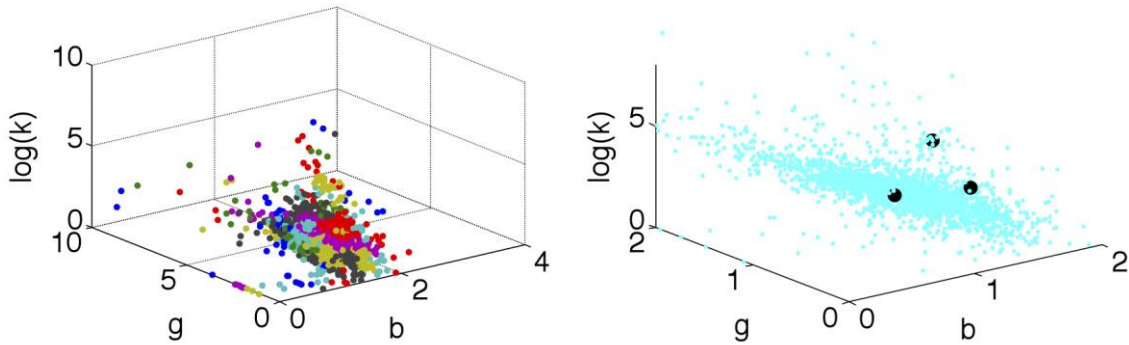


Figure 75: Camp Butner single-object inverted data clustering. *Left:* Results of weighted-linkage clustering using Mahalanobis distances for single-object inverted EMI features. *Right:* All four identified UXO (black) after a second clustering within a smaller domain ( $\log k \in [2;8]$ ,  $b \in [0.05;2]$ ,  $g \in [0.05;2]$ ) using Ward linkage and Euclidean distances.

Figure 75 shows the results of the first two clustering processes, corresponding to steps (a)–(d) above. Only four UXO targets were identified at this step: two 37-mm (with features very close to each other in Figure 75), one 48-mm and one 105-mm.

Figure 76 illustrates the training data used to create a 3-component GMM classifier in step (f) and the resulting score distribution histogram. The external interaction from the expert in this case consisted in selecting a threshold value for scoring beyond which the ground truth would be requested. We picked the value of  $\log(\text{score}) \sim 0.5$ , which resulted in the right peak in the histogram being probed, and yielded a high number of 118 confirmed UXO out of 131 probed items.

The newly acquired data was then used to re-train the GM-classifier (step g), using the features from a precise 3-object EMI inversion set (note that, since the 3-object inversion data set provides a set of

seven decay curves per anomaly, only the features closest to already identified UXO centroids were considered for GM training). The results of the updated GM-based clustering are demonstrated in Figure 77. The broadening of the histogram peak corresponding to UXO is observed. Based on the updated histogram, the ground truth from additional 20 suspicious items was requested to statistically challenge the classifier. The region was identified to be corresponding to  $\log(score)$  in the region between -6 and -5, based on the external input from the expert (visually observing the isosurfaces and how they encompass the existing UXO clusters, and considering the spread of the histogram peak corresponding to the UXO. This step can potentially be automated in the future to increase process efficiency). At this stage, if all of the 20 items were returned as clutter, the process would stop and the scored items would be used to create the final dig list. However, it turned out that 4 out of 20 items were UXO, and therefore the classifier had to be updated once again to ensure that all possible outliers were accounted for.

In order to resolve possible biases from simultaneous treatment of different types of targets, all confirmed UXO were separated into three categories based on their type (105-mm, 48-mm and 37-mm, without further discriminating between the differences within each group), and each group was used to train a separate 1-component GMM classifier, which was then used to score all of the targets with a separate score for each target type (step (i)). The ground truth was then selected individually for each of the object types, based on threshold score values that were identified visually, using external expert input, as before. Figure 78, Figure 79, and Figure 80 present the results obtained with these individual classifiers for 37-mm, 48-mm and 105-mm target clusters respectively.

The ground truth obtained as a result of steps (a) through (k) constituted 322 requested anomalies, with 160 of them being confirmed as UXO. At the final stage, a 3-component GMM classifier was trained on the confirmed UXO from the accumulated ground truth, and further used to score all of the unknown targets (Figure 81). A specific threshold was then selected manually and the final dig list produced. As a result, 100% of the UXO were identified correctly (Figure 74), with a total of 295 non-TOI items (false positives) exposed in the process (total number of anomalies in the data set was 2291).

The overall process yielded a successful ROC curve. In the future, the combined clustering and GMM algorithm should be researched for further improvement to automatically find ways for optimal data clustering, scoring and thresholding. While external inputs from an expert are valuable for guiding the learning process, it is desirable to minimize human involvement, reducing it to a system-wide quality check and classification control. For example, an ideal learning mechanism would first utilize all possible information contained in the data before delegating the crucial decision-making to human experts. Since humans are still better at some tasks involving pattern recognition, matching or classification, such a combined framework may result in overall improved performance and effective resource allocation.

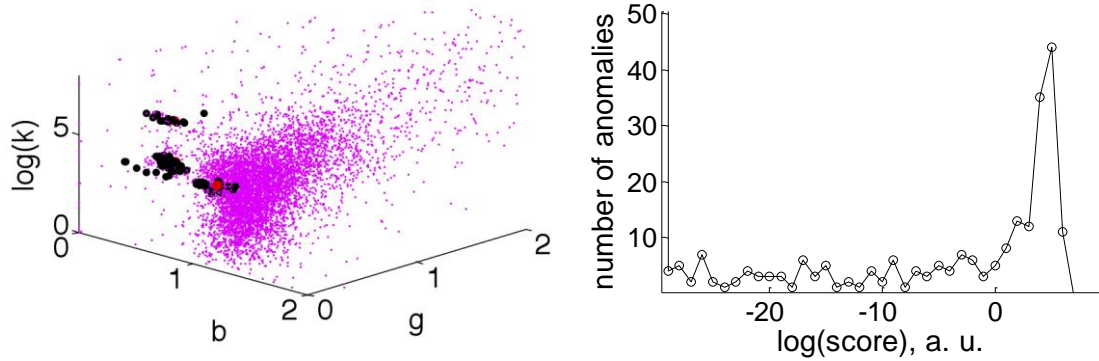


Figure 76: Camp Butner clusters used to train the first GM classifier and its results. *Left*: Assumed UXO clusters used to generate the 3-component GM classifier. *Right*: Score histogram showing the number of anomalies scored within a particular range of the log(probability density) in arbitrary units. The ground truth was requested based on thresholding the log(score) at the externally selected value of  $\sim 0.5$ .

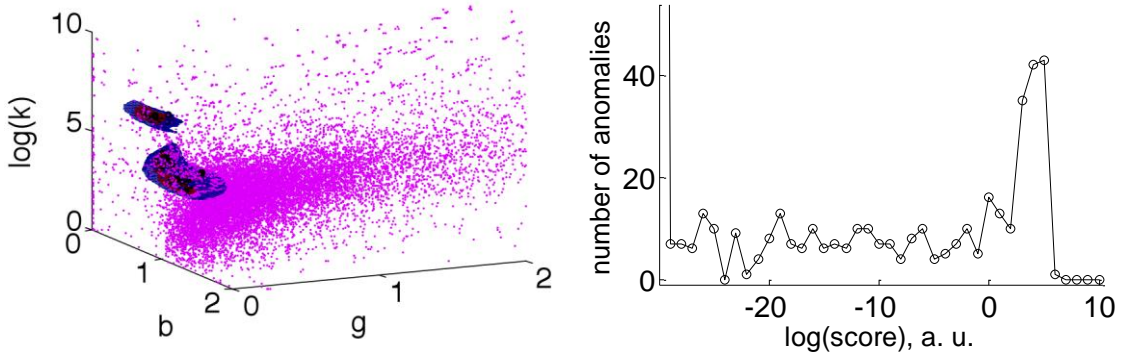


Figure 77: Updated GMM classifier after confirming 118 UXO in the Camp Butner data. *Left*: GM-classifier score iso-surfaces in the classification case based on all currently identified UXO targets (118 items), in the feature space corresponding to 3-object EMI inversion. *Right*: Updated score histogram showing the number of anomalies scored within a particular range of the log(probability density) in arbitrary units. An additional 20 items were requested for statistics to probe the region corresponding to  $\log(score)$  within  $[-6; -5]$  (this region was identified with external input from an expert by observing the corresponding score iso-surfaces and the histogram behavior).

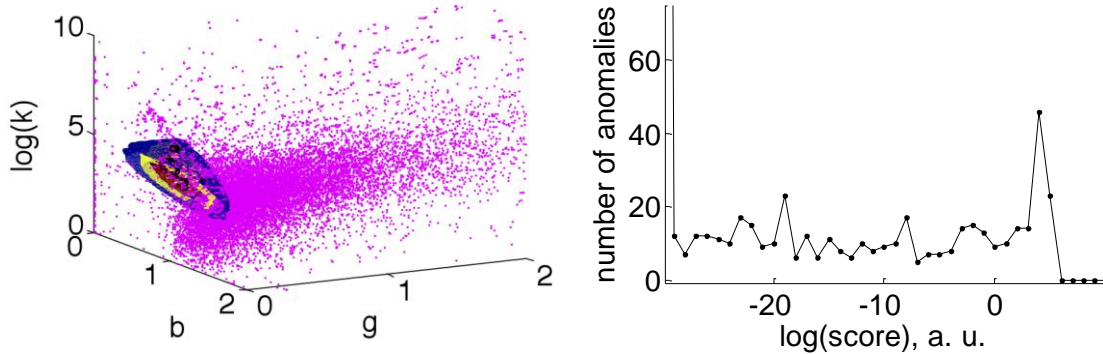


Figure 78: GMM classifier results for 37-mm targets. *Left*: 1-component GM-classifier score iso-surfaces in the classification case based solely on identified 37-mm UXO targets, in the feature space corresponding to 3-object EMI inversion. *Right*: Score histogram showing the number of anomalies scored within a particular range of the log(probability density) in arbitrary units. A total of 174 anomalies were requested (with 118 being already known) based on the  $\log(score)$  cut-off value of about  $-6$  (specified externally by an expert to allow enough statistics).

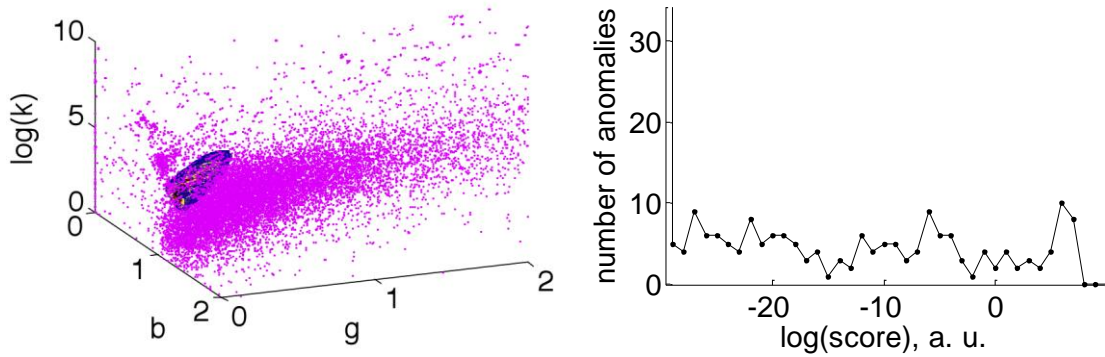


Figure 79: GMM classifier for 48-mm targets. *Left*: 1-component GM-classifier score iso-surfaces in the classification case based solely on identified 48-mm UXO targets, in the feature space corresponding to 3-object EMI inversion. *Right*: Score histogram showing the number of anomalies scored within a particular range of the  $\log(\text{probability density})$  in arbitrary units. A total of 53 anomalies were requested (with 27 being already known) based on the  $\log(\text{score})$  cut-off value of about  $-5$  (specified externally by an expert to allow enough statistics).

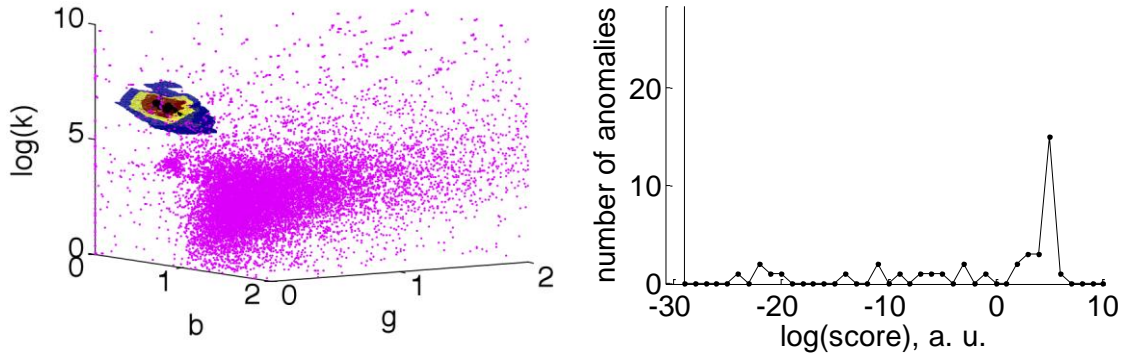


Figure 80: GMM classifier for 105-mm targets. *Left*: 1-component GM-classifier score iso-surfaces in the classification case based solely on identified 105-mm UXO targets, in the feature space corresponding to 3-object EMI inversion. *Right*: Score histogram showing the number of anomalies scored within a particular range of the  $\log(\text{probability density})$  in arbitrary units. A total of 36 anomalies were requested (with 18 being already known) based on the  $\log(\text{score})$  cut-off value was about  $-20$  (specified externally by an expert to allow enough statistics).

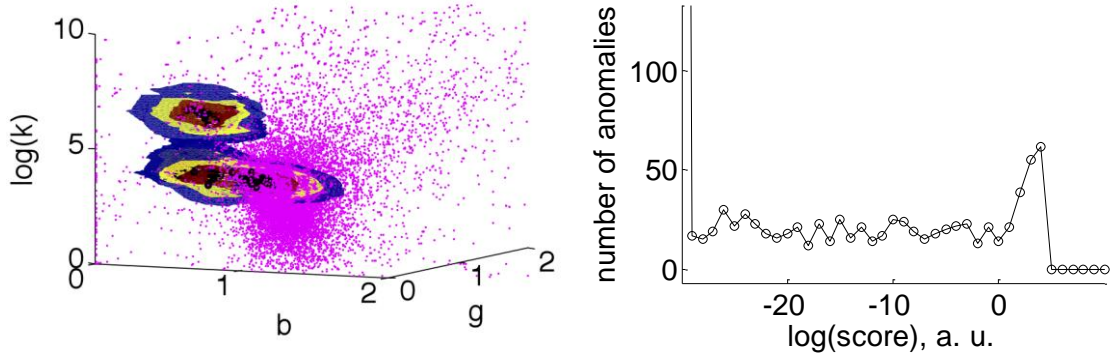


Figure 81: Final GMM classifier for Camp Butner. *Left*: 3-component GM-classifier score iso-surfaces in the classification case based on all identified UXO targets, in the feature space corresponding to 3-object EMI inversion. *Right*: Score histogram showing the number of anomalies scored within a particular range of the  $\log(\text{probability density})$  in arbitrary units. A total of 377 anomalies were scored as UXO based on the  $\log(\text{score})$  cut-off value of about  $-10$  (specified externally by an expert to allow enough statistics and iso-surface separation from identified UXO clusters).

#### *6.4.4.2 remarks*

A hierarchical agglomerative clustering approach followed by Gaussian mixture probabilistic modeling was applied in a blind-test format to a live UXO site Camp Butner. The ground truth for a total of 322 items was requested in a 5-level iterative prediction-correction process, resulting in 160 correctly identified UXO. A probabilistic GM model was then used for final scoring. Overall, this method yielded 100% accuracy in UXO detection, at a cost of 295-object false alarm rate (with a total number of buried anomalies of 2291). Machine-learning techniques therefore hold promise for high-quality automated UXO discrimination, reducing the expert workload and improving the process speed. Novel ways of process improvement can be studied in the future to reduce the false-alarm rate and improve overall classification quality. An attractive direction for further research is the creation of a UXO library containing the features extracted from UXO EMI curves from various live camps, and using this knowledge in the process of a new live site UXO identification in an automatic format, with minimal involvement by human experts.

## 7 Conclusions

Project MM-1572 supported the development of several innovative, robust, and noise-tolerant EMI forward models and statistical signal processing methodologies for use in subsurface target localization, characterization, and classification at live-UXO sites. In this report we have outlined the mathematical fundamentals, physical meaning, and practical realization of forward models such as the normalized surface magnetic source (NSMS) model (using both charges and dipoles as sources) and the orthonormalized volume magnetic source (ONVMS) technique. Both of these procedures have been seen to provide an accurate representation of the EMI responses of subsurface metallic targets. The models were combined with data-inversion approaches—gradient search, direct search/differential evolution, and the like—to invert data collected by current advanced EMI sensors. We also developed and used the HAP method for estimating target locations directly. In addition, we explored several advanced statistical signal processing and classification approaches—support vector machines, Gaussian mixture models, etc.—as possible tools for discriminating UXO from non-hazardous anomalies.

We adapted every model we developed to a complete suite of next-generation sensors, including the MetalMapper, TEMTADS, MPV, and BUD. Comparison between gradient search, DE, and HAP showed DE to be the most robust, noise-tolerant and reliable method to determine extrinsic parameters of targets; the procedure, moreover, requires no regularization, and works quite well when confronted with multi-target cases. For these reasons we consider DE to be our foremost choice to estimate target location and orientation. The combination of DE with the NSMS and ONVMS models was extensively tested on actual data and provided excellent agreement with the ground truth at every instance, regardless of the number of targets in the cell. The models were further combined with state-of-the-art classification algorithms and applied to live-UXO sites.

Initially, we tested the NSMS-HAP-SVM and NSMS-HAP-Gaussian combinations on EM-63 data taken by ESTCP over 216 test cells at Camp Sibert in Alabama. The Gaussian mixture model provided excellent classification performance, with neither false positives nor false negatives, while SVM had a tiny number of false alarms. In the next test we applied the NSMS-HAP and NSMS-DE combinations to TEMTADS data taken at the APG standardized test site. We found that the inverted classification feature parameters (the total NSMS in this case) were well-constrained for all objects and that the locations inverted using DE were in good agreement with the ground truth. There were 214 anomalies and six types of targets in the APG data set: 25-mm, 37-mm, 60-mm, 81-mm, and (two kinds of) 105-mm projectiles. For each cell we determined the total NSMS, extracted discrimination features from the NSMS decay curves, and classified the features using the Gaussian mixture model and a library-

matching technique with the help of test-stand and calibration data. The results of independent scoring were the following: 1) All UXO were correctly identified as such and correctly identified by type/caliber. 2) There was a false positive rate of ~5%.

The classification abilities of the NSMS-HAP and NSMS-DE algorithms in combination with the Gaussian mixture model and library matching were again put to the test with data taken at Camp San-Luis Obispo in California using TEMATDS, MM, and BUD. There were four types of TOI: 60-mm, 81-mm, 2.36", and 4.2" munitions. Comparisons between the different methods demonstrated NSMS-DE to be more robust and stable than NSMS-HAP when extracting extrinsic parameters from to actual live-site data sets, particularly in multi-target cases. This made us adopt DE as our "official" procedure for target pinpointing. The blind test at SLO showed that NSMS-DE can be combined with the Gaussian mixture model and library matching to reliably classify single well-separated targets and anomalies with high SNR. However, the method was unable to identify all targets correctly (it missed respectively one, five, and one targets for MM, TEMATDS, and BUD). We then conducted a retrospective study that clearly demonstrated the main difficulties at the SLO site: a low SNR and the abundance of multi-target cases. To address those issues we extended the NSMS technique, developed the ONVMS model, and adapted the JD method to next-generation sensors.

The ONVMS model assumes that measured secondary fields are due to a volume distribution of interacting magnetic dipoles; the corresponding Green functions are Gram-Schmidt orthonormalized to avoid the ill-conditioning and instabilities that plague multi-object inversion and to make the method run faster. The JD technique, based on diagonalizing a multi-static response matrix and associating the number of eigenvalues above a certain threshold with the number of illuminated targets, is reliable and robust and, since it requires no inversion, essentially instantaneous. Additionally, the eigenvalues allow one to perform a preliminary target discrimination.

The resulting ONVMS-DE-JD combined technique was first used to conduct a retrospective analysis of the SLO data. After that we applied the procedure to yet another ESTCP blind test, this one held at Camp Butner, North Carolina, using the MetalMapper and TEMTADS instruments. The TEMATDS and MM data were analyzed independently of each other. The total time-dependent ONVMS was extracted, inverted, and classified for each cell using ONVMS-DE-JD and both the Gaussian mixture model and library matching. Our results, scored by the Institute for Defense Analyses, consistently demonstrated that our methods do a superb job of classifying anomalies. There were no false negatives, and less than 5% of the anomalies had to be dug to achieve 100% correct classification. A high-quality automated UXO discrimination process based on machine-learning techniques has been demonstrated for reducing the expert workload and improving the process speed.

Both the SLO retrospective study and the Camp Butner blind test clearly demonstrated that the suite of advanced modeling and classification tools developed by our group are robust and noise-tolerant and provide excellent classification results using real-world data collected by next-generation EMI sensors. ONVMS proved superior to *NSMS and simple dipole model* for inversion and classification purposes and shall remain our preferred method of analysis. The ONVMS-DE-JD combination, supplemented by our classification algorithms, was further tested under ESTCP Project 201101 using MetalMapper, MPV, and  $2 \times 2$  3D TEMATDS data collected at Camp Beale in California. Not only were the advanced EMI models able to classify all “easy seed UXO items”, they also managed to identify all other targets, no matter how unexpected or site-specific, and as small as 3-cm fuzes [108].

## 8 Publications

### 8.1 Journal Articles

J. P. Fernández, F. Shubitidze, I. Shamatava, B. Barrowes, and K. O'Neill, "Realistic subsurface anomaly discrimination using electromagnetic induction and an SVM classifier," *EURASIP Journal on Advances in Signal Processing* vol. 2010, p. 305890, 2010.

F. Shubitidze, J. P. Fernández, I. Shamatava, L. R. Pasion, B. Barrowes, and K. O'Neill, "Application of the normalized surface magnetic source model to a blind unexploded ordnance discrimination test," *Applied Computational Electromagnetics Society Journal*, vol. 25, pp. 89–98, 2010.

D. Karkashadze, J. P. Fernández, and F. Shubitidze, "Scatterer localization using a left-handed medium," *Optics Express*, vol. 17, pp. 9904–9917, 2009.

### 8.2 Ph.D Thesis

Alex Bijamov "Numerical Methods in Electromagnetics: Evanescent Nanometry for DNA Sequencing, and EM Induction for UXO Detection and Discrimination", Ph.d Thesis, Dartmouth College, Thayer School of Engineering, Hanover, NH, September 2011.

### 8.3 Conference Papers

J. P. Fernández, B. E. Barrowes, A. Bijamov, T. M. Grzegorczyk, K. A. O'Neill, I. Shamatava, and F. Shubitidze, "Combining electromagnetic induction and automated classification in a UXO discrimination blind test," in R. S. Harmon, J. T. Broach, and J. H. Holloway, eds., *Detection and Sensing of Mines, Explosive Objects, and Obscured Targets XV, Proceedings of SPIE*, vol. 7664, p. 7664-02 (2010).

F. Shubitidze, J. P. Fernández, B. E. Barrowes, I. Shamatava, K. A. O'Neill, T. M. Grzegorczyk, and A. Bijamov, "Applying a volume dipole distribution model to next-generation sensor data for multi-object data inversion and discrimination," *Proceedings of SPIE*, vol. 7664, p. 7664-06 (2010).

F. Shubitidze, J. P. Fernández, I. Shamatava, B. E. Barrowes, K. A. O'Neill, and T. M. Grzegorczyk, "Comparison of the physically complete model with a simple dipole model for UXO detection and discrimination," *Proceedings of SPIE*, vol. 7664, p. 7664-07 (2010).

I. Shamatava, F. Shubitidze, J. P. Fernández, B. E. Barrowes, K. A. O'Neill, and T. M. Grzegorczyk, "SLO blind data set inversion and classification using physically complete models," *Proceedings of SPIE*, vol. 7664, p. 7664-03 (2010).

K. A. O'Neill, B. E. Barrowes, F. Shubitidze, J. P. Fernández, I. Shamatava, and T. M. Grzegorczyk, "Upward projection of EMI data for sensing of subsurface UXO in cluttered, multi-object cases," *Proceedings of SPIE*, vol. 7664, p. 7664-11 (2010).

J. P. Fernández, B. Barrowes, K. O'Neill, I. Shamatava, and F. Shubitidze, "A vector handheld frequency-domain sensor for UXO identification," in R. S. Harmon, J. T. Broach, and J. H. Holloway, eds., *Detection and Sensing of Mines, Explosive Objects, and Obscured Targets XIV, Proceedings of SPIE*, vol. 7303, p. 7303-31 (2009).

I. Shamatava, F. Shubitidze, B. Barrowes, J. P. Fernández, and K. O'Neill, "Physically complete models applied to the ESTCP Camp Sibert Pilot Study EM-63 data," *Proceedings of SPIE*, vol. 7303, p. 7303-23 (2009).

I. Shamatava, F. Shubitidze, B. Barrowes, J. P. Fernández, and K. O'Neill, "Physically complete models applied to BUD time-domain EMI data," *Proceedings of SPIE*, vol. 7303, 7303-22 (2009).

F. Shubitidze, B. Barrowes, J. P. Fernández, I. Shamatava, and K. O'Neill, "APG UXO discrimination studies using advanced EMI models and TEMTADS data," *Proceedings of SPIE*, vol. 7303, 7303-21 (2009).

F. Shubitidze, J. P. Fernández, B. E. Barrowes, I. Shamatava, and K. O'Neill, "Normalized Surface Magnetic Source model applied to Camp Sibert data: discrimination studies," in *Applied Computational Electromagnetics Symposium, ACES-2009* (Monterey, CA, March 8–12) (2009).

J. P. Fernández, F. Shubitidze, and D. Karkashadze, "Left-handed media as a tool to determine scatterer location," in *Applied Computational Electromagnetics Symposium, ACES-2009* (Monterey, CA, March 8–12) (2009).

F. Shubitidze, B. E. Barrowes, I. Shamatava, J. P. Fernández, and K. O'Neill, "Data-derived generalized SEA applied to MPV TD data", in *Applied Computational Electromagnetics Symposium, ACES-2008* (Niagara Falls, ON, March 30–April 4) (2009).

F. Shubitidze, E. Demidenko, B.E. Barrowes, I. Shamatava, J.P. Fernández, and K. O'Neill, "Combining dipole and mixed model approaches for UXO discrimination," in R.S. Harmon, J.T. Broach, and J.H. Holloway, eds., *Detection and Sensing of Mines, Explosive Objects, and Obscured Targets XIII, Proceedings of SPIE*, vol. 6953, p. 6953-04 (2008).

F. Shubitidze, B. Barrowes, I. Shamatava, J.P. Fernández, and K. O'Neill, "Application of the NSMS model to multi-axis time domain EMI data," in R.S. Harmon, J.T. Broach, and J.H. Holloway, eds.,

*Detection and Sensing of Mines, Explosive Objects, and Obscured Targets XIII, Proceedings of SPIE*, vol. 6953, p. 695302 (2008).

F. Shubitidze, J. P. Fernández, B. E. Barrowes, I. Shamatava, and K. O'Neill, "Combining NSMS and high-quality MPV-TD data for UXO discrimination," in *2008 IEEE International Geoscience & Remote Sensing Symposium* (Boston, MA, July 6-11) (2008).

F. Shubitidze, J. P. Fernández, B. E. Barrowes, I. Shamatava, "Rapid and accurate Estimate of the effect of magnetically susceptible soil on MPV-TD sensor data using the method of images", *DIPED-2008* (Tbilisi, Georgia, September 22–25) (2008).

## 8.4 Presentations and posters

F. Shubitidze, B. Barrowes, I. Shamatava, J. P. Fernández, and K. O'Neill, "Advanced EMI Forward and Statistical Signal Processing Approaches for UXO Discrimination," in *SERDP/ESTCP Partners in Environmental Technology Technical Symposium and Workshop*, (Washington, DC) (2008).

F. Shubitidze, B. Barrowes, K. O'Neill, I. Shamatava, and J. P. Fernández, "NSMC for UXO discrimination in cases with overlapping signatures," in *UXO/Countermine/Range Forum* (Orlando, FL, August 27–30) (2007).

F. Shubitidze, I. Shamatava, E. Demidenko, D. Karkashadze, "Advanced EMI forward and statistical signal processing approaches for UXO discrimination," in *SERDP/ESTCP Partners in Environmental Technology Technical Symposium and Workshop*, (Washington, DC, December 4–6) (2007).

## 9 References

1. I. Shamatava, F. Shubitidze, K. A. O'Neill, K. Sun, and K. D. Paulsen, "Simple magnetic charge model for representation of emi responses from a buried UXO," in *DIPED*, 2004, pp. 155-159.
2. F. Shubitidze, K. A. O'Neill, B. E. Barrowes, I. Shamatava, J. P. Fernández, K. Sun, and K. D. Paulsen, "Application of the normalized surface magnetic charge model to UXO discrimination in cases with overlapping signals," *Journal of Applied Geophysics*, vol. 61, pp. 292-303, 2007.
3. F. Shubitidze, K. O'Neill, I. Shamatava, K. Sun, and K. D. Paulsen, "A simple magnetic charge model for classification of multiple buried metallic objects in cases with overlapping signals," in *SAGEEP*, 2005.
4. F. Shubitidze, K. A. O'Neill, I. Shamatava, K. Sun, and K. D. Paulsen, "Combined differential evolution and surface magnetic charge model algorithm for discrimination of UXO from non-UXO items: simple and general inversions," in *SPIE*, 2005, p. 346.
5. J. D. Jackson, *Classical Electrodynamics*, 3rd ed. New York: Wiley, 1999.
6. S. D. Billings, "Practical Discrimination Strategies for Application to Live Sites," presented at the SERDP and ESTCP Partners in Environmental Technology Technical Symposium & Workshop, Washington, DC, 2006.
7. Y. Zhang, L. M. Collins, H. Yu, C. E. Baum, and L. Carin, "Sensing of unexploded ordnance with magnetometer and induction data: Theory and signal processing," *IEEE Transactions on Geoscience and Remote Sensing*, vol. 41, pp. 1005-1015, 2003.
8. W. Hu, S. L. Tantum, and L. M. Collins, "EMI-based classification of multiple closely spaced subsurface objects via independent component analysis," *IEEE Transactions on Geoscience and Remote Sensing*, vol. 42, pp. 2544-2554, Nov 2004.
9. E. Gasperikova, J. T. Smith, H. F. Morrison, A. Becker, and K. Kappler, "UXO detection and identification based on intrinsic target polarizabilities - A case history," *Geophysics*, vol. 74, pp. B1-B8, Jan-Feb 2009.
10. J. T. Smith and H. F. Morrison, "Optimizing receiver configurations for resolution of equivalent dipole polarizabilities in situ," *IEEE Transactions on Geoscience and Remote Sensing*, vol. 43, pp. 1490-1498, Jul 2005.
11. J. T. Smith and H. F. Morrison, "Estimating equivalent dipole polarizabilities for the inductive response of isolated conductive bodies," *IEEE Transactions on Geoscience and Remote Sensing*, vol. 42, pp. 1208-1214, Jun 2004.
12. T. H. Bell, B. J. Barrow, and J. T. Miller, "Subsurface discrimination using electromagnetic induction sensors," *IEEE Transactions on Geoscience and Remote Sensing*, vol. 39, pp. 1286-1293, 2001.
13. J. T. Miller, T. H. Bell, J. Soukup, and D. Keiswetter, "Simple phenomenological models for wideband frequency-domain electromagnetic induction," *IEEE Transactions on Geoscience and Remote Sensing*, vol. 39, pp. 1294-1298, 2001.

14. F. Shubitidze, B. E. Barrowes, J. P. Fernández, I. Shamatava, and K. A. O'Neill, "APG UXO discrimination studies using advanced EMI models and TEMTADS data," presented at the Detection and Sensing of Mines, Explosive Objects, and Obscured Targets XIV, Orlando, FL, 2009.
15. N. Geng, C. E. Baum, and L. Carin, "On the low-frequency natural response of conducting and permeable targets," *IEEE Transactions on Geoscience and Remote Sensing*, vol. 37, pp. 347-359, Jan 1999.
16. L. R. Pasion and D. W. Oldenburg, "A Discrimination Algorithm for UXO Using Time Domain Electromagnetics," *Journal of Environmental and Engineering Geophysics*, vol. 6, pp. 91-102, 2001.
17. G. A. Korn and T. M. Korn, *Mathematical Handbook for Scientists and Engineers*. New York: McGraw-Hill, 1968.
18. J. E. Gentle, *Matrix algebra : theory, computations, and applications in statistics*. New York, N.Y. ; London: Springer, 2007.
19. L.-P. Song, F. Shubitidze, L. R. Pasion, D. W. Oldenburg, and S. D. Billings, "Computing transient electromagnetic responses of a metallic object using a spheroidal excitation approach," *IEEE Geoscience and Remote Sensing Letters*, vol. 5, pp. 359-363, 2008.
20. J. P. Fernández, B. E. Barrowes, T. M. Grzegorczyk, N. Lhomme, K. A. O'Neill, and F. Shubitidze, "A Man-Portable Vector Sensor for Identification of Unexploded Ordnance," *IEEE Sensors Journal*, vol. 11, pp. 2542-2555, Oct 2011.
21. P. Comon, "Independent Component Analysis, a New Concept," *Signal Processing*, vol. 36, pp. 287-314, Apr 1994.
22. A. Belouchrani, K. AbedMeraiq, J. F. Cardoso, and E. Moulines, "A blind source separation technique using second-order statistics," *IEEE Transactions on Signal Processing*, vol. 45, pp. 434-444, Feb 1997.
23. S. Harmeling, A. Ziehe, M. Kawanabe, and K. R. Muller, "Kernel-based nonlinear blind source separation," *Neural Computation*, vol. 15, pp. 1089-1124, May 2003.
24. B. N. Flury and W. Gautschi, "An Algorithm for Simultaneous Orthogonal Transformation of Several Positive Definite Symmetrical-Matrices to Nearly Diagonal Form," *Siam Journal on Scientific and Statistical Computing*, vol. 7, pp. 169-184, Jan 1986.
25. J. F. Cardoso and A. Souloumiac, "Jacobi angles for simultaneous diagonalization," *Siam Journal on Matrix Analysis and Applications*, vol. 17, pp. 161-164, Jan 1996.
26. F. Shubitidze, B. E. Barrowes, K. O'Neill, I. Shamatava, and J. Fernández, "NSMC for UXO discrimination in cases with overlapping signatures," pp. 65530F-1.
27. B. E. Barrowes, K. A. O'Neill, T. M. Grzegorczyk, X. Chen, and J. A. Kong, "Broadband analytical magnetoquasistatic electromagnetic induction solution for a conducting and permeable spheroid," *IEEE Transactions on Geoscience and Remote Sensing*, vol. 42, pp. 2479-2489, 2004.

28. B. E. Barrowes, K. A. O'Neill, D. D. Snyder, D. C. George, and F. Shubitidze, "New man-portable vector time domain EMI sensor and discrimination processing," 2006.
29. F. Shubitidze, K. A. O'Neill, I. Shamatava, K. Sun, and K. D. Paulsen, "Analysis of EMI scattering to support UXO discrimination: heterogeneous and multiple objects," 2003, p. 928.
30. F. Shubitidze, K. A. O'Neill, I. Shamatava, K. Sun, and K. D. Paulsen, "Use of standardized source sets for enhanced EMI classification of buried heterogeneous objects," 2004, p. 263.
31. F. Shubitidze, K. A. O'Neill, I. Shamatava, K. Sun, and K. D. Paulsen, "Fast and accurate calculation of physically complete EMI response by a heterogeneous metallic object," *IEEE Transactions on Geoscience and Remote Sensing*, vol. 43, pp. 1736-1750, 2005.
32. K. Sun, K. A. O'Neill, F. Shubitidze, I. Shamatava, and K. D. Paulsen, "Fast data-derived fundamental spheroidal excitation models with application to UXO discrimination," *IEEE Transactions on Geoscience and Remote Sensing*, vol. 43, pp. 2573-2583, 2005.
33. R. Storn and K. Price, "Differential evolution - A simple and efficient heuristic for global optimization over continuous spaces," *Journal of Global Optimization*, vol. 11, pp. 341-359, Dec 1997.
34. R. Storn, "System design by constraint adaptation and differential evolution," *IEEE Transactions on Evolutionary Computation*, vol. 3, pp. 22-34, 1999.
35. H. Braunisch, C. O. Ao, K. A. O'Neill, and J. A. Kong, "Magnetoquasistatic response of conducting and permeable prolate spheroid under axial excitation," *IEEE Transactions on Geoscience and Remote Sensing*, vol. 39, pp. 2689-2701, 2001.
36. C. O. Ao, H. Braunisch, K. A. O'Neill, and J. A. Kong, "Quasi-magnetostatic solution for a conducting and permeable spheroid with arbitrary excitation," *IEEE Transactions on Geoscience and Remote Sensing*, vol. 40, pp. 887-897, 2002.
37. J. T. Smith, H. F. Morrison, and A. Becker, "Resolution depths for some transmitter-receiver configurations," *IEEE Transactions on Geoscience and Remote Sensing*, vol. 42, pp. 1215-1221, 2004.
38. B. E. Barrowes and H. Nelson, "Model-based characterization of electromagnetic induction signatures obtained with the MTADS electromagnetic array," *IEEE Transactions on Geoscience and Remote Sensing*, vol. 39, pp. 1279-1285, 2001.
39. D. W. Marquardt, "An Algorithm for Least-Squares Estimation of Nonlinear Parameters," *Journal of the Society for Industrial and Applied Mathematics*, vol. 11, pp. 431-441, 1963.
40. K. Levenberg, "A method for the solution of certain problems in least squares," *Quarterly of Applied Mathematics*, vol. 2, pp. 164-168, 1944.
41. J. E. Dennis and R. B. Schnabel, *Numerical methods for unconstrained optimization and nonlinear equations*. Philadelphia: Society for Industrial and Applied Mathematics, 1996.

42. K. Tavzarashvili, C. Hafner, X. D. Cui, R. Vahdieck, D. Karkashadze, and G. Ghvedashvili, "Model-based parameter estimation (MBPE) for metallic photonic crystal filters," *Applied Computational Electromagnetics Society Journal*, vol. 22, pp. 228-235, Jul 2007.
43. M. V. Berry, "Waves as catastrophes," *Physics Bulletin*, vol. 107, p. 108, 1976.
44. V. I. Arnold, *Catastrophe theory*: Springer, 1992.
45. N. Bliznyuk, R. J. Pogorzelski, and V. P. Cable, "Localization of Scattered Field Singularities in Method of Auxiliary Sources," in *Proceedings of the IEEE AP-S/URSI Symposium*, 2005.
46. A. G. Kyurkchan, B. Y. Sternin, and V. Shatalov, "Singularities of continuation of wave fields," *Physics-Uspekhi*, vol. 39, p. 1221, 1996.
47. J. D. McNeill and M. Bosnar, "Application of time domain electromagnetic techniques to UXO detection," 1996, pp. 34-42.
48. K. A. O'Neill, I. J. Won, A. Oren, F. Shubitidze, K. Sun, and I. Shamatava, "A new handheld vector EMI sensor with precise 3-D positioning," 2004.
49. J. A. Stratton, *Electromagnetic theory*, 1st ed. New York, London,: McGraw-Hill book company, inc., 1941.
50. R. S. Zaridze, G. Bit-Babik, K. Tavzarashvili, D. P. Economou, and N. K. Uzunoglu, "Wave field singularity aspects in large-size scatterers and inverse problems," *IEEE Transactions on Antennas and Propagation*, vol. 50, pp. 50-58, 2002.
51. F. Shubitidze, D. Karkashadze, B. E. Barrowes, I. Shamatava, and K. A. O'Neill, "A New Physics-based Approach for Estimating a Buried Object's Location, Orientation and Magnetic Polarization from EMI Data," *Journal of Environmental and Engineering Geophysics*, vol. 13, pp. 115-130, Sep 2008.
52. E. Gasperikova, J. T. Smith, H. F. Morrison, and A. Becker, "Berkeley UXO Discriminator (BUD)," 2007.
53. L. M. Collins, Y. Zhang, J. Li, H. Wang, L. Carin, S. J. Hart, S. L. Rose-Pehrsson, H. H. Nelson, and J. R. McDonald, "A comparison of the performance of statistical and fuzzy algorithms for unexploded ordnance detection," *IEEE Transactions on Fuzzy Systems*, vol. 9, pp. 17-30, Feb 2001.
54. A. J. van der Veen, M. C. Vanderveen, and A. Paulraj, "Joint angle and delay estimation using shift-invariance techniques," *IEEE Transactions on Signal Processing*, vol. 46, pp. 405-418, Feb 1998.
55. L. Beran and D. W. Oldenburg, "Selecting a discrimination algorithm for unexploded ordnance remediation," *IEEE Transactions on Geoscience and Remote Sensing*, vol. 46, pp. 2547-2557, 2008.
56. J. P. Fernández, K. Sun, B. E. Barrowes, K. A. O'Neill, I. Shamatava, F. Shubitidze, and K. D. Paulsen, "Inferring the location of buried UXO using a Support Vector Machine," presented at

the Detection and Remediation Technologies for Mines and Minelike Targets XII, Bellingham, WA, 2007.

57. A. Aliamiri, J. Stalnaker, and E. L. Miller, "Statistical Classification of Buried Unexploded Ordnance Using Nonparametric Prior Models," *IEEE Trans. Geosci. Remote Sens.*, vol. 45, pp. 2794-2806, September 2007.
58. S. J. Hart, R. E. Shaffer, S. L. Rose-Pehrsson, and J. R. McDonald, "Using physics-based modeler outputs to train probabilistic neural networks for unexploded ordnance (UXO) classification in magnetometry surveys," *IEEE Transactions on Geoscience and Remote Sensing*, vol. 39, pp. 797-804, 2001.
59. E. Demidenko, *Mixed models : theory and applications*. Hoboken, N.J.: Wiley-Interscience, 2004.
60. T. W. Anderson, *An introduction to multivariate statistical analysis*: John Wiley & Sons, 1958.
61. G. A. F. Seber and C. J. Wild, *Nonlinear regression* vol. 503: LibreDigital, 2003.
62. T. F. Cox and M. A. A. Cox, *Multidimensional scaling*, 2nd ed. Boca Raton: Chapman & Hall/CRC, 2001.
63. R. O. Duda, P. E. Hart, and D. G. Stork, *Pattern classification* vol. 2: wiley New York, 2001.
64. A. C. Rencher, *Methods of multivariate analysis*: Wiley New York, 1995.
65. B. D. Ripley, *Pattern recognition and neural networks*: Cambridge Univ Pr, 2008.
66. J. Chen and X. Tan, "Inference for multivariate normal mixtures," *Journal of Multivariate Analysis*, vol. 100, pp. 1367-1383, 2009.
67. C. Cortes and V. N. Vapnik, "Support-Vector Networks," *Machine Learning*, vol. 20, pp. 273-297, Sep 1995.
68. A. J. Smola and B. Schölkopf, "A tutorial on support vector regression," *Statistics and Computing*, vol. 14, pp. 199-222, August 2004.
69. C.-W. Hsu and C.-J. Lin, "A Comparison of Methods for Multiclass Support Vector Machines," *IEEE Trans. Neural Netw.*, vol. 13, pp. 415-425, 2002.
70. J. Byrnes, Ed., *Unexploded Ordnance Detection and Mitigation* (NATO Science for Peace and Security Series B: Physics and Biophysics. Dordrecht: Springer Netherlands, 2009, p.^pp. Pages.
71. J. P. Fernández, B. E. Barrowes, K. A. O'Neill, K. D. Paulsen, I. Shamatava, F. Shubitidze, and K. Sun, "Evaluation of SVM classification of metallic objects based on a magnetic-dipole representation," presented at the Detection and Remediation Technologies for Mines and Minelike Targets XI, Bellingham, WA, 2006.
72. X. Chen, "Inverse problems in electromagnetics," 2005.

73. B. Zhang, K. A. O'Neill, J. A. Kong, and T. M. Grzegorczyk, "Support vector machine and neural network classification of metallic objects using coefficients of the spheroidal MQS response modes," *IEEE Transactions on Geoscience and Remote Sensing*, vol. 46, pp. 159-171, Jan 2008.
74. E. Bermani, A. Boni, S. Caorsi, and A. Massa, "An Innovative Real-Time Technique for Buried Object Detection," *IEEE Trans. Geosci. Remote Sensing*, vol. 41, pp. 927-931, April 2003.
75. A. Massa, A. Boni, and M. Donelli, "A Classification Approach Based on SVM for Electromagnetic Subsurface Sensing," *IEEE Trans. Geosci. Remote Sensing*, vol. 43, pp. 2084-2093, September 2005.
76. A. B. Tarokh, E. L. Miller, I. J. Won, and H. Huang, "Statistical classification of buried objects from spatially sampled time or frequency domain electromagnetic induction data," *Radio Science*, vol. 39, Jun 12 2004.
77. M. A. Aizerman, E. M. Braverman, and L. I. Rozonoer, "Theoretical foundations of the potential function method in pattern recognition learning," *Automation and Remote Control*, vol. 25, pp. 821-837, 1964.
78. C. J. C. Burges, "A Tutorial on Support Vector Machines for Pattern Recognition," *Data Mining and Knowledge Discovery*, vol. 2, pp. 121-167, 1998.
79. O. L. Mangasarian and D. R. Musicant, "Lagrangian Support Vector Machines," *Journal of Machine Learning Research*, vol. 1, pp. 161-177, March 2001.
80. J. Mercer, "Functions of positive and negative type and their connection with the theory of integral equations," *Philos. Trans. Roy. Soc. London, A*, vol. 209, pp. 415-446, 1909.
81. E. Bermani, A. Boni, A. Kerhet, and A. Massa, "Kernels evaluation of SVM-based estimators for inverse scattering problems," *Progress in Electromagnetic Research*, vol. 53, 2005.
82. U. Kreßel, "Pairwise classification and Support Vector Machines," in *Advances in Kernel Methods: Support Vector Learning*, B. Schölkopf, *et al.*, Eds., ed Cambridge, MA: MIT Press, 1999, pp. 255-268.
83. M. Prouty, "Detection and Classification with the MetalMapper™ at Former Camp San Luis Obispo," presented at the ESTCP Project No. MM-0603, Geometrics, Inc, 2009.
84. ESTCP, "2009 ESTCP UXO Classification Study, Former Camp San Luis Obispo, CA," presented at the Environmental Security Technology Certification Program Demonstration Plan, Arlington, VA, 2009.
85. ESTCP, "2010 ESTCP UXO Classification Study, Former Camp Butner, NC," presented at the Environmental Security Technology Certification Program Demonstration Plan, Arlington, VA, 2010.
86. H. Nelson, K. Kaye, and A. Andrews, "ESTCP Pilot Program, Classification Approaches in Munitions Response," in *Environmental Security Technology Certification Program*, Arlington, VA, 2007.

87. F. Shubitidze, "Camp Butner UXO Data Inversion and Classification Using Advanced EMI Models," presented at the SERDP and ESTCP Partners in Environmental Technology Technical Symposium & Workshop, Washington, DC, 2010.
88. A. Paski, "Former Camp Butner Site Description and EM61 Data Collection and Analysis," presented at the SERDP and ESTCP Partners in Environmental Technology Technical Symposium & Workshop, Washington, DC, 2010.
89. L. R. Pasion, "UXO Discrimination Using Full Coverage and Cued Interrogation Data Sets at Camp Butner, NC," presented at the SERDP and ESTCP Partners in Environmental Technology Technical Symposium & Workshop, Washington, DC, 2010.
90. N. Cristianini and J. Shawe-Taylor, *An Introduction to Support Vector Machines and other Kernel-Based Learning Methods*. Cambridge: Cambridge University Press, 2000.
91. Y. Zhang, X. Liao, and L. Carin, "Detection of buried targets via active selection of labeled data: Application to sensing subsurface UXO," *IEEE Transactions on Geoscience and Remote Sensing*, vol. 42, pp. 2535-2543, 2004.
92. C.-C. Chang and C.-J. Lin, "(LIBSVM): a library for support vector machines," 2001.
93. F. Shubitidze, J. P. Fernández, B. E. Barrowes, I. Shamatava, and K. A. O'Neill, "Normalized Surface Magnetic Source Model Applied to Camp Sibert Data: Discrimination Studies," presented at the Applied Computational Electromagnetics Symposium (ACES), Monterey, CA, 2009.
94. F. Shubitidze, J. P. Fernández, I. Shamatava, L. R. Pasion, B. E. Barrowes, and K. A. O'Neill, "Application of the Normalized Surface Magnetic Source Model to a Blind Unexploded Ordnance Discrimination Test," *Applied Computational Electromagnetics Society Journal*, vol. 25, pp. 89-98, Jan 2010.
95. Q. Liu, X. Liao, and L. Carin, "Detection of unexploded ordnance via efficient semisupervised and active learning," *IEEE Transactions on Geoscience and Remote Sensing*, vol. 46, pp. 2558-2567, Sep 2008.
96. I. Shamatava, F. Shubitidze, B. E. Barrowes, J. P. Fernández, and K. A. O'Neill, "Physically complete models applied to BUD time-domain EMI data," presented at the Detection and Sensing of Mines, Explosive Objects, and Obscured Targets XIV, Orlando, FL, 2009.
97. S. D. Billings, "Discrimination and classification of buried unexploded ordnance using magnetometry," *IEEE Transactions on Geoscience and Remote Sensing*, vol. 42, pp. 1241-1251, 2004.
98. R. E. Grimm, "Triaxial Modeling and Target Classification of Multichannel, Multicomponent EM Data for UXO Discrimination," *Journal of Environmental and Engineering Geophysics*, vol. 8, pp. 239-250, 2003.
99. F. Shubitidze, D. Karkashadze, J. P. Fernández, B. E. Barrowes, K. O'Neill, T. M. Grzegorczyk, and I. Shamatava, "Applying a Volume Dipole Distribution Model to Next-Generation Sensor Data for Multi-Object Data Inversion and Discrimination," in *Proceedings of SPIE*, 2010.

100. D. Williams, Y. Yu, L. Kennedy, X. Zhu, and L. Carin, "A bivariate Gaussian model for unexploded ordnance classification with EMI data," *IEEE Geoscience and Remote Sensing Letters*, vol. 4, pp. 629-633, Oct 2007.
101. D. Williams, C. P. Wang, X. Liao, and L. Carin, "Classification of unexploded ordnance using incomplete multisensor multiresolution data," *IEEE Transactions on Geoscience and Remote Sensing*, vol. 45, pp. 2364-2373, Jul 2007.
102. Y. Zhang, L. M. Collins, and L. Carin, "Unexploded ordnance detection using Bayesian physics-based data fusion," *Integr. Comput.-Aided Eng.*, vol. 10, pp. 231-247, 2003.
103. J. H. Ward, "Hierarchical Grouping to Optimize an Objective Function," *Journal of the American Statistical Association*, vol. 58, pp. 236-&, 1963.
104. A. K. Jain and R. C. Dubes, *Algorithms for clustering data*. Englewood Cliffs, N.J.: Prentice Hall, 1988.
105. R. Xu and D. Wunsch, *Clustering*, 1 ed.: Wiley-IEEE Press, 2008.
106. G. N. Lance and W. T. Williams, "A General Theory of Classificatory Sorting Strategies. 2. Clustering Systems," *Computer Journal*, vol. 10, pp. 271-&, 1967.
107. P. C. Mahalanobis, "On the generalized distance in statistics," 1936, pp. 49-55.
108. F. Shubitidze, "Camp Beale Live-Site UXO Data Inversion and Classification Using Advanced EMI Models," Washington, DC2011.